BIOMATERIAL THERAPY STRATEGIES

FOR TREATING THE INFARCTED HEART

Cagla Eren Cimenci

A thesis submitted to the
University of Ottawa
in partial fulfillment of the requirements
for the Doctorate in Philosophy degree
in Cellular and Molecular Medicine

Department of Cellular and Molecular Medicine

Faculty of Medicine

The University of Ottawa

Acknowledgements

You know how it is. I feel extremely lucky and I want to thank every single person who helped me to create this thesis. I know not all can be mentioned, but none will be forgotten.

Firstly, I would like to give my most sincere gratitude to my supervisor, Dr. Erik Suuronen, for giving me the opportunity to work in his lab at the Ottawa Heart Institute, and for his excellent mentorship, guidance, trust and support all these years. I would not have been able to publish all that high-quality work without his feedback and strong work ethic. I truly could not have asked for a better supervisor.

I would also like to thank all of the members of my thesis advisory committee including Dr. Balwant Tuana, Dr. Alex Stewart and Dr. Emilio Alarcon who kept me on track. I appreciate all the feedback and guidance you have provided me throughout my PhD. Dr. Alarcon is worthy of a special mention for always keeping his doors open whenever I need a discussion. Thanks Emilio, for always caring and for supporting my personal and professional development.

I would like to thank Dr. Chao Deng, Dr. Zhiyuan Zhong and Dr. Jing Chen at the Soochow University, China for graciously hosting me in Suzhou for almost 2 months and teaching me new techniques. I am forever grateful for this deeply cherished experience.

I would like to thank the current and former members of the BEaTS research group for their constant support and for creating a very positive lab environment. I would like to especially thank Dr. Brian McNeill and Dr. Nick Blackburn for mentoring me and making my first year easier in Canada. I would also like to thank Dr. Veronika Sedlakova, Dr. Marcelo Munoz, Dr. Justina Pupkaite, Dr. Sarah McLaughlin, Dr. Hiroki Takaya, Dr. Christopher McTiernan, Dr.

Godwin Dogbevia, Danielle Giroux, Ashley Baldwin, Madison Bak, Nicole MacMullin, Ines Amara, Alex Ross and Xixi Guo for their help, support, guidance and encouragement. I would also like to express profound gratitude to Rick Seymour, Vivian Franklin, and the animal care team from the University of Ottawa Heart Institute.

I would also like to express my most sincere thanks to my best friends/lab-mates Mayté Gonzalez-Gomez and Irene Guzmán-Soto for always being there when I needed to talk and for sharing endless laughs and coffee breaks with me. Your loving hearts will always be with mine no matter where we are in the world. Special shout-out to Mayté for designing ToC figures of my articles. She has the talent, she has the eye and she always pushes herself to excel each and every time in her art. I owe you a lot Maytécita.

And last but not least, I wish to express my deepest gratitude to my family members. Thanks mom, Başak and Can for always supporting my adventures and for cheering me up from 5000 miles away. You are my inspiration. Hepinizi çok seviyorum, iyi ki benim ailemsiniz.

I want to dedicate this thesis to my husband, Kadir Çimenci, who has been a constant source of support and encouragement during the challenges in our new life and graduate school. Thank you for being there for me always. I am truly thankful for having you in my life; my love for you can never be quantified.

Finally, I would like to send big thanks to all my friends in Ottawa, Istanbul, and Ankara. You make my life colorful.

I love you with all my heart.

Çağla

Sources of Funding

This thesis work was supported by a Collaborative Research Grant from the Canadian Institutes of Health Research (CIHR; CPG-158280) and the Natural Sciences and Engineering Research Council (NSERC; 523794-18) to Erik Suuronen, Emilio Alarcon, and Marc Ruel. Cagla Eren Cimenci was funded by Queen Elizabeth II Scholarships in Science and Technology (QEII-GSST) and Graduate Scholarship from the University of Ottawa Cardiac Endowment Fund.

Article III: This work was made possible by funding from the Natural Sciences and Engineering Research Council (NSERC) RGPIN-2015-0632 to EIA. This work was also supported by a Collaborative Health Research Program grant from the Canadian Institutes of Health Research (CPG-158280) and the Natural Sciences and Engineering Research Council (CHRP 523794-18) (to EJS, EIA and MR). EIA thanks the New Frontiers Research Program Exploration fund and the Government of Ontario for an Early Career Research Award. CEC was supported by a Graduate Scholarship from the University of Ottawa Cardiac Endowment Fund. MM thanks the University of Ottawa Heart Institute and the Strategic Research Endowed Funds for a Strategic Research Postdoctoral Fellowship.

Disclosure

Erik Suuronen, Emilio Alarcon and Marc Ruel are listed inventors on a patent application for the recombinant human collagen materials presented in this study.

Patent applicant: Ottawa Heart Institute Research Corporation, 40 Ruskin Street H2406 Ottawa, Ontario K1Y 4W7, Canada.

Application number: PCT/CA2018/050537.

Status of the application: Published as WO/2018/201260.

The specific aspect of this thesis covered in the patent application: Composition of matter for the hydrogel, a method for regenerating or repairing heart tissue, the method for preparing the composition of matter or the hydrogel, and the use of the hydrogel.

Table of Contents

Acknowledgements ii

Sources of Funding iv

Disclosure v

Table of Contents vi

List of TOC Illustrations x

List of Figures x

List of Abbreviations and Acronyms xii

Abstract xvii

List of Publications Covered in This Thesis and Contribution Statements xix

Additional Publications - Not Included in This Thesis xxi

1 General Introduction 1

1.1 Myocardial Infarction and Heart Failure 1

1.2 Phases of Infarct Evolution 2

1.3 The Role of Cardiac ECM 5

1.4 Methylglyoxal, Advanced Glycation End-products and Glyoxalase-1 Enzyme 8

1.5 Antioxidant Molecules and Fisetin 11

1.6 Biomaterial Therapies for Cardiac Regeneration 13

1.7 Nanoparticle Technology 16

2 Rationale, Hypotheses and Aims 17

3 Article I - Combined Methylglyoxal Scavenger and Collagen Hydrogel Therapy Prevents Adverse Remodeling and Improves Cardiac Function Post-Myocardial Infarction 18

Article I - Abstract 19

3.1 Introduction 20

3.2 Results 23

3.2.1 Fisetin-HG Characterization 23

3.2.2 Effect of Fisetin-HG on Cell Viability, Angiogenesis and Intracellular MG Level 24

3.2.3 HG Delivery Increases Retention of Fisetin 27

3.2.4 Fisetin-HG Matrix Improves Cardiac Function Post-MI 28

3.2.5 Fisetin-HG Treatment Reduces Scar Size and Prevents Cell Death 31

3.2.6 Fisetin-HG Improves Vascular Density, Reduces Inflammation, and Promotes Polarization of Pro-Wound Healing Macrophages 33

3.2.7 Fisetin-HG Treatment Reduces MG-AGEs and Oxidative Stress Post-MI 34

3.3 Discussion 38

3.4 Conclusion 45

3.5 Experimental Section 45

3.6 Supporting Information 56

3.7 Acknowledgements 56

4 Article II – Targeted delivery of glyoxalase-1 loaded nanoparticles reduces methylglyoxal and improves cardiac function after myocardial infarction 57

Article II – Abstract 57

4.1 Introduction 58

4.2 Results 60

4.2.1 Characterizations of Empty and Glo1-loaded NPs 60

4.2.2 *In vitro* Assessment of Glo1-NP Treatment on ECs 62

4.2.3 MG Exposure Increases CD44 Expression in ECs 64

4.2.4 CD44 Receptor is Responsible for Nanoparticle Uptake 64

4.2.5 Glo1-NPs Improve Cardiac Function Post-MI 66

4.2.6 Glo1-NPs Find Their Target When Delivered Intravenously 69

4.2.7 Glo1-NP Treatment Reduces Scar Size and Prevents Cell Death 69

4.2.8 Glo1-NP Treatment Reduces Inflammation and Promotes the Recruitment of Pro-Wound Healing Macrophages 72

4.2.9 Glo1-NPs Increase Glo1 levels in MI hearts 73

4.2.10 Glo1-NPs Inhibit MG-AGEs and Oxidative Stress Post-MI 74

4.3 Discussion 76

4.4 Conclusion 81

4.5 Experimental Section 82

4.6 Acknowledgements 90

5 Article III – Nanoengineered Sprayable Therapy for Treating Myocardial Infarction 91

Article III – Abstract 91

5.1 Introduction 93

5.2 Results and Discussion 94

5.2.1 Custom designed peptides for nanogold 94

5.2.2 Spray-on miniaturization and optimization 97

5.2.3 *In vitro* and *in vivo* performance of the spray-on nanotherapeutic 100

5.2.4 Spray-on nanotherapeutic application improves vascularization and increases number of pro-healing macrophages 106

5.2.5 Spray-on nanotherapeutic application increases number of cardiomyocytes and supports gap junction formation in the border zone post-MI 108

5.3 Conclusion 116

5.4 Experimental Section 117

5.5 Supporting Information 126

5.6 Acknowledgements 126

6 General Discussion 127

7 Conclusions 133

8 Appendices 134

8.1 Supplementary Information for Article I 134

8.2 Supplementary Information for Article III 138

References 151

List of TOC Illustrations

Table of Content (TOC) Illustration of Article I 20

Table of Content (TOC) Illustration of Article II 58

Table of Content (TOC) Illustration of Article III 92

List of Figures

Figure 1.1 Illustration of ventricular remodeling after myocardial infarction. 4

Figure 1.2 Cardiac ECM and cell composition. 7

Figure 1.3 Methylglyoxal and Glyoxalase System. 10

Figure 1.4 Fisetin reduces MG levels by upregulating Nrf2 or direct MG scavenging. 12

Figure 1.5 Biomaterial-based applications for cardiac tissue engineering. 15

Figure 3.1 Hydrogel characterization. 24

Figure 3.2 Viability and angiogenesis results. 26

Figure 3.3 HG delivery increases fisetin retention in the heart post-MI 28

Figure 3.4 Fisetin-HG improves cardiac function and contractility post-MI. 30

Figure 3.5 Assessment of morphology and cell death in tissue sections. 32

Figure 3.6 Fisetin-HG treatment increases myocardial vascularity. 34

Figure 3.7 Fisetin-HG treatment promotes pro-healing macrophage polarization. 36

Figure 3.8 Fisetin-HG treatment reduces oxidative stress. 37

Figure 4.1 Synthesis and characterization data of nanoparticles. 61

Figure 4.2 Viability and adhesion of Glo1-NP treated ECs..... 63

Figure 4.3 Representative immunostaining images of CD44 expression and NP accumulation in cultured ECs. 66

Figure 4.4 Glo1-NP treatment improves cardiac function and contractility post-MI. 69

Figure 4.5 In vivo delivery of Glo1-NPs and histology analyses post-MI. 71

Figure 4.6 Glo1-NP treatment promotes anti-inflammatory macrophage recruitment at 4 weeks post-MI. 73

Figure 4.7 Glo1-NP treatment increased Glo1 levels and reduced oxidative stress. 75

Figure 5.1 Gold Nanoparticle Characterizations. 96

Figure 5.2 Spray-on Nozzle Design..... 99

Figure 5.3 *In vivo* applications of spray-on treatment. 102

Figure 5.4 Multi-AuNP treatment reduces the scar size *in vivo*. 105

Figure 5.5 Assessment of vascularization and macrophages. 107

Figure 5.6 Connexin 43 staining and quantification. 109

List of Abbreviations and Acronyms

ACC	Animal care committee
ACS	Acute Coronary Syndrome
AF	Alexa Fluor
AGEs	Advanced Glycation End Products
AKT	Protein Kinase B
ANOVA	Analysis of Variance
AP-1	Activator Protein 1
ARE	Anti-oxidant Response Element
ATP	Adenosine Triphosphate
AuNP	Gold Nanoparticles
AVC	Aortic Valve Closure
Calcein AM	Calcein Acetoxymethyl Ester
CABG	Coronary Artery Bypass Grafting
CAD	Computer Aided Design
CD44	Cluster of Differentiation 44
CLKRS peptide	Cysteine-leucine-lysine-arginine-serine peptide
CO	Cardiac Output
CS	Chondroitin Sulfate
cTnT	Cardiac Troponin T
CVD	Cardiovascular Disease
Cx43	Connexin 43

DAPI	4′,6-diamidino-2-phenylindole
DIC	Differential Isothermal Calorimetry
DLS	Dynamic Light Scattering
DMEM	Dulbecco's Modified Eagle Medium
EB	Evans Blue
ECG	Electrocardiogram
Echo	Echocardiogram
ECM	Extracellular Matrix
ECs	Endothelial Cells
EDC	1-Ethyl-3-(3-Dimethylaminopropyl) Carbodiimide Hydrochloride
EDV	End Diastolic Volume
ELISA	Enzyme-Linked Immunosorbent Assay
ESV	End Systolic Volume
EthD-1	Ethidium Homodimer-1
FAC	Fractional Area Change
FBS	Fetal Bovine Serum
FETEM	Field Emission Transmission Electron Microscopy
Fisetin-HGs	Fisetin-loaded Hydrogels
FOV	Field of View
FS	Fractional Shortening
Glo1	Glyoxalase-1
Glo1-NP(s)	Glyoxalase-1-loaded Nanoparticle(s)

GSH	Glutathione
GSSG	Oxidized Glutathione
HA	Hyaluronic Acid
HEPES	4-(2-hydroxyethyl)-1-piperazineethanesulfonic acid
HF	Heart Failure
HGs	Hydrogels
HKR	HEPES-Krebs-Ringer's buffer
HUVEC	Human Umbilical Vein Endothelial Cell
ICP	Induced Couple Plasma
ICP-MS	Inductively coupled plasma mass spectrometry
IL-6	Interleukin 6
IVC	Inferior Vena Cava
IVIS	*In vivo* Imaging Systems
JNK	c-Jun N-terminal Kinase
LAD	Left Anterior Descending Coronary Artery
LV	Left Ventricle
LVEF	Left Ventricular Ejection Fraction
MBo	Methyl Diaminobenzene-BODIPY
MES	2-(N-morpholino)ethanesulfonic acid
MG	Methylglyoxal
MG-AGEs	Methylglyoxal Derived Advanced Glycation End Products
MG-H1	MG-derived hydroimidazolone-1

MI	Myocardial Infarction
MMP	Matrix Metalloproteinase
MRM	Multi Reaction Monitoring Analysis
NF-κB	Nuclear Factor Kappa B
NHS	N-hydroxysuccinimide
NP(s)	Nanoparticle(s)
Nrf2	Nuclear factor erythroid 2-related
NRG	Neuregulin
PBS	Phosphate Buffered Saline
PDI	Polydispersity Index
PECAM-1	Platelet Endothelial Cell Adhesion Molecule-1
PFA	Paraformaldehyde
PI3K	Phosphatidylinositol 3-kinase
PPAR-γ	Peroxisome proliferator- activated receptor gamma
PVDF	Polyvinylidene difluoride
RIPA Buffer	Radioimmunoprecipitation Assay Buffer
ROS	Reactive Oxygen Species
SD	Standard Deviation
SEM	Standard Error of the Mean
Src Kinase	Sarcoma Kinase
STEMI	ST-Elevation Myocardial Infarction
SV	Stroke Volume

Syk	Spleen tyrosine kinase
TBS	Tris-buffered saline
TCEP	Tris(2-carboxyethyl)phosphine
TCP	Tissue Culture Polystyrene
TEM	Transmission Electron Microscopy
TIMP	Tissue Inhibitor of Matrix Metalloproteinase
TNF-α	Tumor Necrosis Factor-Alpha
TUNEL	Terminal deoxynucleotidyl transferase dUTP nick end labeling
UPLC	Ultra Performance Liquid Chromatography
UV-vis	Ultraviolet–visible Spectroscopy
WGA	Wheat Germ Agglutinin
α-SMA	Alpha Smooth Muscle Actin

Abstract

Ischemic cardiomyopathies, such as myocardial infarction (MI), are a leading cause of heart failure in both men and women throughout the world. Despite timely intervention post-MI, the loss of viable myocardium can lead to global remodeling and loss of function in many patients due to the limited regenerative potential of heart tissue. Thus, there is a critical need to better understand the repair mechanisms involved and to develop new preventative and reparative therapies for treating MI and preventing progression to heart failure.

Methylglyoxal (MG) is a highly reactive dicarbonyl metabolite of glycolysis and the main precursor of advanced glycation end-products (AGEs), which can cause oxidative stress and wound healing delay. MG was shown to play an important causative role in the cellular changes, adverse remodeling and functional loss of the infarcted heart. This suggests MG as a target for therapy to restore cell-ECM signaling, inhibit oxidative stress and improve cardiac function post-MI.

The aim of this PhD project was to develop new biomaterial therapies that can reduce the effects of MG, decrease oxidative stress, enhance electrical conductivity and improve cardiac contractility and function post-MI. There were three primary objectives: **1)** To develop an injectable antioxidant and hydrogel system for minimizing the effects of MG and promoting cardiac repair post-MI; **2)** To synthesize a nanoparticle system for targeted delivery of Glyoxalase-1 (Glo1) enzyme to cardiac tissue for reducing the accumulation of MG, limiting adverse remodeling and preserving cardiac function following MI; and **3)** To design a sprayable nano-therapeutic that uses surface engineered custom designed multi-armed peptide grafted nanogold for on-the-spot coating of infarcted myocardial surface for increasing contractility of the myocardium post-MI.

In the first study, a fisetin-loaded collagen type I hydrogel (fisetin-HG) was injected intramyocardially in mice at 3h post-MI, and compared to fisetin-alone, hydrogel-alone, or saline treatment. The fisetin-HG treatment increased the level of glyoxalase-1 (the main MG-metabolizing enzyme), reduced MG-AGE accumulation, and decreased oxidative stress in the MI heart, which was associated with smaller scar size and improved cardiac function. Treatment with fisetin-HG also promoted neovascularization and increased the number of pro-healing macrophages in the infarct area, while reducing the number of pro-inflammatory macrophages.

The second study revealed that when delivered intravenously at 3h post-MI, our Glo1-loaded nanoparticles specifically targeted the damaged cardiac tissue, led to improved cardiac function, protected cell viability and limited infarct expansion by reducing oxidative stress post-MI.

Lastly, the third study showed that, when applied at 1-week post-MI, the sprayed nanogold treatment remained at the treatment site for at least 28 days with no significant off-target organ infiltration. Our results demonstrated a remarkable increase in cardiac function, muscle contractility, and myocardial electrical conductivity post-MI.

Overall, these findings show that reducing MG levels through both increased activity of Glo1 and direct MG scavenging as well as increasing cardiac contractility may be a promising approach to limit adverse cardiac remodeling, prevent damage, and preserve function of the infarcted heart.

List of Publications Covered in This Thesis and Contribution Statements

Article I: Eren Cimenci C., Blackburn N.J.R., Sedlakova V., Pupkaite J., Munoz M., Rotstein B.H., Spiegel D.A., Alarcon E.I., Suuronen E.J., *Combined Methylglyoxal Scavenger and Collagen Hydrogel Therapy Prevents Adverse Remodeling and Improves Cardiac Function Post-Myocardial Infarction*. Advanced Functional Materials. 2021 Oct 12; doi doi.org/10.1002/adfm.202108630

C.E.C., N.J.R.B. and E.J.S. designed the study. C.E.C., V.S., J.P. and M.M. performed the lab work and data analyses. D.S. provided expertise and reagents for MBo studies. E.J.S. and E.I.A. supervised the trainees and coordinated the experiments. The manuscript was written by C.E.C and E.J.S. through contributions from all authors. All authors have reviewed and approved the final version of the manuscript.

Article II: Eren Cimenci C., Chen J., Bak M., Baldwin A., Labranche E., Deng C., I. Alarcon E.I., Zhong Z., Suuronen E.J. *Targeted delivery of glyoxalase-1 loaded nanoparticles reduces methylglyoxal and improves cardiac function after myocardial infarction.*

C.E.C and E.J.S designed the study. C.E.C planned and performed the experimental work and wrote the manuscript through contributions from all authors. J.C. helped with the nanoparticle synthesis and characterizations. C.D and Z.Z provided the precursor molecules and supervised the design and synthesis of nanoparticles. M.B. assisted with the nanoparticle synthesis and confocal microscopy. A.B and E.L helped with the histological staining, slide scanner microscopy imaging and data analyses. E.I.A provided expertise and guidance on chemical processes and nanoparticles. E.J.S coordinated the study, supervised the trainees and proofread the manuscript. All the authors read and approved the final version of this manuscript.

<u>Article III</u>: Eren Cimenci C[±]., Muñoz M.[±], Goel K., Comtois-Bona M., Hossain M., McTiernan C. D., Zuñiga-Bustos M., Ross A., Truong B., Davis D. R., Liang W., Rotstein B., Ruel M., Poblete H., Suuronen E.J., Alarcon E. I.. *Nanoengineered Sprayable Therapy for Treating Myocardial Infarction*. ACS Nano.

Accepted for publication at the time of thesis submission. ACS Manuscript ID: nn-2021-08890w.

C.E.C and M.M. share first authorship for this manuscript. C.E.C., Planned and performed *in vitro, in vivo,* and *ex vivo* work, and conducted data analyses; M.M., Designed the peptides, planned the study, performed the characterizations, and conducted data analyses; K.G., Assessed the *in vitro* work for the peptide stability; M.C-B. and M.H., Designed and optimized the spray-on nozzle device; C.D.M., Assisted with the nozzle optimization and conducted *in vivo* experiments; M.Z-B., Conducted the molecular simulations and data analysis; A.R., Synthesized the peptides and assessed the stability assays for the peptides; B.T., Assessed the *in vitro* toxicity of the materials; D.R.D., and W.L. Supervised the ECG data collection and analysis; B.R., Supervised the design, synthesis and characterization of the peptides; M.R., Supervised functional cardiac data collection and analysis; H.P. Supervised the molecular dynamic simulation; E.J.S. and E.I.A., Designed the study, coordinated the project execution, supervised trainees, and wrote the manuscript jointly with M.M. and C.E.C. All the authors read and approved the final version of this manuscript.

Additional Publications - Not Included in This Thesis

- Blackburn NJR, Vulesevic B, McNeill B, **Eren Cimenci C**, Ahmadi A, Gonzalez-Gomez M, Ostojic A, Zhong Z, Brownlee M, Beisswenger PJ, Milne RW, Suuronen EJ. Methylglyoxal-derived advanced glycation end products contribute to negative cardiac remodeling and dysfunction post-myocardial infarction. *Basic Research in Cardiology*. **2017** Sep 1;112(5):57. doi: 10.1007/s00395-017-0646-x. PMID: 28864889.
- Lazurko C, Khatoon Z, Goel K, Sedlakova V, **Eren Cimenci C**, Ahumada M, Zhang L, Mah TF, Franco W, Suuronen EJ, Alarcon EI. Multifunctional Nano and Collagen-Based Therapeutic Materials for Skin Repair. *ACS Biomaterials Science and Engineering*. **2020** Feb 10;6(2):1124-1134. doi: 10.1021/acsbiomaterials.9b01281. Epub 2020 Jan 7. PMID: 33464871.
- Jacques E, Hosoyama K, Biniam B, **Eren Cimenci C**, Sedlakova V, Steeves AJ, Variola F, Davis DR, Stewart DJ, Suuronen EJ, Alarcon EI. Collagen-Based Microcapsules As Therapeutic Materials for Stem Cell Therapies in Infarcted Myocardium. ACS *Biomaterials Science and Engineering*. **2020** Aug 10;6(8):4614-4622. doi: 10.1021/acsbiomaterials.0c00245. Epub 2020 Jun 22. PMID: 33455166.
- Pupkaite J, Sedlakova V, **Eren Cimenci C**, Bak M, McLaughlin S, Ruel M, Alarcon EI, Suuronen EJ. Delivering More of an Injectable Human Recombinant Collagen III Hydrogel Does Not Improve Its Therapeutic Efficacy for Treating Myocardial Infarction. *ACS Biomaterials Science and Engineering*. **2020** Jul 13;6(7):4256-4265. doi: 10.1021/acsbiomaterials.0c00418. Epub 2020 Jun 22. PMID: 33463355.
- Muñoz M, Comtois-Bona M, Cortes D, **Eren Cimenci C**, Du Q, Thompson C, Figueroa JD, Franklin V, Liu P, Alarcon EI. Integrated photothermal decontamination device for

N95 respirators. *Scientific Reports*. **2021** Jan 19;11(1):1822. doi: 10.1038/s41598-020-80908-8. PMID: 33469049; PMCID: PMC7815715.

- Munoz M, El-Khoury A, **Eren Cimenci C**, Gonzalez-Gomez M, Hunter RA, Lomboni D, Variola F, Rotstein BH, Vono LLR, Rossi LM, Edwards AM, Alarcon EI. Riboflavin Surface Modification of Poly(vinyl chloride) for Light-Triggered Control of Bacterial Biofilm and Virus Inactivation. *ACS Applied Materials Interfaces*. **2021** Jul 14;13(27):32251-32262. doi: 10.1021/acsami.1c08042. Epub 2021 Jun 28. PMID: 34181389.
- Razavipour, M., Gonzalez, M., Singh, N., **Eren Cimenci C**., Chu N., Alarcon EI., Villafuerte J., Jodoin B. Biofilm Inhibition and Antiviral Response of Cold Sprayed and Shot Peened Copper Surfaces: Effect of Surface Morphology and Microstructure. *Journal of Thermal Spray Technology*. **2022** https://doi.org/10.1007/s11666-021-01315-7

1 General Introduction

1.1 Myocardial Infarction and Heart Failure

Cardiovascular disease is a condition that involves the impaired function of the heart and/or blood vessels. It is a leading cause of death of both men and women throughout the world resulting in over 17 million annual deaths.[1,2] Myocardial infarction (MI), also known as a heart attack, occurs due to occlusion of one of the coronary arteries that supply the oxygen-rich blood to the heart muscle which leads to the formation of a fibrotic collagen scar and such scar substitutes the dead cardiac area post-MI.[3] However, as scar tissue is not able to actively contract, its presence decreases the overall contractile capacity of the heart, thus aggravating the function of the heart as a pump.[4] As such, acute MI is associated with high mortality and morbidity if not treated with appropriate reperfusion therapy in a timely manner. Major developments in non-invasive and invasive treatment methods have greatly increased the survival and quality of life of many patients suffering from MI.

Current treatments for MI include angioplasty, pharmacotherapy and bypass surgery, which aim to revascularize the heart, limit ongoing cell death and prevent loss of cardiac function.[5–7] Despite the success of early revascularization therapy to restore blood flow, 10% of the MI patients still suffer irreversible heart damage, leading to adverse ventricular remodeling and eventually, heart failure.[8,9] Therefore, novel therapeutic approaches are urgently needed to improve cardiac tissue repair and functional restoration post-MI. Therapies that limit infarct evolution and remodeling would greatly help to reduce the number of patients at risk of heart failure.

1.2 Phases of Infarct Evolution

The human heart has an insufficient ability to replace lost cardiac tissue due to its limited capacity for regeneration. Damaged heart tissue is initially comprised of a necrotic core surrounded by a marginal (or border) zone that can either recover to normal function or become irreversibly damaged. Collateral blood flow is an important determinant of infarct size and whether or not the border zone becomes seriously injured.[10] The infarcted tissue does not contribute to tension generation during systole and therefore can alter the ventricular systolic and diastolic function and put stress on the heart. As a result, after several weeks, the infarcted tissue forms a fibrotic scar.[11]

Cardiac repair/healing can simply be divided into three distinct but overlapping phases: the inflammatory phase, proliferative phase and maturation phase (**Figure 1.1**).[12] The acute repair process is called the inflammatory phase, which is mediated by cytokines and inflammatory cells. Since cell death begins within minutes after injury, induction of pro-inflammatory mediators and leukocyte infiltration into the infarcted myocardium plays a crucial role in phagocytosis and removal of necrotic cells and debris, and this action cascade promotes tissue repair and scar formation.[13] As a result of these changes, an infarct region is formed with high levels of necrosis and apoptosis.[14] Another important factor, oxidative stress, is dramatically increased following an MI. The predominant cells at work here are the phagocytic cells, the neutrophils and macrophages, which lyse tissue debris and necrotic material to clear the infarct region of necrotic cells and debris in order to facilitate scar formation.[15]

During the proliferative phase, the wound is rebuilt with new granulation tissue, which is comprised of various cells and collagen and other extracellular matrix (ECM) proteins and into which a new network of blood vessels grows, a process known as neovascularization. The

deposition of ECM is mediated primarily by fibroblasts that differentiate into contractile myofibroblasts. Additionally, endothelial cells play an essential role in post-MI healing, not only through the supply of blood to the infarcted myocardium, but also in the way that endothelial cells guide cardiomyocyte organization.[16] Endothelial cells also proliferate in the region of the myocardium bordering the infarct, increasing blood vessel formation and nutrient flow.[17]

The last phase, the maturation phase, involves excessive fibrosis and remodeling of the deposited ECM into the form of a stiff scar. Cellular activity within the scar is reduced and the fibroblasts and blood vessels in the scar area regress.[18] Pathological remodeling of the myocardium begins during the wound healing process and can continue post-MI, leading to progressive loss of cardiac function and heart failure.[19] Therefore, improving infarct repair and wound healing post-MI is a critical therapeutic opportunity to prevent heart failure progression.

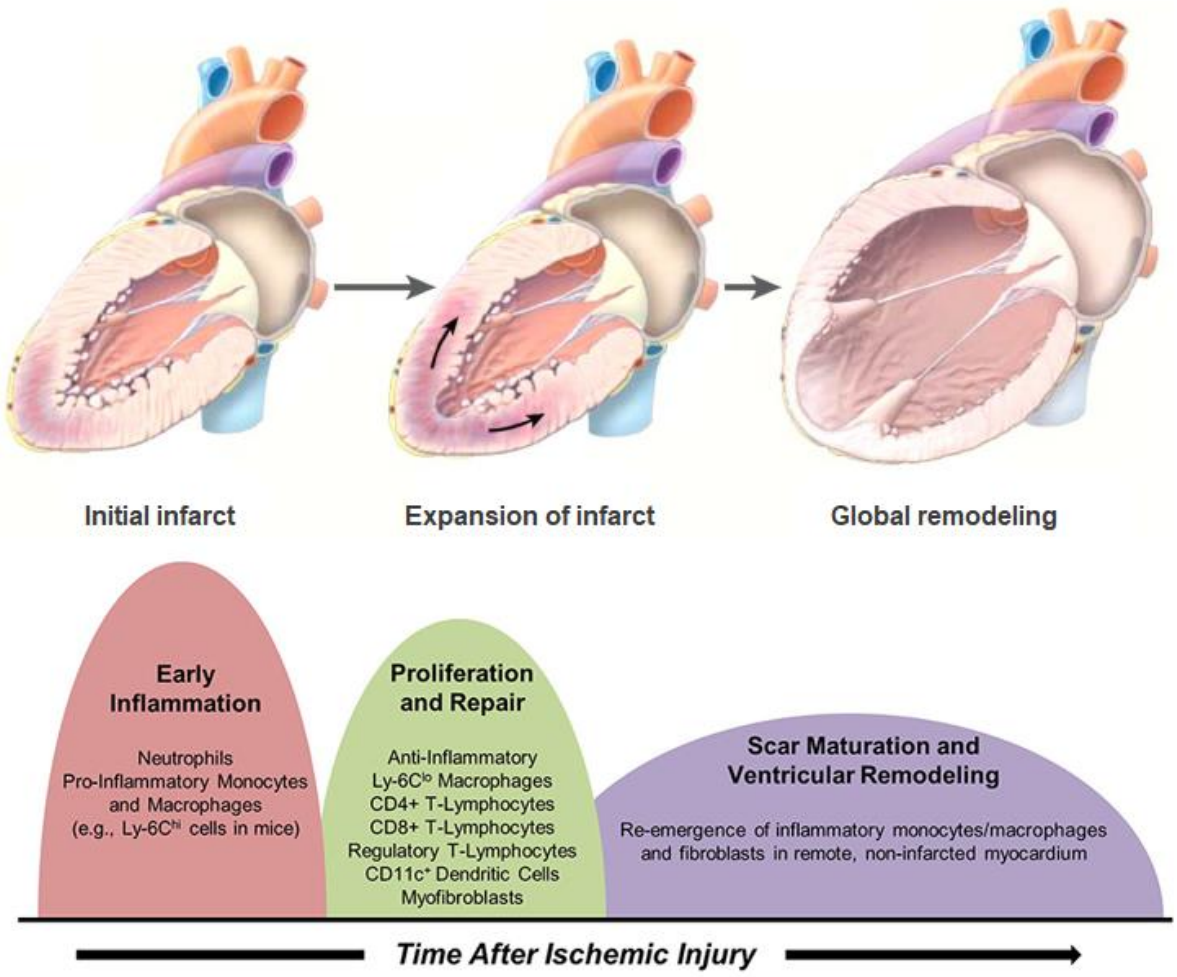

Figure 1.1 **Illustration of ventricular remodeling after myocardial infarction. MI results in the activation of a multiphase healing process, involving three overlapping phases: the inflammatory, proliferation, and maturation phases. This repair process prevents ventricular rupture, but it is insufficient to protect the myocardium from massive tissue loss, dilation and adverse remodeling. The dilated left ventricle has reduced cardiac function and results in systolic heart failure. Adapted from (Jessup, M., and Brozena, S., 2003). With permission, New England Journal of Medicine *348*, 2007-2018.**

1.3 The Role of Cardiac ECM

The ECM is involved in nearly all cellular activities, such as cell adhesion, migration, survival, proliferation, and differentiation.[20] The cardiac ECM is a complex meshwork of structural and non-structural proteins and sugars that are further subdivided into glycoproteins, proteoglycans, and glycosaminoglycans. Some proteins serve a structural function in the ECM (e.g., collagen, elastin), whereas others have non-structural roles, such as matricellular proteins. In addition, there are glycoproteins such as fibronectin that can act as both. This reservoir of glycosylated proteins allows for flexibility and diversity in how cardiac ECM functions in different tissues in health and disease.[21] During tissue development and regeneration, the ECM not only serves as a scaffold to support proliferating and migrating cells but also provides a wide variety of biochemical and physical signaling to facilitate the processes.[22]

The human heart is composed of several major cell types including cardiomyocytes, fibroblasts, endothelial cells, smooth muscle cells and macrophages [23,24] **(Figure 1.2)**. Cardiomyocytes and fibroblasts constitute the largest cellular populations of the heart and produce most of the enzymes that regulate ECM remodeling, such as matrix metalloproteinases (MMPs) that degrade the ECM, and their inhibitors, the tissue inhibitors of metalloproteinases (TIMPs).[25] Cardiac endothelial cells express and release a variety of auto- and paracrine agents, such as nitric oxide, endothelin, prostaglandin I2, and angiotensin II, which directly influence cardiac metabolism, growth, contractile performance, and rhythmicity of the adult heart.[26,27]

In the case of injury, ECM proteins interact with cell surface receptors such as integrins to regulate various signaling pathways in order to initiate repair processes.[28] The primary components of the ventricular ECM network are collagen I and III, among other structural proteins. Collagen I predominates in healthy myocardium comprising about 70% of the ECM,

and type III is the second most abundant collagen in cardiac ECM at 12%.[29,30] Collagen type I helps the heart to maintain its structural integrity, whereas collagen type III provides primarily elasticity.[31,32] Both the ratio of collagen III : I and MMP/TIMP increase when the heart is injured, causing ECM degradation and physiological stress on the ventricle wall.[33–35] In addition to collagens, elastin, proteoglycans and adhesive proteins such as laminin and fibronectin constitute a dynamic structure of cardiac ECM.[36] Post-MI, cell-ECM interactions are disrupted, which damages homeostatic mechanisms. Another factor that plays an important role in the composition of the cardiac ECM is aging.

With age, oxidative stress and inflammation is increased, resulting in gradual cell loss and the development of cardiac fibrosis.[37] In order to compensate progressive cardiomyocyte loss, the ECM content increases, in particular collagen I. Along with the increased collagen deposition and cross-linking, the ECM degradation capacity also augments through the production of MMPs.[38] Increased MMP activity also attenuates angiogenic activity, contributing to the formation of a hypoxic environment. The excessive accumulation of ECM and imbalance on ECM degradation can lead to tissue scarring and cardiac dysfunction. Interstitial fibrosis has a detrimental effect on myocardial function by interfering with cardiomyocyte electrical coupling.[39]

Our growing knowledge on cardiac ECM function paves the way for new and promising therapeutic targets that can limit the extent of damage post-MI and repair the injured heart. As ECM intrinsically maintains environmental homeostasis and assists cardiac remodeling upon MI, the use of ECM-like or ECM-supporting biomaterials is an attractive therapeutic strategy for regenerative medicine applications.[28,40–42]

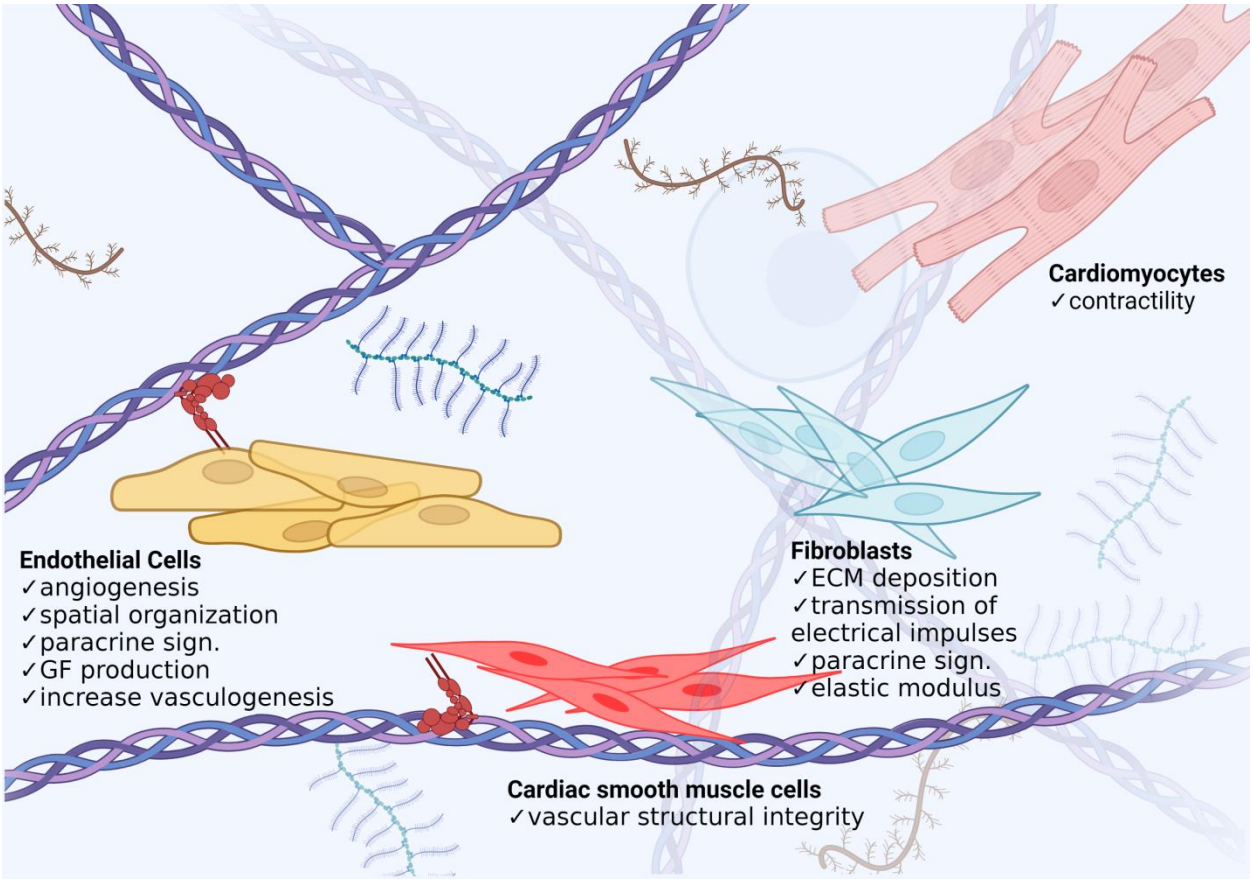

Figure 1.2 **Cardiac ECM and cell composition. Schematic representation of the main cardiac extracellular matrix components and their direct interaction with endothelial cells, cardiomyocytes and fibroblasts. Myocardial ECM connects cardiomyocytes, provides structural stability, and enables the transmission of chemical signals and contractile forces. The ECM contains structural proteins such as collagen and elastin, proteoglycans such as heparan sulfate, and adhesive glycoproteins such as fibronectin and laminin. Illustration was created with BioRender.com**

1.4 Methylglyoxal, Advanced Glycation End-products and Glyoxalase-1 Enzyme

Methylglyoxal (MG) is a highly reactive dicarbonyl compound, which is formed mostly as a by-product of glycolysis. It is involved in the formation of advanced glycation end-products (AGEs), reacting with free amino groups of lysine and arginine and with thiol groups of cysteine.[43] AGEs are proteins or lipids that become glycated as a result of exposure to free sugars and reactive carbonyls.[44] The accumulation of AGEs has been shown to cause inflammation and wound healing delay during tissue regeneration.[45] AGEs can also bind to the receptor for advanced glycation end products (RAGE), which then contributes to age- and diabetes-related chronic inflammatory diseases.[46] Notably, AGEs have been linked with the severity and prognosis of heart failure, and AGE accumulation has been associated with a one-year incidence of major cardiac events and death following ST-elevated MI.[47,48] However, a mechanistic or causative role of AGEs in cardiovascular diseases, particularly in MI, is unclear.

Glyoxalase-1 (Glo1) is a ubiquitous cellular enzyme that under normal physiological conditions renders MG inert via the glyoxalase pathway.[49] Stress factors such as hyperglycaemia, hypoxia, ischemia, inflammation and oxidative stress stimulate MG production, while inhibiting the activity of Glo1, leading to intra- and extra-cellular accumulation of MG and MG-derived AGEs (MG-AGEs).[50–52] Although AGEs are not membrane permeable, most of their precursors, including MG, are. The majority of MG basally produced is metabolized and rendered inert by the glyoxalase system through a 2-step process **(Figure 1.3)**. In the first step, Glo1 facilitates the formation of an S-D-lactoylglutathione intermediate from the hemithioacetal that is formed by the non-enzymatic reaction between MG and glutathione (GSH). During the second step Glo2 hydrolyzes the S-D-lactoylgutathione to D-lactate and thus recycles the GSH that was used to

create the hemithioacetal intermediate.[50,53] Glo1 is the rate limiting enzyme, and its activity is proportional to the cellular concentration of GSH.

MG accumulates during periods of oxidative stress and anaerobic glycolytic metabolism and can contribute to oxidant-induced cytotoxicity.[54,55] The major route through which MG generates ROS is by the direct modification of proteins like mitochondrial and antioxidant enzymes.[54,56] Besides being a major precursor in the formation of AGEs, MG is also a key factor in the acceleration of oxidative stress. MG can be subjected to auto-oxidation and can thereby generate ROS. Additional free radicals can be generated from MG via various pathways. Studies have shown that during the conversion of aminoacetone and acetol to MG, H_2O_2 can be formed.[57] In addition, the breakdown of MG also produces free radicals. Interestingly, MG formation can be stimulated by ROS, thereby creating a vicious cycle.[58]

The harmful effects of MG accumulation can be reduced by the prevention of AGE formation, the direct scavenging of MG and/or by enhancing the expression of the detoxifying enzyme Glo1. Chronic hyperglycaemia or an acute ischemic injury stimulate the production of MG and the depletion of GSH, while also down-regulating the expression of Glo1.[59] Ischemia, inflammation and oxidative stress are all present post-MI. Moreover, as the infarcted heart also undergoes a metabolic shift to derive ATP from anaerobic glycolysis.[60,61] Taken all together, this strongly suggests that MG and its AGEs are produced post-MI and contribute to heart failure progression. Indeed, data from our lab showed that MG-AGEs accumulate in the heart post-MI and that preventing this accumulation by Glo1 overexpression resulted in less adverse remodeling and led to improved cardiac function, suggesting MG as a target for therapy to restore cell-ECM signaling, improve endogenous repair responses and limit cellular and functional loss post-MI.[62]

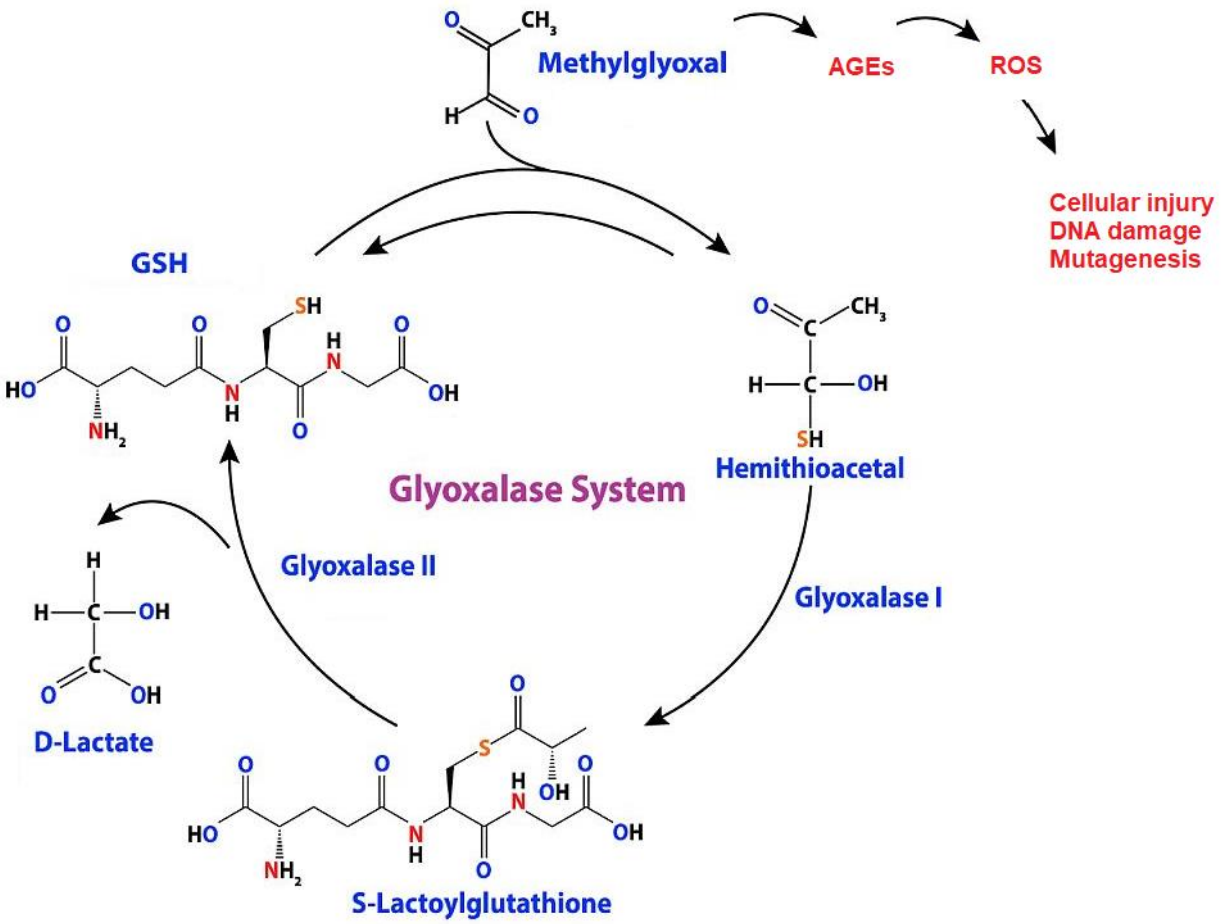

Figure 1.3 **Methylglyoxal and Glyoxalase System. The glyoxalase cyclic pathway consists of two enzymes (Glyoxalase I and Glyoxalase II), and is responsible for the detoxification of MG. In normal physiological conditions, MG is eliminated via the glyoxalase system. The first step involves the production of a hemithioacetal intermediate from the reaction between MG and GSH, which is converted to S-D-lactoylglutathione. The second step involves the production of D-lactate, while recycling GSH. GSH: glutathione; AGEs: advanced glycation end-products; ROS: reactive oxygen species. Adapted from BioVision's website https://www.biovision.com/glyoxalase-pathway.**

1.5 Antioxidant Molecules and Fisetin

Following MI, reactive oxygen species (ROS) are produced, which then initiate a wide range of toxic oxidative reactions.[63] The extent of ROS-induced oxidative damage can be exacerbated by a decreased efficiency of antioxidant defense mechanisms. Antioxidant molecules are protective agents against cardiac necrosis and free radical production, and have shown to be beneficial in preventing complications and cardiac event rate in MI patients.[64,65]

Fisetin is an organic dietary flavonoid present in numerous fruits and vegetables such as strawberries, mangoes and cucumbers. Fisetin has been shown to reduce inflammation *in vitro* and extend the life of simple organisms like yeast, worms and flies.[66,67] It can also reduce MG levels through both increased Glo1 activity and direct MG scavenging **(Figure 1.4)**.[68] It has been shown to upregulate the levels of an endogenous antioxidant, glutathione, by inducing Nrf2 protein expression.[69,70] Nrf2 is a transcription factor that binds to the antioxidant response element (ARE), stimulating the transcription of several protective genes. This makes Nrf2 a key element in mediating oxidative stress. Considering that Nrf2 levels can be increased by fisetin, this flavonoid is able to maintain GSH levels and Glo1 activity under conditions of stress.

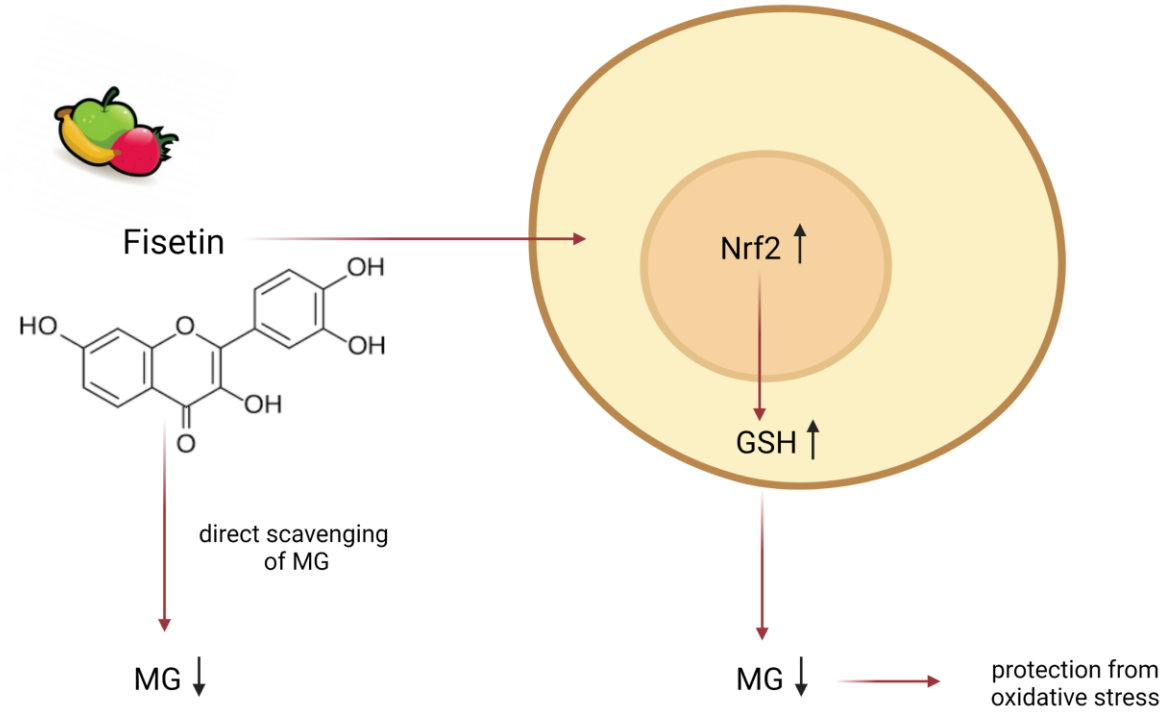

Figure 1.4 **Fisetin reduces MG levels by upregulating Nrf2 or direct MG scavenging. Fisetin regulates Nrf2 levels which is responsible for the enhancement of GSH levels. GSH is a glyoxalase pathway element that controls MG levels. Reduction of MG protects cells from oxidative stress. GSH: glutathione; MG: methylglyoxal; Nrf2: nuclear factor erythroid 2-related factor 2. Illustration was created with BioRender.com**

1.6 Biomaterial Therapies for Cardiac Regeneration

Biomaterials are synthetic or natural materials that have been engineered to interact with biological systems to evaluate, treat, augment or replace any tissue, organ or function of the body for a medical purpose.[71] The biomaterial field remains a rich area for research and invention because no material alone is suitable for all biomaterial applications, and new applications are continually being developed as medicine advances. Developments in biomaterial technology have made it possible to fabricate materials that can efficiently facilitate the repair and/or regeneration of different tissue types by mimicking architectural and biomechanical features of the ECM.

Biomaterial-based applications for cardiac repair can simply be divided into 4 main categories based on their delivery and therapeutic strategies: a) injectable hydrogels; b) cell / protein delivery vehicles; iii) 3D patch / matrix; and iv) drug delivery systems **(Figure 1.5)**. Various injectable hydrogels have been shown to provide physical support, reduce scar formation and stimulate repair signals by mimicking ECM elements. Cell- or protein-delivering biomaterials can improve cell and/or protein retention within the heart and improve cell survival after transplantation. Three-dimensional matrices can be fabricated with or without cells, then implanted to the heart's surface as patches to improve cardiac function. Lastly, biomaterials designed to release drugs and bioactive molecules may induce cardiac repair in a sustained effective manner.[72–74] The ability to support vascularization is one of the most important requirements for biomaterials or any type of tissue engineering constructs in order to support tissue repair in the damaged myocardium.[75] In this thesis work, we present examples of an injectable hydrogel system (article 1), a protein delivery vehicle (article 2) and a 3D patch system (article 3).

Another way to classify biomaterials in cardiac tissue engineering can be based on the manufacturing methods, i.e., naturally derived biomaterials, synthetic scaffolds and composite (hybrid) scaffold. Naturally-derived scaffolds have been used to advance cardiac regenerative medicine by creating biomimetic organ scaffolds at clinically relevant scales.[76] Such materials are popular scaffolding options to integrate cells or other molecules for a functional organ analog. For cardiac tissue engineering, natural biomaterials include those made from well-characterized biopolymers such as chitosan, collagen, gelatin, Matrigel, chitosan, alginate, and decellularized ECM.[77,78] Their ease of use, their biocompatibility, their biodegradability, the ease with which therapeutic agents can be encapsulated within their network formation, as well as their ability to be delivered to the target tissue using minimally invasive techniques, make hydrogel-based therapy a promising alternative or concomitant treatment for cardiomyopathies. Several studies have shown that injectable biomaterials successfully provided physical stability to the infarcted myocardium, improved cardiac function, increased vascularization and limited adverse remodeling in pre-clinical models.[78,79]

Incorporating conductive elements (often at the nanoscale level) to biomaterial systems has been successful in improving electrical propagation in cardiac tissue. For example, gold nanowire-infused alginate has been shown to improve electrical propagation in porous matrices that otherwise interfere with cell-cell connections.[80] Cardiac patches generated from these materials showed enhanced synchronized contractile function. The incorporation of gold nanorods into hydrogels has also yielded increased mechanical stability and electric conductivity.[81] These are just a few examples of the many strategies being investigated for improving electroconductive properties of biomaterials for cardiac applications.[82–84]

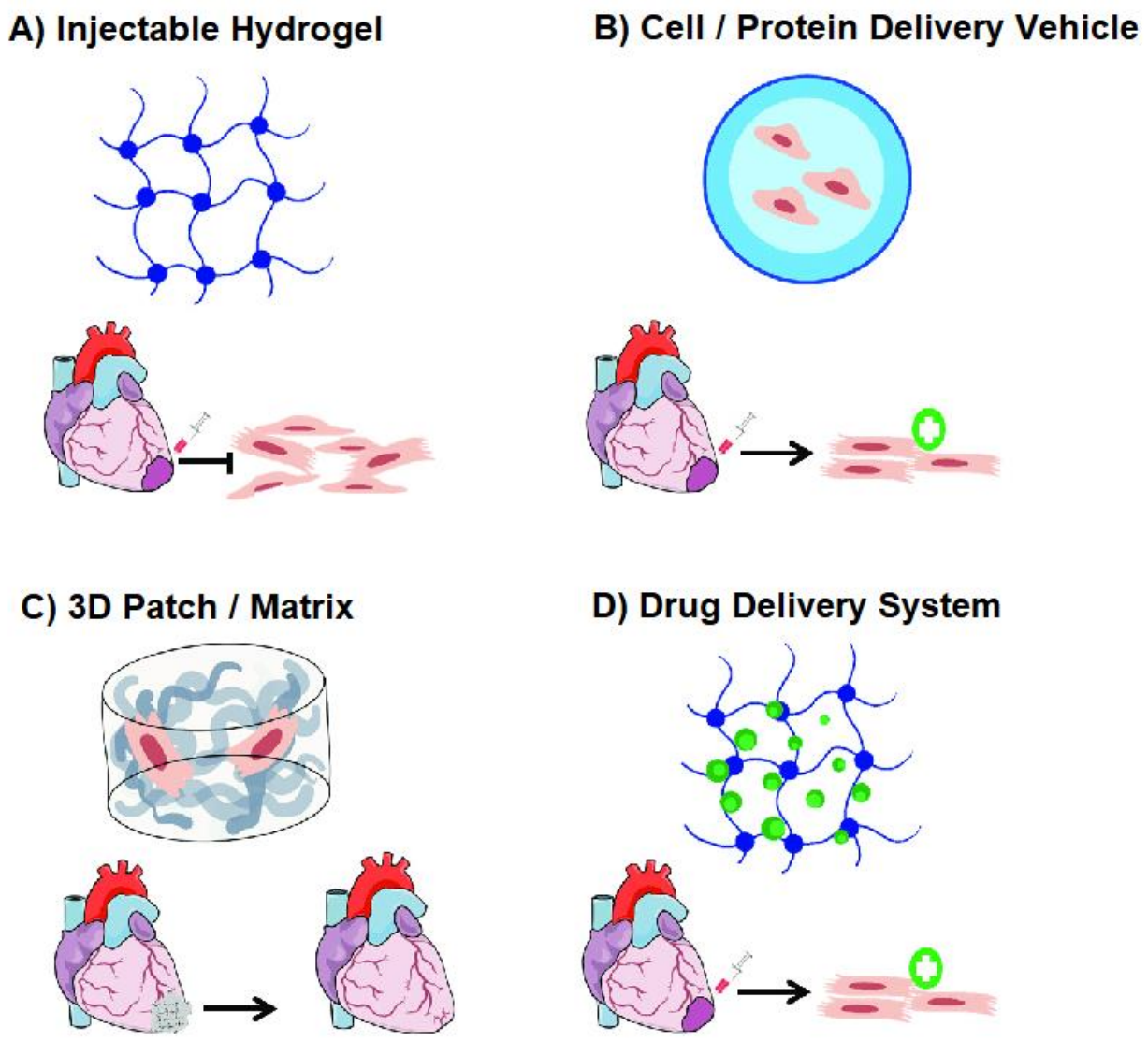

Figure 1.5 **Biomaterial-based applications for cardiac tissue engineering. (A) Biomaterials can be injected alone into the infarcted region to promote tissue repair; (B) cell- or protein-delivery using injectable hydrogels can improve retention of the therapeutic product and promote cell survival after transplantation; (C) three-dimensional matrices can be fabricated with or without cells, then implanted as cardiac patches to improve cardiac function; and (D) biomaterials can be designed to encapsulate and sustainably release drugs and bioactive molecules for cardiac repair. Illustration was adapted and re-created from DOI: 10.3389/fbioe.2020.00126**

1.7 Nanoparticle Technology

Research into the use of nanoparticles (NPs) for treating cardiovascular disease, and more specifically for drug or small molecule delivery, is expanding rapidly owing to the unique capabilities of NP delivery compared to traditional drug administration methods. In addition to drug delivery, nanoparticles can also be added to biomaterials to modify their physical and biological properties, making them stable, non-toxic and biodegradable. Thus, different hybrid scaffolds containing various types of nanomaterials, with mechanical and/or electroconductive properties, have been receiving increasing attention in cardiac tissue engineering applications.[85]

Depending on the formulation, the NPs can be injected directly into the heart alone or combined with another material, or they can be designed to accumulate at a target site following intravenous injection.[86] NPs have been shown to improve protein bioavailability and decrease their potential toxic effects due to lower dosages required when encapsulated and delivered in NPs.[87] NP systems allow researchers to control the size and route of administration of the therapy in a predefined, targeted and versatile way.[88] By controlling the design, NPs can be surface-modified to target specific receptors, epitopes or cell types. All of these properties make NPs promising agents for cardiac tissue engineering applications. Nanoparticle technology in cardiac tissue engineering is more widely discussed in Chapter 4 (article #2) of this thesis.

2 Rationale, Hypotheses and Aims

The main aim of this thesis was to further elucidate the role of MG, MG-related AGEs and oxidative stress in post-MI cardiac remodeling and to test biomaterial therapies that could reduce the effects of MG and protect the infarcted myocardium, and promote cardiac function. The second aim was to develop a sprayable biomaterial coating that could improve electrical propagation and contractility of the infarcted heart. To accomplish these objectives, a mouse MI model was used to test three types of biomaterial systems that were developed to reduce adverse ventricular remodeling and improve cardiac function. The studies in this thesis were designed to address three specific aims:

Aim 1: Evaluate a combined fisetin and hydrogel therapy for reducing the effects of MG and improving repair of the post-MI myocardium, and elucidate some underlying mechanisms. We hypothesized that combining an injectable collagen hydrogel with an MG scavenger, fisetin, would improve cardiac function post-MI by reducing oxidative stress-related damage and limiting tissue loss and adverse remodeling.

Aim 2: Design and synthesize Glo1-loaded NPs that can be delivered intravenously and target CD44-expressing cells in the infarcted myocardium, and to assess the ability of this therapy to reduce MG-induced damage and promote repair. Our hypothesis was that Glo1-NPs would target CD44 expressing cells in the heart, deliver Glo1 into the damaged tissue and improve cardiac function by reducing MG levels post-MI.

Aim 3: Develop a peptide-based gold nanoparticle engineered sprayable material for increasing electroconductivity post-MI and determine its therapeutic effects on the infarcted myocardium when sprayed directly onto the heart's surface. We hypothesized that spraying gold NP-based peptides would enhance electroconductivity and contractility of the heart post-MI.

3 Article I - Combined Methylglyoxal Scavenger and Collagen Hydrogel Therapy Prevents Adverse Remodeling and Improves Cardiac Function Post-Myocardial Infarction

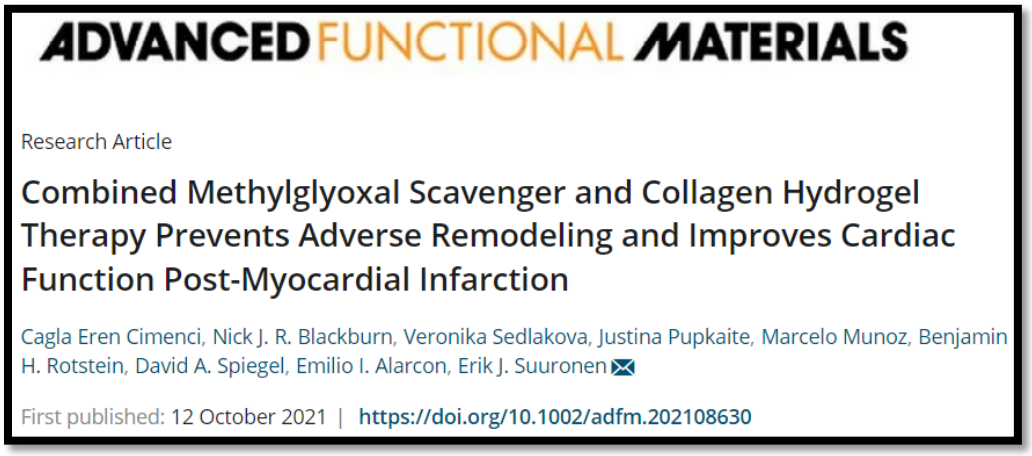

Website / link of the publication: https://doi.org/10.1002/adfm.202108630

***Cagla Eren Cimenci*[1,2]**, *Nick J. R. Blackburn*[1,2], *Veronika Sedlakova*[1], *Justina Pupkaite*[1,2,3], *Marcelo Munoz*[1], *David A. Spiegel*[4], *Emilio I. Alarcon*[1,5], *Erik J. Suuronen*[1,2,*]

*[1] BEaTS Research, Division of Cardiac Surgery, University of Ottawa Heart Institute, Ottawa, K1Y 4W7, Ontario, Canada; [2] Department of Cellular and Molecular Medicine, Faculty of Medicine, University of Ottawa, Ottawa, K1H 8M5, Ontario, Canada; [3] Division of Cell Biology, Department of Clinical and Experimental Medicine, Linköping University, Linköping, 582 25, Sweden; [4] Department of Chemistry, Yale University, New Haven, Connecticut, U.S.A., 06510;[5] Department of Biochemistry, Microbiology, and Immunology, Faculty of Medicine, University of Ottawa, Ottawa, K1H 8M5, Ontario, Canada. * Corresponding author: Erik J. Suuronen.*

Article I - Abstract

Methylglyoxal (MG) is a highly reactive dicarbonyl and the main precursor of advanced glycation end-products (AGEs). After myocardial infarction (MI), MG-derived AGEs accumulate in the heart and contribute to adverse remodeling and loss of cardiac function. In this study, the flavonoid fisetin, a dicarbonyl scavenger, is used to reduce the negative effects of MG in the post-MI heart. A fisetin-loaded collagen type I hydrogel (fisetin-HG) is injected intramyocardially in mice at 3 h post-MI, and compared to fisetin-alone, hydrogel-alone, or saline treatment. Fisetin-HG treatment increases the level of glyoxalase-1 (the main MG-metabolizing enzyme), reduces MG-AGE accumulation, and decreases oxidative stress in the MI heart, which is associated with smaller scar size and improved cardiac function. Treatment with fisetin-HG also promotes neovascularization and increases the number of pro-healing macrophages in the infarct area, while reducing the number of pro-inflammatory macrophages. Taken together, the results demonstrate that the fisetin-collagen hydrogel therapy can reduce the accumulation and negative effects of MG post-MI. This therapy may be a promising approach to limit adverse cardiac remodeling, prevent damage, and preserve function of the infarcted heart.

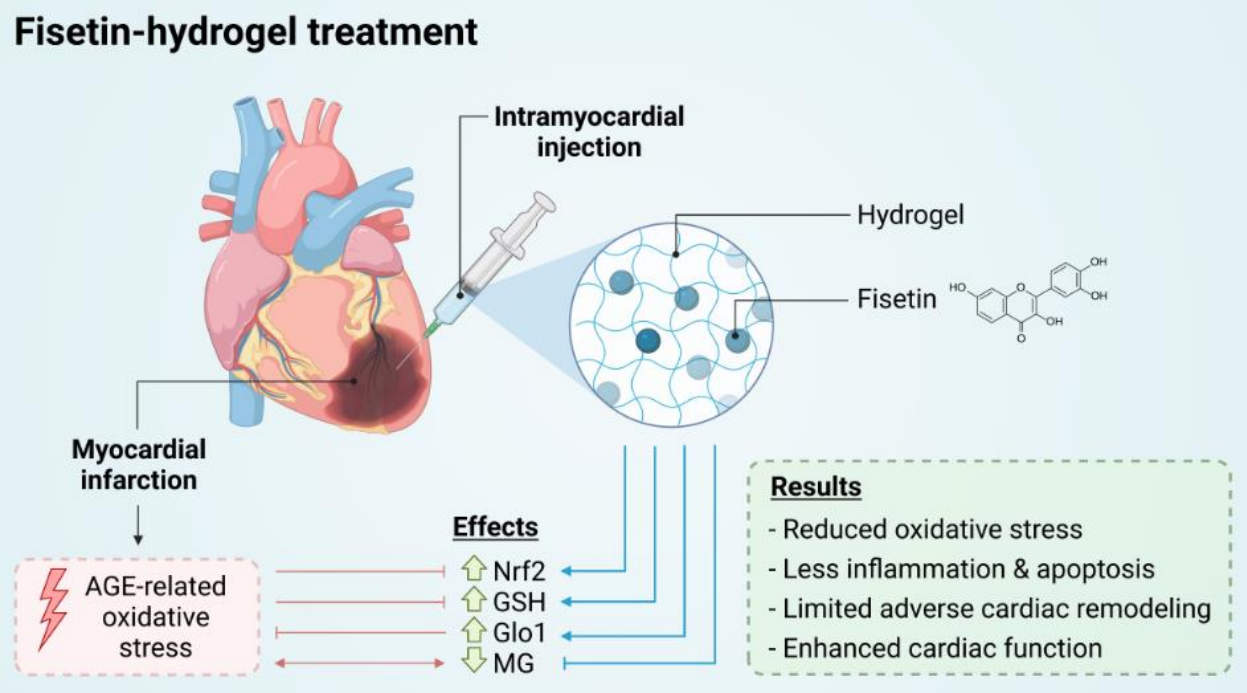

Table of Content (TOC) Illustration of Article I

3.1 Introduction

Cardiovascular disease (CVD) is the most common underlying cause of death globally, accounting for an estimated 32% of all deaths worldwide.[89] Occlusion of one or more coronary arteries is the most common consequence of CVD, which restricts blood flow to the heart, leading to myocardial infarction (MI).[90] MI results in the loss of viable myocardium from both the initial ischemic event and subsequent infarct expansion. Timely pharmacological or surgical intervention post-MI can restore perfusion and improve post-MI outcomes in patients, but they do not address the loss of viable myocardium. The extensive cell death can lead to adverse ventricular remodeling, loss of cardiac function, and ultimately heart failure in many patients. Thus, there is a need to develop new therapies that can limit cell death and prevent adverse remodeling post-MI.[6,91]

Advanced glycation end-products (AGEs) are proteins or lipids that become glycated from exposure to free sugars and reactive carbonyls. They are a primary cause of metabolic and oxidative stress, and lead to wound healing delay during tissue repair and regeneration.[44,45] AGEs have been linked to the severity and prognosis of heart failure, and their accumulation was associated with a greater incidence of major cardiac events and death at 1-year following ST-elevated MI.[47,48] Therefore, AGEs represent a potential therapeutic target for improving cardiac repair and preventing heart failure progression in MI patients.

Methylglyoxal (MG) is a highly reactive dicarbonyl compound, which is formed mostly as a by-product of glycolysis. It is considered to be the most significant precursor for AGEs, reacting with free amino groups of lysine and arginine and with thiol groups of cysteine.[92] Under normal physiological conditions, MG is metabolized mainly by the enzyme glyoxalase-1 (Glo1). However, in conditions of oxidative stress, factors such as hypoxia, ischemia, inflammation and hyperglycaemia all stimulate MG production in the body, while also limiting the activity of Glo1. As a result, MG accumulation leads to MG-derived AGE production (MG-AGEs), with MG-derived hydroimidazolone-1 (MG-H1) as the main MG-AGE formed.[50–52,93] We previously demonstrated that MG-AGEs accumulate in the heart acutely post-MI, and that they contribute to the cellular changes, adverse remodeling and loss of cardiac function in the infarcted heart.[62] Therefore, it is likely that the repair and function of the post-MI heart could be improved through strategies that aim to reduce MG and its detrimental effects.

The use of naturally occurring compounds, such as the dietary flavonoid fisetin, for reducing MG toxicity is an attractive and clinically translational strategy. Fisetin is able to decrease MG levels through both increased activity of Glo1 and direct MG scavenging.[68] It has also been reported to upregulate glutathione, an endogenous antioxidant and co-factor of Glo1.[69] While

fisetin has been shown to reduce MG levels and improve outcomes in experimental models of neurodegenerative disorders (as reviewed in Nabavi et al.[94]), it has seen limited testing for the treatment of cardiovascular disease, particularly after MI.

Intrapericardial, epicardial, intracoronary and intramyocardial administration strategies are being investigated for the delivery of therapeutics to the injured heart with minimal side-effects.[95] However, factors such as size of the therapeutic agent, solubility and high cardiac blood perfusion limit retention within the myocardium. Therefore, to achieve greater persistence and/or sustained delivery, therapeutics are being combined with vehicles, such as biomaterials and micro- or nanoparticles.[95,96] Micro- and nanoparticles can be liposomal, metallic, silica or polymeric and can be manufactured using various techniques including self-assembly for the generation of complex hierarchal assemblies with superior tunability and functionality.[96,97] Biomaterials offer tailorable carrier properties and can also provide mechanical support to the injured area and bioactive cues for cell adhesion, survival, or differentiation.[98] They can be synthetic or natural, with peptide- and protein-based materials being among the most popular for use in cardiac repair.[99,100] Collagen is the primary structural protein of the heart that also supports the function of neighboring cells.[98] As a stand-alone therapy, collagen hydrogels have been shown to promote post-MI repair and improve cardiac function.[101–103]

Herein we report, for the first time, the use of fisetin administered directly to the myocardium within a thermoresponsive collagen hydrogel for treating MI at a clinically relevant time-point. In this study, a combined fisetin-collagen hydrogel treatment delivered at 3h post-MI reduced MG toxicity, minimized inflammation and promoted vascularization, resulting in improved cardiac function of the infarcted mouse heart, which was superior to either treatment alone. This highlights that a combined collagen hydrogel and MG scavenging therapy could act together to

improve cardiac repair and function and constitutes a promising approach for treating MI patients.

3.2 Results

3.2.1 Fisetin-HG Characterization

Fisetin-loaded collagen HG (fisetin-HG) and collagen HG matrices were synthesized as thermoresponsive biomaterials; they are kept on ice in the liquid state until the time of injection and then solidify into a gel upon exposure to physiological temperatures (≈37 °C). Our data shows that once crosslinked, there was a trend ($p = 0.06$) for lower viscosity in the HG group compared to fisetin-HG **(Figure 3.1A)**. The water content of the 2 HG systems was similar and calculated to be ≈94% **(Figure 3.1B)**. Their degradation rate was evaluated by exposure to collagenase and was similar between fisetin-HG and HG (0.53 and 0.45 mg min−1, respectively; **Figure 3.1C**). In order to characterize the fisetin release profile, fisetin-HG was degraded with or without collagenase and free fisetin was measured over time. The results showed that 98% of the fisetin was released over 24 h in the presence of collagenase, but only 19% of the fisetin was released over 24 h in the absence of collagenase **(Figure 3.1D)**. Overall, our fisetin-HG system presented suitable characteristics for *in vivo* application, which included its high water content, biodegradability and steady release kinetics.

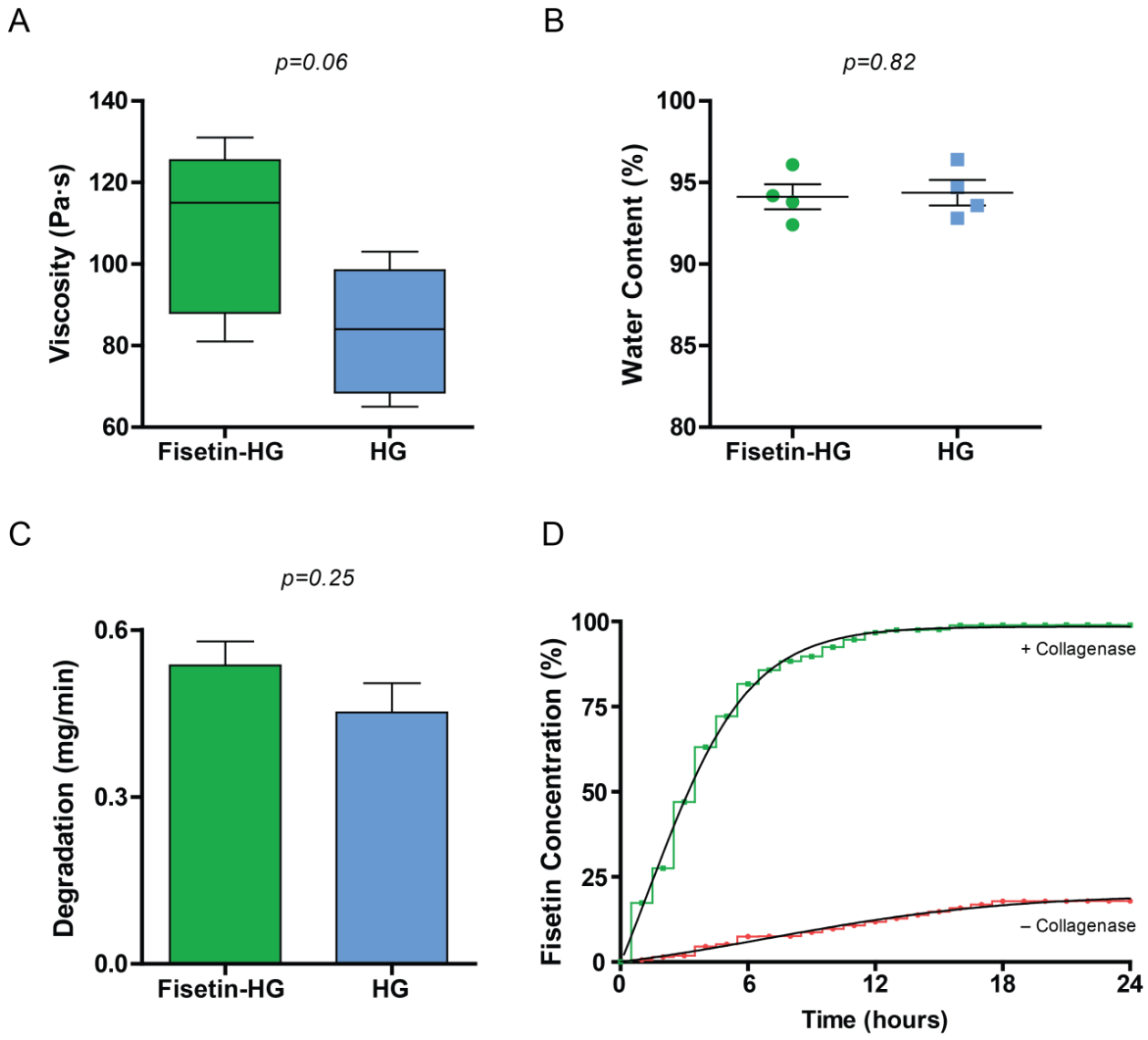

Figure 3.1 Hydrogel characterization. A) Viscosity measurements for fisetin-HG and hydrogel alone (HG; n=5). B) Total water content of the hydrogels (n=4). C) *In vitro* degradation rate of hydrogels in collagenase (n=4). D) Fisetin release profile from HGs with/without collagenase measured in the supernatant over a period of 24 hours (n=3)

3.2.2 Effect of Fisetin-HG on Cell Viability, Angiogenesis and Intracellular MG Level

To assess the ability of fisetin to prevent MG effects on cell viability, HUVECs without any treatment were compared to cells treated with MG alone, fisetin alone or a combination of MG +

fisetin **(Figure 3.2A)**. Exposure to 25 μM MG resulted in a 1.4-fold decrease in HUVEC viability, which was prevented by fisetin treatment **(Figure 3.2B)**. In the *in vitro* angiogenesis assay, HUVEC capillary-like network formation was reduced by 1.3-fold when the cells were treated with 25 μM MG, whereas fisetin alone and MG + fisetin treated HUVECs had equivalent angiogenic potential compared to the control group **(Figure 3.2C and 3.2D)**.

Having established that fisetin is capable of preserving the viability and angiogenic function of MG-treated endothelial cells, we then used a fluorescent MBo probe to test the ability of fisetin released from our hydrogel to reduce intracellular MG levels. The MBo probe emits a detectable fluorescent signal upon reaction with MG, but exhibits some cross-reactivity with nitric oxide.[104] Since endothelial cells produce high levels of nitric oxide, we performed this assay using cardiac fibroblasts, which have low nitric oxide expression (see Methodology for more details). MG levels were reduced over time in both the fisetin-HG and fisetin-alone groups with a reduction of ≈ 15% at 1 hour up to a reduction of ≈ 40% after 6 hours compared to the HG and control groups **(Figure 3.2E)**. This demonstrates that our fisetin-hydrogel can reduce intracellular MG levels.

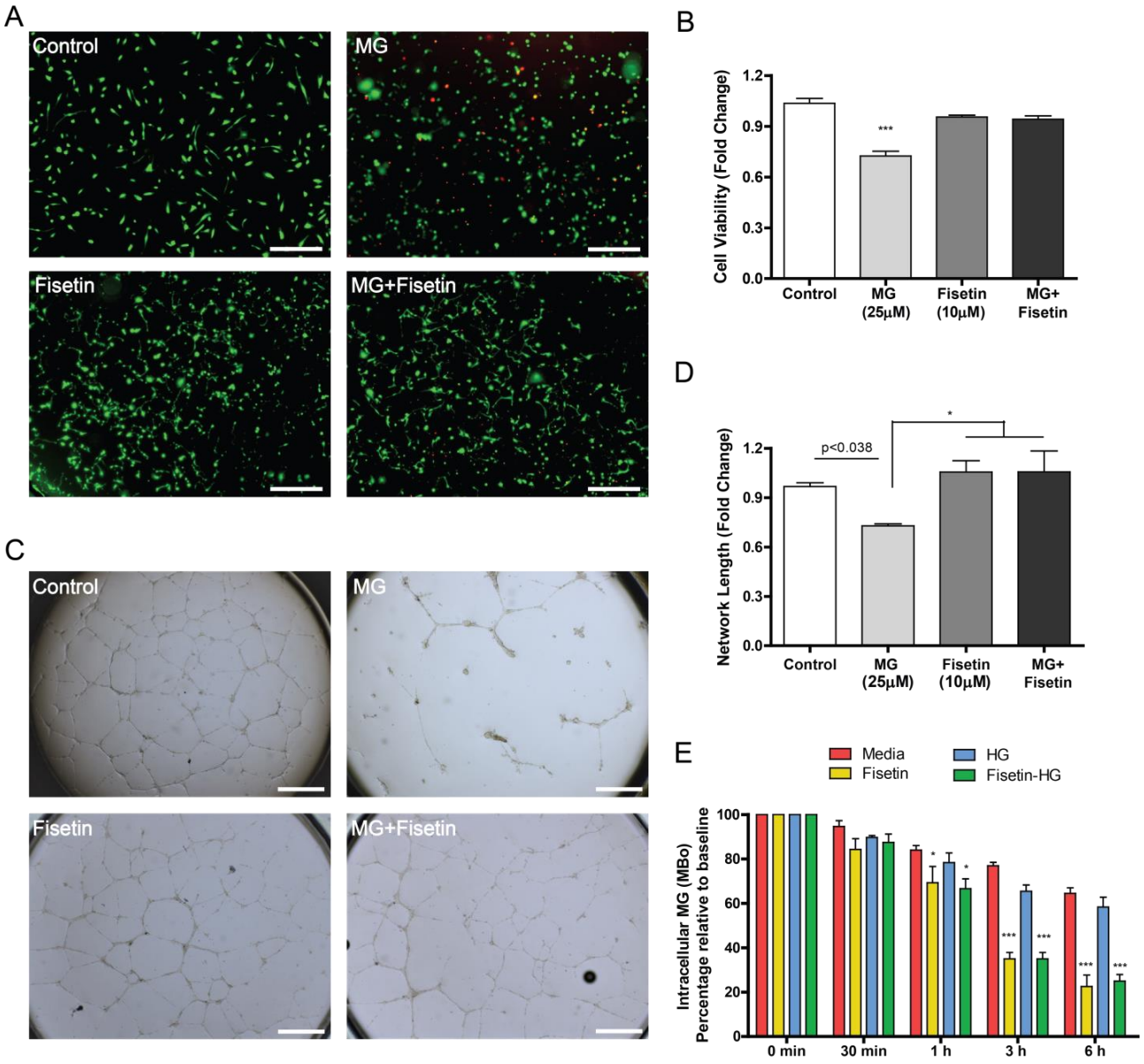

Figure 3.2 Viability and angiogenesis results. A) Representative live/dead assay images of cultured HUVECs at 24 h. Fisetin treatment rescued endothelial cell viability after MG treatment *in vitro*. Scale bar = 100 µm. B) Quantification of cell viability data (n = 6). C) *In vitro* angiogenesis assay shows that fisetin treatment reversed the anti-angiogenic effects of MG. Scale bar = 1 mm. D) Quantification of *in vitro* angiogenesis (total capillary-like network length was determined; n = 3). E) An MBo probe assay revealed that fisetin treatment reduced the intracellular MG concentration in MG-treated cardiac fibroblasts *in vitro* starting at 1 h post-treatment (n = 6; ***p < 0.001, *p < 0.05, compared to media control and HG).

3.2.3 HG Delivery Increases Retention of Fisetin

The hydrogels and fisetin were chemically tagged with AF594 (which labels both the hydrogel and fisetin) to monitor their distribution and retention *ex vivo* over time. IVIS images showed that the treatment spread throughout the left ventricle upon injection **(Figure 3.3A)**. Quantitative analysis of the images revealed that 85.3% of fisetin-HG is present in the myocardium at 1-day post-injection, which dropped to 15.4% at day 3 **(Figure 3.3B)**. The retention of HG alone was 68.1% at day 1 and 8.6% at day 3, while fisetin retention was 5.9% at day 1 and 0.3% at day 3. Since AF594 labels both the hydrogel and fisetin, we performed ultra-performance liquid chromatography to measure fisetin more accurately in the heart at 1- and 3-days post-treatment. When delivered with the hydrogel, 42.2% and 14.1% of the injected fisetin was present in the myocardium at day 1 and day 3, respectively, which was greater than the 5.0% and 2.8% that was present at day 1 and day 3 when fisetin was delivered alone **(Figure 3.3C)**.

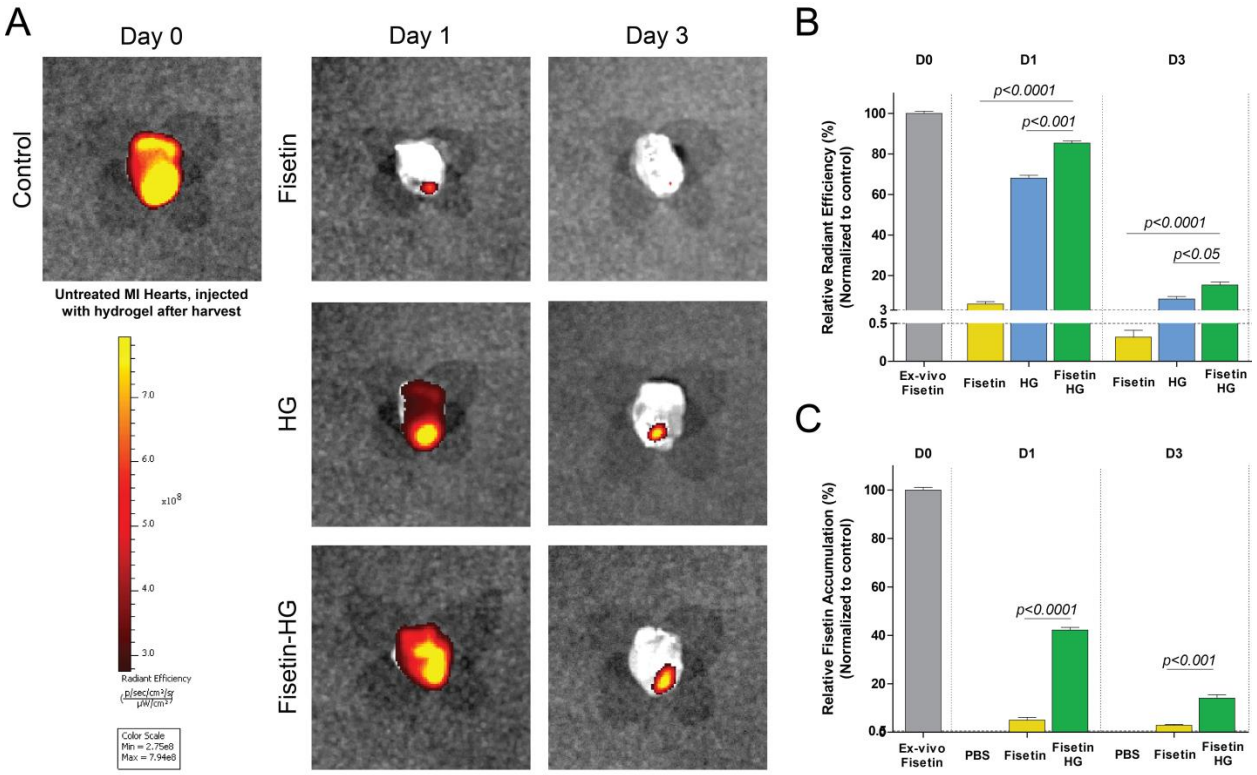

Figure 3.3 HG delivery increases fisetin retention in the heart post-MI A) Representative IVIS images of *ex vivo* MI mouse hearts taken 1 and 3 days after treatment with fisetin, HG, or fisetin-HG, labeled with Alexa-Fluor 594-NHS dye. A heart injected with HG *ex vivo* was used as the 100% positive control. B) Quantification of IVIS data reported as radiant efficiency for the different time points relative to the 100% control (n = 4). C) Ultra performance liquid chromatography of harvested myocardial tissue showed increased fisetin retention at 1 day and 3 days post-injection when delivered with the HG (n = 3). Data was normalized to hearts injected with fisetin *ex vivo* representing a 100% positive control group.

3.2.4 Fisetin-HG Matrix Improves Cardiac Function Post-MI

MI surgeries were performed at day 0 with a 94% overall postsurgical survival rate. The survival rates after treatment injections (performed at 3 h post-MI) were 94% for fisetin-HG, 95% for HG, 94% for fisetin, and 95% for phosphate buffered saline (PBS), with no statistical difference between the treatment groups. Echocardiographic measurements were taken at 3 h and 5 weeks post-MI and mice were sacrificed at 5 weeks **(Figure 3.4A)**. Baseline values of left ventricular

ejection fraction (LVEF) were comparable for all treatment groups **(Figure S1A**, Supporting Information). Treatment with fisetin-HG significantly improved LVEF from 38.1 ± 1.5% at baseline to 46.7 ± 2.1% at 5 weeks ($p = 0.0026$). Also, LVEF was superior in the fisetin-HG group compared to all other treatment groups **(Figure 3.4B)**. Notably, LVEF between baseline and 5 weeks deteriorated in mice that were treated with fisetin-alone or PBS ($p = 0.001$ and $p = 0.0009$, respectively).

Other determinants of cardiac function including cardiac output (CO), stroke volume (SV), end-systolic volume (ESV) and end-diastolic volume (EDV) were also calculated. Fisetin-HG treatment improved CO and SV compared to the other treatments **(Figure 3.4C and 3.4D)**. The change in ESV was reduced in fisetin-HG treated hearts compared to the fisetin-alone and PBS treatment groups **(Figure 3.4E)**, whereas no difference in EDV fold-change was observed between the groups after 5 weeks **(Figure 3.4F)**.

Longitudinal endocardial strain values were measured at the anterior apex region at aortic valve closure (AVC) and were comparable for all treatment groups at baseline and ranged from ≈−0.7 to −1.3% (**Figure S1B**, Supporting Information). Results showed that fisetin-HG treatment significantly improved the cardiac strain from ≈−1.1% at baseline to −5.7% at 5 weeks post treatment ($p = 0.013$); negative strain values indicate better cardiac contractility. Notably, cardiac strain (i.e., contractility) was significantly greater in fisetin-HG treated mice compared to those that received fisetin-alone or PBS treatment **(Figure 3.4G)**. For this analysis, the anterior apex segment of the myocardium was targeted as it contains the injection sites and the infarct zone (**Figure S1C**, Supporting Information). This segment is represented as the purple trace by the Vevo Strain analysis software, showing the peak longitudinal endocardial strain during cardiac shortening **(Figure 3.4H)**.

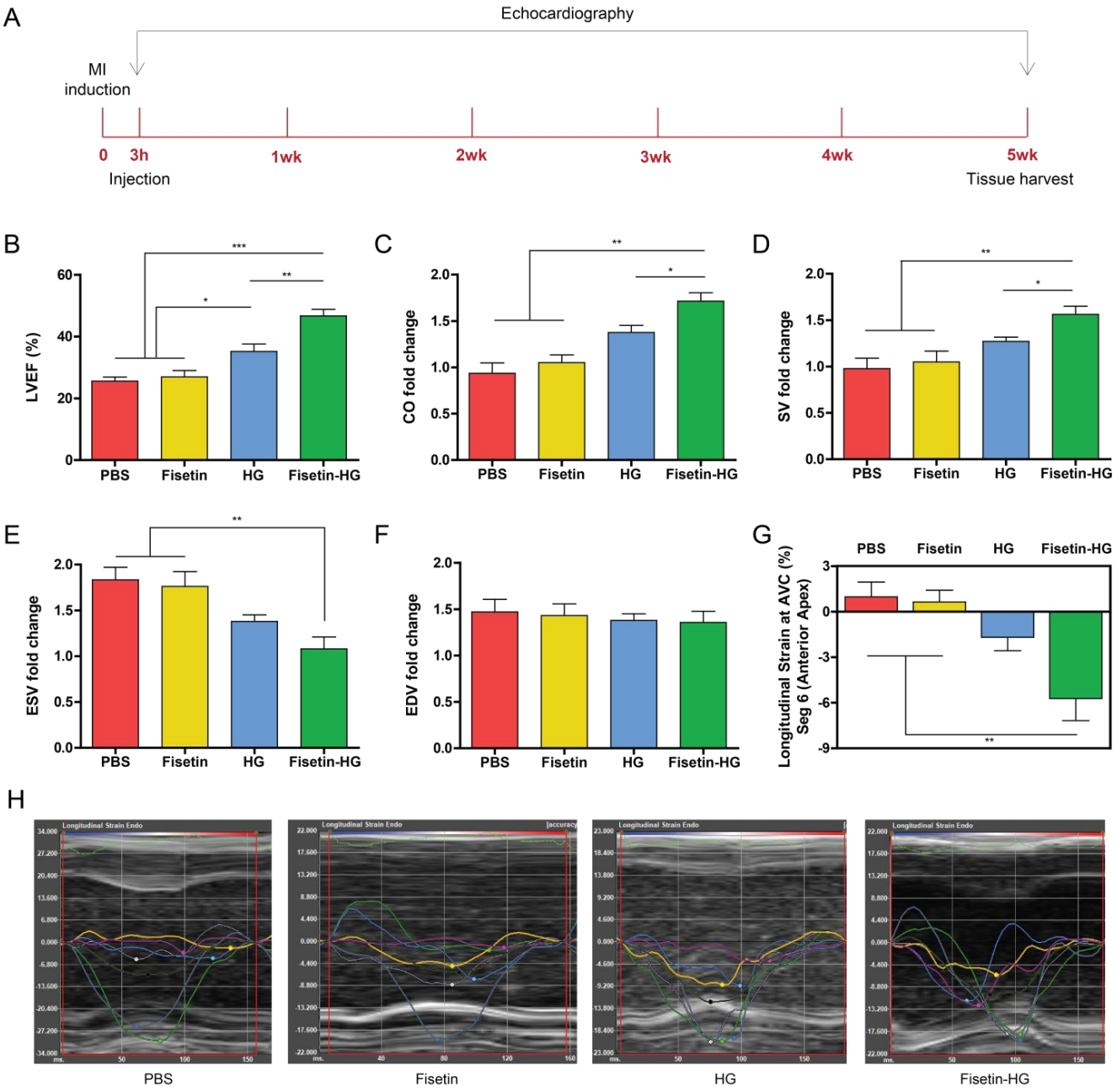

Figure 3.4 Fisetin-HG improves cardiac function and contractility post-MI. A) Schematic of the *in vivo* study timeline. B) % LVEF at 5 weeks post treatment (n = 13–16). The fold-change in C) CO, D) SV, E) ESV, and F) EDV between baseline and 5 weeks post-treatment (n = 13–16). G) Endocardial longitudinal strain reached at AVC within the anterior apex segment at 5 weeks post-MI (n = 7). H) Representative longitudinal strain curves over the course of a single contraction for the four treatment groups. The purple traces correspond to the anterior apex segment. ***p < 0.001, **p < 0.01, *p < 0.05.

3.2.5 Fisetin-HG Treatment Reduces Scar Size and Prevents Cell Death

Masson's Trichrome staining revealed that the fisetin-HG and HG treatment groups had a reduction in final scar size compared to control hearts at 5 weeks post-MI (by 20.3% and 17.2%, respectively; **Figure 3.5A and 3.5B**). Additionally, fisetin- HG treated hearts had increased remote ventricular wall and scar wall thickness compared to all other treatment groups (**Figure 3.5C and 3.5D**). The Fisetin-HG treatment also resulted in a greater area of viable myocardium compared to the fisetin and PBS groups **(Figure 3.5E)**. This was associated with reduced ongoing cell death in the myocardium of fisetin-HG treated mice at 5 weeks post-MI. Specifically, the scar area of fisetin-HG mice contained 33.7%, 64.3%, and 65.1% less active caspase-3+ apoptotic cells compared to the HG, fisetin-alone and PBS treatment groups, respectively **(Figure 3.5F)**. TUNEL and wheat germ agglutinin (WGA) staining revealed less death specifically in cardiomyocytes in Fisetin-HG treated mice by 19.1%, 68.9%, and 68.5% compared to HG, fisetin, and PBS groups, respectively **(Figure 3.5G)**. Overall, treating the MI mouse heart with fisetin-HG decreased final scar size, reduced on-going cardiomyocyte cell death and preserved viable myocardium.

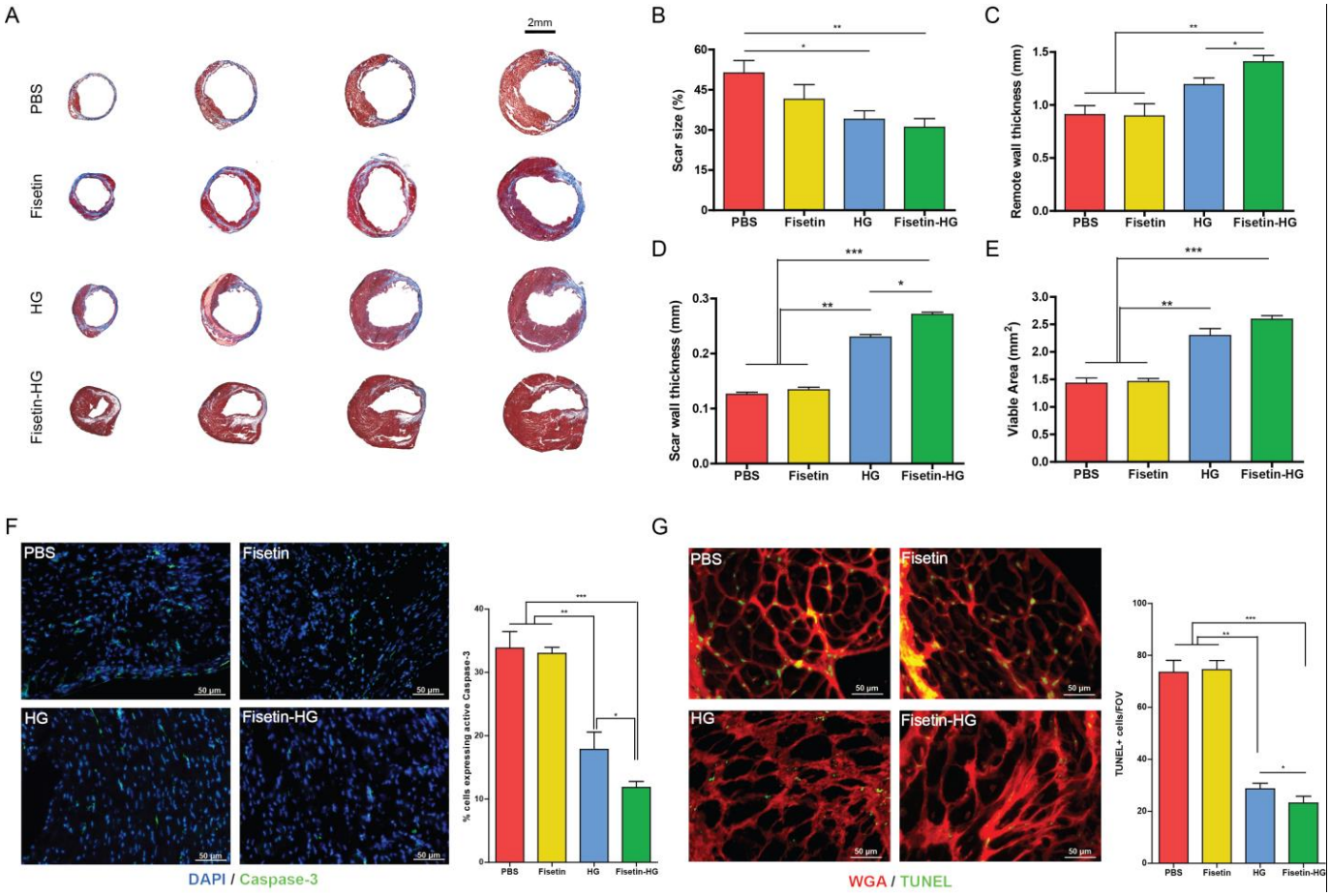

Figure 3.5 Assessment of morphology and cell death in tissue sections. A) Representative images of Masson's Trichrome stained sections. Multiple sections are shown from the apex to the base. Scale bar = 2 mm. B) Scar size calculated as the % of section circumference (n = 13–16). C) Wall thickness of the remote myocardium (n = 13–16). D) Scar wall thickness (mm) and E) viable area (mm2) were calculated from Masson's Trichrome stained tissue sections (n = 13–16). F) Representative images and quantification of active caspase-3 staining to identify apoptotic cells (n = 5). Scale bars = 50 µm. G) Representative images and quantification of tissue sections stained with TUNEL and WGA to identify dying cardiomyocytes (n = 6) ***p < 0.001, **p < 0.01, *p < 0.05.

3.2.6 Fisetin-HG Improves Vascular Density, Reduces Inflammation, and Promotes Polarization of Pro-Wound Healing Macrophages

As MG has been shown to impair angiogenesis and promote inflammation at the cellular level in the MI heart,[62] we performed immunohistochemistry at 5 weeks post-MI to assess the effect of fisetin-HG treatment on vascularity and the inflammatory response. Our results showed that fisetin-HG treated hearts had a greater number of CD31+α-SMA+ arterioles in the scar region compared to HG, fisetin-alone, and PBS treated groups (by 1.6-fold, 2.0-fold, and 2.1-fold, respectively; **Figure 3.6A (upper panel),3.6B**). A vascular permeability assay using Evans blue (EB) administered to mice via tail vein injection prior to sacrifice at 5 weeks post-MI demonstrated that the vasculature was functional (**Figure 3.6A, lower panel**). There were no differences detected in the number of α-SMA+ myofibroblasts between groups at 5 weeks post-treatment **(Figure 3.6C).**

The transition of pro-inflammatory M1 macrophages to pro-wound healing M2 macrophages leads to the resolution of inflammation and plays a critical role in MI repair.[105,106] Thus, we assessed the number of $CD86^+$ pro-inflammatory M1 macrophages and $CD206^+$ pro-wound healing M2 macrophages in mouse hearts 5 weeks after treatment. The number of $CD86^+$ cells was lower in hearts treated with fisetin-HG or HG compared to fisetin-alone and PBS groups (by up to 1.5-fold and 1.4-fold, respectively), suggesting that inflammation is suppressed by matrix treatment **(Figure 3.7A)**. We also observed an increase in the number of $CD206^+$ M2 macrophages (up to 2.4-fold) in the infarct region of the fisetin-HG group compared to all other treatment groups at 5 weeks post-MI **(Figure 3.7B)**. Taken together, these results suggest that fisetin-HG treatment enhances vascularization, reduces inflammation and promotes a pro-healing environment post-MI.

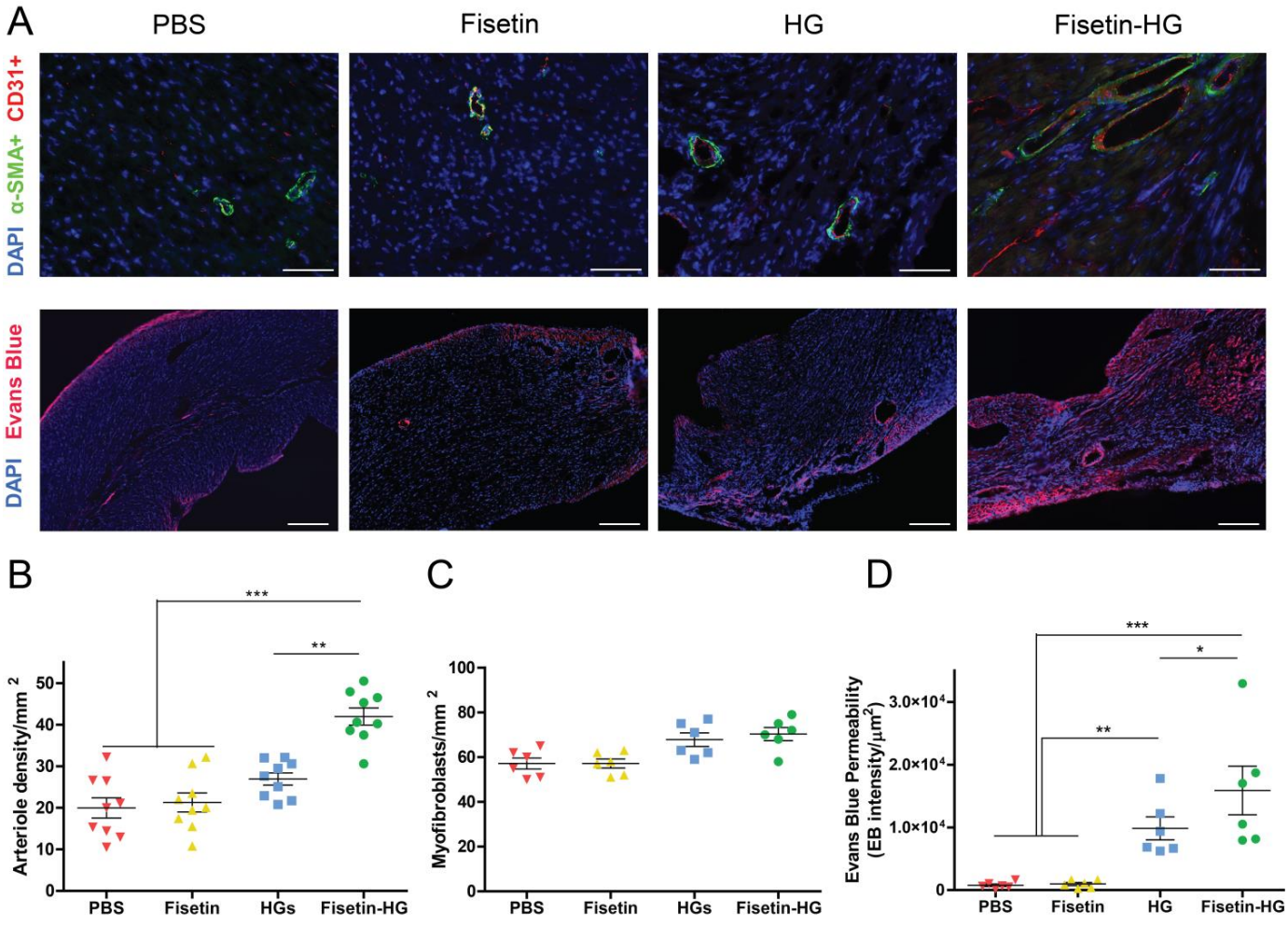

Figure 3.6 Fisetin-HG treatment increases myocardial vascularity.A) Upper panel: Representative immunohistochemistry images of double positive α-SMA+ (green) and CD31+ (red) arterioles, CD31+ capillaries (red) and DAPI stained cell nuclei (blue). Scale bar = 100 μm. Lower Panel: EB (red) positive cells, DAPI (blue). Scale bar = 300 μm. B) Quantification of arteriole density (number cells mm−2). C) Myofibroblast density (number cells mm−2). (n = 6–9) ***p < 0.001, **p < 0.01, *p < 0.05.

3.2.7 Fisetin-HG Treatment Reduces MG-AGEs and Oxidative Stress Post-MI

We next assessed how fisetin-HG treatment may be affecting molecular factors underlying oxidative stress by evaluating the expression of oxidative stress markers at 5 weeks post-MI.

Since MG-derived AGEs play a critical role in oxidative stress, we first determined the protein levels of MG-derived hydroimidazolone-1 (MG-H1), the primary MG-specific adduct. The level of MG-H1 in fisetin-HG treated hearts was significantly lower compared to all other treatment groups (by 5.1-fold, 4.3-fold and 1.7-fold vs. PBS, fisetin, and HG treatment, respectively; **Figure 3.8A**). We then assessed the effect of treatment on the activation of Nrf2, a transcription factor and antioxidant response element that protects against oxidative damage, in part by reducing AGE levels.[107] Notably, Nrf2 protein levels in the myocardium were significantly increased in the fisetin-HG group compared to hearts treated with HG, fisetin or PBS **(Figure 3.8B)**. We also examined the levels of Glo1, the primary enzyme responsible for MG metabolism. Our results show that Glo1 protein levels were markedly higher in the fisetin-HG treated group compared to all other three treatment groups **(Figure 3.8C)**. Lastly, we measured glutathione (GSH) levels as indicator of the oxidative stress status. GSH is an endogenous antioxidant, and co-factor in the glyoxalase pathway that detoxifies MG and protects cells from oxidative damage.[108] We detected a significantly higher ratio of GSH/GSSG (reduced/oxidized GSH) in the myocardium of the fisetin-HG group compared to the HG, fisetin and PBS treatment groups **(Figure 3.8D)**. Since the fisetin-HG treatment promoted greater vascularity and reduced cardiomyocyte death, it was of interest to examine the effect of treatment on the level of the pro-survival factor neuregulin (NRG) in the myocardium. We observed that the fisetin-HG treatment resulted in increased NRG protein levels at 5 weeks post-treatment compared to all other treatment groups **(Figure 3.8E)**. Taken together, these results demonstrate that the myocardium of fisetin-HG treated mice had a greater activation of factors regulating MG metabolism and superior reduction of oxidative stress post-MI.

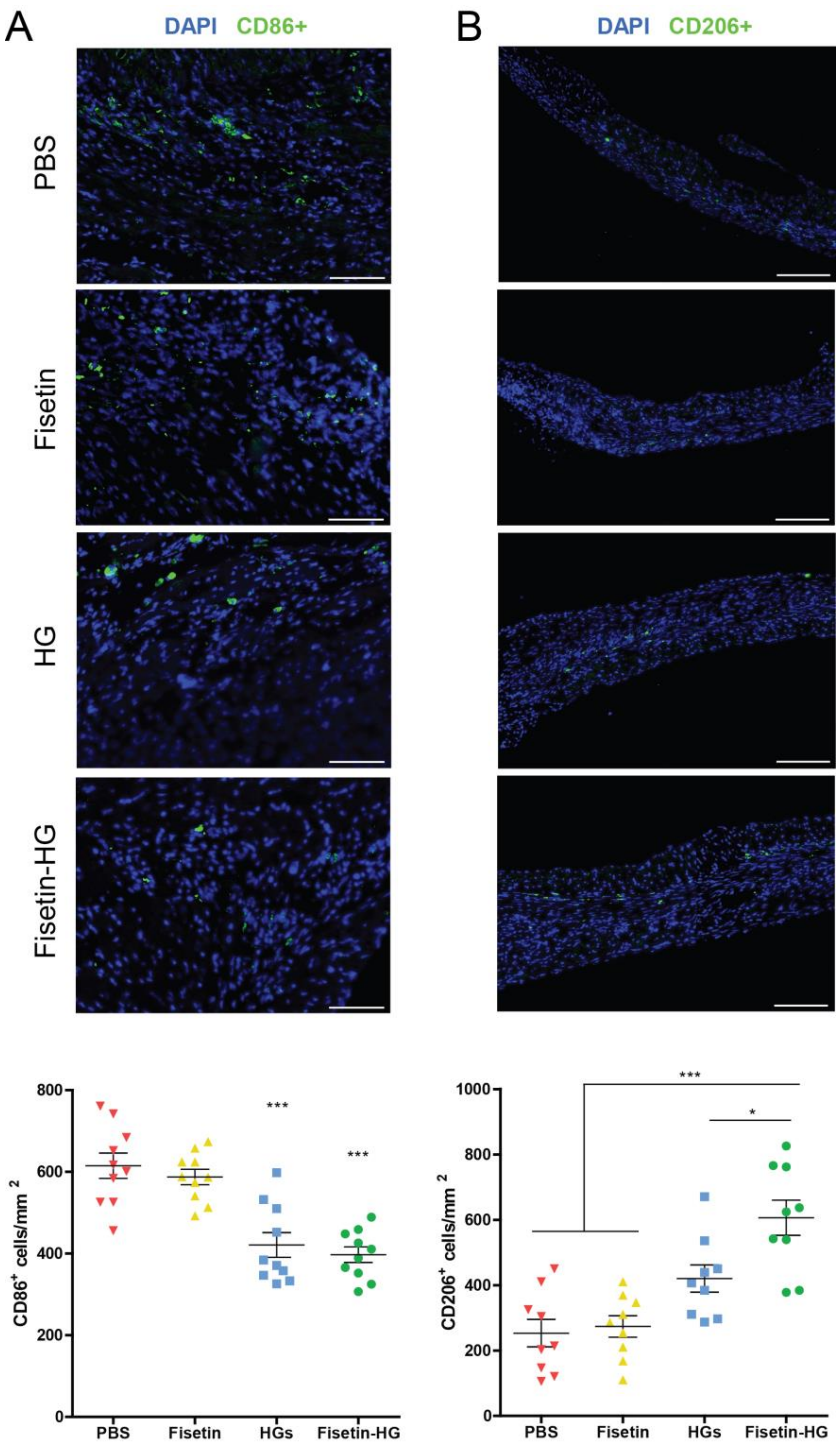

Figure 3.7 Fisetin-HG treatment promotes pro-healing macrophage polarization.A) Representative images and quantification of CD86+ pro-inflammatory macrophages (green). Scale bar = 100 µm. B) Representative images and quantification of CD206+ pro-wound healing macrophages (green). Scale bar = 300 µm. Data is presented as the number of cells mm−2 (n = 9) ***p < 0.001, **p < 0.01, *p < 0.05

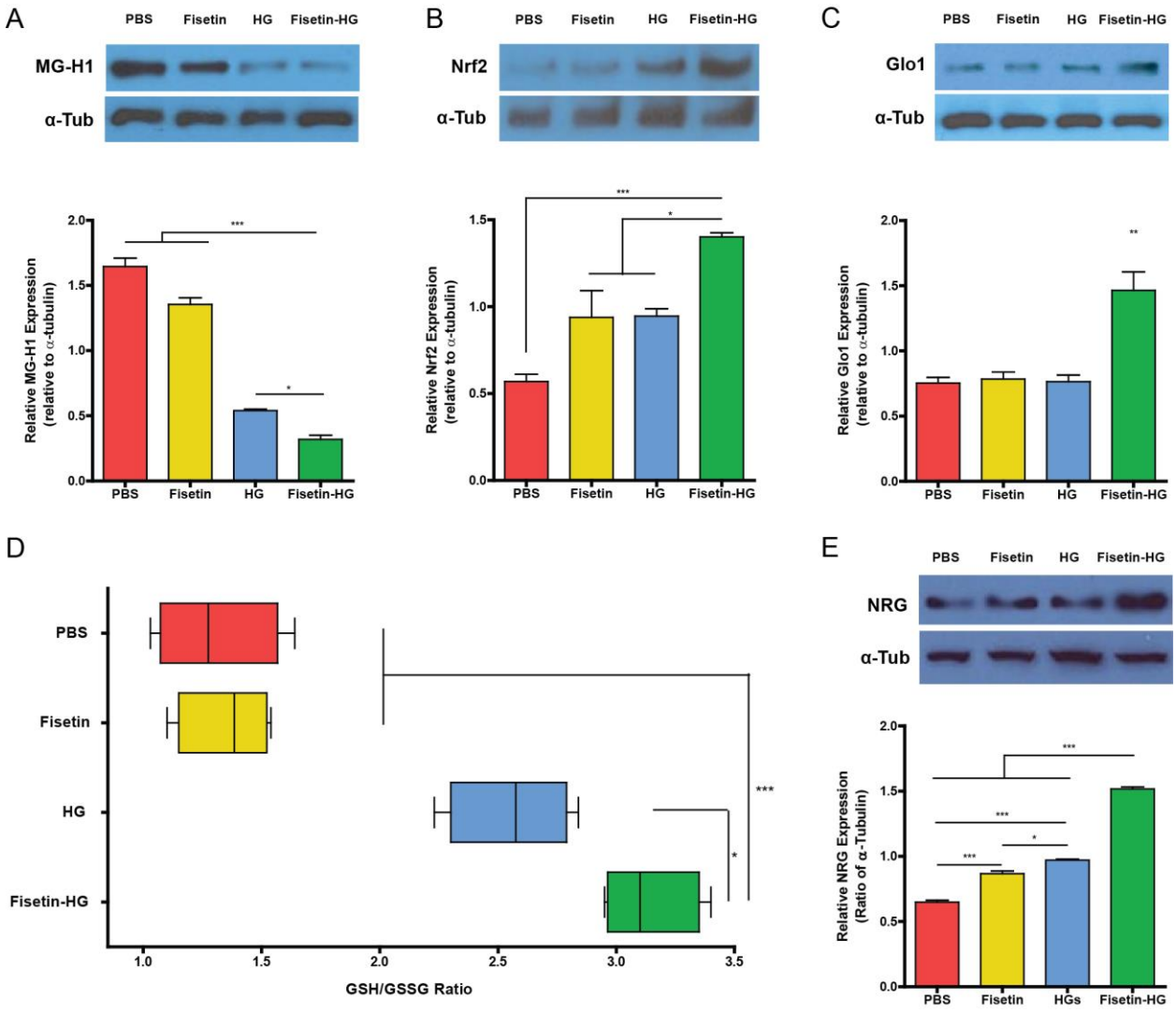

Figure 3.8 Fisetin-HG treatment reduces oxidative stress.A) Representative western blots for MG-H1 protein expression and quantification. B) Representative western blots for Nrf2 protein expression and quantification. C) Representative western blots for Glo1 protein expression and quantification. D) The GSH/GSSG ratio (for reduced versus oxidized GSH levels; n = 3). E) Representative western blots for NRG protein expression and quantification. Results for all western blots were normalized to α-tubulin levels; n = 9 for all, except n = 4 for NRG; ***p < 0.001, **p < 0.01, *p < 0.05.

3.3 Discussion

Methylglyoxal is a reactive dicarbonyl mostly produced as a degradation product during glycolysis, which accumulates during periods of oxidative stress and anaerobic glycolytic metabolism, contributing to oxidant-induced cytotoxicity.[54,55] MG is typically present at very low levels and is primarily eliminated by the glyoxalase system in healthy tissue; however, stress conditions (such as ischemia) can lead to increased MG and AGE production and compromised tissue function.[43,109,110] We previously identified that MG accumulates acutely post-MI, which contributes to the adverse cardiac remodeling and functional loss of the infarcted heart.[62] In this study, we developed a therapy that aimed to reduce methylglyoxal-induced damage as an approach to improve the endogenous repair response and restore LV function post-MI. We demonstrated that the flavonoid fisetin delivered to the myocardium within a collagen hydrogel can reduce methylglyoxal-related oxidative stress, minimize inflammation, promote neovascularization, and improve LV function and cardiac contractility of the infarcted heart.

Fisetin was our chosen therapeutic due to its antioxidant properties and ability to reduce inflammation. It performs these functions through its ability to upregulate glutathione levels, increase Glo1 activity and directly scavenge MG.[68,69] To-date, only a few studies have examined its therapeutic effects in the context of heart disease. For example, Garg *et al*. showed that oral administration of fisetin (prior to induction of cardiac injury) could protect the heart from ischemia-reperfusion injury in a PPAR-γ dependent manner by suppressing oxidative stress and reducing inflammation and scar size.[111] Other studies have similarly shown protective effects of fisetin through anti-hypertrophic effects, suppression of oxidative stress, inhibition of inflammation and/or reduced apoptosis in models of ischemia-reperfusion injury, doxorubicin-induced cardiotoxicity, pressure overload-induced cardiac hypertrophy and isoproterenol-

induced cardiac-ischemic injury.[112–115] In *in vitro* studies, fisetin treatment was shown to enhance the viability of cultured cardiomyocytes after hypoxia/starvation and re-oxygenation by decreasing the generation of reactive oxygen species, inhibiting apoptosis and protecting the cells from DNA damage.[116] To our knowledge, our study is the first to evaluate the effect of fisetin administered directly into the injured myocardium after myocardial infarction at a clinically relevant time.

Prior to the *in vivo* experiments, the hydrogels were first characterized and tested *in vitro* for their ability to reduce the effects of MG in cultured cells. Characterization experiments were performed to determine if the addition of fisetin had any significant effect on the physical properties of the hydrogel. The fisetin-loaded collagen hydrogel (fisetin-HG) and the control hydrogel (HG) exhibited comparable properties in terms of viscosity, water content and enzymatic degradation rate. Their high water content and mechanical properties make collagen hydrogels ideal for injection to the myocardium following MI, as previously reported.[103] The release assay showed a steady release of fisetin from the hydrogel over 24 hours in untreated conditions. As expected, exposure to collagenase resulted in an initial burst release of fisetin from the hydrogel up to 6 hours, followed by a steady release over 24 hours. The release profile *in vivo* may be affected by the more complex tissue environment compared to the simpler *in vitro* conditions tested; however, given that the majority of the collagen hydrogel has been shown to be degraded *in vivo* within 2-7 days post-injection to the myocardium,[103] fisetin is likely to be fully released within this time. The expected degradation/loss of the injected hydrogel was demonstrated by *ex vivo* fluorescence imaging showing that the hydrogel was localized within the myocardium upon injection and that the amount remaining dropped from 68.1% at day 1 to 8.6% at day 3. The imaging results also showed that fisetin retention in the myocardium was

increased when delivered with the hydrogel compared to fisetin delivery alone, which was confirmed by the more accurate UPLC analysis for fisetin content in myocardial tissue. Given these retention results, we expect that most of the fisetin was released from the HG and metabolized within the myocardium and that only minimal off-target accumulation occurred; however, a tissue biodistribution analysis was not performed to confirm this. Upon its release from the HG, any fisetin that managed to escape the myocardium into the circulation likely localized primarily in the liver, as has been shown previously with intraperitoneal delivery.[117] Toxicity concerns for off-target fisetin accumulation would be deemed negligible since its administration at doses up to 2 g kg^{-1} has been reported to be non-toxic when examined in multiple tissues (lungs, spleen, liver, kidneys, heart, stomach, intestine, testes, and ovary) in mice.[117,118]

To establish that fisetin could prevent MG-induced toxicity, we initially demonstrated that MG exposure reduced the viability of cultured endothelial cells and that this was prevented by treatment with fisetin. We also observed that total network length in an *in vitro* angiogenesis assay was reduced after MG treatment, and that this reduction was prevented by the addition of fisetin. These findings are similar to previous reports showing that protecting cells from the effects of MG can reduce cell death and increase angiogenesis.[51,62,119] Not surprisingly, our MBo probe assay confirmed that treatment with fisetin alone or released from the hydrogel significantly lowered the intracellular concentration of MG in cultured cells. This supports that fisetin's rescue effect is mediated in part through its ability to reduce cellular levels of MG.

Having established that the fisetin-HG system can reduce MG levels and its negative cellular effects, we tested its therapeutic efficacy in treating MI mouse hearts. We assessed the performance of our therapy administered during the inflammatory phase (at 3 hours post-MI), as

it was previously shown that the therapeutic efficacy of our collagen hydrogel was greatest when delivered at this time.[102] Given that healing of the infarcted mouse heart occurs about twice as fast compared to humans, this time-point is equivalent to ≈6 h in humans.[35] Therefore, our treatment protocol is clinically relevant as it mimics the setting of an acute MI patient presenting to the emergency room. In terms of administration of the treatment, the intramyocardial injection method used in our study is a minimally invasive ultrasound-guided procedure, which could be translated into clinical practice using catheter-based delivery approaches, which are becoming more routine in cardiac procedures. Similar to our previous study,[102] functional analyses demonstrated that treatment with the HG alone administered at 3 hours post-MI resulted in improved cardiac function 5 weeks later. Notably, treatment with fisetin-HG conferred an even greater increase in LVEF. Improvements in cardiac output, stroke volume and end-systolic volume were also observed in only the fisetin-HG group, suggesting overall superior cardiac function with this treatment. We also assessed the longitudinal strain of the endocardium at aortic valve closure, which is representative of cardiac contractility,[120] and observed an improvement only in the fisetin-HG group. It is important to note that negative strain represents better contractility, indicating superior *in vivo* functional outcomes. Histological analyses revealed a decrease in the scar size, and an increase in remote myocardium thickness in the fisetin-HG treated group. Taken together, it was demonstrated that fisetin-HG treatment reduces adverse ventricular remodeling, limits cardiac dilation and improves contractility post-MI, leading to superior cardiac function. These results highlight the synergistic effect of a combined fisetin and collagen hydrogel treatment *in vivo* and demonstrate its potential for future clinical applications.

To gain mechanistic insight into our therapy, we examined processes reported in the literature that are associated with detrimental MG effects. MG-AGEs have been shown to trigger cell death and apoptosis via oxidative stress in the body.[121,122] In our study, we observed reduced levels of active caspase-3 at 5 weeks post-treatment in mice receiving fisetin-HG treatment. Notably, we observed greater viable myocardium and less death specifically in cardiomyocytes (by TUNEL and WGA staining) after treatment with fisetin-HG. This greater survival of cardiomyocytes may be partially attributed to the associated increase in NRG observed in fisetin-HG treated hearts. NRG is a pro-survival factor produced by endothelial cells adjacent to cardiomyocytes that acts in a paracrine fashion to preserve cardiomyocyte viability.[123,124] MG has been shown to reduce NRG expression in the myocardium,[119] and NRG therapy for MI improves cardiomyocyte survival.[125,126] Taken together, the data suggests that reducing MG with the fisetin-HG treatment limits on-going cell death in the myocardium, which leads to less ventricular remodeling, less scar expansion and overall smaller scar size.[62,127]

Another important healing process post-MI is angiogenesis. Endothelial cells have been identified as a therapeutic target for treating MI and preventing the progression to heart failure.[128,129] Angiogenesis has been shown to be negatively impacted by MG accumulation, in part through the up-regulation of anti-angiogenic factors and dysregulation of VEGF signaling.[130,131] Our *in vitro* results showed that fisetin-HG can prevent MG-induced defective angiogenesis in cultured endothelial cells, and we observed an increase in arteriole density in the MI mouse model after fisetin-HG treatment. EB staining demonstrated the functionality of the vessels. This suggests that fisetin-HG can promote vascularization, thus improving the supply of oxygen and nutrients to the myocardium.

MG can activate an inflammatory response in the heart,[119] and chronic inflammation post-MI is associated with adverse ventricular remodeling, which can progress to heart failure.[14,132] Treatment of the MI mouse heart with fisetin-HG resulted in a decrease in the number of CD86+ pro-inflammatory M1 macrophages and an increase in the number of pro-healing CD206+ M2 macrophages in the infarcted myocardium. The promotion of wound healing versus inflammatory macrophages is likely induced by both the fisetin and the collagen HG. It has been shown that MG glycation of macrophages promotes their pro-inflammatory function.[133] Fisetin has been reported to reduce the expression of pro-inflammatory genes in macrophages, such as tumor necrosis factor-α and interleukin-6, which are involved in the inflammatory response post-MI.[66,134–136] Fisetin exerts its anti-inflammatory effects through the suppression of the transcription factors NF-κB and AP-1. Specifically, fisetin directly inhibits the kinase activity of Src and Syk, which are involved in the NF-κB cascade,[134] and it reduces the phosphorylation of c-Jun N-terminal kinase (JNK) and its target c-Jun, which are key mediators of the AP-1 signaling pathway.[66]

We and others have previously reported that collagen biomaterials can reduce inflammatory M1 macrophage numbers, induce M2 macrophage polarization, and promote anti-inflammatory cytokine production by macrophages while reducing the production of pro-inflammatory factors.[102,103,137,138] This effect could be due to collagen-mediated activation of AKT and/or miR-21-JNK signaling pathways that lead to M2 polarization, the production of anti-inflammatory cytokines and improved efferocytosis.[138,139] Given that the M1-to-M2 macrophage phenotype transition corresponds to a change from a pro-inflammatory to pro-healing status,[106,140] it appears that the fisetin-HG can promote healing and the resolution of inflammation. While the literature provides compelling mechanistic insight, an evaluation of how the fisetin-HG treatment

specifically mediates macrophage phenotype and inflammation in the context of MI repair constitutes an area of future investigation.

Oxidative stress plays a pivotal role in the pathophysiology of MI; and the accumulation of MG and its AGEs has been shown to promote oxidative stress.[141,142] Fisetin has been shown previously to reduce MG by direct scavenging, and also by increasing Glo1 levels.[68] Therefore, we expected that our fisetin-HG treatment would reduce MG levels leading to less MG-AGE formation and oxidative stress within the infarcted heart. We observed an increase in Glo1 expression in fisetin-HG treated hearts, suggesting that the glyoxalase system may be activated by the treatment to detoxify MG through its conversion D-lactate.[143] This was accompanied by a reduction in MG-H1 (the primary MG adducts) in fisetin-HG treated hearts. Further supporting this mechanism, we found an increase in the levels of Nrf2, a transcription factor that regulates Glo1 expression and induces Glo1 activity leading to MG metabolism,[144,145] which has also been shown to be upregulated by fisetin.[146] As expected, the reduction of MG and its AGEs correlated with less oxidative stress (as determined by the GSH/GSSG ratio) in the myocardium of the fisetin-HG group. Notably, HG treatment alone also reduced MG-H1 levels and oxidative stress but had no effect on Glo1 or Nrf2 expression. Collagen, and in particular its arginine residues, is a major target for MG glycation,[147,148] which has been demonstrated in the post-MI myocardium.[62] It is hypothesized that the injected collagen hydrogel is targeted by MG, thus sequestering it away from the myocardial tissue and reducing its contribution to the formation of MG-AGEs and induction of oxidative stress. As the hydrogel is degraded within a week of injection,[103] the "trapped" MG is then removed from the tissue. Altogether, our results suggest that fisetin-HG treatment reduces the accumulation of MG and its AGEs through increased Nrf2, GSH and Glo1 levels.

3.4 Conclusion

In this study, we demonstrated that a combination of the antioxidant fisetin with a collagen HG acted synergistically to decrease MG-related oxidative stress, reduce inflammation, increase cell survival, limit adverse cardiac remodeling and improve cardiac function when administered during the inflammatory phase post-MI. In addition to its MG scavenging function, the fisetin-HG treatment was shown to increase the activity of Nrf2, GSH, and Glo1, factors known to contribute to MG detoxification. Taken together, the results suggest that targeting MG metabolism may be a promising approach to limit adverse cardiac remodeling, prevent damage and preserve function of the infarcted heart. These findings may help guide the development of new strategies, such as the fisetin-biomaterial therapy, for treating MI patients and reducing the incidence of heart failure.

3.5 Experimental Section

Preparation and characterization of fisetin hydrogel: Fisetin stock solution (10 mM) was prepared by dissolving 2.87 g of fisetin (Sigma Aldrich) in 1 ml of sterile dimethyl sulfoxide (DMSO). Chondroitin sulphate (CS) solution (40%) was prepared by dissolving 40 g of CS (Wako) in 100 ml phosphate buffered saline (PBS, calcium and magnesium free). The fisetin-loaded collagen hydrogel (fisetin-HG) was prepared on ice using an enclosed syringe system that allows homogenous mixing without introducing bubbles. Briefly, 1% rat-tail collagen type I (Corning®, Cat#354236), fisetin (diluted to 100 µM), 40% CS, N-ethyl-N-(3-dimethylaminopropyl) Carbodiimide (EDC) and N-hydroxysuccinimide (NHS) were added to produce a final mixture with a mass ratio of 1:4:0.5:0.3 for collagen, CS, NHS, and EDC, respectively. After thorough mixing, the pH was adjusted to 7.4 by adding NaOH (1.0 N). Collagen hydrogel (HG) without fisetin was also prepared following the same protocol.

Viscosity measurement: Viscosity measurements of hydrogels (fisetin-HG and HG) were carried out using a Brookfield R/S plus rheometer (Brookfield) at 37°C. A C25–2/30 conical spindle was used to compress the material (50 μm displacement) onto a temperature-controlled pedestal. Viscosity was measured with a ramp rotational block at a speed of 1/min units pre-set at a shear rate of five units over a time of 30 min.

Equilibrium water content: Water content of the hydrogels was measured by measuring the wet weight (W_0) of the sample, equilibrated in PBS for 96 h at 4°C. The material was then vacuum-dried at room temperature for 96 h to obtain the dry mass (W). The total water content of the hydrogels (W_t) was then calculated according to the equation: $W_t = \frac{(W_0 - W)}{W_0} \times 100$

Hydrogel degradation and fisetin release assay: Enzymatic degradation was measured using 50–100 mg of hydrogel placed in 5ml of type I collagenase (10 U/ml in PBS) at 37 °C. The remaining solid mass was measured over a period of up to 24 h. The degradation rate is calculated from the initial slope of the plots of remaining mass vs. time and reported as mg/min. The fisetin release profile was also assessed by measuring the amount of fisetin in the supernatant with/without type I collagenase (10 U/ml in PBS) at 37 °C. For this, fisetin-HG (containing 100 μM of fisetin) was prepared and the released fisetin concentration was determined using UV-Vis spectroscopy at 360 nm over a period of up to 24 h.

In vitro endothelial cell cultures and viability assay: Human umbilical vein endothelial cells (HUVECs; Life Technologies) were cultured in tissue culture plates for 24 h and maintained in HUVEC media (10% FBS, 1% L-glutamine, 2 μg/ml sodium heparin, 1% penicillin/streptomycin, 30 μg/ml endothelial growth supplement (BD Biosciences) in M199 media, pH 7.2).

To establish a toxic dose of MG for cell culture experiments, HUVECs were treated with increasing concentrations of MG (from 0 to 100 µM, in HUVEC media) and subjected to an *in vitro* viability assay. Briefly, HUVECs were stained using a Calcein-AM and Ethidium Homodimer-1 (CaAM/EthD-1) viability kit (ThermoFisher Scientific, Cat# L3224) according to the manufacturer's instructions. Stained cells were imaged by fluorescence microscopy, and fifteen random images were taken for each experimental group. Total cell numbers were calculated using ImageJ2® software (NIH, USA). Each condition was performed in triplicate. It was observed that MG at a concentration ≥ 10 µM reduced endothelial cell viability **(Figure S2A and S2B)**. A MG concentration of ≥ 10 µM also impaired network-like formation in ECMatrix™ angiogenesis plates (procedure described below; results shown in **Figure S2C and S2D**). Based on these viability and angiogenesis results, and in consultation with the literature,[119] we carried out further *in vitro* experiments using a "toxic" MG dose of 25 µM. To assess the effect of fisetin on cell viability, HUVECs were treated with 25 M MG ±fisetin (10 µM) and the same CaAM/EthD-1 assay as described above was performed.

In vitro angiogenesis assay: An *in vitro* angiogenesis network formation assay (Ibidi® µ-Plate angiogenesis slides, Cat# 81506) was performed following the manufacturer's protocol. First, wells were coated with 10 µL of ECMatrix™ and HUVECs were seeded at a density of 5×10^3 cells/well. To test fisetin effects, HUVECs were treated with 25 µM MG ±fisetin (10 µM) and compared to cells without MG exposure. Total capillary-like network length was quantified per field-of-view (1.25× using light microscopy). Each condition was performed in triplicate.

Animal experiments: All procedures were approved by the University of Ottawa Animal Care Committee and performed in accordance with the National Institute of Health Guide for the Care and Use of Laboratory Animals.

Mouse cardiac fibroblast isolation and culture: Hearts of 8-week old wild-type C57BL/6 mice were perfused with ice-cold PBS, harvested and kept in PBS on ice. Next, the hearts were cut into small pieces, resuspended in lysis buffer containing 0.08% DNase I (20U/mL), 0.9% of 1 M HEPES and 2.5% of collagenase blend (Liberase Blendzyme 3 TH, Roche) in sterile Hanks' Balanced Salt solution (HBSS) and incubated for 45 min at 37°C. Enzymatic digestion was supported by vortexing every 5 minutes. Digested tissue was filtered through a 70 µm cell strainer followed by centrifugation for 2 min at 50 g to remove remaining undigested tissue. The supernatant was then filtered through a 40 µm cell strainer, centrifuged at 450 g for 5 min and washed with PBS two times. Cells were resuspended and cultured in Dulbecco's Modified Eagle's Medium/Nutrient Mixture F-12 Ham (DMEM/F-12, Sigma) supplemented with 1% penicillin/streptomycin and 10% FBS. Non-adherent cells were removed after 2 days by washing with PBS and the medium was replenished. The adherent fibroblasts were maintained with the medium changed every 3 days.

Detection of MG in live cells using MBo fluorescence probe: To evaluate the ability of fisetin released from the hydrogel to reduce intracellular MG levels, a "turn on" fluorescent sensor methyl diaminobenzene-BODIPY (MBo) was used as described.[104] The MBo probe exhibits some cross-reactivity with nitric oxide.[104] Since endothelial cells produce high levels of nitric oxide, we performed the MBo studies using cardiac fibroblasts, which have low nitric oxide expression. Briefly, one of the following was added to the wells of tissue culture plates: 1) fisetin-HG, 2) HG, 3) fisetin, or 4) nothing. Next, plates were incubated for 30 min, and then fibroblasts were seeded at a density of 5×10^3 cells/well and cultured with 25 µM MG in DMEM/F-12 supplemented with (1% pen/strep, 10% FBS). After 24 h, the media was replaced with 1 ml of HEPES-Krebs-Ringer's buffer (HKR) (140 mM NaCl, 2 mM KCl, 1 mM $CaCl_2$, 1

mM $MgCl_2$, 10 mM HEPES pH 7.4) and 5 µM of MBo fluorophore in complete medium (from stock in DMSO) was added and incubated for 1 h. Cells were then rinsed once with HKR buffer, and incubated for an additional 1 h in 5 µM of MBo fluorophore containing phenol-free media to prevent background fluorescence. The fluorescence signal was then measured using a plate reader at 470±40 nm / 540±50 nm at baseline (0 min), 30 min, 1 h, 3 h and 6 h, and expressed as a fold-change relative to baseline for each group. Data are represented as mean ± SEM of at least three replicates.

Myocardial infarction model and intramyocardial injection: MI was induced in 8-week old C57BL/6 female mice (Charles River) and treatment delivery was performed using a previously established intramyocardial injection protocol.[101–103] Briefly, mice were anesthetized (2% isoflurane), intubated, and the heart was exposed via a fourth intercostal thoracotomy. The left anterior descending coronary artery (LAD) was then ligated just below its emergence from the left atrium. This procedure results in a mid/large MI involving the anterolateral, posterior, and apical parts of the left ventricle. MI size was confirmed at the time of surgery by myocardial blanching in the region supplied by the artery. Short-acting buprenorphine was administered at least an hour prior to surgery, and long-acting buprenorphine was administered subcutaneously immediately before surgery for perioperative analgesia. Immediately following the MI surgery, the chest was closed and sutured. At 3h post-MI (baseline), mice were randomly assigned to receive one of 4 treatments: 1) PBS (control); 2) fisetin-alone; 3) collagen hydrogel (HG); or 4) fisetin-hydrogel (fisetin-HG). The treatment was administered in five equivolumetric intramyocardial injections (10 µl each site, 50 µl total) through a 27-G needle using a minimally invasive echocardiography-guided closed-chest procedure, established by our group.[103,149] The syringe is secured in a micromanipulator (VisualSonics, USA) and the needle and MX400

scanhead probe are aligned along the heart long-axis. Via the ultrasound field-of-view, the micromanipulator is used to position the needle tip in the desired location within the myocardium for injection of the treatment. Mice were euthanized by terminal anesthesia at 5 weeks post-treatment and hearts were collected for histology and/or molecular analysis.

Echocardiography and strain analysis: Transthoracic echocardiography was performed on parasternal long-axis views using a Vevo3100 system in B mode with a MX400 series real-time microvisualization scanhead probe and analysis performed with its accompanying Vevo LAB 3.1.1 software (VisualSonics). The imaging was carried out at 3 hours (right before the treatment) and 5 weeks post-MI to determine left ventricular ejection fraction (LVEF), stroke volume (SV), cardiac output (CO), left ventricular end systolic volume (ESV) and end diastolic volume (EDV). To assess contractility, cardiac strain analysis was performed through the longitudinal axis since longitudinal strain is most representative of myocardial shortening at the level of the endocardium.[120,150] The longitudinal endocardial strain at the time of aortic valve closure (representing end systole) in segment 6 (anterior apex segment), corresponding to the infarct zone area, was calculated. As strain is calculated as the final length [L]/initial length [L_0], negative strain values represent improved contractility (shortening of a given myocardial segment relative to its original length).[151] Results for both echocardiography and strain analyses were analyzed by a researcher blinded to the treatment groups.

Hydrogel imaging: The fluorescently tagged HG and Fisetin-HG matrices (25 nmol of Alexa-Fluor®594 dye per hydrogel) were injected to the infarcted mouse heart as described above. Animals were euthanized 1 and 3 days after treatment, and hearts were harvested and imaged *ex vivo* by IVIS® Spectrum (PerkinElmer) to visualize HG and Fisetin-HG distribution and retention within the hearts (λ excitation: 570 nm; λ emission: 640 nm). As a positive control

group, untreated hearts were collected, and the injection of hydrogel was performed *ex vivo*. These were immediately imaged by IVIS and used to represent 100% HG retention. The data was reported as relative radiant efficiency (%) and normalized to the positive control hearts.

Ultra-performance liquid chromatography: Heart tissue samples were collected at day 1 and day 3 post-treatment. Tissue preparation followed a previously described protocol with some modification.[152] Briefly, two liquid extraction solutions were prepared. Extraction solution A was made of methanol/water (50/50) with Chrysin (500 ng/mL) added as an internal standard. Extraction solution B was made of dichloromethane/methanol (50/50) with Chrysin (500 ng/mL) added as an internal standard. Heart samples were kept on ice immediately after harvest to avoid molecular degradation. The heart was surface blotted, weighed, and transferred to a pre-cooled 2 mL glass tissue grinder (Tenbroeck type). Pre-cooled extraction solution A (250 µL) was added to the tissue grinder, the sample was homogenized with 10 vertical and 10 rotational shear movements, and the liquid phase was collected. The extraction with solution A was performed twice, and then repeated twice with 250 µL of extraction solution B. All the collected liquid extractions were mixed, sonicated for 1 minute, and centrifuged for 15 minutes at 12,000 RPM. The supernatant was filtered through 0.45 µm filter and centrifuged for another 15 minutes at 12,000 RPM. This supernatant was injected directly into the UPLC.

Sample analysis was performed with a RP-UPLC-MSMS Waters Acquity UPLC Xevo TQD system using a 2.1x100 mm UPLC BEH C8 column. The analysis conditions were modified from a previous report.[153] Briefly, the extracted solution was placed in sealed vials and 2 µL was injected for each analysis. The autosampler was set to cold temperature to avoid evaporation, and the flow was set to 0.5 mL/min. Water, acetonitrile, and formic acid 5% (in water) were used as eluents. The initial flow conditions were: water 96%, acetonitrile 2%, and formic acid 2% (last

one was kept constant in all runs). Acetonitrile was increased up to 60% over a period of 10.5 min with linear gradient. A column washing step was then performed: acetonitrile was increased to 96% min and kept for 1 min, followed by a re-equilibration step back to the initial conditions for 2.5 min. The column was kept at 35ºC. A multi reaction monitoring analysis (MRM) was set up for fisetin and chrysin (internal standard). The analysis was performed in MSMS ESI mode with a capillary voltage of 3.50 kV, a source temperature of 500ºC, a desolvation gas flow of 600 mL/h, and a cone flow of 25 mL/h. The first quadruple analyzer was set to LM resolution of 13, HM 11.5, and ion energy of 0.3. Argon was used for gas collision in the second quadruple. The third quadruple was set up to LM of 12, HM 13, and 2.5 of ion source. For fisetin, the cone voltage was 40V, and the collision energy was 20V. For chrysin, the cone voltage was 20V, and the collision energy was 17V. Representatives MRM analysis for fisetin and chrysin can be seen in **Figures S3A and S3B**. The calibration curve was prepared by triplicate analysis of several calibration concentrations of fisetin. Chrysin was used as internal standard (IS) at a concentration of 500 ng/mL, and the following was plotted: (fisetin area)×([IS concentration]/[IS area]) vs. the concentration of fisetin. The calculated limit of detection (LOD) and limit of quantification (LOQ) were 6.4 ng/mL and 6.9 ng/mL, respectively. The calibration curve was reported in **Figure S3C**.

Vascular Permeability Assay: Vascular permeability was performed using Evans blue (EB) dye delivered by intravenous lateral tail vein injection at 5 weeks post-treatment. Briefly, 2% sterile EB dye was prepared in PBS and filter sterilized to remove any undissolved particles. Mice were placed into a restraint device that allows the tail to be handled. EB dye (4 ml/kg) was then slowly injected using a 27G needle via the lateral tail vein. Mice were put back into their

cages for 20 minutes and then sacrificed. Hearts were collected, fixed in 4% PFA and embedded for histology sectioning. Sections were imaged using a fluorescence microscope at 590 nm.

Histology and immunohistochemistry: Hearts were harvested at 5 weeks post-MI, embedded in OCT compound (Fisher Scientific), and snap frozen in liquid nitrogen. Sections (10 μm) were cut using a Thermo Scientific HM550 Cryostat. To evaluate scar size, tissue sections were fixed in 4% PFA for 1 h and stained with Masson's Trichrome stain (Electron Microscopy Sciences). Images were taken with a Celestron Handheld Digital Microscope Pro, and 8 sections per mouse were used to measure remote wall thickness and to determine scar size by the mid-line arc method using ImageJ2® software.[154] For immunohistochemistry, tissue sections were fixed in acetone for 20 min, washed with 0.05% Tween-20 in PBS, permeabilized with 0.1% Triton X-100 for 10 min and then blocked in 10% serum in PBS for 1 h at room temperature. Primary antibodies were applied overnight at 4°C in 10% serum, and then slides were rinsed and treated with secondary antibodies for 1 h in the dark at room temperature. Nuclei were stained with DAPI (1:1000) before being mounted with ProLongTM® Gold antifade reagent (Invitrogen). For the detection of apoptotic cells, an anti-active caspase-3 primary antibody (Abcam, Rabbit, Cat#ab2302 at 1:250 dilution) was used with AF488 anti-rabbit secondary (ThermoFisher, Cat#A-11008 at 1:1000 dilution). A TUNEL kit (Abcam, Cat#ab66108) was used together with wheat germ agglutinin (WGA; Alexa Fluor™ 594 Conjugate, ThermoFisher Cat# W11262) to assess cardiomyocyte cell death. For the detection of blood vessels and myofibroblasts, anti-CD31 (also known as PECAM-1, Santa Cruz, Rat, Cat#sc-101454 at 1:100 dilution) and anti-α-smooth muscle actin (α-SMA; Abcam, Rabbit, Cat#ab5694 at 1:250 dilution) primary antibodies were used and detected with AF594 anti-rat secondary (ThermoFisher, Cat#A-11007 at 1:1000 dilution) and AF488 anti-rabbit secondary (ThermoFisher, Cat#A-11008 at 1:1000 dilution),

respectively. To detect inflammation, M1 macrophages were detected with an anti-CD86 primary antibody (Abcam, Rat, Cat#119857 at 1:200 dilution) and visualized by AF488 anti-rat secondary (Invitrogen, Cat#A-11007 at 1:600 dilution). M2 macrophages were detected by an AF488-conjugated anti-CD206 antibody (BioLegend, Cat#141710 at 1:100 dilution). Fluorescent images were obtained using a Zeiss Axio Observer upright microscope with a ×20 objective. For all samples, four sections per mouse were analyzed and for each section 3 images within the infarct region were used for quantification.

Western blot: Total proteins were extracted from LV tissue samples using RIPA buffer (supplemented with protease inhibitor cocktail) and protein concentrations were determined by the Bicinchoninic acid (BCA) protein quantification method. Equal amounts of protein (20 μg) were denatured and loaded onto SDS polyacrylamide gels, subjected to electrophoresis, and transferred to a polyvinylidene fluoride (PVDF) membrane. Protein samples were probed with anti-MG derived AGE Antibody (Cell Biolabs, Mouse, Cat#STA-011 at 1:1000 dilution), anti-Nrf2 (Abcam, Rabbit, Cat#ab137550 at 1:1000 dilution), anti-Glo1 (Abcam, Rabbit, Cat#ab96032 at 1:1000 dilution), anti-NRG (Abcam, Rabbit, Cat#ab180808 at 1:100 dilution) and anti-α-tubulin (Cell Signaling, Rabbit, Cat#2125 at 1:1000 dilution) primary antibodies overnight. After washing with TBS-T several times, membranes were incubated with anti-rabbit (Novus Biologicals, HRP, Cat#N7185 at 1:10000 dilution) or anti-mouse (Abcam, HRP, Cat#ab205719 at 1:5000 dilution) secondary antibodies for 1 hour at RT. Bands were quantified by densitometry analysis using ImageJ2® software and intensities of the bands were normalized to α-tubulin.

Oxidative stress analysis: Tissue lysates of LV samples were prepared in mammalian lysis buffer (Abcam Cat#ab179835) and enzymes were subsequently removed by using a

deproteinizing sample kit (Abcam Cat# ab204708). Reduced glutathione (GSH) and oxidized glutathione disulfide (GSSG) levels were measured with the GSH/GSSG ratio detection assay kit II (Fluorometric – Green; Abcam Cat#ab205811) according to the manufacturer's instructions. The standard curve method was applied to calculate RFU readings. The concentration of GSSG (µM) in the test samples was calculated as: GSSG = (total glutathione – GSH)/2 and the ratio of GSH/GSSG was plotted.

Statistical analysis: Statistical analysis was performed using GraphPad Prism 8.0® software. All data are presented as the mean ± SEM. Outliers were identified using Tukey's fences (inter-quartile range) method for each measurement and removed from the statistical analysis. For the comparison of data between treatments, a one-way ANOVA was used followed by Bonferroni's correction for multiple comparisons. Scar size was analyzed using a multiple regression, including treatment group (HG, fisetin-HG, fisetin, and PBS) and baseline LVEF.

3.6 Supporting Information

Supporting Information of this article is available in Chapter 8 – Appendices section 8.1 at the end of this thesis.

3.7 Acknowledgements

The authors would like to thank Rick Seymour for surgical assistance (University of Ottawa, Animal Care and Veterinary Service) and Mayte Gonzalez for designing the table of contents figure with the use of BioRender. This work was supported by a Collaborative Health Research Program grant from the Canadian Institutes of Health Research (CPG- 158280) and the Natural Sciences and Engineering Research Council (CHRP 523794-18) (to E.J.S. and E.I.A.). C.E.C. was funded by Queen Elizabeth II Graduate Scholarships in Science and Technology. V.S. was funded by the Lawrence Soloway Endowed Fellowship from the University of Ottawa Heart Institute Foundation and M.M. by a strategic research postdoctoral fellowship from the University of Ottawa Heart Institute and the Strategic Research Endowed Fund.

4 Article II – Targeted delivery of glyoxalase-1 loaded nanoparticles reduces methylglyoxal and improves cardiac function after myocardial infarction

Manuscript:

Cagla Eren Cimenci[1,2], *Jing Chen*[3], *Madison Bak*[1,2], *Ashley Baldwin*[1], *Emilie Labranche*[1], *Chao Deng*[4], *Emilio I. Alarcon*[1], *Zhiyuan Zhong*[4], *Erik J. Suuronen*[1,2,*]

1 BEaTS Research, Division of Cardiac Surgery, University of Ottawa Heart Institute, Ottawa, K1Y 4W7, Ontario, Canada. 2 Department of Cellular and Molecular Medicine, Faculty of Medicine, University of Ottawa, Ottawa, K1H 8M5, Ontario, Canada. 3 Department of Biological and Environmental Engineering, Cornell University, 14850, NY, USA. 4 Department of Chemical Engineering and Materials Science, Soochow University, Suzhou, Jiangsu, China

Article II – Abstract

The targeted delivery of protein therapeutics using nanoparticles (NPs) may offer highly specific treatments for several diseases. However, only a few are being used in the clinical setting because of their potential side effects and difficulty in tracking their localization. Here we report on cross-linked multifunctional CD44 targeting hyaluronic acid NPs carrying glyoxylase-1 (Glo1-NPs) protein for reducing methylglyoxal (MG), which accumulates in cardiac tissue following myocardial infarction (MI). When delivered intravenously in mice at 3 hours post-MI, the Glo1-NPs specifically targeted damaged cardiac tissue, protected cell viability and limited infarct expansion by reducing oxidative stress, and led to improved cardiac function. These findings demonstrate the potential of NP-based targeted-delivery of Glo1 as a new approach for treating MI with promising implications for clinical translation due to its ease of application.

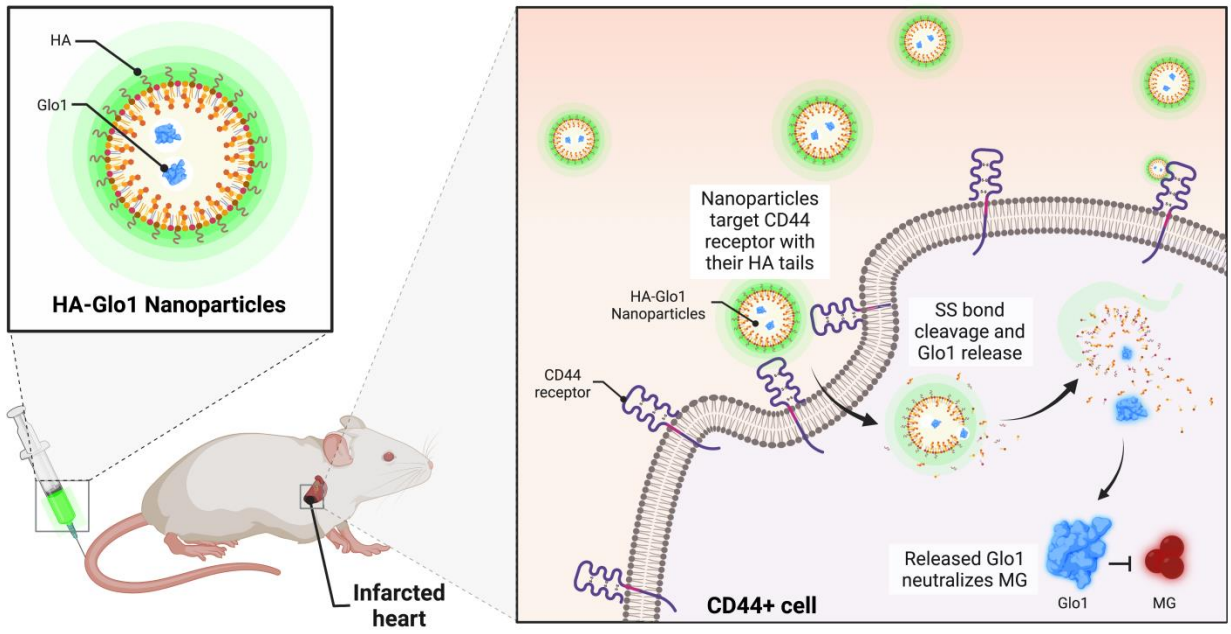

Table of Content (TOC) Illustration of Article II

4.1 Introduction

Cardiovascular disease is a leading cause of death, constituting ≈32% of the deaths worldwide; and nearly 70% of heart failure cases are attributed to adverse left ventricle (LV) remodeling caused by myocardial infarction (MI).[89,155] After MI, ischemia-mediated cell death leads to tissue necrosis, adverse LV remodeling, and contractile and functional loss of the myocardium.[156] Hypoxia post-MI inhibits oxidative phosphorylation, resulting in higher glycolytic activity, excess production of reactive oxygen species (ROS) (oxidative stress) and accumulation of advanced glycation end-products (AGEs) that are normally cleared from healthy tissue.[157,158]

Methylglyoxal (MG), a highly reactive dicarbonyl compound that is formed mainly as a by-product of glycolysis, is the primary precursor of AGEs.[92] In normal physiological conditions, MG is metabolized primarily by the glyoxalase-1 enzyme (Glo1). However, conditions such as hypoxia, inflammation, ischemia and oxidative stress augment MG production, while also limiting Glo1 activity, leading to increased MG-derived AGE (MG-AGE) formation.[50–52,93] MG

can lead to inflammation and endothelial cell (EC) damage and loss,[119,159–161] and we have previously shown that MG-AGEs accumulate acutely in the heart post-MI and that they contribute to reduced vascularization, adverse remodeling and loss of cardiac function.[62] The evidence identifies that the reduction of MG could be a potential therapeutic target for promoting vascular repair and cardiac function of the post-MI heart.[162]

Recent advances in nanoparticle technology have created considerable optimism for the development of new diagnosis tools and therapies for many conditions including cancer, neurodegenerative diseases, and fighting human pathogens like bacteria or viruses.[163–170] While these therapies have demonstrated great potential, there are still challenges to meet. Additionally, current approaches for delivering cardioprotective agents have relied mainly on surgical interventions or catheters to find the target tissue, and often do not have a way of being tracked after delivery.[171–173] Thus, actively targeting the damaged tissue while being able to monitor the NPs and/or their contents is immensely desired.

In this study, we developed Glo1-loaded CD44-targeting nanoparticle (Glo1-NP) therapy for reducing the effects of MG and enhancing vascular repair and cardiac function post-MI. Our NPs are cross-linked particles with high water content, offering excellent biocompatibility and suitable interior space for protein loading and delivery.[167,174,175] Additionally, the pyrazoline cycloadducts in their structure, which are formed by "tetrazole-alkene" photoclick reaction, give the NPs an intrinsic fluorescence that allow them to be visualized and tracked *in vitro* and *in vivo*.[166,167,176,177] It is also possible to modify and/or control the size, charge and release profile by changing the precursor molecule concentrations. The NPs have been designed with hyaluronic acid (HA), which is natural non-immunogenic, biocompatible and biodegradable glycosaminoglycan present in the human body, and a ligand for the cell surface receptor

CD44.[178,179] CD44 is expressed by ECs of the myocardium upon cardiac injury, whereas healthy ECs express little to no CD44.[180–184] Taking advantage of the HA-CD44 interaction, the NP system we develop successfully targeted the infarct region post-MI, reduced the negative effects of MG and improved cardiac function.

4.2 Results

4.2.1 Characterizations of Empty and Glo1-loaded NPs

Empty nanoparticles (NPs) and Glo1-loaded nanoparticles (Glo1-NPs) were prepared via inverse nanoprecipitation and photoclick reaction followed by UV irradiation. They were synthesized from hyaluronic acid (HA)-based precursor molecules: hyaluronic acid grafted with lysine tetrazole (HA-Lys-Tet) and hyaluronic acid grafted with cystamine methacrylamide (HA-Cys-MA) **(Figure 4.1A)**. When the precursors self-assemble, the encapsulated protein, Glo1, is trapped in the core of the NP, and HA chains stay on the surface, allowing the nanoparticle to interact with available CD44 receptors **(Figure 4.1B)**. After the crosslinking step, UV-Vis measurement showed that the NPs emit green fluorescence light (Excitation: 405, Emission: 450), while non-crosslinked NPs remained non-fluorescent, demonstrating that the crosslinked NPs are fluorescent by nature **(Figure 4.1C)**.

Dynamic light scattering (DLS) showed that empty NPs have an average size of 189 nm with a narrow polydispersity index (PDI) of 0.036 and zeta potential of -18.2 mV. Glo1-NPs were slightly larger (213 nm), with a PDI of 0.102 and zeta potential of -21.5 mV **(Figure 4.1D and 4.1E)**. Our results indicate that the NPs are small and suitable for systemic administration.

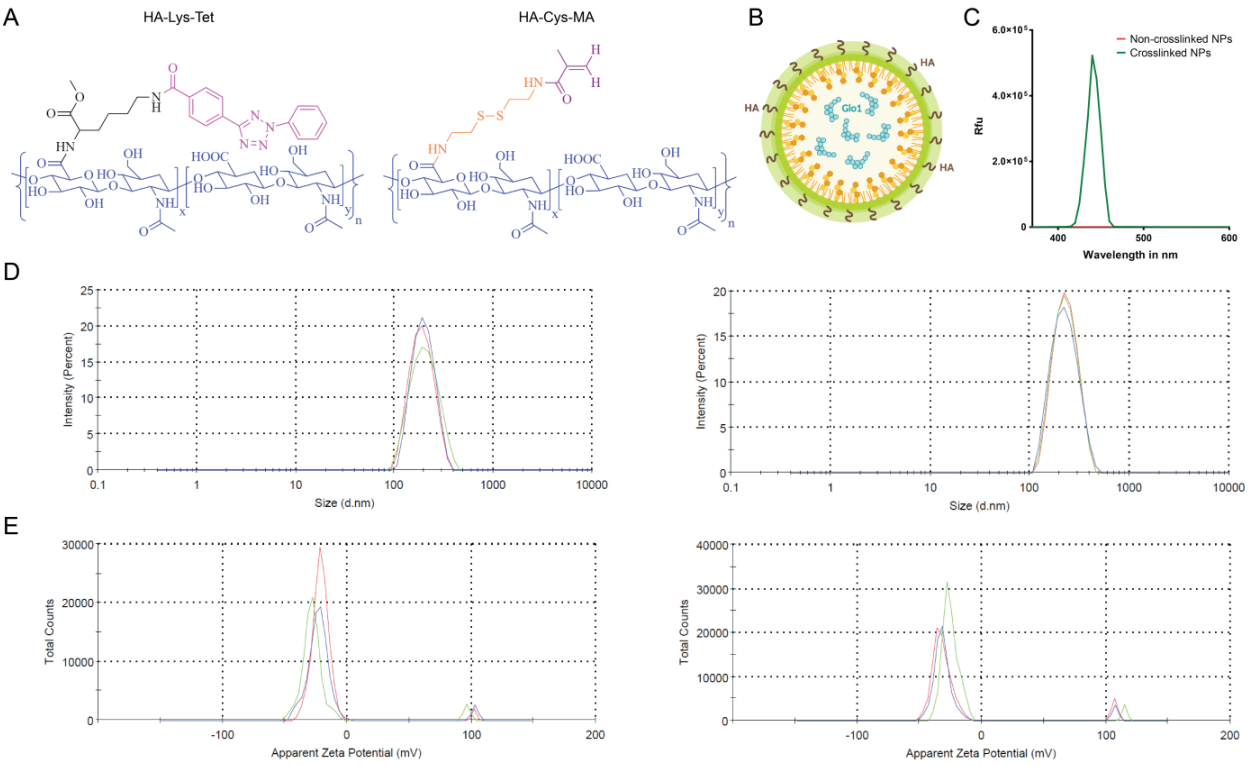

Figure 4.1 Synthesis and characterization data of nanoparticles. (A) ChemDraw illustrations of precursor molecules HA-Lys-Tet and HA-Cys-MA. (B) BioRender illustration of Glo1-NPs. (C) UV-vis spectrophotometric analyses of non-crosslinked and crosslinked nanoparticles. (D) DLS size measurement of empty (left) and Glo1-loaded (right) nanoparticles. (E) Zeta potential graphs of empty (left) and Glo1-loaded (right) nanoparticles.

4.2.2 *In vitro* Assessment of Glo1-NP Treatment on ECs

To evaluate the effects of NPs on cell viability, human umbilical vein endothelial cells (HUVECs) without any pre-treatment were compared to HUVECs treated with MG (100 μM). The cells were then exposed to empty NPs, Glo1-NPs or no NPS **(Figure 4.2A)**. After 24 hours, there was no difference between treatment groups in the viability of HUVECs grown in the non-MG environment with an average viability of ≈95%. However, MG treatment lowered the viability by 7.4 % in the control (no NP_S) and by 6.3 % in the NPs group, while this negative effect was prevented by Glo1-NPs treatment **(Figure 4.2B)**.

The adhesive property of ECs was then evaluated with the same treatment groups (no NP, empty NPs and Glo1-NPS) **(Figure 4.2C)**. Two hours after cell seeding, HUVECs showed comparable adhesion for all of the treatment groups when the cells were not exposed to MG. MG exposure reduced EC adhesion by 65.1 % in the control (no NPs) and by 69.3% in the empty NP group, whereas ECs treated with Glo1-NPs did not exhibit a reduction in adhesion **(Figure 4.2D)**. Overall, these results demonstrate that our Glo1-NPs can preserve the viability and adhesion of ECs exposed to MG.

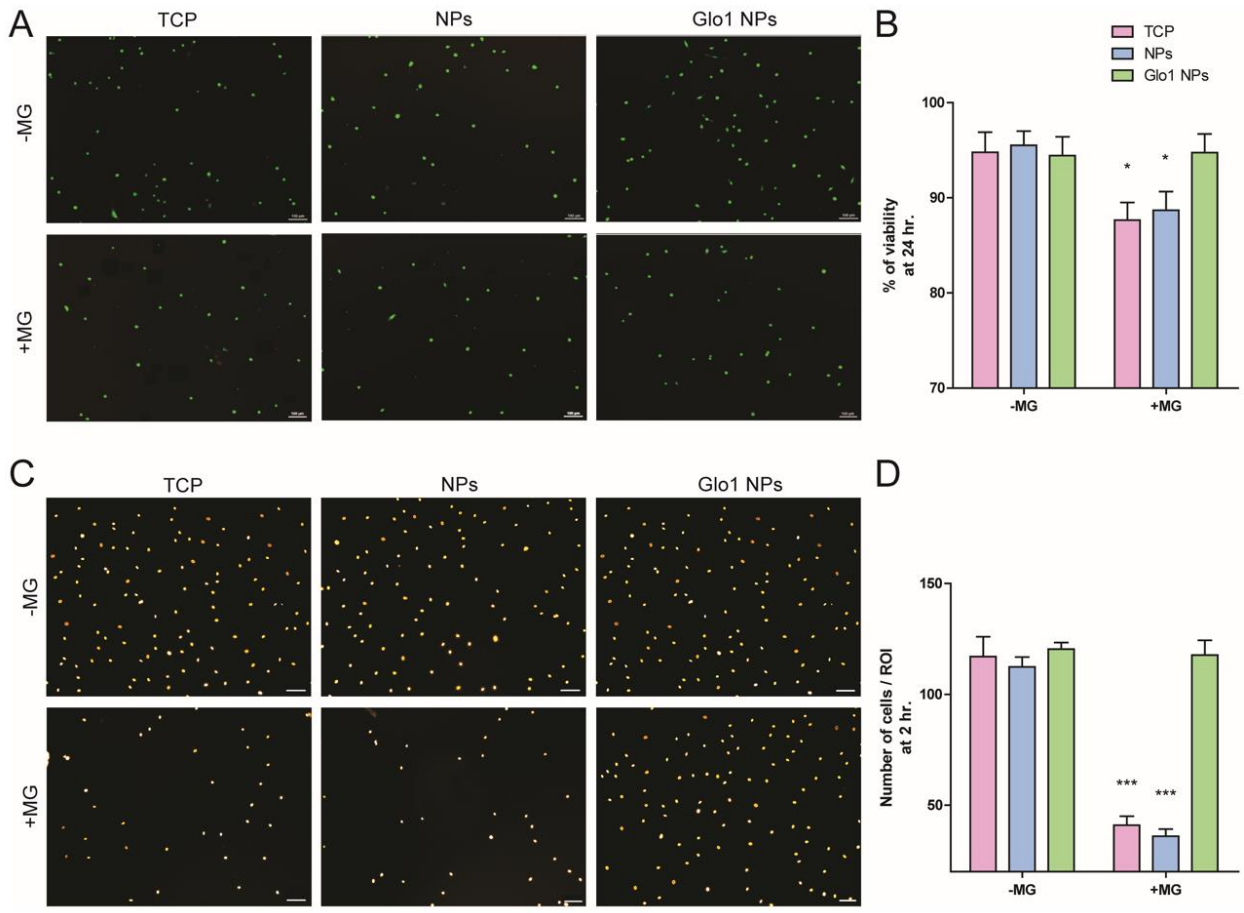

Figure 4.2 Viability and adhesion of Glo1-NP treated ECs. (A) Representative viability images of HUVECs at 24 hours in MG-treated and untreated wells following NPs, Glo1-NPs or no NP (TCP) treatment. (B) Quantification of viability data. MG treatment reduced cell viability which was rescued by Glo1-NP treatment. (C) Representative adhesion assay images of HUVECs at 2 hours in MG-treated and untreated wells with NPs, Glo1-NPs or no NP (TCP) treatment. (D) Quantification of adhesion data. MG exposure reduced cell adhesion, which was rescued by Glo1-NP treatment. (n = 3 for all groups and three images were taken from each well; ***p < 0.001, *p < 0.05)

4.2.3 MG Exposure Increases CD44 Expression in ECs

We then tested the effect of MG on CD44 expression in cultured ECs by immunostaining. Taking advantage of their fluorescent nature, we also visualized the presence of NPs in the cytoplasm after treatment. CD44 expression increased in ECs after MG exposure. Notably, the increased CD44 expression led to greater uptake of NPs into ECs, while limited numbers of NPs were taken up by untreated ECs **(Figure 4.3A)**. Our results show that high MG levels increase CD44 expression.

4.2.4 CD44 Receptor is Responsible for Nanoparticle Uptake

We next designed an experiment to confirm that CD44 acts as the primary target for NP uptake. With the use of a CD44 blocker, we blocked the CD44 receptor in cultured ECs. Interestingly, for ECs treated with MG and CD44 blocker, NP uptake was significantly reduced **(Figure 4.3B)**. These results indicate that the CD44 receptor is responsible for NP uptake into the cells. Our Glo1 ELISA results showed that Glo1 uptake was facilitated in +MG treated cells when treated with Glo1-NPs, suggesting that NPs deliver Glo1 into ECs under MG stress **(Figure 4.3C)**.

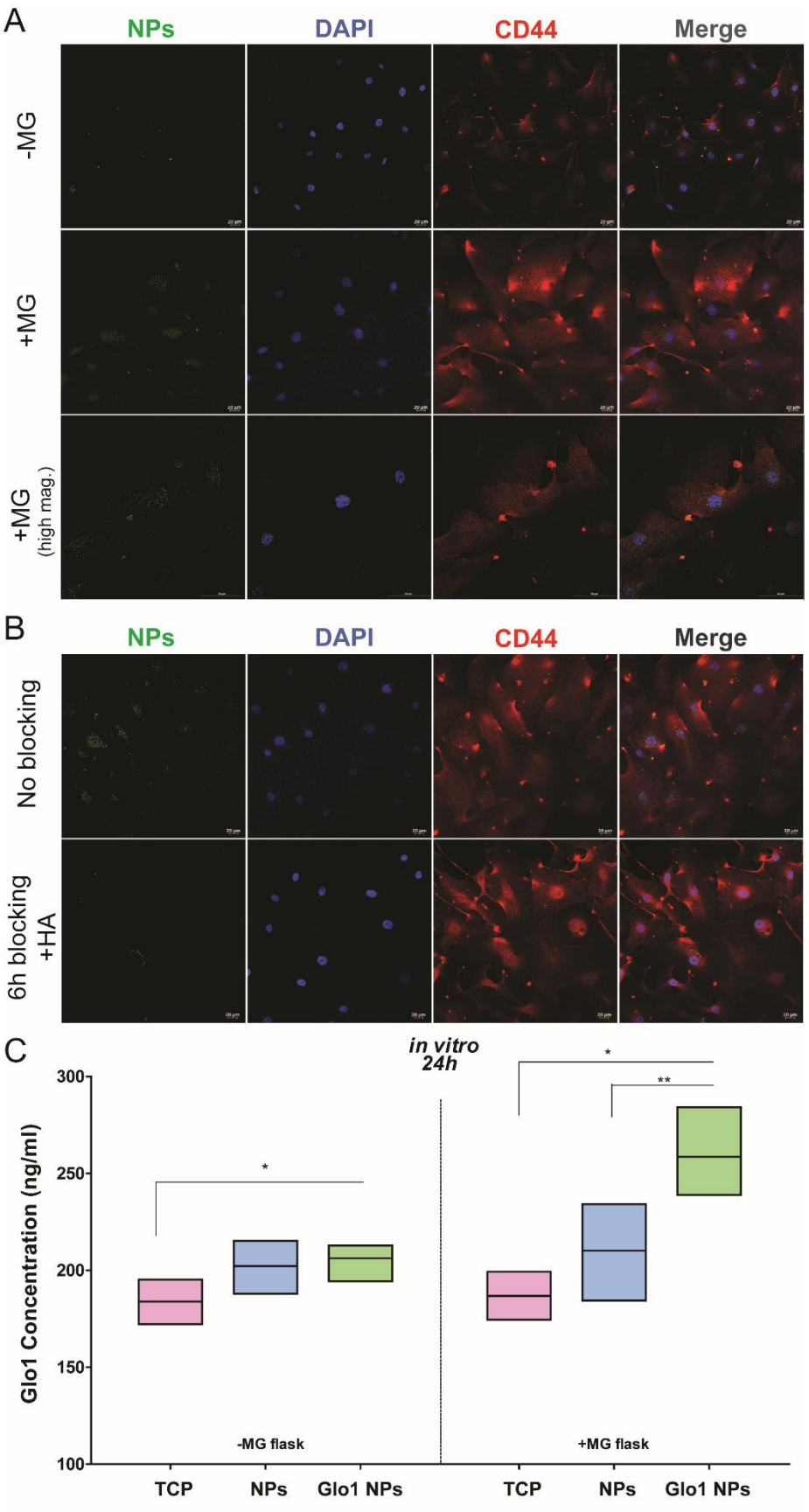
A
NPs
DAPI
CD44
Merge
-MG
+MG
+MG (high mag.)
B
NPs
DAPI
CD44
Merge
No blocking
6h blocking +HA
C
in vitro 24h
Glo1 Concentration (ng/ml)
300
250
200
150
100
*
*
**
-MG flask
+MG flask
TCP
NPs
Glo1 NPs
TCP
NPs
Glo1 NPs

Figure 4.3 Representative immunostaining images of CD44 expression and NP accumulation in cultured ECs. (A) CD44 expression in ECs increases following MG treatment leading to increased NP uptake. (B) NP uptake was significantly reduced upon CD44 blocking, showing that the CD44 receptor is responsible for NP uptake. (Green=NPs, DAPI=Nuclei, Red=CD44) (C) *In vitro* Glo1 ELISA assay performed for ECs cultured with and without MG and treated with Glo1-NPs, empty NPs or no NPs.

4.2.5 Glo1-NPs Improve Cardiac Function Post-MI

MI surgeries were performed at day 0 with a 95% survival rate. Mice were randomized into 3 groups and 50 µl of each treatment (PBS, NPs and Glo1-NPs) were administered via tail-vein injection at 3 hours post-MI. Echocardiographic measurements were taken and tissue collection was performed at 4 weeks post-MI (see experimental timeline in **Figure 4.4A**). Left ventricular ejection fraction (%LVEF) values were comparable for all treatment groups at the beginning of the study (baseline). LVEF was significantly greater in the Glo1-NP mice (41.8 %) compared to the NP (30.8 %) and PBS (26.5 %) treatment groups at 4 weeks **(Figure 4.4B)**. Notably, the Glo1-NP treatment significantly increased LVEF by 14.7% after 4 weeks compared to its own baseline, whereas the NP and PBS treatments resulted in no change over time **(Figure 4.4B)**. No difference in fractional shortening (FS) was observed between the treatment groups after 4 weeks **(Figure 4.4C)**, whereas cardiac output (CO) was significantly improved in the Glo1-NP group CO compared to PBS (by 42 %) and NPs alone (by 15.8 %) **(Figure 4.4D)**.

To evaluate cardiac contractility, echocardiographic recordings were used to calculate longitudinal endocardial strain values at the anterior apex region at aortic valve closure (AVC). Results showed that the baseline values were comparable with mean values ranging around zero. Notably, Glo1-NPs treatment significantly improved the cardiac strain from ≈0.2% at baseline to ≈-7.2% at endpoint (**Figure 4.4E and 4.4F**). Cardiac strain remained unchanged between

baseline to endpoint for the NP group (from ≈0.3% to ≈-0.2%) and for the PBS group (from ≈0.4% to ≈0.04%). The anterior apex segment of the myocardium was targeted for strain analysis as it comprises the infarct zone and that region is represented as the purple trace. A negative peak in longitudinal endocardial strain during cardiac shortening indicates better contractility. Overall, our findings showed that *in vivo* application of Glo1-NPs treatment improves cardiac function and contractility post-MI.

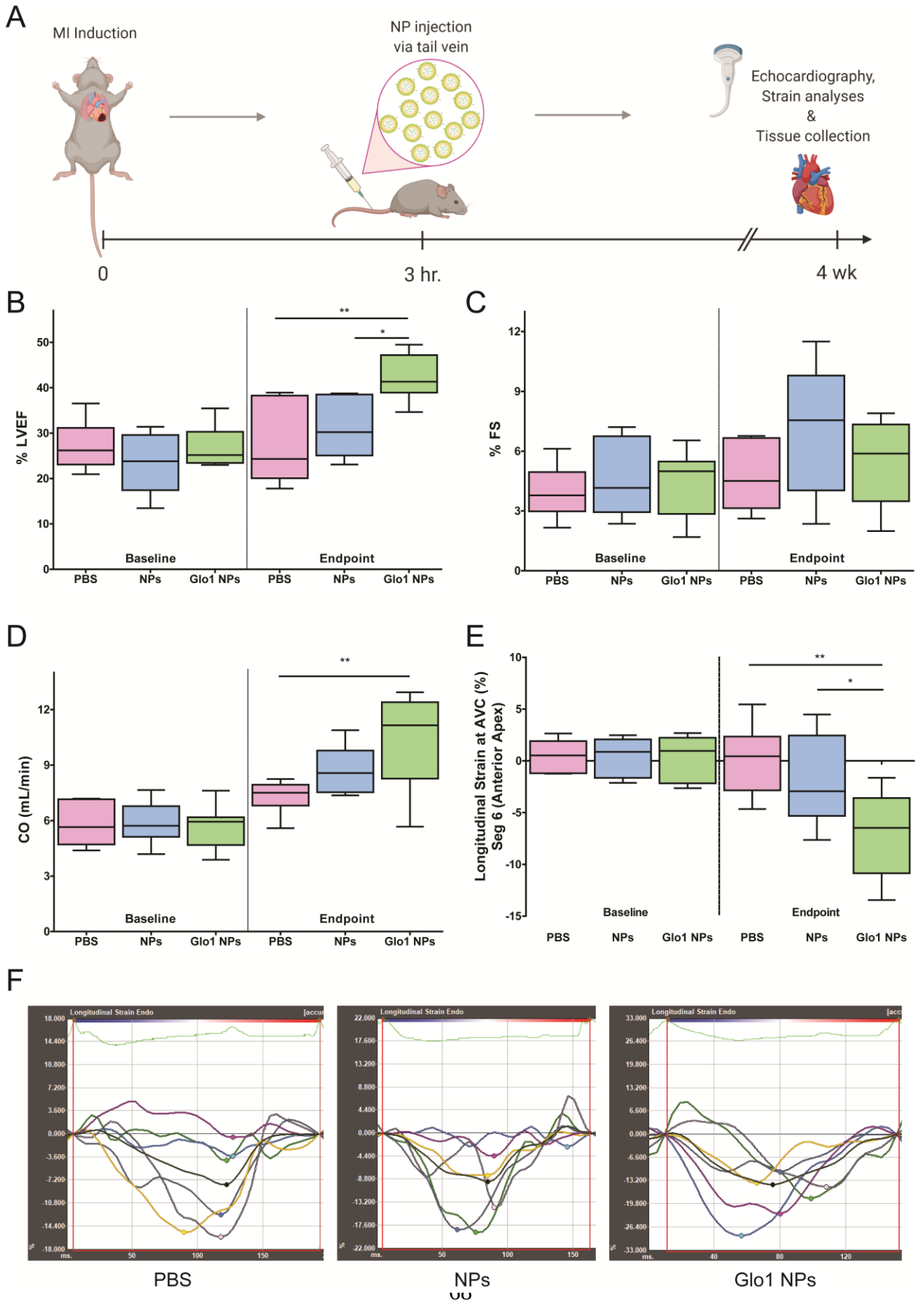
A
MI Induction
NP injection
via tail vein
Echocardiography,
Strain analyses
&
Tissue collection
0
3 hr.
4 wk
B
% LVEF
Baseline
Endpoint
PBS
NPs
Glo1 NPs
C
% FS
D
CO (mL/min)
E
Longitudinal Strain at AVC (%)
Seg 6 (Anterior Apex)
F
Longitudinal Strain Endo
PBS
NPs
Glo1 NPs

Figure 4.4 Glo1-NP treatment improves cardiac function and contractility post-MI. (A) Illustration of the *in vivo* study timeline. (B) %LVEF values at baseline and 4 weeks post-treatment. (C) %FS values at baseline and 4 weeks post-treatment. (C) CO values at baseline and 4 weeks post-treatment. (E) Endocardial longitudinal strain reached at AVC within the anterior apex segment at 4 weeks post-MI. (F) Representative longitudinal strain curves over the course of a single contraction for the 3 treatment groups. The purple traces correspond to the anterior apex segment. ***p < 0.001, **p < 0.01, *p < 0.05.

4.2.6 Glo1-NPs Find Their Target When Delivered Intravenously

We used NPs' intrinsic fluorescence ability to monitor their distribution and accumulation in the infarct region *ex vivo*. Treatments were injected to infarcted hearts 3 hours post-MI and hearts were extracted 3 hours after treatments. IVIS images showed that, 3 hours after injection, NPs accumulated in the heart; mainly in the infarct region meanwhile the PBS group has not shown any signal as expected **(Figure 4.5A)**. Quantitative analysis of the IVIS data showed no difference in NP accumulation between NPs and Glo1-NPs injected groups, suggesting that the Glo1 encapsulation has no additional effect in targeted delivery **(Figure 4.5B)**.

4.2.7 Glo1-NP Treatment Reduces Scar Size and Prevents Cell Death

Masson's Trichrome staining showed that the Glo1-NP treatment group had a significant reduction in final scar size compared to PBS and NPs treated hearts at 4 weeks post-MI (by 31.3% and 24.9%, respectively; **Figure 4.5C and 4.5D**). The calculations of scar wall thickness also demonstrated that Glo1-NPs better protected the scar wall compared to PBS and NPs treated groups **(Figure 4.5E)**. Although no significant difference in remote wall thicknesses was observed between treatments, Glo1-NP treated hearts had a greater thickness of viable tissue areas compared to PBS and NPs groups, respectively **(Figure 4.5G)**.

In terms of cell death, active caspase-3 staining showed that the borderzone area of Glo1-NP treated hearts contained 54.5% and 32.4% less active caspase-3^{+} apoptotic cells compared to PBS and NPs alone. There was no difference detected in the number of caspase-3^{+} cells between groups in the infarct zone areas **(Figure 4.5H and 4.5I)**. This indicates that treating mouse hearts with Glo1-NPs at 3h post-MI limits cell death and decreases the final scar size.

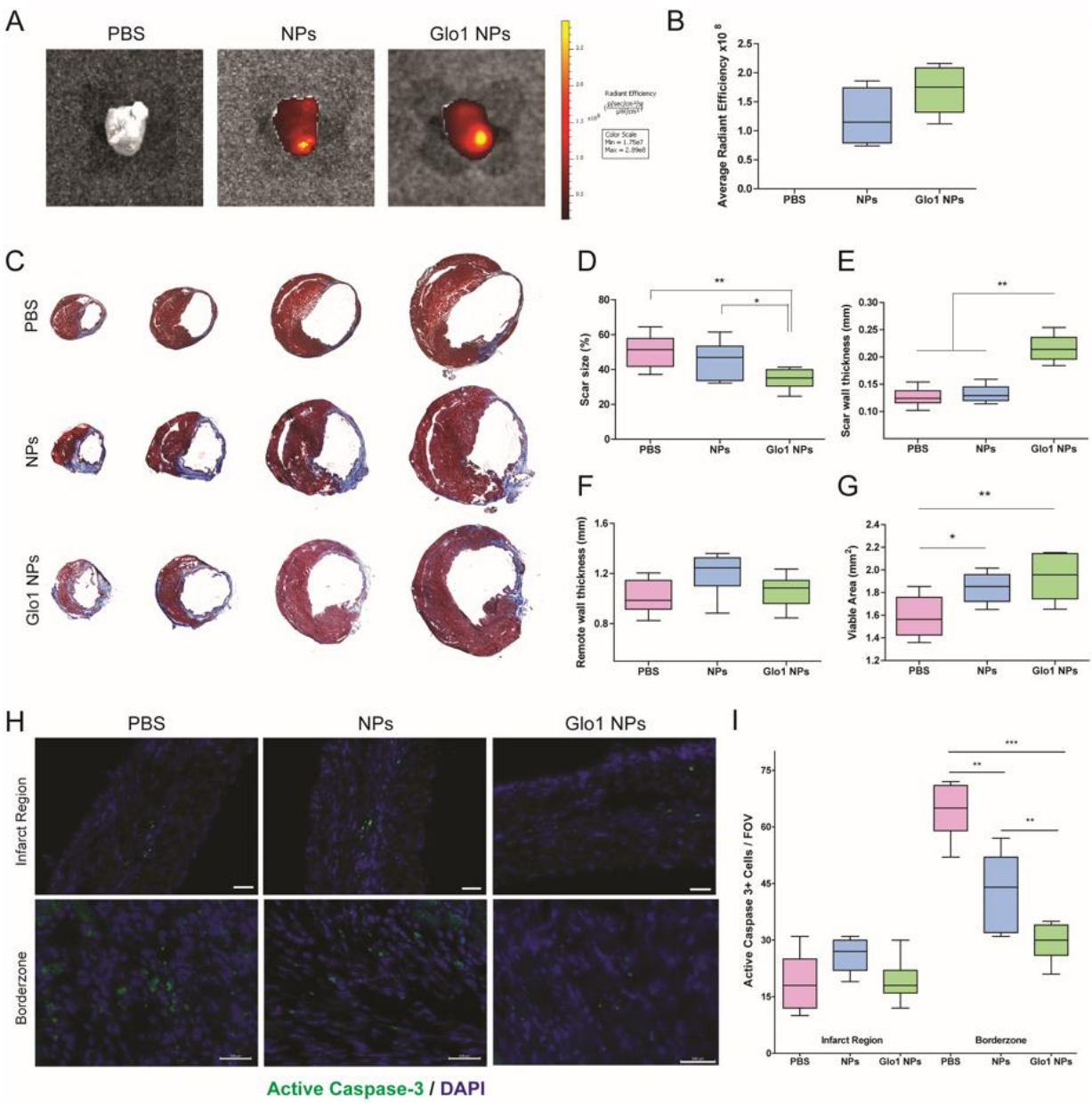

Figure 4.5 ***In vivo*** **delivery of Glo1-NPs and histology analyses post-MI. (A) Representative IVIS images of** ***ex vivo*** **MI mouse hearts taken 3 hours after treatment with NPs and Glo1-NPs. PBS hearts were also collected as control. Nanoparticles show intrinsic green fluorescence and they target infarcted tissue when delivered intravenously. (B) Quantification of IVIS data reported as average radiant efficiency. (C) Representative Masson's Trichrome images 4 weeks after PBS, NP and Glo1-NP treatment. Multiple sections were shown from apex to base. (D) Scar size calculated as the % of section circumference. (E) Scar wall thickness, (F) remote wall thickness of the myocardium and (G) viable area were calculated from histology images. (H)**

Representative images of active caspase-3 staining to identify apoptotic cells. (Green=active caspase-3^+, Blue=DAPI) (I) Quantification of active caspase-3^+ cells per FOV. ***p < 0.001, **p < 0.01, *p < 0.05.

4.2.8 Glo1-NP Treatment Reduces Inflammation and Promotes the Recruitment of Pro-Wound Healing Macrophages

As Glo1 functions to reduce MG levels, and MG has been shown to promote the inflammatory response post-MI, we performed immunohistochemistry at 4 weeks to assess the effects of Glo1-NP treatment on chronic inflammation. We evaluated both infarct and border areas and our results showed that Glo1-NP treated hearts had significantly fewer $CD86^+$ pro-inflammatory M1 macrophages at the borderzone (1/4 and 1/2 the number vs. PBS and NPs, respectively), whereas its expression was comparable for all treatment groups within the infarct region 4 weeks post-MI. This finding suggests that inflammation is suppressed by Glo1-NP treatment mainly at the borderzone **(Figure 4.6A)**. We also calculated the number of $CD206^+$ anti-inflammatory M2 macrophages and observed that Glo1-NP treated hearts had a greater number of these cells within the borderzone compared to PBS and NPs (by 2.2-fold and 1.6-fold, respectively). In the infarct region, the Glo1-NP treated group had significantly more $CD206^+$ cells compared to PBS (by 2.1-fold; **Figure 4.6B**). Taken together, these results suggest that Glo1-NP treatment reduces inflammation and promotes a pro-healing environment post-MI, primarily in the border zone.

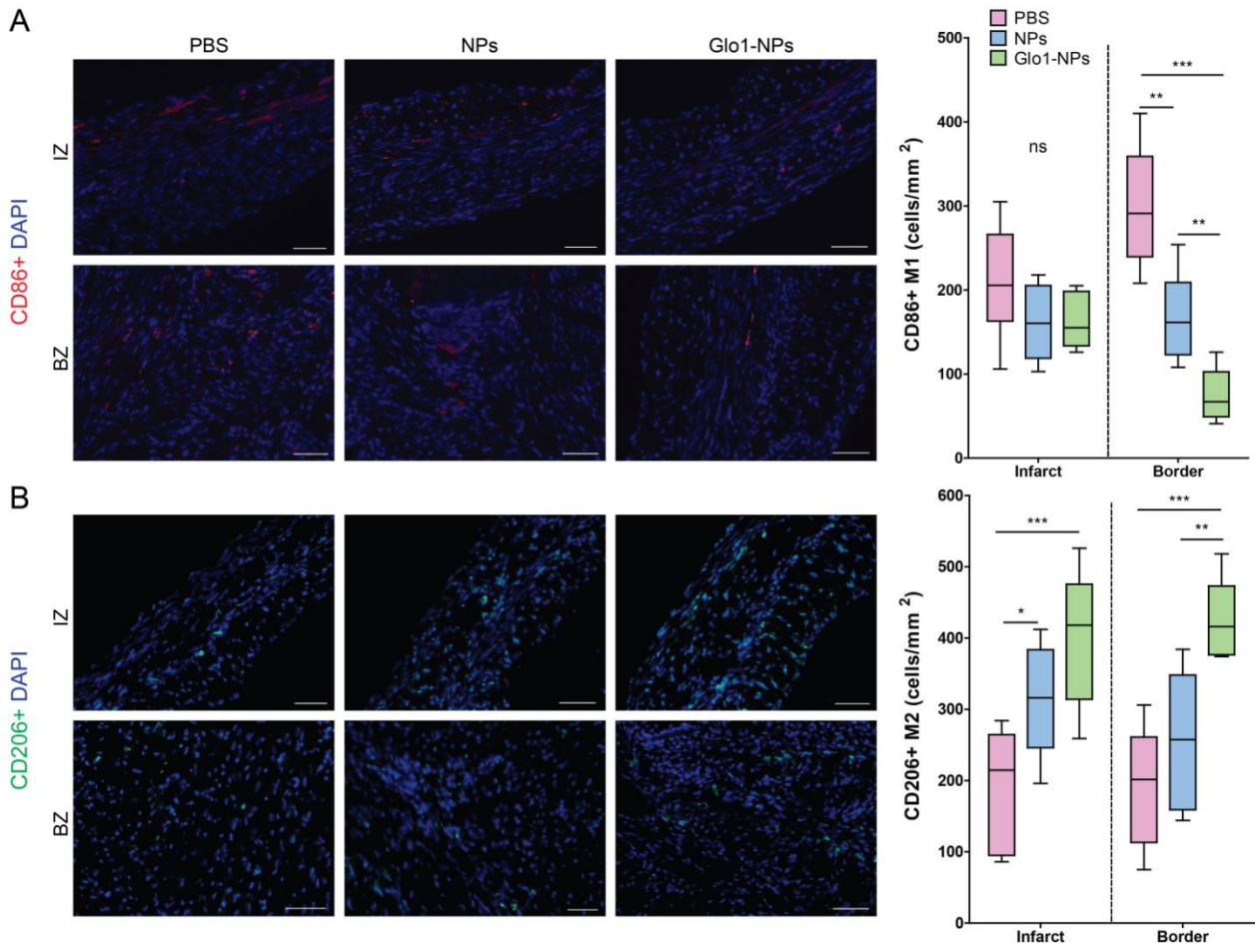

Figure 4.6 Glo1-NP treatment promotes anti-inflammatory macrophage recruitment at 4 weeks post-MI. (A) Representative images and quantification of CD86$^+$ pro-inflammatory M1 macrophages (red). (B) Representative images and quantification of CD206$^+$ anti-inflammatory M2 macrophages (green). Scale bars = 100 µm. Data is presented as the number of cells per mm^2. ***p < 0.001, **p < 0.01, *p < 0.05

4.2.9 Glo1-NPs Increase Glo1 levels in MI hearts

To assess Glo1 function after treatment with our NPs, a Glo1 ELISA assay was performed *in vivo*. Our results indicate that in the presence of MG, Glo1-NP treatment increased Glo1 levels *in vivo* (**Figure 4.7A**). Notably, no change in Glo1 concentration was observed when mice with healthy hearts were treated with Glo1-NPs, suggesting that the MI-induced upregulation of CD44 in the myocardium leads to increased Glo1-NP recruitment and localization in the heart.

4.2.10 Glo1-NPs Inhibit MG-AGEs and Oxidative Stress Post-MI

We measured GSH levels at 3 hours and 28 days post-MI as an indicator of oxidative stress in the myocardium. GSH is an endogenous antioxidant, and co-factor in the glyoxalase pathway that detoxifies MG and protects tissues from oxidative damage.[108] We detected a significantly higher ratio of GSH/GSSG (reduced/oxidized GSH) in the myocardium of the Glo1-NP group compared to PBS and NP treatment groups at both time-points **(Figure 4.7B).**

Finally, we assessed how Glo1-NPs treatment could be affecting the generation of MG-AGEs by evaluating the levels of MG-H1 at 4 weeks post-MI. Our western blot results showed that the level of MG-H1 in Glo1-NP treated tissues was significantly lower compared to the PBS and NP treatment groups (by 1.5-fold and 1.4-fold, respectively; **Figure 4.7C and 4.7D**), indicating that less MG-related AGEs had accumulated after Glo1-NP treatment. Taken together, our results suggest that the Glo1-NP treatment inhibits oxidative stress by increasing anti-oxidant molecules post-MI.

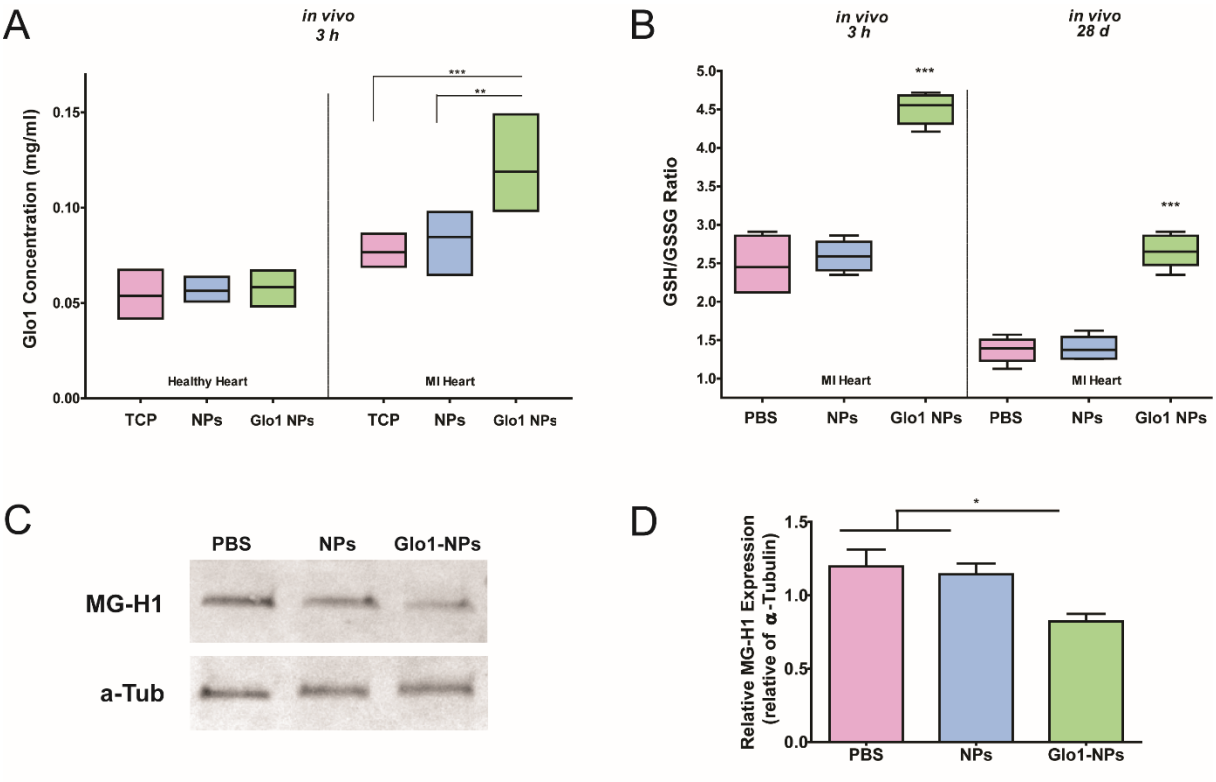

Figure 4.7 Glo1-NP treatment increased Glo1 levels and reduced oxidative stress. (A) *In vivo* Glo1 ELISA assay performed using tissue harvested from healthy hearts and at 3h in post-MI hearts following treatment with PBS, NPs or Glo1-NPs. (B) The GSH/GSSG ratio (for measuring the reduced versus oxidized GSH levels), showed increased glutathione levels in Glo1-NP treated hearts at 3 h and 28 days. (C) Representative western blots for MG-H1 protein expression and (D) quantification at 4 weeks post-MI, normalized to α-tubulin. ***p < 0.001, **p < 0.01, *p < 0.05.

4.3 Discussion

Nano-based delivery systems offer multiple benefits including, but not limited to, small size, biosafety, biodegradability, bioactivity and versatility of their design.[185] Recently, there has been great developments in the field of delivery systems particularly in the active-compound containing bioagent area for the diagnosis and treatment of various diseases. [186] Although many effective applications of nanoparticle systems have been reported previously, mainly in theranostic applications, there are still certain challenges that need to be addressed. For example, a more advanced technology is needed to develop delivery systems that able to reach their target sites more effectively.[187,188] The ability to track the nanocarriers is another important issue as confirmation of the delivery location could provide insight into the treatment response. In this study, we developed a Glo1-loaded, fluorescent, HA-based nanoparticle therapy that targets the CD44 receptor as an approach to reduce oxidative and protect the myocardium post-MI. We demonstrated that the Glo1-NP treatment decreased MG-related oxidative stress, reduced inflammation, limited apoptotic activity and improved cardiac function and contractility of the infarcted mouse myocardium.

The NPs were synthesized by following a previously established protocol, using HA-Lys-Tet and HA-Cys-MA precursor molecules in an inverse nanoprecipitation reaction, allowing the particles to be photo-crosslinked via tetrazole-alkene chemistry that provides great specificity, allowing encapsulated proteins to maintain their bioactivity.[164–167,177] As anticipated, the cross-linked NPs exhibited strong fluorescence with excitation at 405 and emission at 450, similar to those previously reported,[167,176] whereas non-crosslinked NPs did not exhibit fluorescence, suggesting that the pyrazoline cycloadducts could only form the fluorescent core when crosslinked. This useful feature gives the NPs an intrinsic fluorescence that make them traceable

in vitro and *in vivo*.[166,167,176,177] The DLS measurements showed that Glo1-NPs had slightly larger size (213 nm) compared to empty NPs (189 nm), confirming that the Glo1 encapsulation caused the NP to grow in size as expected. The empty NPs exhibited a negative surface charge (-18.2 mV) caused by the HA carboxyl groups on the surface, as observed previously for other HA-based NPs.[177,189,190] The Glo1-NPs exhibited an even greater negative surface charge of about -21.5 mV. The negative zeta potential of Glo1-NPs also supports that the negatively charged Glo1 protein was loaded into NPs successfully.[191] By its loading into NPs, Glo1 is protected from degradation and provides excellent colloidal stability to NPs.[192] Overall, our results support that NPs are small with a narrow size distribution suitable for systemic administration, and are able to be loaded with the bioactive Glo1 protein.

To show that the Glo1-NPs could prevent MG-induced cellular toxicity, we applied them to cultured endothelial cells (ECs) with and without exposure to MG. MG exposure reduced the viability of cultured ECs and this was prevented by Glo1-NP treatment. These findings are similar to previous reports showing that protecting the cells from the negative effects of MG can reduce cell death.[51,162,193]

In order to validate that NP uptake by ECs is through the targeting of CD44 on the cell surface, we performed culture experiments. It is known that healthy ECs express little to no CD44, and that its expression is increased in response to stress or injury, such as ischemia.[180–184] Our confocal images showed that non-treated ECs express very little CD44, while CD44 expression was markedly increased in ECs after treatment with MG, suggesting that a MG exposure induces CD44 expression. Concurrently, limited numbers of NPs were taken up by untreated ECs, whereas MG-treatment significantly increased NP uptake. Moreover, for ECs treated with MG and a CD44 blocking agent, NP uptake was reduced, indicating that the CD44

receptor is primarily responsible for NP trafficking. Additionally, our Glo1 ELISA results showed that Glo1-NP treatment significantly enhanced Glo1 levels in ECs exposed to MG stress. Non-MG stressed ECs showed no increase in Glo1 content compared to empty NPs, confirming that Glo1-NPs are taken up by ECs via CD44 receptor-mediated endocytosis. Our results are consistent with previous studies that investigated NPs that target the CD44 receptor.[164,165,167] Overall, the specificity of the NPs to target the CD44 receptor make them promising vehicles for the targeted delivery of therapeutics in cardiovascular disease or other settings in which CD44 expression is augmented.

Having established that Glo1-NP cellular uptake is mediated by NP-CD44 interaction, we tested its therapeutic effect *in vivo* using a mouse MI model. We administered the NPs via tail-vein injection, which is a commonly used minimally invasive approach for administering targeted delivery agents.[194,195] For example, the tail vein route has been used previously in studies of organ-targeting gene delivery[196] and targeted antitumor therapies.[197,198] To our knowledge, the direct targeting of the damaged myocardium by nanocarrier systems injected via the tail vein has not yet received much attention. We injected our NP therapy 3 hours post-MI, during the inflammatory phase, as it was previously shown that MG accumulates soon after MI and MG-targeted treatments are effective when delivered in the early inflammatory phase.[62,162]

Functional analyses demonstrated that the Glo1-NP treatment resulted in improved cardiac function at 4 weeks post-treatment. When compared to their baseline values, Glo1-NP treated hearts showed an increase in %LVEF and CO, suggesting that the overall cardiac function was improved after Glo1-NP treatment. Additionally, cardiac strain of the endocardium in the infarct region was significantly improved after Glo1-NP treatment. Cardiac strain represents cardiac contractility and negative strain values, such as observed with NP treatment, indicate better

contractility.[120] Thus, it could be concluded that our Glo1-NP treatment resulted in superior *in vivo* functional outcomes when compared to NPs only and PBS control groups.

Taking advantage of their green fluorescence, NPs were tracked *in vivo* and their homing is monitored while PBS injection was used as a negative control. Strikingly, IVIS images showed that both NPs and Glo1-NPs accumulated in the heart 3 h post treatment, indicating that the treatment systems target cardiac tissue when injected intravenously. A very important observation is that the NPs mainly observed in the center of the infarct region but they also spreaded into the right ventricle and atrial regions as well. This indicates the main difference between myocardial injection vs tail-vein injection as we previously observed our treatment localized predominantly in myocardial area.[162] Because of their ability to target CD44+ cells, NPs appear to deliver Glo1 into the whole heart starting from the MI region. This pattern allowed us to confirm the upregulation of CD44 at the cardiac tissue following MI. Lastly, we did not observe any difference between Glo1-NPs and NPs in terms of their targeting abilities, suggesting that the Glo1 encapsulation has no negative effects on the NP's surface structure.

Histological analyses revealed a decrease in scar size, and increases to scar wall thickness and viable tissue area in Glo1-NP treated hearts. Taken together with the strain results, Glo1-NP treatment reduces the scarring, limits cardiac dilation, prevents adverse remodeling and improves cardiac contractility post-MI, leading to superior cardiac function. Additionally, we measured the apoptotic activity in the myocardium to better elucidate a potential mechanism for the observed increase in viable tissue in response to our therapy. It has been previously shown that MG and its AGEs trigger cell death and apoptosis via oxidative stress.[121,122] Our findings indicated that Glo1-NP treatment significantly reduced the number of active caspase-3^+ cells in the borderzone, suggesting that reducing MG with Glo1-NP treatment may prevent on-going cell death and

expansion of the infarct. It is worth noting that we previously showed that transgenic overexpression of Glo1 in mice reduced MG-AGE levels, limited apoptosis and exhibited superior cardiac function post-MI.[62] Thus, the benefit of our Glo1-NP treatment is likely due, in part, to reducing MG-AGEs and promoting cell survival.

Another important factor contributing to myocardial damage post-MI is persistent inflammation, which can be activated by excess MG in the heart.[14,132] MG and its AGEs have been shown to promote the polarization of M1 inflammatory macrophages, repress wound healing M2 macrophage polarization, increase inflammatory cytokine production in macrophages, impair their ability to clear cellular debris, and lead to a delay in wound healing.[133,199] Our Glo1-NP treatment resulted in a decrease in the number of $CD86^+$ pro-inflammatory M1 macrophages at the borderzone. Furthermore, we observed an increase in $CD206^+$ anti-inflammatory M2 macrophage numbers in both the infarct and border zones, suggesting that the Glo1-NP treatment reduces inflammation and activates wound healing macrophages post-MI. This is likely induced by Glo1-related inhibition of MG-AGE production post-MI. To further evaluate this, we measured Glo1 levels and oxidative stress in the myocardium post-MI. The concentration of Glo1 was increased in MI hearts compared to the hearts of healthy animals. Notably, MI hearts of mice treated with Glo1-NPs had the highest concentration of Glo1, indicating that the NPs were successful in delivering and releasing their Glo1 contents into cells of the infarcted myocardium.

Oxidative stress is caused by the imbalance between the production of reactive oxygen species (ROS) and the endogenous antioxidant defence system, and the accumulation of MG and its AGEs has been shown to promote oxidative stress.[141,142] As Glo1 reduces MG levels, we expected that our Glo1-NP treatment would also reduce MG-AGE formation and oxidative stress

post-MI. MG detoxification by the glyoxalase pathway begins with the conjugation of MG and glutathione (GSH), yielding a hemithioacetal product that is subsequently transformed by the glyoxalase enzymes into d-lactate and GSH.[200,201] As such, we examined the levels of glutathione in the treated hearts by calculating the GSH/GSSG ratio. We observed that Glo1-NP treatment resulted in greater antioxidant activity (higher GSH/GSSG ratio), suggestive of increased glyoxalase pathway activity and MG metabolism. Lastly, we measured the protein level of MG-H1, which is the primary MG adduct and an indicator of MG-related oxidative stress.[202] We observed that MG-H1 levels were significantly reduced in Glo1-NP treated hearts. Taken together, our results demonstrate that Glo1-NP treatment reduces oxidative stress and the accumulation of MG-AGEs in the post-MI myocardium.

4.4 Conclusion

In this study, we have demonstrated that a Glo1-loaded CD44-interacting nanoparticle system can target the infarcted myocardium when delivered intravenously. Glo1-NP treatment decreased MG-related oxidative stress, reduced inflammation, inhibited apoptotic activity and improved cardiac function and contractility post-MI. Through its minimally invasive intravenous application, this treatment does not require any surgical intervention. In summary, our Glo1-NP system represents a promising nanoplatform for targeted, traceable, safe and efficient intracellular delivery of cardiovascular therapeutics for treating and improving the health of patients with MI.

4.5 Experimental Section

Formation of Precursor Molecules: Firstly, the two precursor molecules HA-Lys-Tet (Hyaluronic Acid - Lysine - Tetrazole) and HA-Cys-MA (Hyaluronic Acid - Cystamine - Methacrylamide) were synthesized by following a previously established protocol.[163,165–167] Briefly, HA-Lys-Tet was prepared by conjugating Tet to HA-Lys-NH_2 by using 1,3-dicyclohexyl Carbodiimide (DCC,99%) and N-hydroxysuccinimide (NHS, 98%) as coupling agents. DCC (232 mg, 1.12 mmol) was then added to Tet (608 mg, 58 μmol) in dimethyl sulfoxide (DMSO, 10.0 ml) under a nitrogen atmosphere. The reaction proceeded for 12 hours at room temperature in the dark. Then, HA-Lys- NH_2 (400 mg, 195 μmol of amino groups) in 30.0 ml of anhydrous formamide and 4-(dimethylamino)-pyridine (DMAP, 80 mg, 655 μmol) was added to that mixture and allowed to react for 48 hours at 40°C. The final HA-Lys-Tet was obtained by dialysis (Spectro/Pore, molecular weight cutoff, MWCO of 3500) in deionized water and DMSO mixture (1:1, v/v). Lastly, HA-Lys-Tet was freeze-dried for long-term storage.

The second precursor molecule, HA-Cys-MA, was synthesized in two steps. First, MA-Cys-NH_2 was obtained by the reaction of Boc-Cys-NH_2 with methacrylic anhydride followed by the deprotection of Boc groups in TFA/Methanol (1:1, v/v) mixed solution. Under a nitrogen atmosphere, a HA (50 mg, 1.43 μmol) solution in 5 ml deionized water activated by EDC (75.9 mg, 0.396 mmol) and NHS (22.8 mg, 0.198 mmol) was slowly added to the MA-Cys-NH_2 solution and the reaction was allowed to proceed at 40°C for 24 hours in the dark. The final HA-Cys-MA was obtained by dialysis (Spectro/Pore, molecular weight cutoff, MWCO of 3500) in deionized water and methanol mixture (1:1, v/v). Lastly, HA-Cys-MA was freeze-dried for long-term storage.

Synthesis and Characterization of Glo1-loaded, CD44-targeting Fluorescent Nanoparticles: Fluorescent NPs were synthesized by a combined inverse nanoprecipitation and catalyst-free "tetrazole-alkene" photoclick reaction by following a previously described protocol.[166,167,177] Briefly, HA was grafted with tetrazole (HA-Lys-Tet) and HA with cystamine methacrylamide (HA-Cys-MA) and dissolved in sterile phosphate buffer (PBS buffer, pH 7.4, 10 mM) at 1:1 Tet:MA ratio in order to obtain 1.25 mg/ml polymer solution. 1 ml of the polymer solution was then injected into 100 ml acetone to form a homogenous solution, followed by UV irradiation (320-390 nm, 50 mW/cm^2) for 3 minutes with 60 seconds intervals. The NPs were then isolated by evaporation of acetone via rotary evaporator, followed by an extensive dialysis (Spectrum™ Spectra/Por™ 3 RC Dialysis Membrane Tubing 3500 Dalton MWCO) in DI water for 24 hours with constant stirring.

For the preparation of Glo1-loaded NPs (Glo1-NPs), 500 μg/ml Glo1 protein solution was added into the HA derivative mixture in PBS solution and the same steps were followed as described above for the empty NPs. Fluorescent properties of NPs were measured by UV-Vis (Ex: 405, Em: 450). The size and charge of NPs were evaluated by dynamic light scattering (DLS) and zeta potential measurement system (Malvern Instruments).

Cellular Toxicity Assessment by Live/Dead Assay: HUVECs were separated into two groups and cultured in tissue culture plates for 24 hours (seeded at a density of 2.5×10^2 cells/cm^2). One group was maintained in regular HUVEC media (M200 media supplemented with LSGS supplement kit, Gibco) while the other group was maintained in 100 μM MG supplemented HUVEC media. After 24 hours, the cells in each group were treated with NPs, Glo1-NPs or left untreated (TCP). The following day, the cells were subjected to an *in vitro* viability assay. Briefly, HUVECs were washed with 1× PBS and stained with Calcein-AM and Ethidium

Homodimer-1 (CaAM/EthD-1) viability dyes (ThermoFisher Scientific Cat#L3224) by following manufacturer's instructions. Stained cells then were imaged by fluorescence microscopy and nine random images were taken from each experimental well. Each condition was performed in triplicate. Total live and dead cell numbers were counted using ImageJ software (NIH, USA) and the % viability was calculated for each group.

Adhesion Assay: The adhesion of HUVECs was assessed Following treatment with each condition described above. Prior to the experiment, cells were treated with/without MG overnight, and then NPs and Glo1-NPs were added into wells or some wells left untreated (TCP). Cells were then trypsinized, lifted and seeded onto new wells followed by incubation at 37°C and 5% CO_2 in serum-free medium for 2 hours. Plates were next washed with 1× PBS and the attached cells were stained with CellTracker™ Orange CMTMR Dye (ThermoFisher Scientific, Cat#C2927). Cells were visualized under fluorescence microscope at excitation/emission spectra of 541/565 nm. Images were taken from 5 different random locations per well, and the experiment was carried out with n=3. Cell adhesion was quantified directly by counting the number of cells using ImageJ software.

CD44 Immunostaining and NP Localization by Confocal Microscopy: For the detection of CD44 expression in cells, cells were fixed in 4% PFA and permeabilized with 0.1% Triton X-100 for 15 minutes. Samples were then blocked with 10% BSA in PBS for 30 minutes and CD44 primary antibody (ab189524, 1:500 dilution) incubation was performed overnight. The following day, goat anti-Rabbit IgG (H+L) Alexa Fluor 594 secondary antibody incubation was performed (A-32740, 1:600 dilution). CD44 blocking experiments were also conducted to confirm the role of CD44 in NP trafficking. Hyaluronic acid solution (HA) was used to block CD44 receptor on cell surface. Six hours after blocking, immunostaining was performed by using the same

antibodies and steps listed above. DAPI was used for marking the nuclei of cells and high magnification images were taken using confocal microscopy (Zeiss LSM 880 System) with appropriate filters. In addition to red and blue filter sets, the green filter was also used to image the naturally fluorescent NPs. Images were presented both individually and merged format in order to show NP accumulation clearly.

Myocardial Infarction and Intravenous Administration of NPs: MI was induced in 10-week old C57BL/6 female mice (Charles River) and NP delivery was performed via tail-vein injection at 3 hours post-MI. Briefly, mice were anesthetized (2% isoflurane), intubated, and the heart was exposed via a fourth intercostal thoracotomy. The left anterior descending coronary artery was then ligated just below its emergence from the left atrium. This procedure resulted in a mid/large MI involving the anterolateral, posterior, and apical parts of the left ventricle. MI size was confirmed at the time of surgery by myocardial blanching in the region supplied by the artery. Short-acting buprenorphine was administered at least an hour prior to surgery, and long-acting buprenorphine was administered subcutaneously immediately before surgery for perioperative analgesia. Immediately following the MI surgery, the chest was closed and sutured. At 3 h post-MI (baseline), mice were randomly assigned to receive one of 3 treatments: 1) PBS (control); 2) NPs (empty nanoparticles); or 3) Glo1-NPs (Glo1-loaded nanoparticles). Animals were placed into an animal restraint device for proper injection. The treatments were administered via tail-vein injection (50μL total) using a 27-G needle.[203] Mice were euthanized at 4 weeks post-treatment and hearts were collected for histology and/or molecular analysis.

Echocardiography and Strain Analysis: Transthoracic echocardiography was performed on parasternal long-axis views using a Vevo3100 system in B mode with a MX400 series real-time microvisualization scanhead probe and analysis performed with its accompanying Vevo LAB

3.1.1 software (VisualSonics). The imaging was carried out at 3 h (right before the treatment) and 4 weeks post-MI to determine cardiac function determinants such as: LVEF, FS and CO. To assess contractility, cardiac strain analysis was performed through the longitudinal axis since longitudinal strain is most representative of myocardial shortening at the level of the endocardium.[120,150] The longitudinal endocardial strain at the time of AVC (representing end systole) in segment 6 (anterior apex segment), corresponding to the infarct zone area, was calculated. As strain is calculated as the final length [L]/initial length [L0], negative strain values represent improved contractility (shortening of a given myocardial segment relative to its original length).[151] Results for both echocardiography and strain analyses were analyzed using Vevo LAB Software (FUJIFILM, VisualSonics).

Ex vivo Nanoparticle Tracking: Taking advantage of their natural fluorescence, NPs were monitored in the heart by IVIS Spectrum bioluminescence imaging (PerkinElmer) following intravenous administration. To increase the intensity of the fluorescent signal for imaging purposes, a concentration of NPs that was 5× greater than the therapeutic dose was used. Three hours after the tail-vein injection, animals were euthanized and hearts were extracted and immediately imaged *ex vivo* by IVIS. Intravenous delivery of PBS was used as a negative control group and the data was reported as average radiant efficiency.

Histology and Immunohistochemistry: Hearts were harvested at 4 weeks post-MI, embedded in OCT compound (Fisher Scientific), and snap frozen in liquid nitrogen. 10 μm sections were cut using a Thermo Scientific HM550 Cryostat. To evaluate scar size, tissue sections were fixed in 4% PFA for 1 h and stained with Masson's trichrome stain (Electron Microscopy Sciences). Images were taken with Leica Aperio VERSA slide scanner, and four sections per mouse were used to measure scar size by applying the mid-line arc method using ImageJ2 software.[154] Scar

wall thickness, remote wall thickness and viable area were also measured from the same images. For immunohistochemistry, tissue sections were fixed in acetone for 20 min, washed with 0.05% Tween-20 in PBS, permeabilized with 0.1% Triton X-100 for 10 min and then blocked in 10% serum in PBS for 1 h at room temperature. Primary antibodies were applied overnight at 4 °C in 10% serum, and then slides were rinsed and treated with secondary antibodies for 1 h in the dark at room temperature. Nuclei were stained with DAPI (1:1000) before being mounted with ProLongTM Gold antifade reagent (Invitrogen). For the detection of apoptotic cells, an anti-active caspase-3 primary antibody (Abcam, Rabbit, Cat#ab2302 at 1:250 dilution) was used with AF488 anti-rabbit secondary (ThermoFisher, Cat#A-11008 at 1:1000 dilution). To detect inflammation, M1 macrophages were stained with an anti-CD86 primary antibody (Abcam, Rat, Cat# 119 857 at 1:200 dilution) and visualized by AF594 anti-rat secondary (Invitrogen, Cat#A-48264 at 1:600 dilution). M2 macrophages were detected by an AF488-conjugated anti-CD206 antibody (BioLegend, Cat#141 710 at 1:100 dilution). Fluorescent images were obtained using a Zeiss Axio Observer upright microscope with a 20× objective. For all samples, three sections per mouse were analyzed by ImageJ and for each section, 3 random images within the border zone and the infarct zone regions were captured and used for quantification.

Glo1 ELISA Assay: For *in vitro* Glo1 concentration assay, cells were incubated with and without MG, and then one of the following treatments was applied: i) no NPs (TCP control), ii) NPs, or iii) Glo1-NPs. After 24 hours , cells were detached from the surface, centrifuged and washed 3 times in cold PBS. Cells were then freeze-thawed and sonicated to form lysates. Finally, the lysates were centrifuged to remove cellular debris, and the supernatant was collected and used in ELISA assay.

For *in vivo* Glo1 ELISA assay, healthy and MI mice received tail-vein injection with one of three treatments: i) PBS, ii) NPs, or iii) Glo1-NPs. After 3 hours, hearts were collected and rinsed with ice-cold PBS to remove excess blood. Next, the tissues were minced and homogenized in tissue homogenizer on ice followed by a sonication step. Homogenates were centrifuged and the supernatant was collected for ELISA assay.

To assess the Glo1 levels, a colorimetric Glo1 ELISA kit was used (Abbexa, abx252549) by following the manufacturer's instructions.[204] Briefly, the kit is based on sandwich ELISA which contains pre-coated Glo1 antibody onto a 96-well plate, which was equilibrated to room temperature. Standards, test samples, and biotin-conjugated reagent were added to the wells as duplicates and incubated. The HRP-conjugated reagent was then added, and the whole plate was incubated. Unbound conjugates were removed using wash buffer at each stage. TMB substrate was used to quantify the HRP enzymatic reaction. After TMB substrate was added, only wells that contain sufficient Glo1 will produce a blue-colored product, which then changes to yellow after adding the acidic stop solution. The intensity of the yellow color is proportional to the amount of Glo1 bound on the plate. The Optical Density (OD) is measured spectrophotometrically at 450 nm using a microplate reader, from which the concentration of Glo1 was calculated from the standard curve.

Oxidative Stress Analysis: Tissue lysates of LV samples were collected at 3 hours and 4 weeks post-treatment to assess oxidative stress levels. Tissue samples were digested in mammalian lysis buffer (Abcam Cat#ab179835) and enzymes were subsequently removed by using a deproteinizing sample kit (Abcam Cat# ab204708). Reduced GSH and oxidized glutathione disulfide (GSSG) levels were measured with the GSH/GSSG ratio detection assay kit II (Fluorometric–Green; Abcam Cat#ab205811) according to the manufacturer's instructions. The

standard curve method was applied to calculate RFU readings. The concentration of GSSG (μm) in the test samples was calculated as: GSSG = (total glutathione − GSH)/2 and the ratio of GSH/GSSG were plotted.

Protein Identification by Western Blot: Total proteins were extracted from LV tissue samples using RIPA buffer (supplemented with protease inhibitor cocktail) and protein concentrations were determined by the bicinchoninic acid protein quantification method (BCA). Equal amounts of protein (20 μg) were denatured and loaded onto SDS polyacrylamide gels, subjected to electrophoresis, and transferred to a polyvinylidene fluoride membrane (PVDF). Protein samples were probed with anti-MG derived AGE Antibody (Cell Biolabs, Mouse, Cat#STA-011 at 1:1000 dilution), and with anti-α-tubulin (Cell Signaling, Rabbit, Cat#2125 at 1:1000 dilution) primary antibodies overnight. After washing with TBS-T three times, membranes were incubated with anti-rabbit (Novus Biologicals, HRP, Cat#N7185 at 1:10,000 dilution) or anti-mouse (Abcam, HRP, Cat#ab205719 at 1:5000 dilution) secondary antibodies for 1 h at RT. Bands were quantified by densitometry analysis using ImageJ2 software and intensities of the bands were normalized to α-tubulin.

Statistical Analysis: Statistical analysis was performed using GraphPad Prism 8.0 software. All data are presented as the mean ± SEM. Outliers were identified using Tukey's fences (inter-quartile range) method for each measurement and removed from the statistical analysis. For the comparison of data between the treatments, a one-way ANOVA was used followed by Bonferroni's correction for multiple comparisons. Echocardiography and cardiac strain data was analyzed by Vevo LAB software.

4.6 Acknowledgements

The authors would like to thank Rick Seymour for his assistance in animal surgeries, the ACVS staff for their care for animals during the course of this study (University of Ottawa, Animal Care and Veterinary Services) and Mayte Gonzalez-Gomez for the ToC figure design in BioRender. This work was supported by by research grants from the Canadian Institutes of Health Research (FRN 125678); and the National Natural Science Foundation of China (NSFC 81261120557); and by a Collaborative Health Research Program grant from the Canadian Institutes of Health Research (CPG- 158280) and the Natural Sciences and Engineering Research Council (CHRP 523794-18). C.E.C was funded by Queen Elizabeth II Graduate Scholarship in Science & Technology and an Endowed Fellowship and Graduate Award from the University of Ottawa Heart Institute.

5 Article III – Nanoengineered Sprayable Therapy for Treating Myocardial Infarction

Accepted for publication in ACS Nano at the time of thesis submission.

ACS Manuscript ID: nn-2021-08890w

Cagla Eren Cimenci1,[2†] *Marcelo Muñoz[1†],* *Keshav Goel[1], Maxime Comtois-Bona[1], Mahir Hossain[1], Christopher D. McTiernan[1], Matias Zuñiga-Bustos[3], Alex Ross[1], Brenda Truong[1], Darryl R. Davis[4,5], Wenbin Liang[4,5], Benjamin Rotstein[6,7], Marc Ruel[1,2], Horacio Poblete[3,8], Erik J. Suuronen[1,2]* & Emilio I. Alarcon[1,7]* †**These authors contributed equally: Marcelo Muñoz and Cagla E. Cimenci.***

[1]BEaTS Research, Division of Cardiac Surgery, University of Ottawa Heart Institute, Ottawa, K1Y 4W7, Ontario, Canada. [2]Department of Cellular and Molecular Medicine, Faculty of Medicine, University of Ottawa, Ottawa, K1H 8M5, Ontario, Canada. [3]Departamento de Bioinformática, Centro de Bioinformática, Simulación y Modelado (CBSM), Facultad de Ingeniería, Universidad de Talca, Campus Talca, 2 Norte 685, Talca, Chile. [4]University of Ottawa Heart Institute, Division of Cardiology, Department of Medicine, University of Ottawa, Ottawa, Ontario K1Y 4W7, Canada. [5]University of Ottawa Heart Institute, Cardiac Electrophysiology Lab, University of Ottawa, Ottawa, Ontario K1Y 4W7, Canada. [6]Department of Biochemistry, Microbiology, and Immunology, Faculty of Medicine, University of Ottawa, Ottawa, K1H 8M5, Ontario, Canada. [7]Molecular Imaging Probes and Radiochemistry Laboratory, University of Ottawa Heart Institute, 40 Ruskin Street, Ottawa, ON, K1Y4W7, Canada. [8]Millennium Nucleus of Ion Channels-Associated Diseases (MiNICAD), Universidad de Talca, 2 Norte 685, Talca, Chile.

Article III – Abstract

We report the development, as well as the *in vitro* and *in vivo* testing, of a sprayable nano-therapeutic that uses surface engineered custom designed multi-armed peptide grafted nanogold for on-the-spot coating of infarcted myocardial surface. When applied to mouse hearts, 1-week after infarction, the spray-on treatment resulted in a remarkable increase in cardiac function (2.4-

fold), muscle contractility, and myocardial electrical conductivity. The applied nanogold remaining at the treatment site 28 days post application with no off-target organ infiltration. Further, infarct size in the mice that received treatment was found to be <10% of the total left ventricle area, while the number of blood vessels, pro-healing macrophages, and cardiomyocytes increased to levels comparable to that of a healthy animal. Our cumulative data suggests that the therapeutic action of our spray-on nanotherapeutic is highly effective and in practice its application is simpler than other regenerative approaches for treating the infarcted heart.

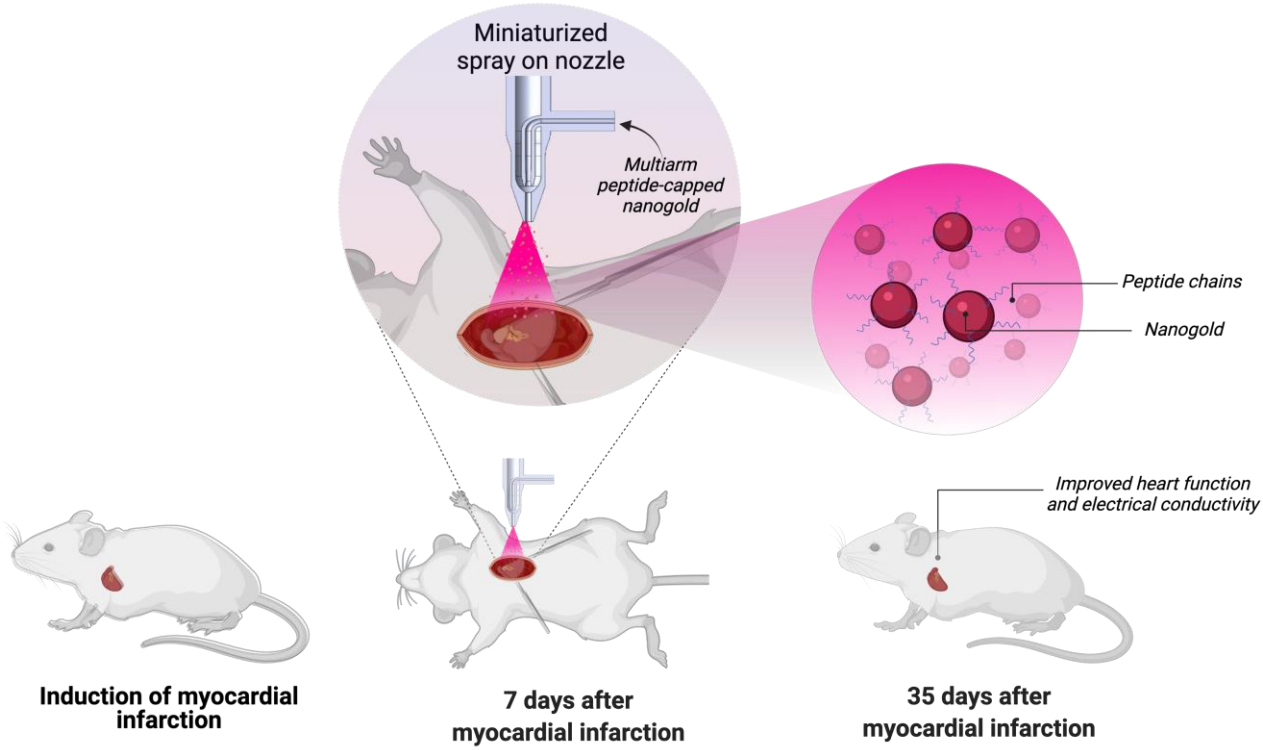

Table of Content (TOC) Illustration of Article III

5.1 Introduction

Cardiovascular disease (CVD) continues to lead worldwide mortality statistics.[205] In Canada, for example, an adult is diagnosed with heart disease every five minutes and CVD is the second most common cause of death. Among CVD patients, myocardial infarction (MI) due to coronary blood flow blockage, commonly known as a heart attack, ranks at the top in the number of annual deaths.[2,206] While surgical procedures can re-establish the blood supply to the myocardium, restoring cardiac function including electroconductivity and electrical synchrony within the ventricle remains a challenge post-MI.[207] Treatments able to improve tissue integrity and cardiac function post-MI have the potential of reducing intramural strain, which may prevent heart failure (HF) that has a five-year mortality of ~50%.[9] In Canada alone, ~50,000 new cases of HF are added every year with over a half million people currently living with HF and it is estimated that heart failure results in direct costs of more than $2.8 billion per year in Canada.[208] This number could further increase given that: (i) heart muscle inflammation persists in patients who have recently recovered from SARS-CoV-2;[209] and (ii) patients are delaying seeking and/or receiving treatment for cardiac events during the COVID-19 pandemic.[210,211]

The promise of using premade cardiac patches as therapeutics for repair of the infarcted myocardium has been demonstrated in pre-clinical studies.[80,212–214] However, despite being potentially effective, these materials must be sutured or glued to the heart, which can be surgically challenging for implantation. Further, in designing pre-made cardiac patches, it has not been considered that the implant should be customized to the shape, size, and location of the infarcted area. For these reasons, pre-made implants may be impractical and overcomplicated for clinical use. Thus, there is an urgent need to develop an in-situ therapy capable of restoring

cardiac function that is also suitable for efficient use in treating infarcts of different geometries and sizes.

In this work, we present the first nano-engineered sprayable therapy for on-the spot-repair of the damaged heart. Our sprayable therapy uses a new generation of nano-engineered peptide-based materials **(Figure 5.1a)**, where nanomolar concentrations of surface engineered spherical nanogold are used to coat the surface of the cardiac muscle. The spray-on treatment was applied in a clinically relevant murine myocardial infarction model at the time when scar formation is typically initiated (mice: 2-7 days; humans: 4-14 days),[14,35,215,216] which is a prime opportunity to intervene to limit pathological cardiac remodeling and promote infarct repair.

5.2 Results and Discussion

5.2.1 Custom designed peptides for nanogold

Our group and others have explored the surface modification of colloidal nanostructures as a cost-effective route for developing functional materials used in diverse purposes ranging from catalysis to biomedical engineering.[82,212,225–227,217–224] Amongst the available low molecular weight molecules, using peptides as functional structures for nanosurface engineering presents several advantages, particularly when considering the flexibility that peptide synthesis has achieved during the last 10 years, and especially for large scale production. Our team reported the use of multi-armed peptide-based structures for the stabilization of nanosilver.[219] In this work, we present further advancements on the specific design of peptides for surface engineering that maximizes the capping of the nanogold surface, while also incorporating free amine groups that are key for *in vivo* tethering of those structures to the infarcted myocardium.

Figure 5.1a includes the schematic for the preparation of 9.8±2.2 nm (see TEM images in **SI Figure S4**) nm colloidal spherical nanogold and the one-pot post-surface functionalization

method using our custom-designed peptides. TEM imaging for nanogold indicates that capping the nanoparticles (≈10 nm in diameter) with the multi-armed peptides does not modify their sizes or shapes (see supplementary **Figure S3**). Colloidal stability was evaluated by monitoring changes in the surface plasmon band (see supplementary **Figure S5** for representative images of the solutions) using different concentrations of the peptides under study (see **Figure 5.1b** and supplementary **Figure S6**). Multiarmed peptides 4-Leg and Multi-2 stabilized the nanoparticle at concentrations of 3.0 and 0.5 μM, respectively with the lower concentrations of peptide **(Figures 5.1b and S6)**. Further experiments for monitoring nanoparticle aggregation at 37ºC indicated that only the multi-2 peptide can produce stable colloidal solutions **(Figure 5.1c)**. AuNPs stability was also evaluated with the peptide 4-Leg at 3.0 μM, but show instability over time (see **Figure S7**). Unprotected AuNP have a negative surface,[228] while the addition of the peptides increases it to positive values, with 4-Leg and Multi-2 peptides showing larger shifts (see **Figure 5.1d**). Molecular modeling was also performed to gain further insights on the peptide attachment to the AuNP surface **(Figure 5.1e)**. Multi-2 displayed the larger surface coverage, and consequently exposes the most amine groups, which aligns well with the increased z-potential values measured. Molecular dynamics simulations for the peptides using a gold nanosurface indicate that the inclusion of additional terminal cysteine groups increases the extent of surface coverage **(Figure 5.1b)**. However, only a slight increase in the number of available amine groups on the surface of the nanogold was observed. From the molecular dynamic analysis of the peptide structures, we observed that the short cysteine-bearing chains (in the 4-Leg peptide, for example) have a reduced mobility. This could hinder the amine residues' exposure, something that we have report-ed as critical for surface stabilization in other systems.[229,230] Our calculations also indicated that the distance between the nanogold surface and the center of mass for the

peptides is found between 5 and 7Å (see supplementary **Figure S8**). Further, isothermal titration calorimetry (**Figure 5.1f**) showed that the addition of the Multi-2 peptide to colloidal nanogold produced greater changes in the heat of the solution as compared to the addition of the 4-Leg peptide **(Figure 5.1f** and inset). These observed differences correlate well with the enhanced stability of the colloidal nanogold illustrated in **Figures 5.1c and 5.1d**. Thus, based on the findings reported in **Figure 5.1** and Supplementary **Figures S4-S8**, the peptides that can stabilize the AuNPs with the lower concentration of peptide and obtain the larger values of Z-potential are the 4-Leg and Multi-2 (referred hereafter as "Multi") peptides were selected for further *in vitro* and *in vivo* experimentation.

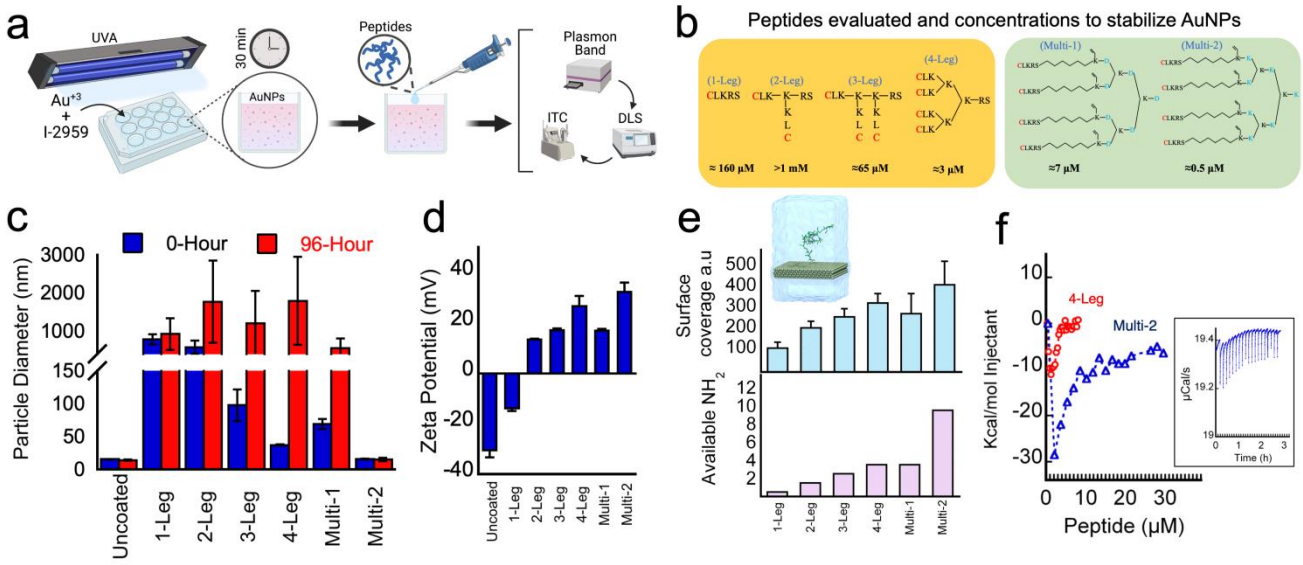

Figure 5.1 Gold Nanoparticle Characterizations. (a) Colloidal nanogold was prepared using photochemical reduction of a gold salt in water. This protocol renders nanoparticles with good size dispersity (PDI<0.1) in minutes.44 Subsequent surface modification of these nanoparticles was carried out using engineered peptides with different architectures containing terminal cysteines (b). The number of cysteines per peptide is indicated by the number before Leg in the abbreviation. The peptides Multi-1 and Multi-2 bear the same number of cysteines but contain different connecting amino acid residues in their chains (K = Lysine, D = Aspartic acid). The concentrations of peptide required to stabilize the AuNP is described under each peptide.

(c) AuNPs stability under the different peptides at time 0 and 96 hours at 37ºC under the same peptide concentration (0.5 µM). Changes were measured in 96-well plates at different incubation times (n=3) (d) Z-potential of the AuNPs capped with the different pep-tides. Measurements were performed immediately after mixing with the peptide. (e) Top: Surface coverage of the modelled nanogold surface observed for the different modelled peptides. Inset: Representative molecular dynamic simulations for the interaction of the engineered peptides and a gold nanosurface. (Bottom) Total numbers of available NH2 groups once the peptides are covering the surface. (f) Changes in heat upon the addition of increasing peptide concentrations up to 5.0 and 30 µM, for 4-Leg and Multi-2 peptides, respectively. Inset: Isothermal titration calorimetry curves for nanogold in the presence of Multi-2.

5.2.2 Spray-on miniaturization and optimization

To apply our spray-on technology, a miniaturized spray nozzle was developed with two main objectives: (1) being suitable for future minimally invasive surgical procedures; and (2) dispensing in a homogenous coating pattern. **Figure 5.2a** depicts a schematic summary for the in situ colloidal nanogold surface modification with our engineered peptides. The details for the spray nozzle design and operation instructions are found in the supplementary information (see supplementary **Figure S9**). The total volume of the spray-on treatment used was 4.0 µL containing a 90 nM solution of freshly prepared nanogold particles and a peptide solution (3.0 µM 4-Leg or 0.5 µM Multi) with 1.0 nM tris (2–carboxyethyl) phosphine hydrochloride (TCEP), a non-toxic reducing agent that prevents thiol oxidation.[228–231] To this solution, an equimolar solution of 1-ethyl-3-(3-dimethylaminopropyl) (EDC) and N-hydroxysuccinimide (NHS) was added and rapidly transferred to the spray system. NHS is approved for use in humans.[232] EDC is considered non-toxic at the micromolar concentration we used (see methodology);[233,234] while some reports have reported toxic effects of EDC when used in the mM range.[235–237] Our spray-on approach for surface grafting takes advantage of the low equimolar concentration of EDC and NHS and the rapid activation of reactions (in seconds)[238] to increase the retention of the

nanogold upon the surface of the myocardium. The spray-on nozzle was optimized for delivering volumes as small as 4 μL with a homogenous pattern formation when sprayed at a 1 cm distance from the target **(Figure 5.2b)**. This resulted in a ≈7.5 mm diameter circular pattern that is approximately the size of the akinetic region of the infarcted mouse hearts used in this study.

Collagen hydrogels were used as a biomimetic translucent model for assessing the spray-on application procedure. Surface plasmon absorbance measurements showed that upon spraying the collagen hydrogel surface with nanogold (functionalized with the Multi peptide), the characteristic nanogold plasmon band centered at 550 nm **(Figure 5.2c)** was present. Additional macroscopic measurements for the electrical resistivity of collagen materials treated with nanogold indicate a net decrease in the electrical resistivity of the materials upon addition of the nanoparticles functionalized with Multi peptide from 975.512 Ω • cm to 824.242 Ω • cm (see **Figure 5.2d)**. Furthermore, the capacitance's property at the collagen's transition point increased from 180 nF to 236 nF with the addition of the Multi-2–AuNP (see supplementary **Figure S10**). This change in capacitance properties increases the phase angle of impedance by >+2.5º.

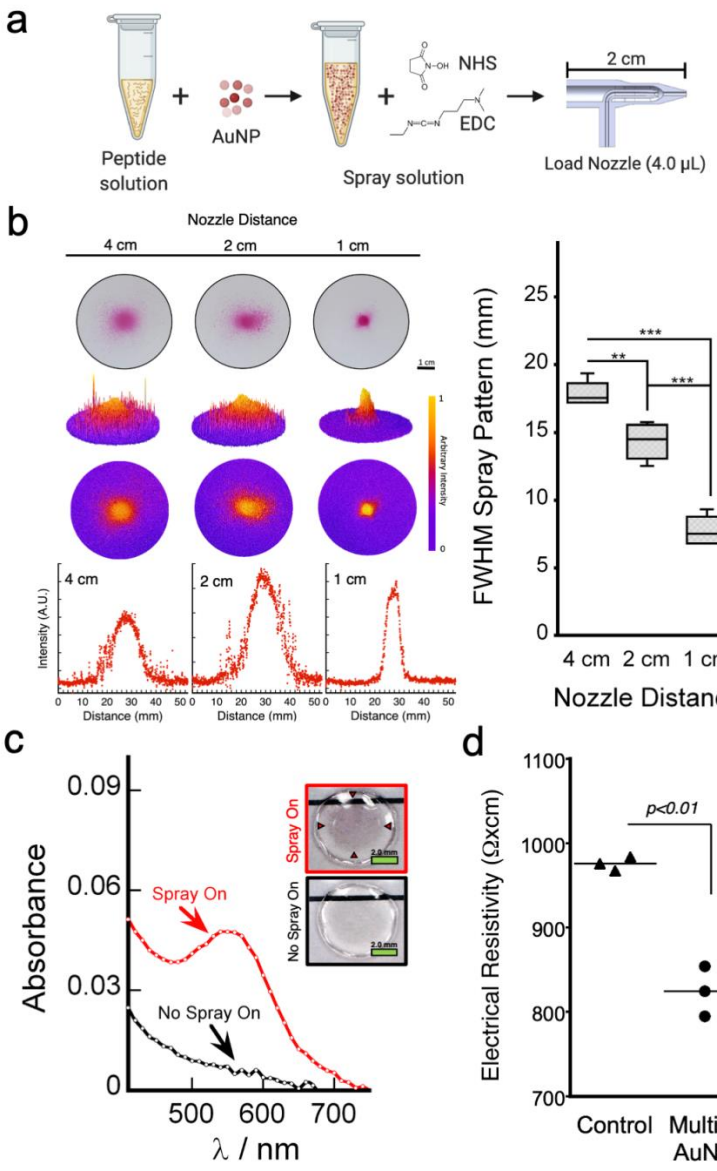

Figure 5.2 Spray-on Nozzle Design (a) Schematic representation of the main steps involved in the preparation of the nanoengineered spray-on therapeutic. Note that sprayed volumes were 4.0 µL in all cases. (b) Uniformity of spray-on pattern at three differ-ent distances from the target surface. Left top: Repre-sentative photographs of spray patterns obtained at dis-tances of 4, 2, and 1 cm. Scale bar = 1 cm. Left middle: 3D surface plot illustrating the intensity of spray patterns as measured using Image-J. Left bottom: Intensity profile of a transverse section of the spray pattern. Right: full width half maximum (FWHM) of the spray patterns as measured from the profile plots. n=4, for all groups, ** $p \leq 0.01$ and *** $p \leq 0.001$ calculated via ANOVA with Tukey post-hoc analysis. (c) Surface plasmon absorption of a type I collagen hydrogel pre- and

post-modification with the Multi peptide modified nanogold spray-on. Insets: Representatives images for the type I collagen surfaces with and without the spray-on treatment. The red arrows in the top image outline the region that received the spray-on treatment. (d) Electrical resistivity for collagen matrices treated and embedded with peptide-modified nanogold. P values were calculated using a t-test (n=3). Values in c are represented as box plots where the box encloses 50% of the data, upper and lower quartile, with the median value of the variable displayed as a line inside the box. The bars extending from the top and bottom of each box mark the minimum and maximum values within the data set.

5.2.3 *In vitro* and *in vivo* performance of the spray-on nanotherapeutic

In vitro experiments were performed to assess the toxicity effects of our spray-on therapeutic. Endothelial and cardiac cells (cardiac fibroblasts and cardiomyocytes) embedded in a 3D collagen matrix did not show any toxic effects upon exposure to the 4-Leg or Multi pep-tide capped nanogold (see supplementary **Figure S11**). We then moved on to test the spray-on nanogold *in vivo* using a clinically relevant mouse model of myocardial infarction.[103] Mice are treated at 7 days after myocardial infarction **(Figure 5.3a)**, which recapitulates patients who have not responded to revascularization therapy or those who have had a delay in seeking medical attention. Our *in vivo* functional assessment showed that all animals experienced a comparable loss in left ventricular ejection fraction (LVEF) at 1-week post-MI, representing baseline function on the day that treatment was administered (**Figure 5.3b, left**). At 28 days post-treatment, LVEF was significantly improved in the Multi-AuNP treated group compared to PBS, AuNP, 4-Leg and Multi peptide only groups (**Figure 5.3b, right**). In terms of LVEF fold change (between baseline and follow-up within each group), the Multi-AuNP treated mice showed a significant improvement compared to all the other experimental groups, except the 4-Leg AuNP group, for which there was a trend for improved LVEF (p=0.07; **Figure 5.3c**).

The change in ESV was reduced in Multi-AuNP treated hearts compared to other treatment groups **(Figure 5.3d)**, whereas no difference in EDV fold-change was observed between the groups after 4 weeks **(Figure 5.3e)**. We also measured cardiac contractility using stress/strain analysis from B-mode echocardiographic recordings. The Multi-AuNP treatment showed significant improvement in cardiac strain force, reaching values closer to those observed for the SHAM mice **(Figure 5.3f)**. Note that a negative strain force is indicative of greater contractility. Our electrocardiogram (ECG) analysis at 28 days post-treatment showed that the Multi-AuNP group has a signal profile that most closely resembles that of the SHAM animals **(Figure 5.3g)**. In line with this finding, the QRS interval assessment indicated that the Multi-AuNP group reached ms values comparable to those obtained from SHAM mice, and showed a significant decrease compared to the other treatment groups **(Figure 5.3h)**. Total gold content within harvested tissues was next evaluated using inductively coupled plasma (ICP) mass spectroscopy **(Figure 5.3i)**. No significant differences were observed for remote MI heart tissue or lungs as well as for liver, spleen, and kidney (see Supplementary Information Table S2). However, the retention of gold within the infarcted myocardial tissue was higher for the Multi-AuNP group in comparison to the 4-Leg AuNP ($p=0.03$ **Figure 5.3i**). Further, the unprotected nanogold group (AuNP) showed very high gold content in the lymph nodes ($p<0.05$ vs. the other two groups), which illustrates the superiority of using our approach for tethering nanogold on the heart muscle. *In vivo* excretion of nanogold has been documented to take place via urine and/or accumulation in the lymphatic and hepatic system, such as the case of unprotected nanogold observed herein,[239,240] and the main cause of toxicity that limits the translation of gold-therapies to the clinic.[241,242]

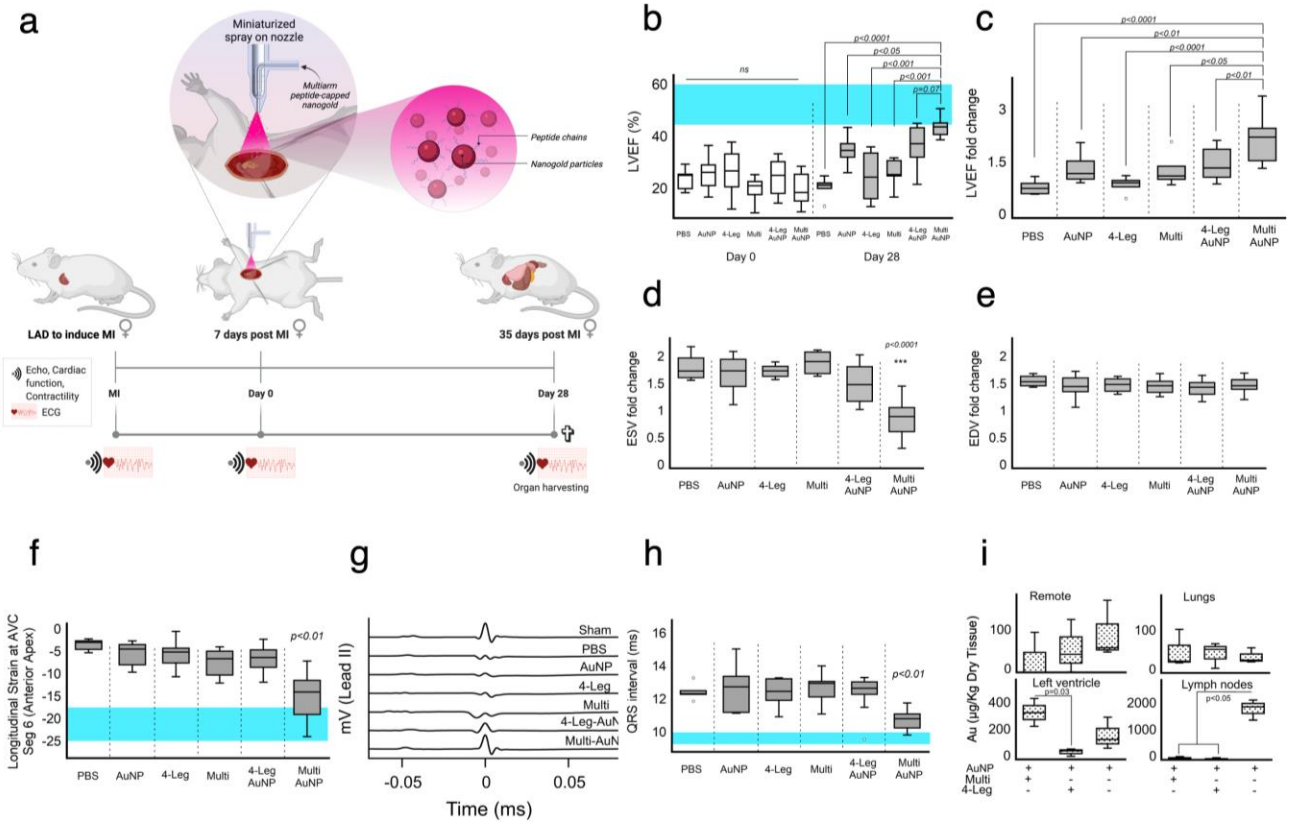

Figure 5.3 *In vivo* applications of spray-on treatment. (a) Schematic of the *in vivo* study timeline. The different treatments were sprayed onto the surface of the infarcted myocardium at 7 days post-MI. (b) Left ventricular ejection fraction (LVEF) at 28 days post-treatment. Note that the horizontal blue line represents values for SHAM mice. (c) Fold change in LVEF at 28 days post-treatment. (d) End systolic volume (ESV) fold change at 28 days post-treatment. (e) End diastolic volume (EDV) fold change at 28 days post-treatment. (f) Endocardial longitudinal strain reached at aortic valve closure within the anterior apex segment at 28 days post-treatment. Note that the horizontal blue line represents values for SHAM mice. (g) Sample ECG profiles for the different treatment groups collected at 28 days post-treatment. (h) QRS interval in ms, calculated from ECG signals at 28 days post-treatment. Note that the horizontal blue line represents values for SHAM mice. (i) Total gold content determined in selected organs collected 28 days post-treatment (n=3). Values in b, c, d, e, f, h and i are represented as box plots where the box encloses 50% of the data, upper and lower quartile, with the median value of the variable displayed as a line inside the box. The bars extending from the top and bottom of each box mark the minimum and maximum values within the data set. Otherwise indicated

group sizes were, n=6-12. P values for b-h were calculated via ANOVA with Holms post-hoc analysis. P values for i were calculated via t-test for unpaired data with unequal variance. Scheme in 3a was generated using BioRender.

Previous work by our team indicates that tethering nanogold to collagen materials result in improved conductivity.[212] However, in situ coating of a tissue, such as the cardiac muscle with nanoparticles, requires use of a capping agent to avoid aggregation while being able to chemically tether the particles to the heart muscle. The lack of cardiac functional restorative properties displayed by gold nanoparticles alone clearly illustrates the relevance of having multifunctional capping agents that can serve as stabilizers and tethering points. The cardiac restorative properties for the Multi-AuNP could be the result of a combination of factors, including: (1) increased incorporation and retention in tissues, which is facilitated by the positive charge of the particles (ICP data),[243] (2) increased stability of the AuNPs and resistance to aggregation due to the peptide surface coating (see **Figure 5.1**), and (3) increased stability of the peptides against enzymatic degradation conferred by the nanogold (see **Figure S12**). Others have reported that cationic peptides can recover cardiac function post-MI;[244,245] however, we hypothesize that our positively charged Multi-2 peptide is not able to promote recovery when delivered alone due to the inflammatory environment within the infarcted area which might result in rapid enzymatic clearance, thus limiting any potential beneficial effect. The combination of the peptide with nanogold could result in a cooperative effect, yet to be elucidated, that allows for functional recovery of cardiac function and electrical signal propagation using submicromolar concentrations of both peptide and nanogold.

Spray-on cardiac nanotherapeutic increases heart wall-thickness and reduces infarct size. At 28 days post-treatment, we collected the hearts and performed histological analyses. Masson's

Trichrome staining results showed that the Multi-AuNP and 4-Leg AuNP treatment groups have a thicker viable remote myocardium compared to PBS, AuNP, 4-Leg and Multi peptide treatment groups (**Figures 5.4a and 5.4b**). Strikingly, with a scar size of ≈10%, the Multi-AuNP-treated hearts had reduced scar size compared to the other treatment groups **(Figure 5.4c)**.

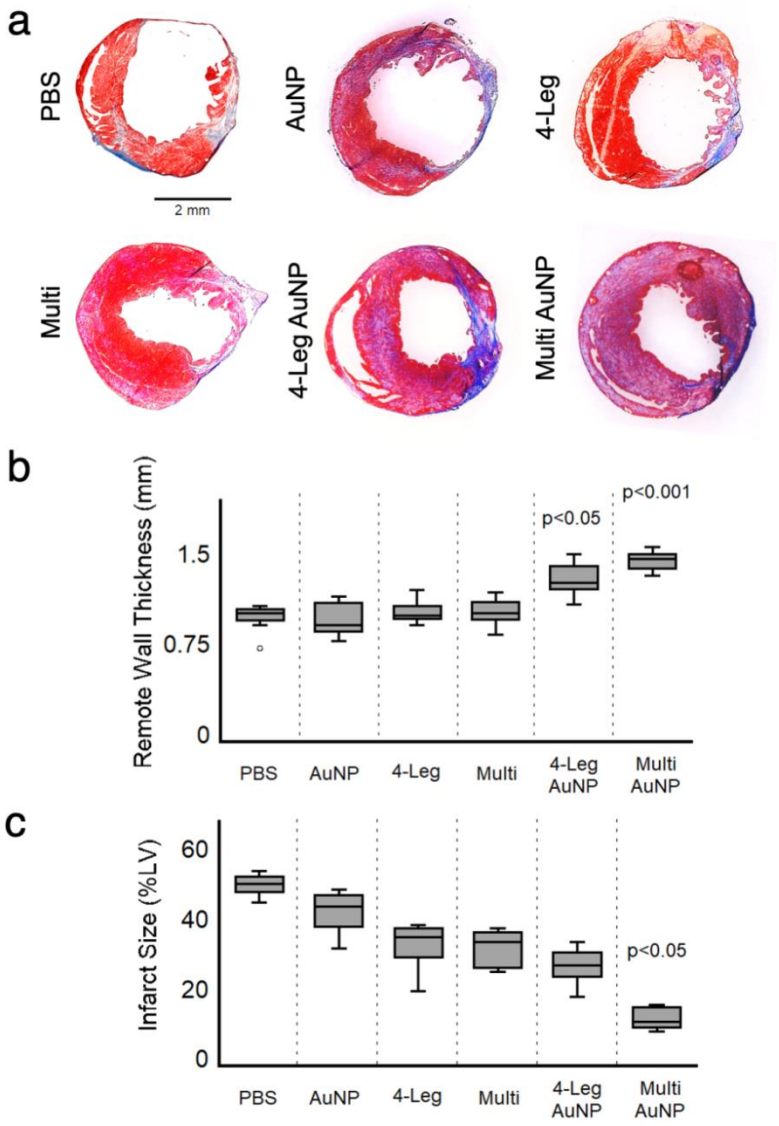

Figure 5.4 Multi-AuNP treatment reduces the scar size *in vivo*. (a) Representative images of Masson's trichrome stained cardiac tissue sections treated with PBS, AuNP, 4-Leg, Multi, 4-Leg AuNP and Multi AuNP. Scale bar = 2 mm. (b) Remote wall thickness of the myocardium measured in Masson's trichrome stained tissue sections at 28 days post-treatment. (c) Scar size (%LV) measured at 28 days post-treatment in Masson's trichrome stained tissue sections. Values in b and c are represented as box plots where the box encloses 50% of the data, upper and lower quartile, with the median value of the variable displayed as a line inside the box. The bars extending from the top and bottom of each box mark the minimum and maximum values within the data set. P values were calculated via ANOVA with Holms post-hoc analysis. Group sizes n=6-12.

5.2.4 Spray-on nanotherapeutic application improves vascularization and increases number of pro-healing macrophages

Immunostaining analysis of tissue sections at 28 days post-treatment showed that the Multi-AuNP or 4-Leg AuNP spray-on increased the number of capillaries and arterioles in the scar region compared to the other treatments, while capillary and arteriole numbers were also greater for the Multi-AuNP compared to the 4-Leg AuNP **(Figure 5.5a)**. Although we did not observe any difference in early inflammation between the treatment groups at 2 days (supplementary **Figure S13**), the number of CD206+ wound healing macrophages was increased for the Multi-AuNP treatment compared to all other groups, and the 4-Leg AuNP treatment resulted in greater numbers of these cells compared to the PBS, AuNP, 4Leg and Multi peptide treatment groups in 4 weeks **(Figure 5.5b)**. Furthermore, the Multi-AuNP and 4-Leg AuNP treatment resulted in a lower density of CD86+ pro-inflammatory macrophages **(Figure 5.5b)**.

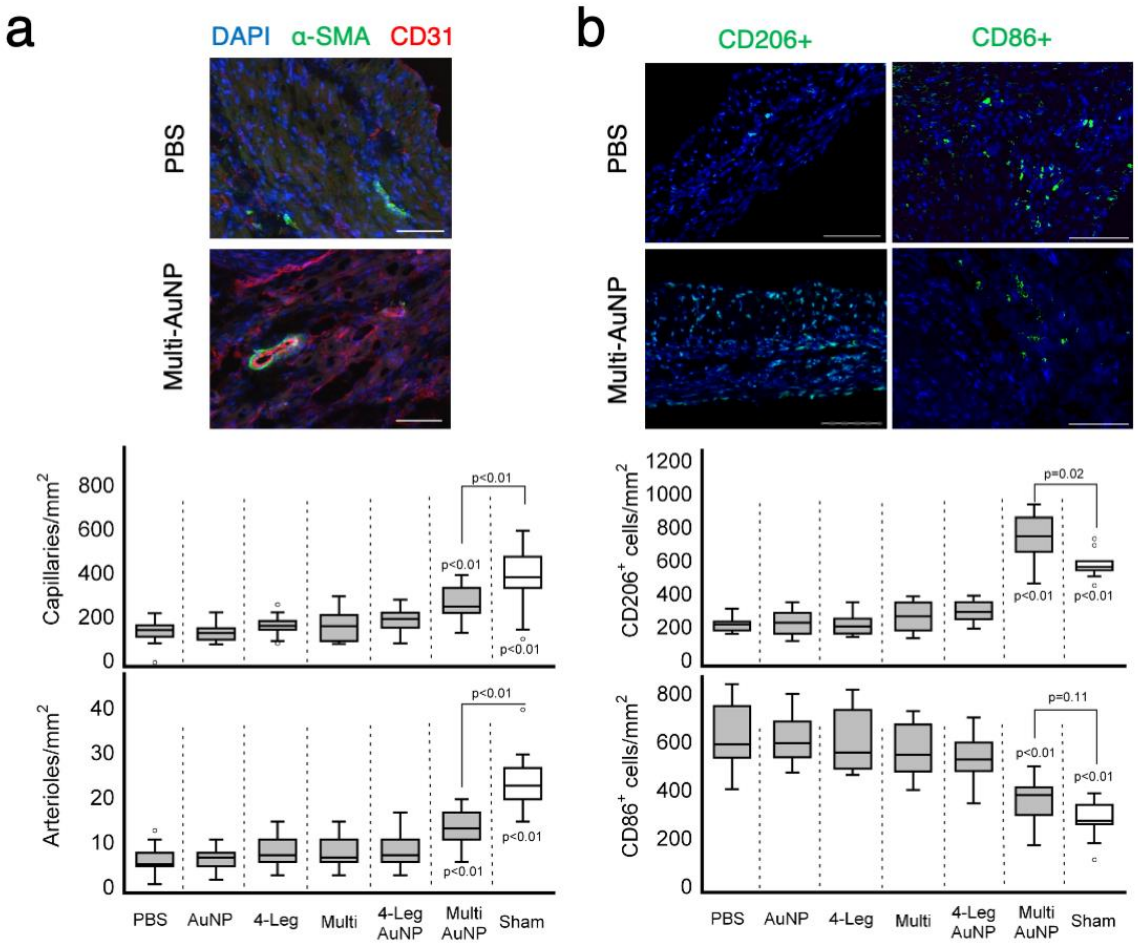

Figure 5.5 Assessment of vascularization and macrophages. (a) Representative immunohistochemistry images and quantification of double positive α-SMA+ (green) and CD31+ (red) arterioles, CD31+ capillaries (red) and DAPI-stained cell nuclei (blue). Scale bar = 100 µm. Representative images for the treatment groups not shown in the main manuscript can be found in supplementary Info (see Supplementary Figure S14). (b) Representative immunohistochemistry images and quantification of CD86+ pro-inflammatory macrophages (green) and CD206+ pro-wound healing macrophages (green). Scale bar = 100 µm. Representative images for the treatment groups not shown in the main manuscript can be found in supplementary information Figure S115. Values plotted are presented as the number of cells/mm2 represented in box plots where the box encloses 50% of the data, upper and lower quartile, with the median value of the variable displayed as a line inside the box. The bars extending from the top and bottom of each box indicate the minimum and maximum values within the data set that fall within an acceptable range. P values were calculated via ANOVA with Holms post-hoc analysis. Samples sizes n=6 for each treatment group.

5.2.5 Spray-on nanotherapeutic application increases number of cardiomyocytes and supports gap junction formation in the border zone post-MI

To further explore possible mechanisms underlying the functional benefit of the spray-on nanotherapeutic application, immunohistochemistry was performed to assess cardiomyocyte preservation and gap junction formation in the border zone at 28 days post-treatment **(Figure 5.6a)**. The area of cardiac troponin T (cTnT) expression, a cardiomyocyte marker, was shown to be greater in the border zone of hearts treated with the Multi-AuNP compared to PBS and gold treatment **(Figure 5.6b)**, suggesting greater preservation of cardiomyocytes. Notably, the level of the gap junction protein connexin-43 (Cx43) expression was significantly greater in the border zone for the Multi-AuNP group compared to all other treatment groups **(Figure 5.6c)**. This is indicative of re-establishment or preservation of the gap junctions and intracellular communication in ventricular myocardium.

Tissue engineering seeks to repair or replace damaged tissues by using biomimetic structures that will integrate and function within the recipient. The human heart has a limited capacity to regenerate cardiomyocytes; as such the loss of cardiomyocytes and their intercellular coupling and electrical conduction post-MI are fundamental in the lack of recovery of cardiac function.[246] Electrical stimuli play a key role in the development and maintenance of cardiomyocyte function, which includes regulation of subcellular cues, protein and gene expression, metal ion content, and action potential propagation.[247] Many biomaterial-based therapies for treating MI have shown potential in pre-clinical settings, with some of them even being currently clinically tested.[77,171,248–250] However, the biopolymers that are often used in such applications, such as collagens, typically lack one important property for achieving functional cardiac recovery, which is that they do not support electrical conductivity.[251–253] Furthermore, in designing a therapy for

cardiac repair that is applied to the surface of the heart, consideration should be given to a material that is able to rapidly coat the infarcted region while boosting the electrical conductivity within the infarcted tissue.[82] Thus, the ideal biomimetic therapy for repairing the infarcted myocardium should: (i) efficiently coat the surface of the infarcted myocardium; (ii) not interfere with muscle con-traction; and (iii) improve electrical conductivity but not be a source of cardiac arrhythmias.

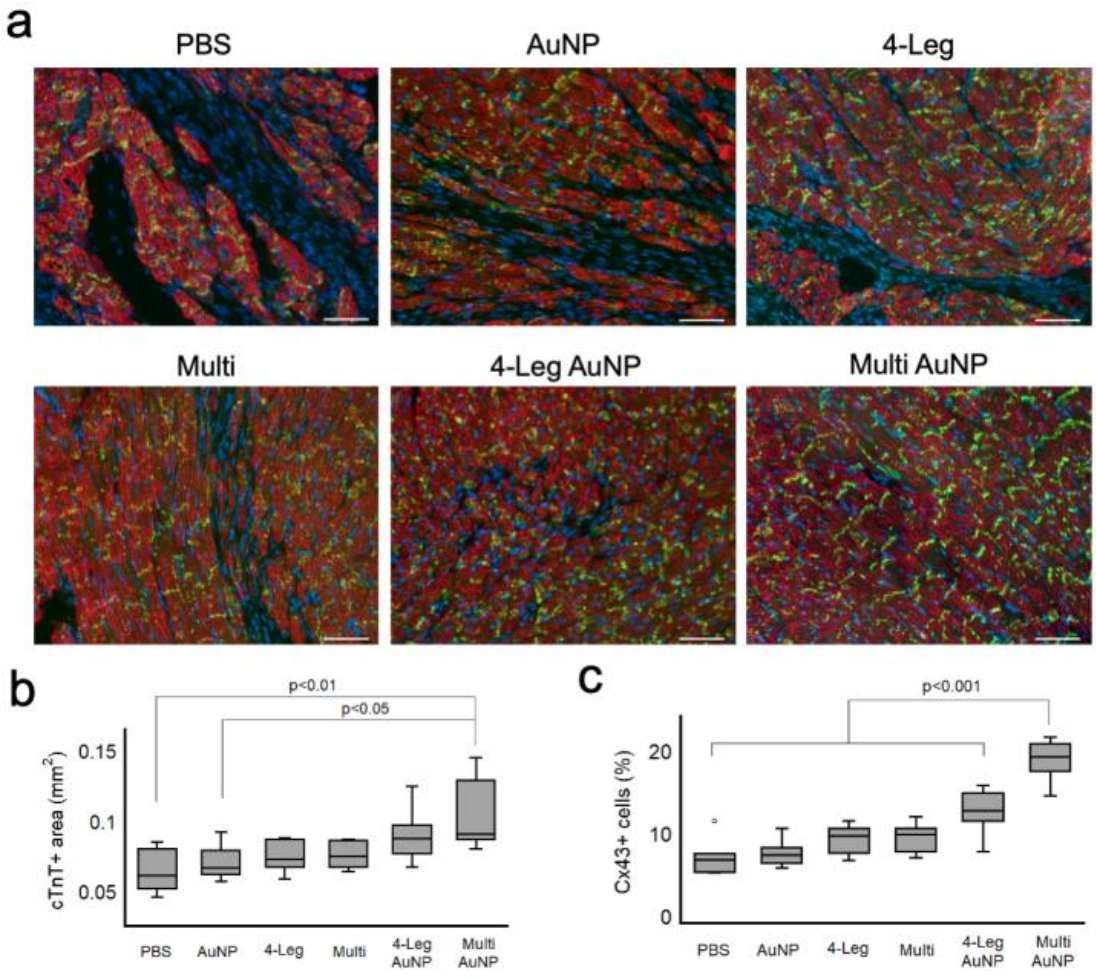

Figure 5.6 Connexin 43 staining and quantification. (a) Representative immunohistochemistry staining images for cardiac troponin T (cTnT) and connexin 43 (Cx43) in the border zone after treatment with PBS, AuNP, 4-Leg, Multi, 4-Leg AuNP and Multi-AuNP; red: cTnT, green: Cx43, blue: DAPI. Scale bar = 100 µm.

(b) Quantification of total cardiac troponin T (cTnT) positive area (in mm2). (c) Quantification of connexin 43+ (Cx43) cells in the remote area. Values in (c) are represented as box plots where the box encloses 50% of the data, upper and lower quartile, with the median value of the variable dis-played as a line inside the box. The bars extending from the top and bottom of each box mark the minimum and maximum values within the data set. Statistical values were determined by one-way ANOVA using Holm's post-hoc analysis. Samples sizes n=6 for each group.

Thus, electroconductive biomatrices prepared using supramolecular aligned structures have gained much attention for heart repair.[247,254,255] For example, the development of a number of hybrid composite materials with enhanced electroconductive properties have been reported, including synthetic polymers,[256–260] collagen-nanofibers containing nanosilver,[222] collagen-based nanosilver and nanogold injectable matrices,[220] nanotube-based composites,[246,258,261] carbon nanofibers,[262–264] graphene and graphene oxide surface modified materials,[265–267] and nanogold containing materials.[80,213,268] However, metal nanoparticles such as silver and copper have demonstrated poor stability under physiological conditions, leading to toxicity.[221,269] Some reports indicate that spherical nanogold with diameters smaller than 20 nm are not toxic *in vitro*[270] and *in vivo*.[271] In addition to the nanoparticle size and/or shape, the surface composition of nanomaterials, meaning the capping agent, also plays a key role in dictating nanoparticle stability and ultimately its toxicity.[217–221,223,224,272–274] Also, for the *in vivo* evaluation of gold toxicity, single-dose therapies for other applications have used standard dosages of several mg/kg.[240,275,276] In our work, we used 240 ng of gold delivered per treatment, which is the equivalent of 2.4 µg/kg, and in terms of body mass of the animal, far below the dosage evaluated for other AuNP therapies reported in the literature. Further, using our nanoengineered peptide-based approach allows for superior retention of such a small quantity of gold to remain on the target heart muscle tissue. Thus, although we used several orders of magnitude smaller quantities

than other nanogold based-therapeutics,[277] this was sufficient to produce a beneficial effect on cardiac function. Also, our on-site local application presents a practical solution for reducing the dosage, which, when using our multi-armed peptide, limits off-target gold biodistribution to other tissues and risk for organ toxicity, as demonstrated by the gold infiltration to lymph nodes and liver observed for the non-protected nanogold.

Using our spray-on approach allows us to deliver very small volumes (<10 µL) that can coat the heart surface within seconds. This methodology has several advantages over direct injection, where larger volumes and concentrations of nanoparticles are needed, which brings a greater risk of off-target accumulation.[203,278] Furthermore, the novelty of our on-site local application presents a practical solution for reducing the dosage, which when using our multi-armed peptide limits off-target gold biodistribution to other tissues and risk for organ toxicity, as demonstrated by the gold infiltration to lymph nodes and liver observed for the non-protected nanogold. Although several orders of magnitude smaller than other nanogold based-therapeutics[277], our delivered amount was sufficient to produce a beneficial effect on cardiac function. Also, our on-site local application presents a practical solution for reducing the dosage, which limits off-target gold biodistribution to other tissues and risk for organ toxicity, as demonstrated by the gold infiltration to lymph nodes observed for the non-protected nanogold. Also, the contactless nature of the spray-on application has a competitive edge over other delivery techniques such as intramyocardial injection, which punctures the damaged cardiac muscle to deliver therapeutic molecules and provides a more localized treatment within the injection area.[203,279] In addition, smearing directly on the heart surface would need considerably larger volumes of solution to effectively cover the total surface of the damaged muscle.

As an alternative to synthetic electroconductive polymers, we have previously reported a patch material that uses collagen fibres containing sub-nanomolar non-toxic nanogold that are combined with an elastic microporous collagen hydrogel[222]. These acellular cardiac patches were able to restore cardiac function when applied to a 7-day old scar (equivalent ≈14 days in humans[14,215]) in a murine MI model[223]. Despite these promising results[212], surgical implantation of the patch remains challenging. Further-more, most of the nanogold in this prior patch is contained within the collagenous fiber structure[222]. There are some other sprayable materials that have been proposed for treating the MI heart. For example, Tang et al. reported a sprayable polymer biomaterial system for cardiac regeneration.[280] These types of systems are promising yet can be improved as they are lacking electroconductive elements and use extracted proteins at high concentrations, which may be limiting for future clinical translation.

In contractile tissues, like the heart muscle, phase change between the voltage and current through the tissue due to capacitance effects of the cell membranes and tissue impedance is directly involved in tissue contraction.[281] *In vitro* experiments for our spray-on material using a fibrotic mimetic model (i.e. a collagen matrix) demonstrated an improved conductivity, increased capacitance and phase angle of impedance for the resulting material when evaluated under alternating voltage, mimicking the oscillatory conductivity conditions of the heart. The collagen matrix possesses resistance and capacitance properties, so it can be evaluated as a simplified resistor–capacitance unit, similar to the infarcted cardiac tissue.[282] This suggests the Multi-2–AuNP is acting as an external nano-capacitor that supports both charge accumulation and release. Note that the resistivity of the heart tissue changes upon myocardial infarction.[283,284] Thus, for example, in the acute phase post-MI, there is an increase in tissue resistivity at the infarcted site, with a severe reduction in the phase angle (between 2º and 10º)[285,286]. Once the myocardial scar

has been established, the resistivity reduces below the values of the healthy muscle and with no detectable phase angle.[284] In terms of tissue conductivity in the infarct tissue, in the maturation phase of post-ischemic event, cardiomyocyte cell survival and cell-to-cell gap junctions are reduced, which decreases tissue conductivity.[287] Gap junctions are instrumental for conductivity within the heart muscle tissue.[287–290] Our experimental data suggests that a reduction in tissue resistivity with increasing impedance dephasing effect could be a potential mechanism underlying the benefits achieved with use of this therapy *in vivo*.

The therapeutic approach reported here presents an advancement in the field of cardiac repair since it encompassed: (i) the use of nanoengineered material surfaces using peptides; and (ii) a micrometric nozzle that produces homogenous and consistent patterns for coating the heart muscle in less than 10 seconds, without the need for puncturing, gluing, or suturing. Our therapy does not affect cellular viability as determined by a viability assay using cardiac fibroblasts and HUVECs. The assessment of the *in vivo* performance for our spray-on treatment was conducted in MI mouse hearts at 1 week following MI, which corresponds to the early proliferative healing phase[14] and it is considered clinically relevant as it represents the patient population who could not receive immediate medical attention or who have not responded adequately to initial revascularization procedures. Further, this time point has become more important as the COVID-19 pandemic has had a significant effect in hospital admission rates. It has been reported that STEMI admissions markedly declined from 48% to 18% during the pandemic.[291,292]

Our *in vivo* data indicated that only the Multi-AuNP improved LVEF compared to all the other groups, suggesting that grafting the surface of nanogold using the Multi pep-tide is able to effectively enhance the pro-reparative properties of nanogold. This effect could be a direct consequence of the greater retention of gold on the myocardial surface. In particular, the

improved function with the Multi-AuNP treatment was also observed in the analysis of stress/strain forces at aortic valve closure, where the mechanical properties of the cardiac muscle in the treated animals' border zone resembled those of SHAM animals. As strain force represents myocardial contractility,[293] it can be concluded that Multi-AuNP treatment was exceptionally effective at improving cardiac function within the border zone compared to the other treatment groups. Furthermore, as determined by ECG tracing, hearts treated with the Multi-AuNP displayed *in vivo* electrical propagation that closely resembled that from healthy hearts, suggesting an improvement in electrical conductivity within the left ventricle.

It has been demonstrated that MI impairs the conductivity of the left ventricle after several days, resulting in an increase in the QRS interval time.[294] At 28 days post-treatment, there was a significant increase in QRS time and qualitative reduction in the QRS signal intensity compared to the healthy group for all groups except the Multi-AuNP group. An increase in QRS interval corresponds to a conductivity disturbance of the ventricular area, associated with a reduction in the amplitude of the R and S wave after MI.[295,296] Multi-AuNP did not recover the conductivity properties of the hearts 1 day after treatment (see Supplementary **Figure S13**), suggesting that its application may activate a biological pathway leading to the recovery of electroconductivity that was observed after 28 days **(Figures 5.3e - 5.3f)**. This aligns well with the immunostaining findings showing an increased number of cardiomyocytes and connexin-43, which are key for muscle contraction and electrical signal propagation.[297] Connexin-43 expressing cardiomyocytes represent increased propagation speed and better dispersion of repolarization, both of which are indicators of effective myocardial repair at the molecular level.[298,299] Immunostaining of heart sections also indicated an increased vascular density and greater numbers of pro-wound healing M2 macrophages within the infarct region. This pro-healing environment is like previous studies

that reported a reduced inflammatory environment with the use of a nanogold treatment.[277,300] Macrophages of various phenotypes participate in important ways at different times of wound healing.[301] It is important to note that macrophage polarization toward the pro-healing M2 profile has been associated with the tissue healing response, in part as a key factor in vascularization.[302–304] This could be related to the observed increase in capillary and arteriole density following Multi-AuNP treatment. Additionally, we found that pro-inflammatory M1 macrophage numbers were reduced with Multi-AuNP treatment. It has been shown that a low or moderate density of M1 macrophages can support tissue repair through the secretion of VEGF, making them relevant in the angiogenesis process.[305,306] This indicates that the use of the Multi-AuNP nanotherapeutic could improve the balance between M1 and M2 macrophage polarization to promote wound healing and vascular remodeling. We also observed that the early inflammation rates were comparable between all the treatment groups, suggesting that the repair at 4 weeks was not a consequence of changes in inflammation following spray-on treatment.

5.3 Conclusion

In summary, we have demonstrated that by combining peptide design and an on-the-spot application, a therapeutic approach was developed that allows nanomolar concentrations of nanogold to restore cardiac function in a clinically relevant animal model of myocardial infarction. While the mechanism of action by which application of nanogold restores cardiac function post-myocardial infarction remains to be fully elucidated, including delivery of the therapy at different timepoints after heart injury. Our findings illustrate how peptide engineering can finely tune the properties of nanomaterials for use in therapeutic applications that in our case improved cardiac contractility and electrical signal propagation.

It is worth emphasizing that despite the progress of cardiac treatments over the last decades, the prevalence of heart failure is on the rise,[307] with significant mortality rates in the elderly population.[308] While interventional procedures can restore blood supply after a myocardial infarction, patients who do not have immediate access or do not respond adequately to such procedures are at higher risk to develop heart failure, which has a mortality rate of 50% over the first 5 years in patients with non-preserved ejection fraction HF.[309] Thus, a non-invasive spray-on technology that uses a miniaturized nozzle catheter-guided system could be used in conjunction with current minimally invasive surgical procedures such as coronary artery bypass surgery.

5.4 Experimental Section

Study design: Here, we conducted a study to (i) develop a new generation of peptides for stabilizing and anchoring nanogold to the cardiac muscle; (ii) design a sprayable therapy for treating infarcted myocardium; (iii) evaluate the therapeutic potential of the materials for treating infarcted murine hearts; and (iv) explore the biological response of this new therapy in our animal model. For *in vivo* experiments, ligation of the artery descending in mice was chosen as a clinically relevant and well-established animal model. In our *in vivo* experiments, the number of animals per group was minimized to nine to twelve mice, as specified in the figure legends. Mice were randomly assigned to treatment groups. During the surgical procedure the operator was blinded to the treatment being used. All analyses were performed in a blinded fashion.

Nozzle printing: The nozzle was designed and customized for the present application. Briefly, at the tip, 2 streamlines generate the micro spray. The internal channel of 337 µm carries the 4 µL liquid, and the external line of 900 µm carries the air pressure. The 3D printed model was fabricated in a Formlabs Form 3 with clear resin. After the print was complete, it was washed with isopropanol, and all the internal channels were flushed with methanol. The device was dried under a stream of nitrogen and cured in a UVA curing device for 1 hour at 60ºC (further details on this device can be found in the supplementary information and supplementary **Figure S9**).

Gold nanoparticles synthesis: 6 mg of $NaAuCl_4x2H_2O$ were dissolved in 50 mL of Milli-Q water. 5 mL of 10 mM I-2959 were added to the mix. The solution was transferred to a 24-well plate (2 mL per well) and irradiated in a photoreactor with UVA light for 15 min at 37ºC (LZC4V, Luzchem Inc.). Color change is indicative of nanoparticles formation.

Peptide synthesis: Peptide synthesis was carried out in-house. All peptides were synthesized using microwave assisted Fmoc solid phase peptide synthesis in a Liberty Blue automated system. Fmoc protected amino acids and Wang resins with preloaded amino acids were purchased from CEM. Briefly, the required amount of resin was swelled with DMF in the system for 5 min. Next, Fmoc deprotection was carried out with 20% piperidine at 90°C for 60s while standard coupling cycles using DIC/Oxyma Pure were run at 90°C for 240s for each amino acid that was added to the sequence. Peptides were cleaved from the resin and deprotected with 92.5/2.5/2.5/2.5% v/v TFA/TIS/EDT/H2O at 42°C for 30 minutes and then pre-cipitated in -20°C diethyl ether. Peptide crude products were then dried under vacuum overnight and purified by RP-HLPC in a Waters 1525EF semi-preparative system with a 21.6x250 mm C18 column at 20 mL/min. Peptide purity and identity was confirmed via RP-UPLC-UV/MS in a Waters Acquity UPLC Xevo TQD using a 2.1x100 mm UPLC BEH C8 column. A purity of >95% was determined through UV peak analysis. The molecular ion found [M+H]+ for each peptide after deconvolution calculation is [molecular ion found m/z [M+H]+ / theoretical molecular ion m/z [M+H]+ (see supplementary **Figure S16**)]: 1-Leg (CLKRS): 606.62 / 606.76. 2-Leg ((CLK)2KRS): 1079.52 / 1079.41. 3-Leg ((CLK)2K(CLK)KRS): 1551.74 / 1552.05. 4-Leg (((CLK)2K)2KRS): 2024.62 / 2024.70. Multi-1 (((CLKRS-Ahx-KD)2KD)2KD): 4861.26 / 4861.76. Multi-2 (((CLKRS-Ahx-KK)2KK)2KK): 4953.72 / 4953.37.

Spray-on setup: The peptide solution (0.5 µM for Multi or 3.0 µM for 4-Leg) is mixed with TCEP (to prevent thiol oxidation) and then added to the nanoparticle solution (1.0 nM final concentration). To this new solution an equimolar concentration of EDC and NHS (≈20 µM) is added and rapidly transferred to the spray system **(Figure 5.2a)**. Our device has a miniaturized

camera and distance sensor that allows for homogenous distribution upon application of the spray-on nanotherapeutic.

Plasmon band measurements: Absorbance measurements were performed in a 96-well plate reader between 450 and 600 nm in a SpectraMax M2e instrument and analyzed with the SoftMax® Pro 7 software (Molecular Devices®). Corrections using blanks were performed accordingly in each condition.

Isothermal titration calorimetry (ITC): Changes in heat from 4-Leg and Multi peptide association to nanogold colloidal solutions were analyzed using a VP-ITC MicroCalorimeter Malvern Isothermal titration calorimeter system. Briefly, 2 mL of a freshly prepared nanogold solution and 2 mL ultrapure water were degassed for 15 min and loaded into the ITC sample cell and reference cell, respectively. The temperature was calibrated to 25 °C and the injection syringe was loaded with 300 µL of the peptides (250 µM). Parameters were set as: 20 injections, 1 µL per injection, 10 s injection time, and 600 s injection spacing. Each run was analyzed using Microcal Origin and data extracted for plotting in Kaleida Graph 4.5 (see below). Enzymatic ITC measurements were performed at 37ºC. 1 nM of trypsin solution (in PBS and degassed) was placed in the cell and equilibrated. In the syringe Multi-2 peptide with and with-out AuNPs was loaded in concentration of 0.5 µM. After system equilibration, 25 µL of peptide were injected in 10 seconds and the reading followed up to 10 min. This was performed in triplicate. ΔH was obtained directly from the software in each measurement and subtracted from the proper blank sample.

Dynamic light scattering (DLS) and zeta potential: DLS measurements for stability of the surface modified nanogold were carried out in a DynaPro PlateReader-II DLS system with a 96-well plate (Wyatt® Technologies). Gold nanoparticles stabilized with 4-Leg peptide (3.0 µM)

and Multi-2 peptide (0.5 μM) was added in triplicate to the well plate up to 100 μL. A small layer of 50 μL of light weight mineral oil was gently added to the top of the wells top to avoid evaporation. No particles were found on the control well with water and mineral oil (no AuNP added), or peptides solution without AuNP. The size was measured every hour for up to 90 hours at 37ºC.

Zeta potential measurements were performed out in a Malvern Zetasizer Nano ZS at 25 °C in cuvettes DTS1070. Samples were measured by triplicate from different batches, and accumulation from each measurement was up to 20 readings.

Transmission electron microscopy (TEM): Samples for TEM were prepared by delivering 10 μL of solution to carbon-coated copper grids (400-mesh) and dried in vacuum overnight. TEM images were taken in an FEI Tecnai G2 F20 Field Emission Transmission Electron Microscope (FETEM) at a 200KV acceleration voltage. Nanoparticle mean size was obtained using ImageJ, were a minimum of 100 particles for group were assessed. A normal distribution statistical system was obtained from each samples, and compared using t-test system, $P<0.05$ for significance difference (Kaleida Graph 4.5).

Electrical resistivity: 10% Collagen type I disks (Theracol®) of 6 mm diameter and 1 mm thickness were fabricated for this experiment and used as is or with an embedded addition of Multi-2–AuNP at a concentration of 150 ng per gram of material. The samples were swelled in milli-Q water at 4ºC and surface blotted. The disk was then placed in a glass custom made support that has 2 copper strips per side, with the larger area of the disks in contact with the strips (copper conductive tape from Electron Microscope Sciences®, was used only once per sample, n=3 samples per condition). The samples were measured at 25ºC in a Potentiostat Parstat 2273 (Princeton Applied Research) with a scan frequency from 100 kHz to 100 mHz. Electrical

resistivity was calculated based on the disk measurements at 9.326 kHz. The transition point was calculated from the Bode Plot at the second derivative point equal to 0 and max phase angle, from where the capacitor and phase angle value were extracted (see Supplementary **Figure S8**).

Computational simulations: All simulations were performed using NAMD 2.131 software[310], including the CHARMM36 force field[311], the particle-mesh Ewald electrostatics[312], Langevin thermostat, and Langevin piston barostat[313], and a 4fs time step scheme.[314] Initial equilibrium simulations of each free peptide with an explicit box water were developed in a simulation time of 500 ns. Next, simulations including solvated AuNP-peptide complexes were carried out using a planar AuNP-111 surface model (50x50 Å2 for 1 to 4-Leg and 78x78 Å2 for Multi-1 and Multi-2) adding the GolP-CHARMM force field parameters[315]. The surface model incorporates charged virtual particles rigidly bonded to each gold atom to model polarizability and to include the image charge effects, as well as virtual interaction sites for Au-111 and Au-100 facets, to ensure the correct absorption on top of gold atoms and not between them. Unrestrained equilibrium simulations were performed for additional 500 ns including five replicas for each system. Each replica was constructed by extracting frames from the initial free-peptide trajectories. All structural and statistical analyses over trajectories were performed using VMD software.[316]

Live/dead viability assay: HUVECs and cardiac fibro-blasts were separately maintained in T-75 cm^2 filter cap flasks in DMEM supplemented with 1% Penicillin Streptomycin / L-glutamine and 10% heat inactivated Fetal Bovine Serum (56°C, 30 min). After reaching 80% confluency, cells were mixed with hydrogel solution and plated into 24-well culture plates. The 3D hydrogel was prepared based on our previously published protocol19 by mixing the following on ice: Theracol, Collagen Medium, Glutaraldehyde, Glycine, PBS and NaOH to reach a pH of ~7.4. The gels

within the wells were then sprayed with PBS, AuNP, 4-Leg, Multi, 4-Leg AuNP or Multi-AuNP and cultured for 24 hours (n=3 for each treatment group). The following day, the culture media was aspirated, and wells were washed with PBS. Cells were then treated with the LIVE/DEAD® assay reagents, 2 µM Calcein AM and 4 µM EthD-1 solutions were dissolved in sterile PBS and incubated for 30 mins at 37°C. Fluorescent imaging was performed for Calcein AM at 530 ± 12.5 nm and EthD-1 at 645 ± 20 nm via inverted microscope (Zeiss AXIO Observer Z1). Three representative images were taken from each well and images were quantified by counting the number of live vs. dead cells.

Cardiomyocyte isolation and culture: Cardiomyocytes were isolated from 8-week old mouse hearts. Briefly, hearts were extracted and placed in a culture dish containing 1x PBS (without Ca^{2+} Mg^{2+}) with 20 mM BDM (2,3-Butanedione Monoxime) on ice. Next, cardiac tissues were minced in 250 µl isolation medium, and incubated on ice for 6 hours. The pellet was digested enzymatically with collagenase/dispase mixture (Roche) supplemented with BDM. Cardiac tissue fragments were digested at 37 °C with gentle agitation for 20-30 min. Cells were then filtered through 70 µm cell strainer and centrifuged for 5 min at 300 rpm. The supernatant was discarded, and the pellet was dissolved in plating medium. Cells were then plated for 1-3 hours for removal of fibroblasts and endothelial cells which will adhere to the cell culture dish quickly. After this incubation, non-adherent cardiomyocytes were collected and transferred onto collagen-coated plates with a density of approximately 1.5 x 10^5 cells per cm^2. Cardiomyocytes were left undisturbed for 12-18 hours to allow for adherence and spreading. Once they reached confluency, the cells were lifted, counted and seeded for live-dead viability assay as explained previously.

Animal experiments: All procedures were approved by the University of Ottawa Animal Care Committee (ACC) and performed in accordance with the National Institute of Health Guide for the Care and Use of Laboratory Animals.

Animal model: After approval from ACC, a clinically relevant mouse model of MI was used, as we have previously reported.[62,317] Briefly, 6–8-week-old female C57BL/6 mice (Charles River) were anaesthetized (2% isoflurane), intubated, and the heart was exposed via fourth intercostal thoracotomy. The left coronary artery (LCA) was then ligated just below its emergence from the left atrium, which produces a large MI involving the anterolateral, posterior, and apical parts of the heart.[318]

Spray-on cardiac nanotherapeutic: The spray-on application involves exposing the heart at 1-week post-MI via a fourth intercostal re-do thoracotomy, removing the pericardium over the infarcted akinetic area and applying the spray-on using our spray nozzle at a 1 cm distance from the heart's surface. Mice were randomly divided into 6 groups to receive one of the following treatments: PBS, AuNP, 4-Leg, Multi, 4-Leg AuNP or Multi-AuNP. All solutions were prepared fresh and stored on ice prior to their addition to the spray system. Surgical mortality was calculated as 3% and those animals were excluded from the study. The mice were monitored for up to 4 weeks post-treatment, and then sacrificed. Hearts were collected for further analysis.

Assessment of cardiac function: Cardiac function was evaluated by long axis echocardiography in B-mode using a Vevo3100 system (VisualSonics, Toronto, Canada) with a MX400 series real-time microvisualization scanhead probe. Measurements were taken at baseline (at 7 days post-MI before treatment), and at day 1 and day 28 (end-point) post-application. Cardiac function and ventricular remodeling were evaluated by determining left ventricular ejection fraction (LVEF), fractional area change (FAC), end systolic volume (ESV), and end diastolic volume (EDV). High

sensitivity electrocardiograms (ECG) were recorded using MLA1203 Needle electrodes (29-gauge, 12 mm) accessorized with MLAC29 and MLAC49 octal bio linking cables connected to a PowerLab OctalBio Amp (FE238) bio-amplifier for 12-lead ECG recording. Data processing was carried out using LabChart 8.1 data acquisition and analysis software. ECG data at 28 days after treatment was extracted for all the groups. Briefly, 20 beats were averaged using a LabChart 8.1 algorithm. Each point of the ECG was certified by 3 independent specialists. A representative ECG tracing of the Multi–AuNP is presented in supplementary **Figure S17**.

Inductively coupled plasma assay for systemic distribution of gold: The total gold concentration in the different tissues was determined using an inductively coupled plasma mass spectroscopy system (ICP-MS; Agilent 7700x). Organs were harvested from freshly euthanized mice (n=3 in each group), flash-frozen, powdered and subsequently freeze-dried for 96 hours. Samples were weighed and homogenized to produce a powder that was digested in a Digi-PREP MS System (SCP Science). Gold was detected using 197 m/z. Samples were processed using argon carrier gas: 0.85 ml min−1, argon plasma gas flow: 15 L min−1.

Strain analysis: Transthoracic echocardiography was performed on long-axis views using a Vevo3100 system in B mode with an MX400 series real-time microvisualization scanhead probe (VisualSonics). The imaging was performed at baseline before treatment injection (7 days post-MI) and at 4 weeks post-application to determine longitudinal endocardial strain at the time of aortic valve closure (representing end systole). Strain in Segment 6 (the anterior apex segment), corresponding to the infarct area targeted for treatment, was analyzed using the VevoStrain application of Vevo LAB 3.1.1 software (VisualSonics), as previously reported.129

Histology and immunohistochemistry: Hearts were harvested at 4 weeks post-treatment, embedded in OCT compound (Fisher Scientific), and snap frozen in liquid nitrogen. Sections (10

μm) were cut using a Thermo Scientific HM550 Cryostat. To evaluate scar size, tissue sections were fixed in 4% PFA for 1 h and stained with Masson's Trichrome stain (Electron Microscopy Sciences). Images were taken with a Celestron Handheld Digital Microscope Pro, and 4 sections per mouse were used to measure remote wall thickness and to determine scar size by the mid-line arc method using ImageJ2® software.[154] For immunohistochemistry, tissue sections were fixed in acetone for 20 min, washed with 0.05% Tween-20 in PBS, permeabilized with 0.1% Triton X-100 for 10 min and then blocked in 10% serum in PBS for 1 h at room temperature. Primary antibodies were applied overnight at 4°C in 10% serum, and then slides were rinsed and treated with secondary antibodies for 1 h in the dark at room temperature. Nuclei were stained with DAPI (1:1000) before being mounted with ProLongTM® Gold antifade reagent (Invitrogen). To detect inflammation, M1 macrophages were detected with an anti-CD86 primary antibody (Abcam, Rat, Cat#119857 at 1:200 dilution) and visualized by AF488 anti-rat secondary (Invitrogen, Cat#A-11007 at 1:600 dilution). M2 macrophages were detected by an AF488-conjugated anti-CD206 antibody (BioLegend, Cat#141710 at 1:100 dilution). Fluorescent images were obtained using a Zeiss Axio Observer upright microscope with a ×20 objective. For the detection of blood vessels and myofibroblasts, anti-CD31 (also known as PECAM-1, Santa Cruz, Rat, Cat#sc-101454 at 1:100 dilution) and anti-α-smooth muscle actin (α-SMA; Abcam, Rabbit, Cat#ab5694 at 1:250 dilution) primary antibodies were used and detected with AF594 anti-rat secondary (ThermoFisher, Cat#A-11007 at 1:1000 dilution) and AF488 anti-rabbit secondary (ThermoFisher, Cat#A-11008 at 1:1000 dilution), respectively. For cardiac troponin T staining, sections were incubated with rabbit cardiac troponin T primary antibody (Abcam ab209813, 1:400) and detected by anti-rabbit AF594 secondary antibody (Abcam, Cat#ab150080 at 1:700 dilution). Finally, for connexin 43 staining, sections were incubated with rabbit connexin

43/GJA1 (Abcam Cat#ab11370, 1:400) antibody followed by detection with AF488 anti-rabbit (Life Technologies Cat#A11007, 1:500). For all samples, 3 sections per mouse were analyzed and for each section 3 images within the infarct region were used for quantification.

5.5 Supporting Information

Supporting Information of this article is available in Chapter 8 – Appendices section 8.2 at the end of this thesis.

5.6 Acknowledgements

The authors would like to thank Mr. Rick Seymour for his help with animal surgeries and Mayte Gonzalez for her help designing the Figures in the article with BioRender app.

6 General Discussion

While the data for each study were discussed within their respective chapters, this general discussion is meant to summarize and compare the work in a broader context, address limitations, as well as to discuss potential future related studies.

In this thesis, three new biomaterial systems for oxidative stress elimination and cardiac infarct repair were developed and tested in a clinically relevant mouse model of myocardial infarction. The overall aim was to determine their therapeutic efficacy, understand their mechanism of action and address some of the challenges in order to facilitate clinical translation. We developed and presented a different biomaterial system in each chapter focusing on three unique objectives:

1) To develop an injectable antioxidant (fisetin) and hydrogel system for minimizing the effects of MG and promoting cardiac repair post-MI.

2) To synthesize a nanoparticle system for targeted delivery of therapeutics to cardiac tissue following MI *in vivo*. We encapsulated the Glo1 enzyme within hyaluronic acid-based nanoparticles for reducing the accumulation of MG, limiting adverse remodeling and preserving cardiac function post-MI; and

3) To design a sprayable nano-therapeutic that uses surface engineered custom-designed multi-armed peptide grafted nanogold for on-the-spot coating of the infarcted myocardial surface for increasing contractility of the myocardium post-MI.

The unique properties of each biomaterial presented in this thesis work can be found summarized in Table 2 below.

Table 2 Summary table comparing the biomaterial systems that were developed in this dissertation

Article ID	Biomaterial Type	Delivery Method	Cargo or Active Ingredient	Target Effect
Article I (Fisetin)	Natural biomaterial (hydrogel)	Intramyocardial Injection (echo guided)	Fisetin (antioxidant)	Reducing MG levels and oxidative stress post-MI
Article II (NPs)	Natural biomaterial (nanoparticle)	Intravenous Injection (Tail-vein)	Glo1 (MG metabolizing enzyme)	Targeting CD44, reducing MG-related oxidative stress
Article III (Spray-on)	Hybrid biomaterial (Gold conjugated peptide)	Direct spray onto heart (3D patch)	AuNP (electrically conductive)	Increasing electroconductivity, providing tissue integrity

The fisetin-hydrogel biomaterial system presented in Article I was crosslinked using EDC/NHS chemistry and intramyocardially injected into the heart 3 hours post-MI. Hydrogel materials used in cardiac tissue engineering have been tested as stand-alone therapies and demonstrated promising results.[319,320] Our results showed that the fisetin-hydrogel system was superior to hydrogel alone since the antioxidant fisetin not only just scavenged excess MG but also activated the Glo1 pathway, leading to a decrease in MG levels. A few studies have shown that MG levels are elevated in cardiac disease patients compared to healthy subjects, and have attempted to elucidate how MG-AGEs and oxidative stress may contribute to cardiovascular dysfunction.[50,51,321] Our results fill a mechanistic information gap in the literature regarding the effects of MG and oxidative stress regulation post-MI. Future pre-clinical studies can be designed to test if the fisetin-hydrogel system can improve cardiac function in more mature scar and/or advanced heart failure models, such as 1-5 weeks post-MI. Additionally, larger animal model studies (such as pig models), and testing the delivery of the hydrogel using catheter technology will be needed to further advance this therapy for use in the clinic.

Transgenic Glo1 overexpression has been shown to decrease oxidative damage while restoring cardiac function, which was also associated with enhanced production of pro-healing factors.[62,322] Thus, we developed a new biomaterial system, described in Article II, which utilized NPs to deliver Glo1 to the heart. These NPs were self-assembled by tetrazole-alkene click chemistry[164,167,177] and the Glo1 enzyme was encapsulated during the self-assembly step, giving them excellent stability. Another important feature of Glo1-NPs was their natural fluorescence, allowing them to be visualized under the microscope. We tracked Glo1-NPs *ex vivo* and monitored their localization. When delivered intravenously in mice at 3 hours post-MI, the Glo1-NPs specifically targeted damaged cardiac tissue via HA-CD44 specific interaction,

protected cell viability and limited infarct expansion by reducing the oxidative stress, leading to improved cardiac function.

Our findings demonstrate the potential of NP-based targeted delivery of Glo1 as a new approach for treating MI with promising implications for clinical translation due to its ease of application. One limitation to be considered for this study is that Glo1-NP localization was measured *ex vivo* by IVIS. *In vivo* imaging or histology staining would provide more accurate localization data for the NPs. Another potential limitation of this study is that Glo1-NP retention/distribution was not quantified for each vital organ such as liver, kidney, spleen and lungs. Although Glo1-NPs have been found to be non-toxic, their body distribution would give valuable information on how efficiently any administered NP dose is reaching the target tissue. Future studies can explore CD44 expression and NP uptake in particular cell types and tissues, since CD44 expression has been shown in cardiac fibroblasts and circulating leukocytes, in addition to ECs post-MI.[181,182] As NPs were delivered via the circulation, we expect enriched NP uptake in $CD44^+$ ECs of the myocardial vasculature post-MI, as well as uptake by leukocytes. We don't expect that Glo1-NP therapy success requires exclusive EC targeting, and the results we presented provide strong evidence of the benefits associated with our CD44 targeting Glo1-NP therapy for post-MI remodeling.

In Article III, the focus moved away from therapeutics targeted at MG and oxidative stress, and instead looked into designing a biomaterial to improve electroconductivity of the heart post-MI. The loss of blood circulation to regions of the heart muscle due to coronary artery occlusion can damage the myocardium, causing electrophysiological and morphological disorders.[323,324] Thus, electroconductivity is an important property for healthy myocardial function that was not directly addressed with the 2 other therapies reported herein.

We designed and developed a spray-on device and AuNP-peptide system that can increase electroconductivity post-MI when delivered via spraying directly onto the surface of the infarcted tissue. This biomaterial system acts as a 3D patch system, adheres to the surface of the heart and stays at the target location with a high retention rate. Our results showed that the AuNP-peptide system increases electrical conductivity, increases left ventricular ejection fraction and improves cardiac ECG post-MI. One limitation of this system is that the procedure currently requires an open-chest surgical procedure. By developing more advanced application devices and approaches, our treatment could be delivered with less invasive techniques (e.g. catheter technology). Another limitation that can be noted for all 3 articles is the use of female mice only. We have performed our proof-of-principal experiments for all three projects using females as they exhibit less fighting, chasing and mounting behaviors and they have a higher survival rate than males after MI.[325,326] As the evidence demonstrates that our biomaterials are safe and they work effectively, future experiments should include a comparison between male and female mice.

AuNPs constitute the electroconductive component of our biomaterial system[173] and it seems likely that the infarct region was also mechanically stabilized with the patch application, causing an acute functional improvement. The incorporation of electrically conductive nano-biomaterials into biocompatible and biodegradable peptide systems not only improves the electrical or electrochemical properties, it can also modify the mechanical properties of hydrogels and introduce topographical cues that resemble the native ECM.[327] This could be a contributing factor for the improved contractility and ECG signals we observed in this study. Lin et al. also showed that hydrogel patches increase the mechanical integrity of the left ventricle and restore cardiac function.[328] Future studies could involve the use of RNA sequencing at various

time-points post-treatment to elucidate mechanisms underlying the benefits conferred by the treatment.

Another potential application of our electroconductive biomaterials could be in 3D bioprinting. The electrically conductive nano-biomaterials may be an excellent candidate for use as a bioink, allowing researchers to build a contractile vascularized myocardium or full-size human heart through advanced 3D bioprinting techniques. Moreover, this research could be translated for use in heart-on-a-chip models to study the interaction of different cell types with the scaffold, to develop and test new drugs, or to assess the cardiotoxicity of anticancer drugs.[327]

The papers presented in this dissertation demonstrate three different biomaterial systems designed for specific regenerative medicine applications: biomaterial therapy, protein/cargo delivery, and tissue bonding. Although all the described hydrogels are based on different chemical arrangements, the biomaterial designs were developed with consideration for each intended application and potential for clinical translation. Hopefully, the work conducted in this thesis will rationalize the design of therapies that could target MG-AGE accumulation post-MI, resulting in more advantageous resolution of MI repair processes for cardiac patients.

7 Conclusions

Overall, the results presented in this thesis have established that:

Paper I – The combination of the antioxidant fisetin with a collagen HG acted synergistically to decrease MG-related oxidative stress by increasing the activity of Nrf2, GSH and Glo1. Our system reduces inflammation, increases cell survival, limits adverse cardiac remodeling and improves cardiac function when administered during the inflammatory phase post-MI.

Paper II – Our Glo1-loaded CD44-interacting NP system can target the infarcted myocardium when delivered intravenously. Glo1-NP treatment decreased MG-related oxidative stress, reduced inflammation, inhibited apoptotic activity and improved cardiac function and contractility post-MI, representing a promising nanoplatform for targeted, trackable, safe and efficient intracellular delivery of cardiovascular therapeutics for treating and improving the health of patients with MI.

Paper III – The combined peptide and gold NP spray-on application showed an excellent retention rate, increased muscle contractility and myocardial electrical conductivity and improved cardiac function when delivered to a mature scar at a clinically relevant time-point post-MI.

Taken together, the results suggest that targeting MG and/or improving electroconductivity of the infarct area may be promising approaches to limit adverse cardiac remodeling, prevent damage and preserve the function of the infarcted heart. These findings may help guide the development of new strategies for treating MI patients and reducing the incidence of heart failure.

8 Appendices

Supplementary information of the articles presented in this thesis can be found in this section.

8.1 Supplementary Information for Article I

For Advanced Functional Materials, DOI: 10.1002/adfm.202108630 Combined Methylglyoxal Scavenger and Collagen Hydrogel Therapy Prevents Adverse Remodeling and Improves Cardiac Function Post-Myocardial Infarction

Cagla Eren Cimenci*, Nick J. R. Blackburn, Veronika Sedlakova, Justina Pupkaite, Marcelo Munoz, Benjamin H. Rotstein, David A. Spiegel, Emilio I. Alarcon, and Erik J. Suuronen**

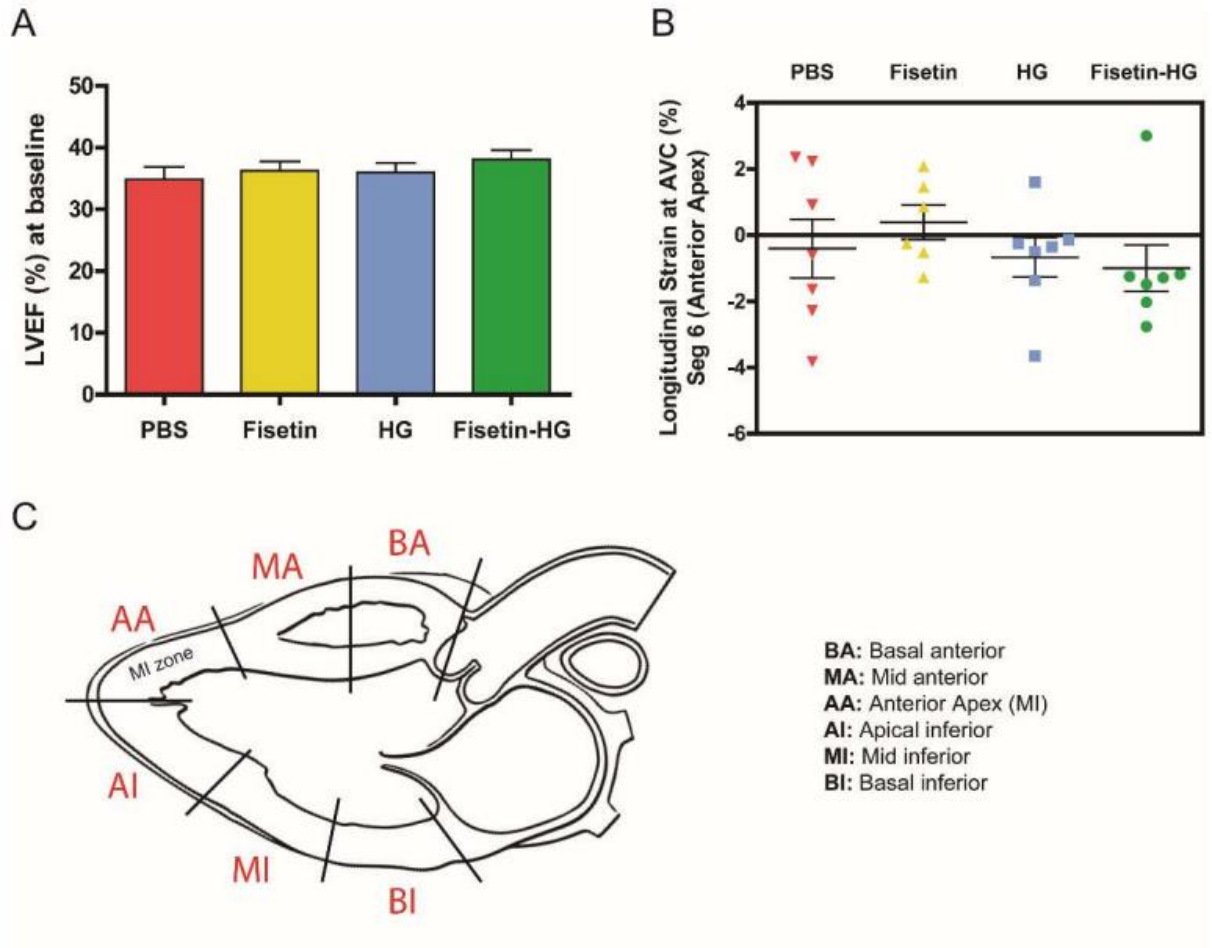

SI Figure S 1 (A) Echocardiography results (% left ventricular ejection fraction (LVEF)) shows no statistical difference between treatment groups at baseline (n=13-16). (B) Longitudinal endocardial strain at aortic valve closure (%) calculated from the anterior apex region (injection site) showing that the contractile function of the hearts was comparable at baseline (n=7). Error bars represent mean ± SEM. (C) Figure showing the different longitudinal LV strain analysis segments of the heart: BA, basal anterior; MA, mid anterior; AA, anterior apex; AI, apical inferior; MI, mid inferior; BI, basal inferior.

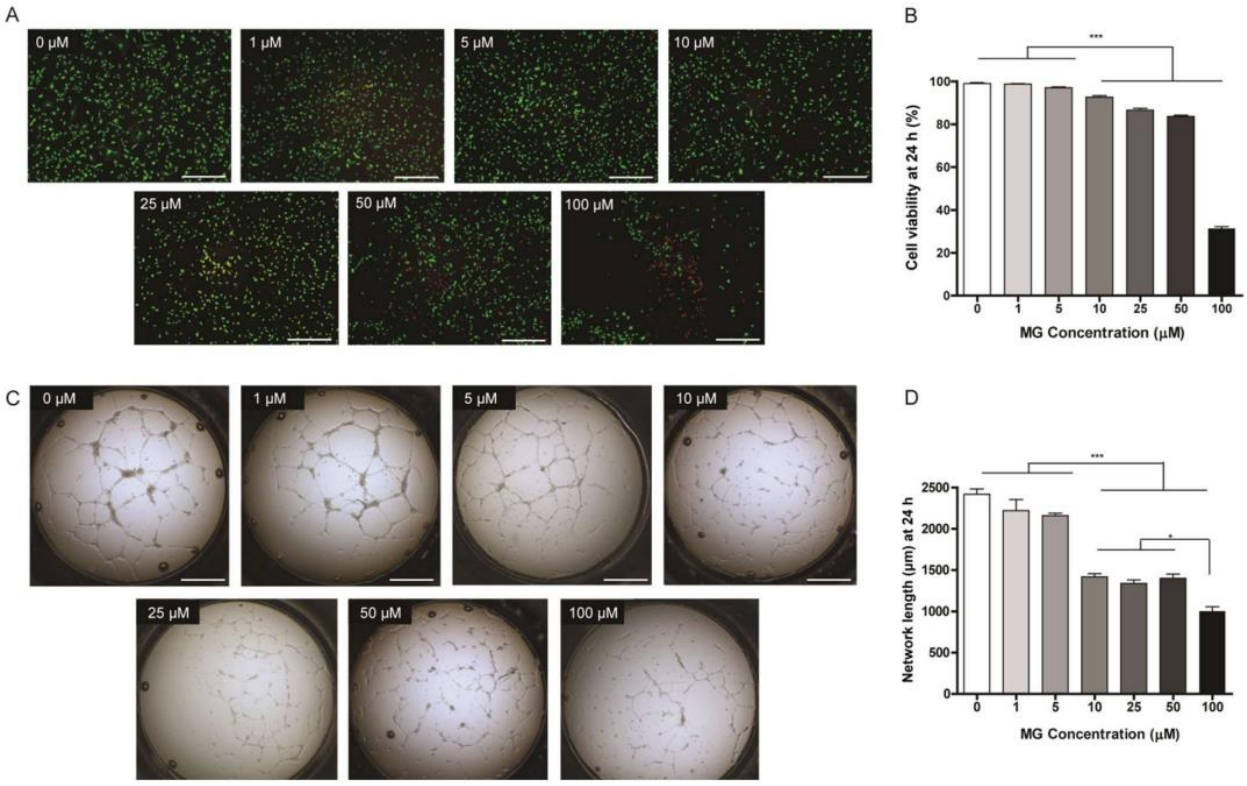

SI Figure S 2 (A) Representative images of a live/dead viability assay for HUVECs treated with different concentrations of MG. Scale bar = 200µm. (B) Quantification of viability data presented as the percentage of viable cells at 24 hours after treatment (n=3). (C) Representative images of an *in vitro* angiogenesis assay performed with HUVECs treated with different concentrations of MG. Scale bar = 1 mm. (D) Total network length calculated for the *in vitro* angiogenesis assay images (n=3). (*p<0.05)**

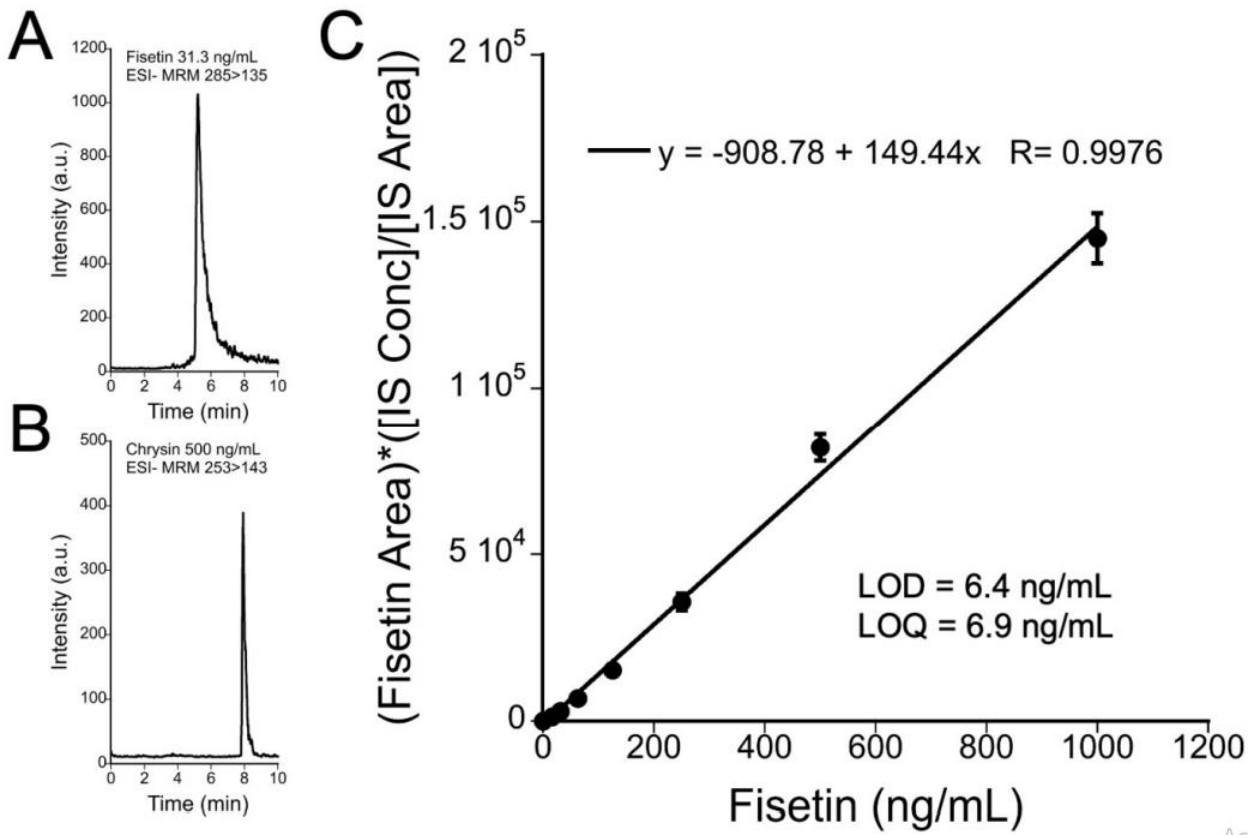

SI Figure S 3 Quantification analysis of fisetin using RP-UPLC-MSMS Waters Acquity UPLC Xevo TQD. (A) Representative multiple reaction monitoring analysis data of fisetin. (B) Representative multiple reaction monitoring data analysis of chrysin. (C) The calibration curve obtained by triplicate analysis of several calibration concentrations of fisetin up to 1000 ng/mL. Chrysin was used as internal standard (IS) at a concentration of 500 ng/mL. (Fisetin Area)*([IS Concentration]/[IS Area]) vs. concentration of fisetin was plotted. The calculated limit of detection (LOD) was 6.4 ng/mL and the limit of quantification (LOQ) was 6.9 ng/mL

8.2 Supplementary Information for Article III

For ACS Nano, Nanoengineered Sprayable Therapy for Treating Myocardial Infarction,

*Marcelo Muñoz[1†], **Cagla Eren Cimenci**[1,2†], Keshav Goel[1], Maxime Comtois-Bona[1], Mahir Hossain[1], Christopher D. McTiernan[1], Matias Zuñiga-Bustos[3], Alex Ross[1], Brenda Truong[1], Darryl R. Davis[4,5], Wenbin Liang[4,5], Benjamin Rotstein[6,7], Marc Ruel[1,2], Horacio Poblete[3,8], Erik J. Suuronen[1,2*] & Emilio I. Alarcon[1,7*]*

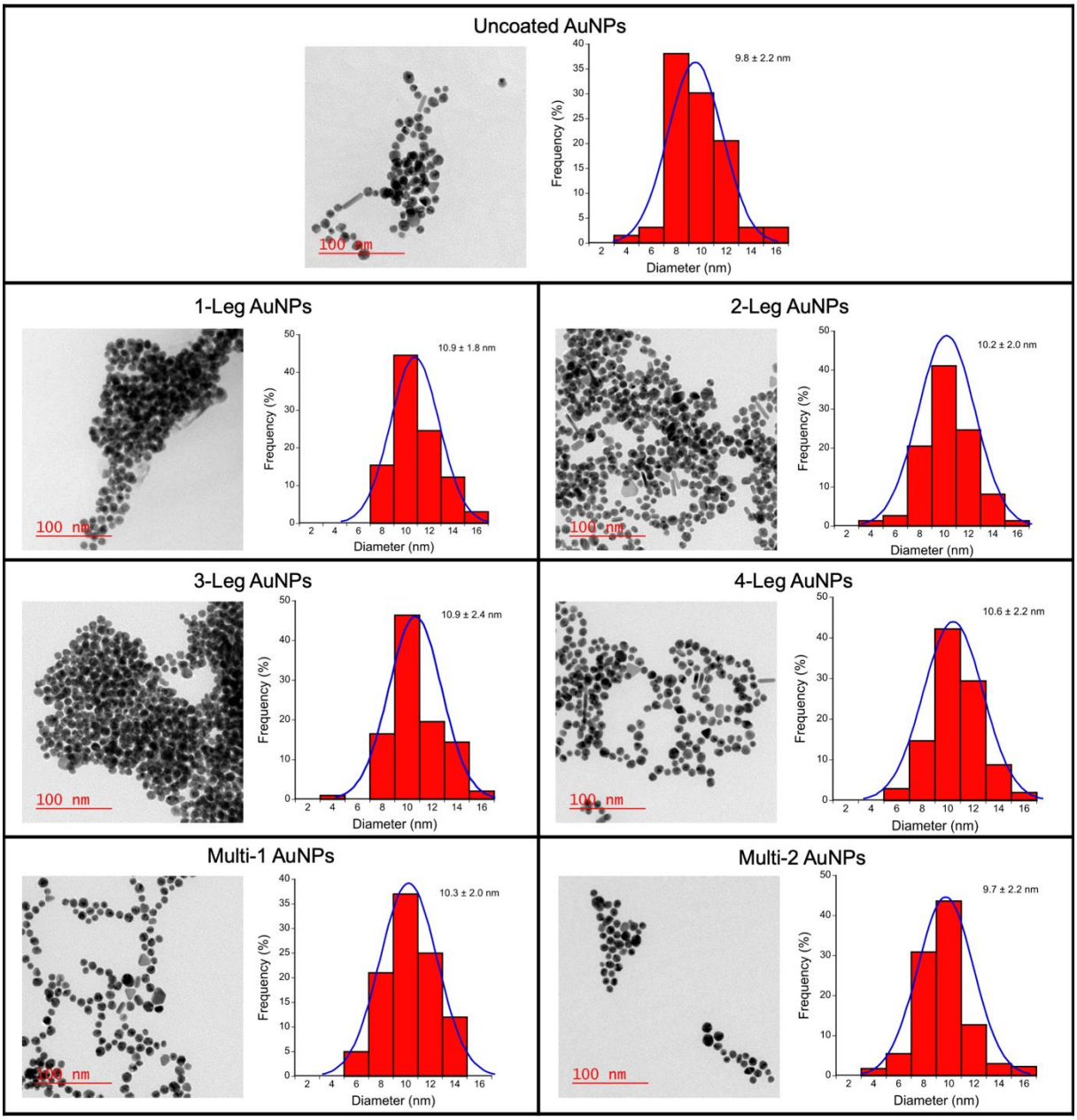

SI Figure S 4 Transmission Electron Microscopy (TEM) of the AuNP uncoated and in the presence of the different coating peptides. Values calculated from measuring 100 individual nanoparticles from different areas in the grid.

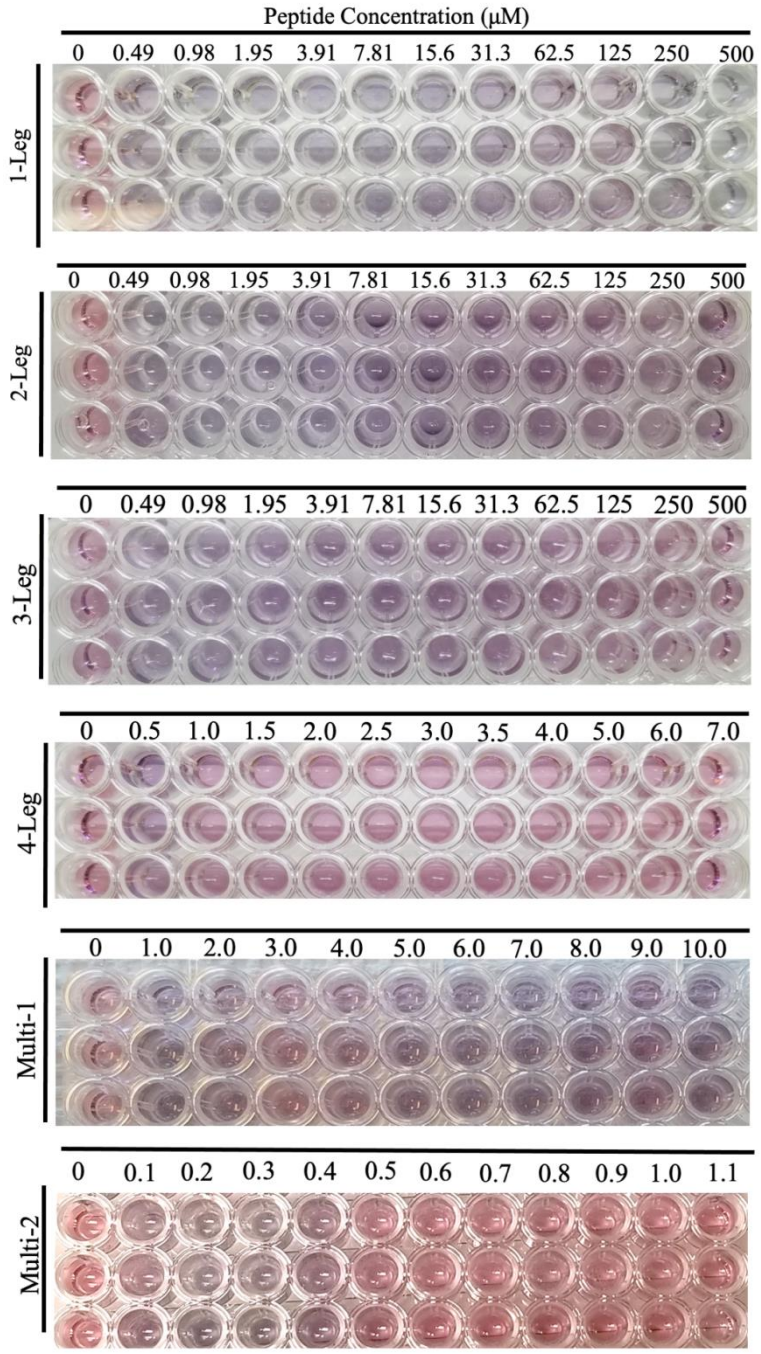

SI Figure S 5 Representative images for colloidal nanogold in 96 well-plates in the presence of different concentrations of peptides (μM as indicated in each image). Nanogold characteristic red colour turns violet or black upon aggregation.

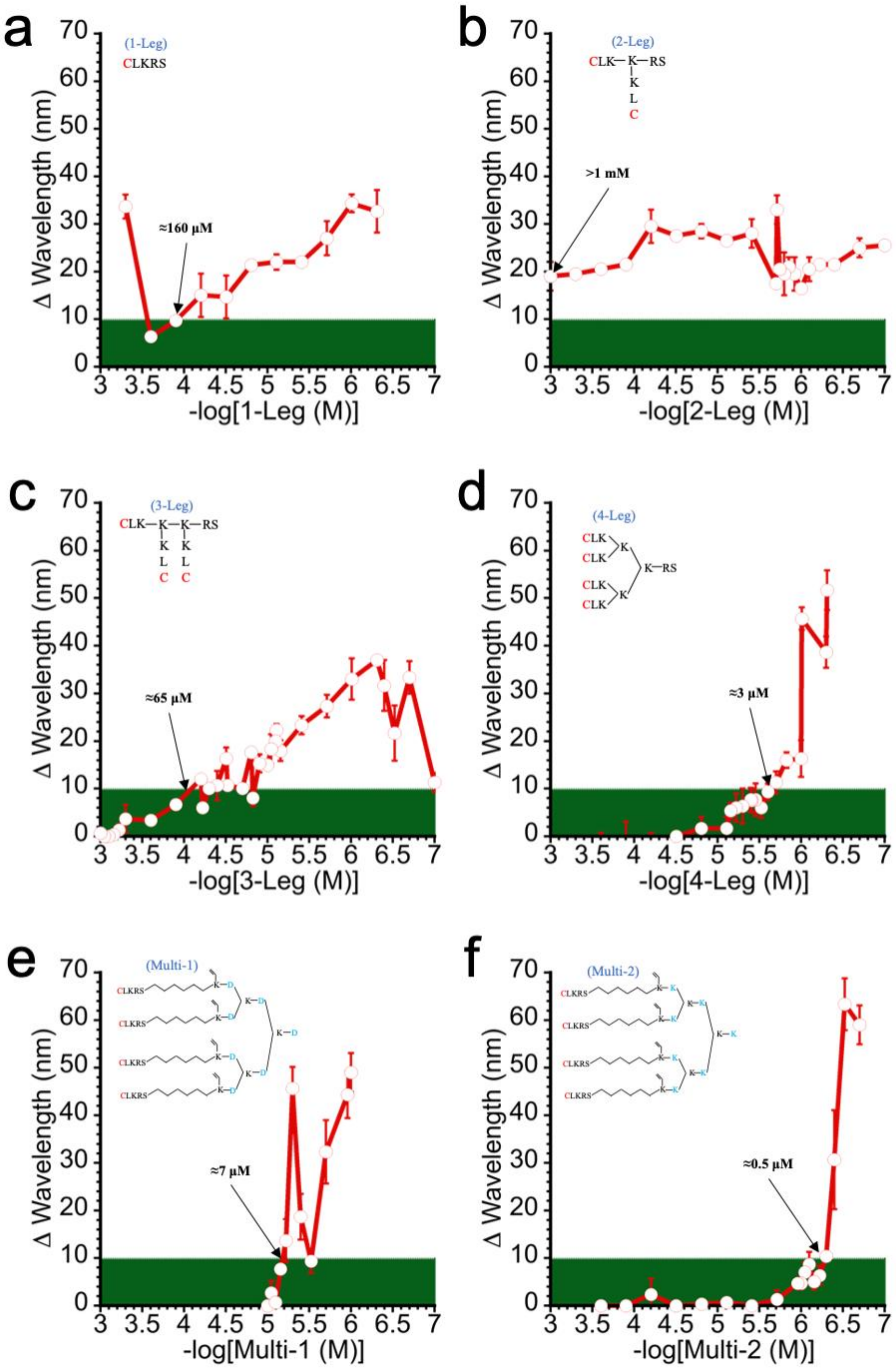

SI Figure S 6 Stability plots for nanogold as a function of the peptide concentration (in logarithmic scale). A change in $\Delta\lambda$ > 10.0 (green area) indicates no stable nanoparticles.

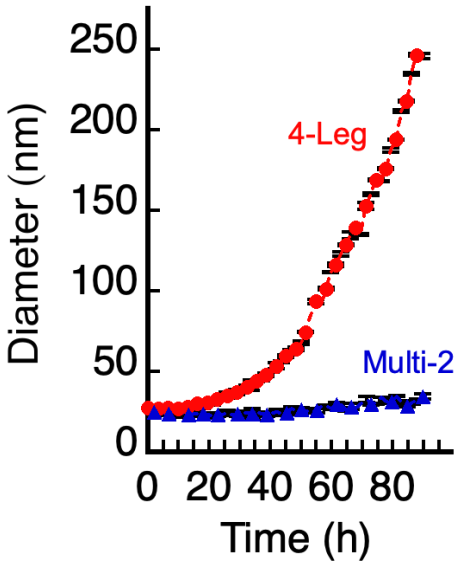

SI Figure S 7 Nanogold hydrodynamic diameter after incubation at 37ºC with 3μM of 4-Leg peptide and 0.5 μM of Multi-2. Diameters measured at different time points post incubation (n=6).

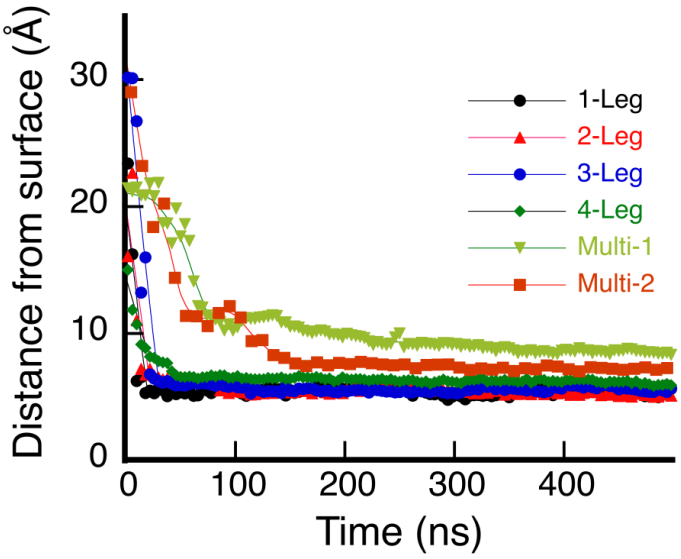

SI Figure S 8 Average distance between the nanogold surface and the center of mass for the peptides tested in this study. Plots were produced from molecular dynamic simulations for up to 500 ns from the initial peptide-nanogold surface interaction.

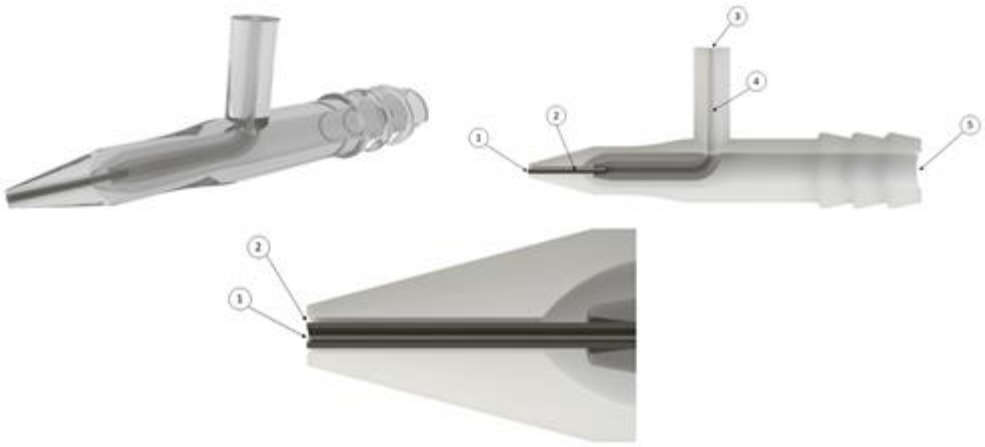

SI Figure S 9 (Top left) Orthogonal View of the nozzle. (Top right) Section view of the nozzle. Output of the nozzle (1), stainless-steel connector to the liquid chamber (2), air inlet for the liquid port (3), liquid reservoir (4), atomizing air inlet (5). (Bottom) Tip of the spray nozzle. Low velocity liquid outlet of the nozzle (1), High velocity atomizing air outlet of the nozzle (2).

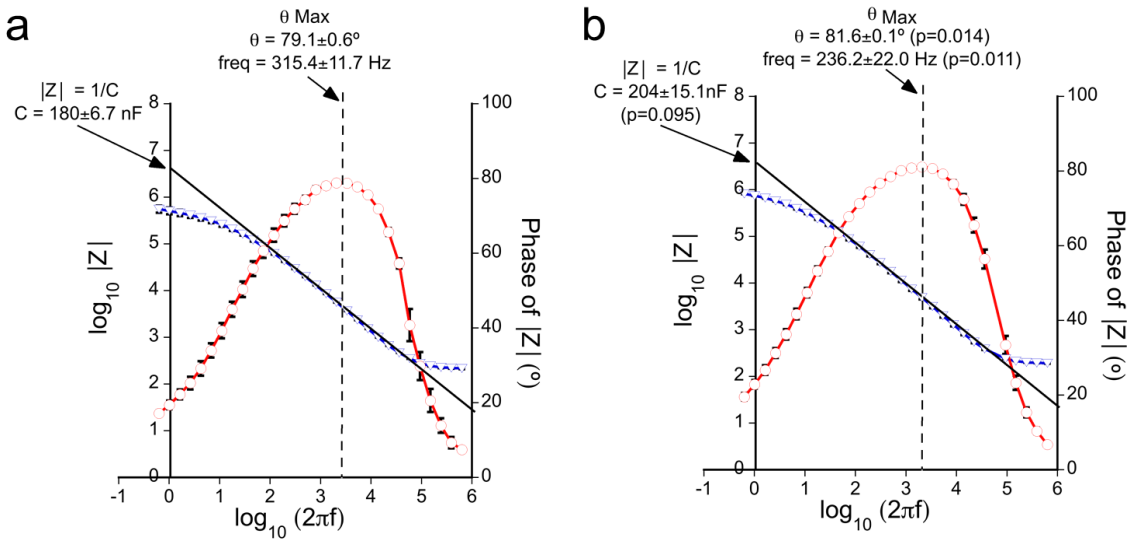

SI Figure S 10 Impedance spectra of a 10% collagen disk (diameter = 6 mm and thickness = 1 mm). (A) The collagen disk was swelled overnight with Milli-Q water overnight at 4ºC and blotted before measurements in a Potentiostat Parstat 2273 (Princeton Applied Research - see methodology). (B) Same as condition (A) including and embedded amount of 150 ng of Multi-2–AuNP per gram of material. Values = mean ± SD. n = 3. Statistical analysis performed with t-test between groups.

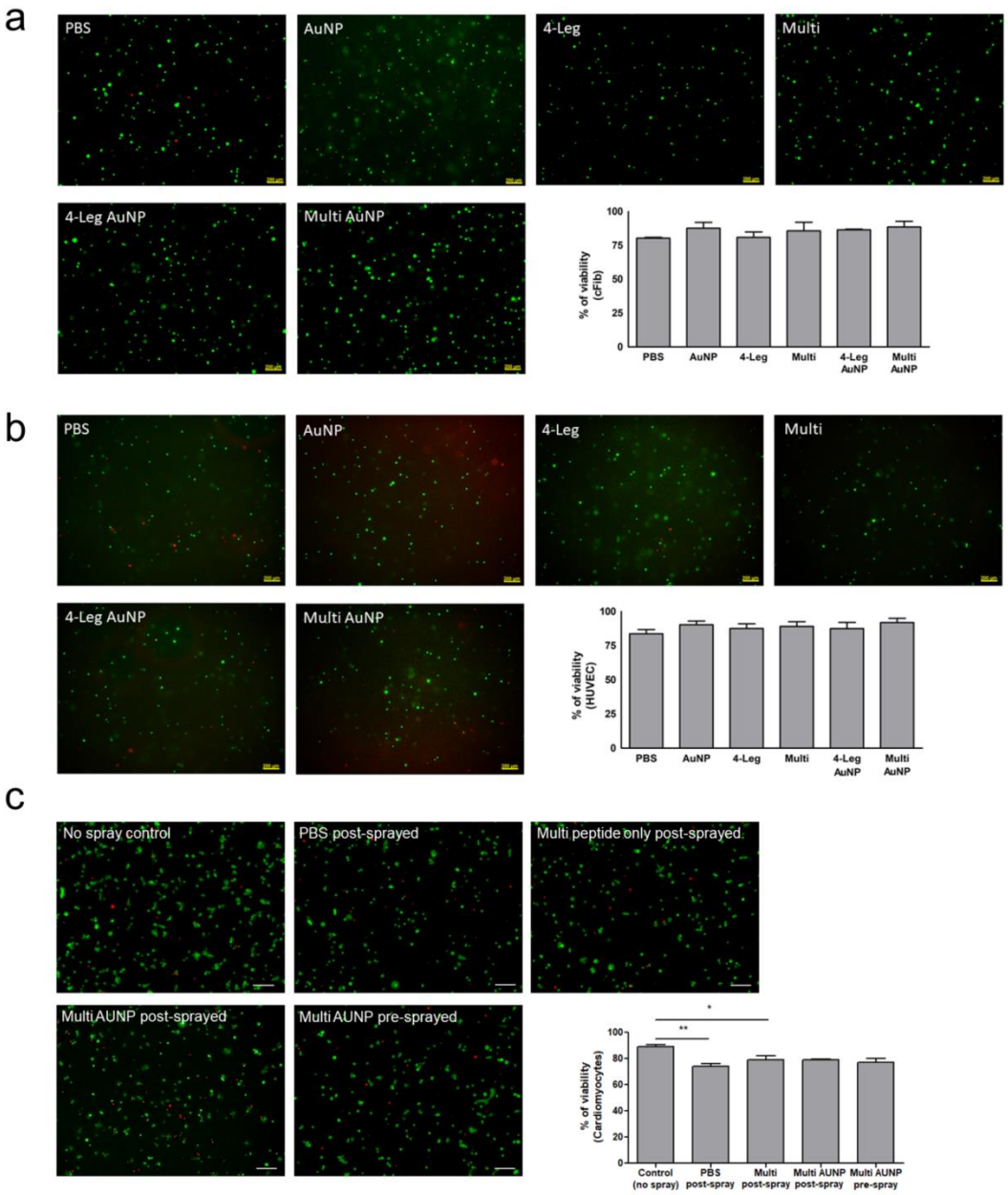

SI Figure S 11 Spray-on treatments were not found to be toxic for the cells. (A) Representative live/dead images and viability quantification data of cardiac fibroblasts sprayed with a treatment of PBS, AuNP, 4-Leg, Multi, 4-Leg AuNP or Multi AuNP. (B) Representative live/dead images and viability quantification data of HUVECs sprayed with a treatment of PBS, AuNP, 4-Leg, Multi, 4-Leg AuNP or Multi AuNP. (C) Representative live/dead images and viability quantification data of cardiomyocytes pre- or post-sprayed with PBS, Multi and Multi AUNP. Cell viability is comparable between the different treatment groups. Scale bar = 100µm. Values are represented as Mean ± SD.

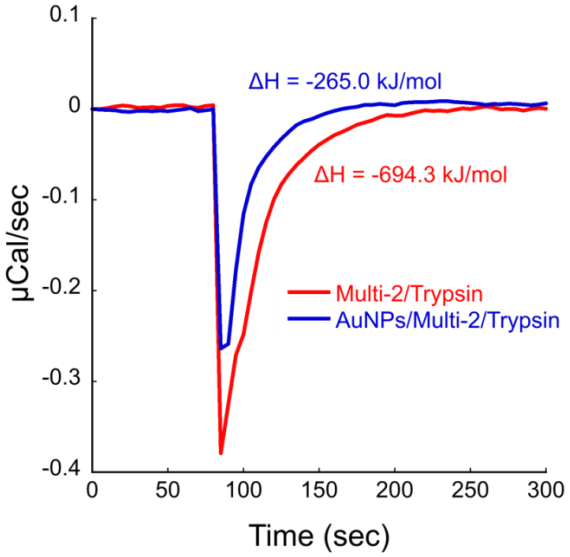

SI Figure S 12 Isothermal Titration Calorimetry (ITC) curves for the Multi-2 (0.5 μM) without and with a hydrolytic enzyme (Trypsin 1 nM). Changes in heat were measured with and without the AuNPs (37ºC).

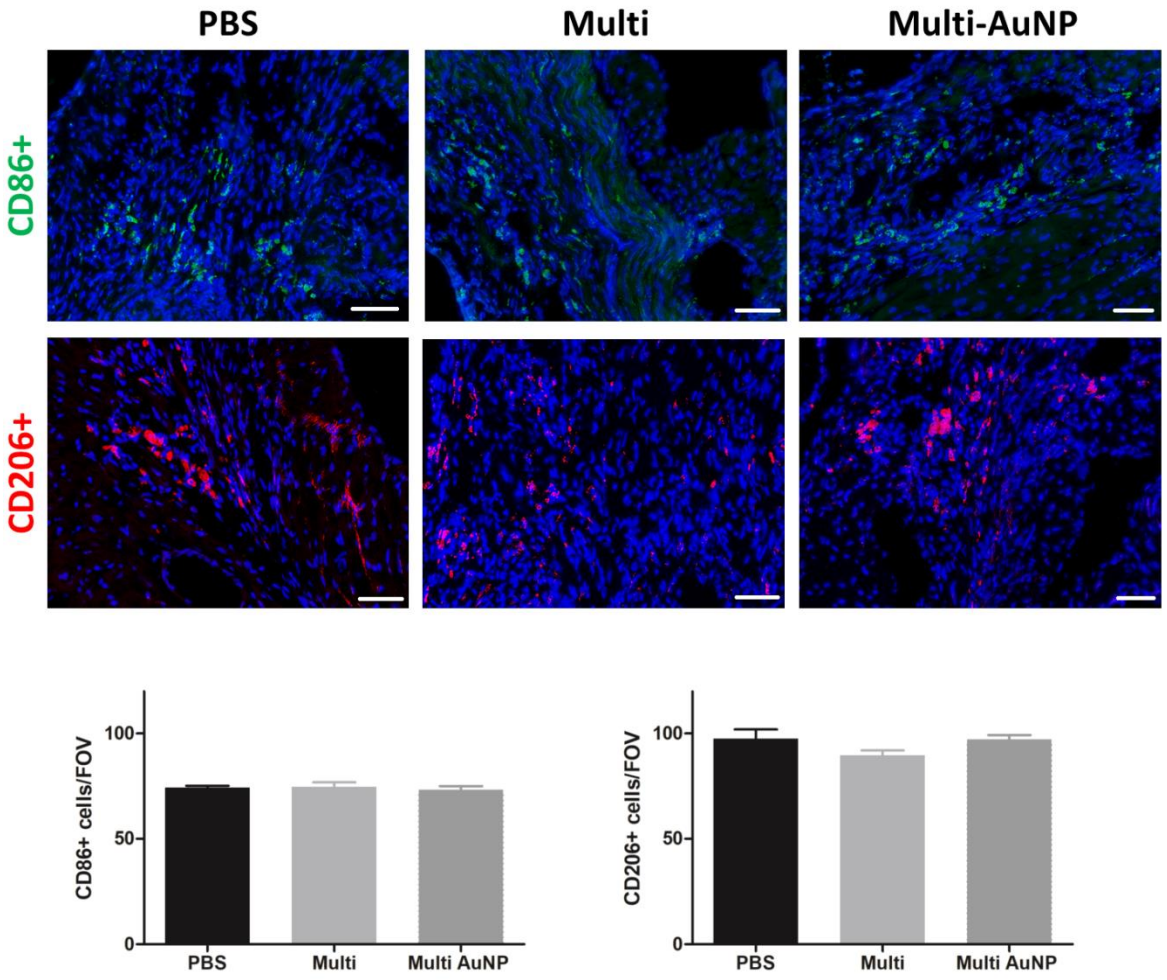

SI Figure S 13 Representative images of macrophage density in MI hearts after PBS, Multi and Multi-AuNP treatments. Representative images of CD86+ (green) and CD206+ (red) immunostained tissue sections collected 2 days after spray-on treatment showed no difference in early inflammation. Scale bar = 100 μm.

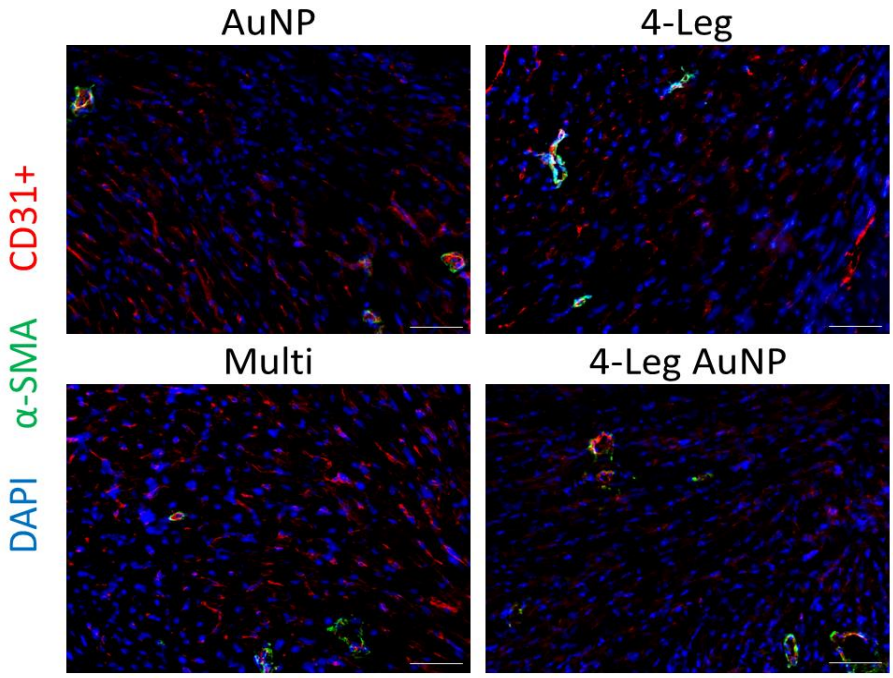

SI Figure S 14 Representative images of vascular density in the infarcted heart after AuNP, 4-Leg, Multi or 4-Leg AuNP treatment. Representative images of α-SMA and CD31 immunostained tissue sections collected 28 days after spray-on treatment with AuNP, 4-Leg, Multi and 4-Leg AuNP. Scale bar = 100 µm.

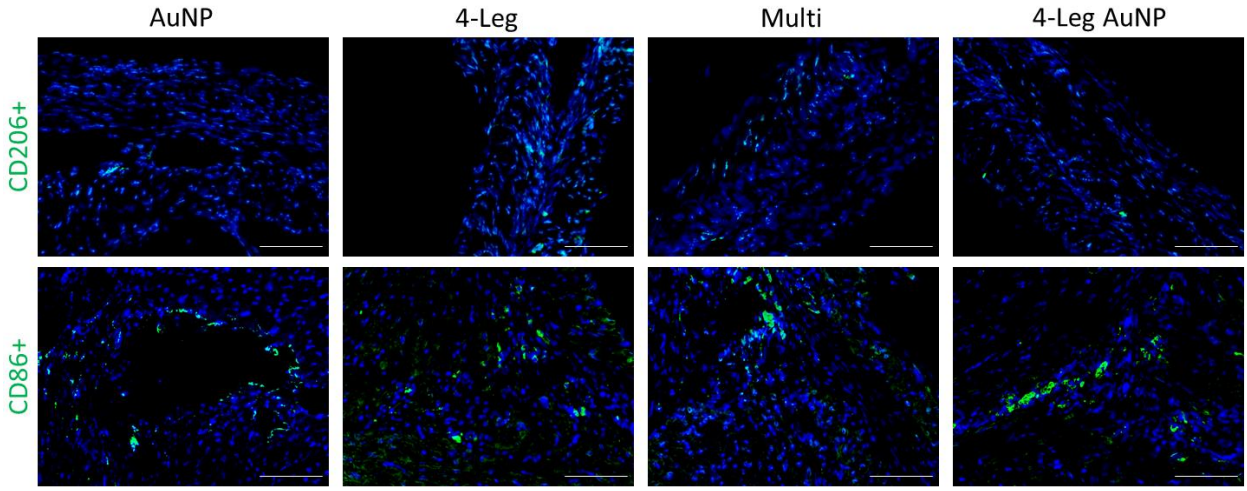

SI Figure S 15 Representative images of macrophage density in MI hearts after AuNP, 4-Leg, Multi and 4-Leg AuNP treatments. Representative images of CD206+ and CD86+ immunostained tissue sections collected 28 days after spray-on treatment. Scale bar = 100 µm.

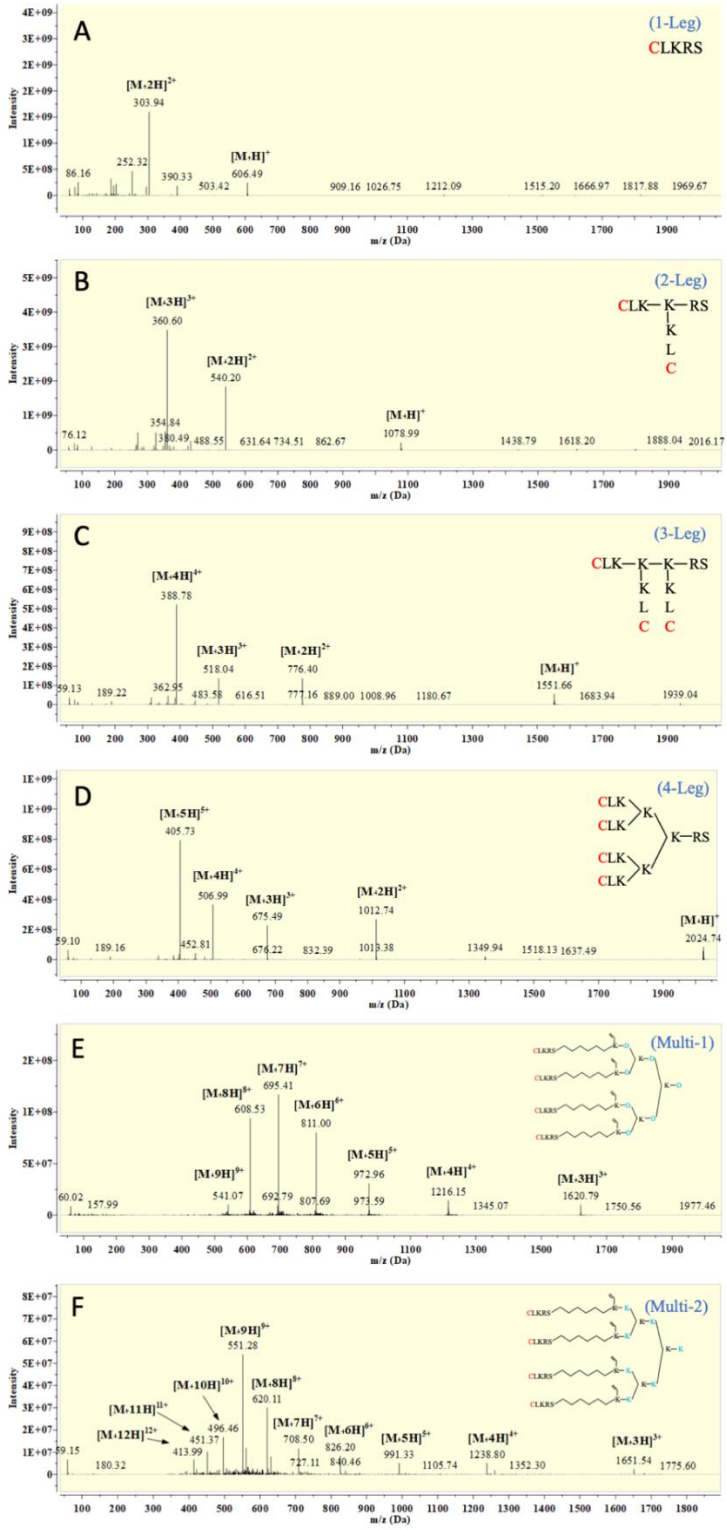

SI Figure S 16 Representative mass spectra with molecular ions description for the peptides prepared in this article. The insets in each plot show the simplified structure of the peptides

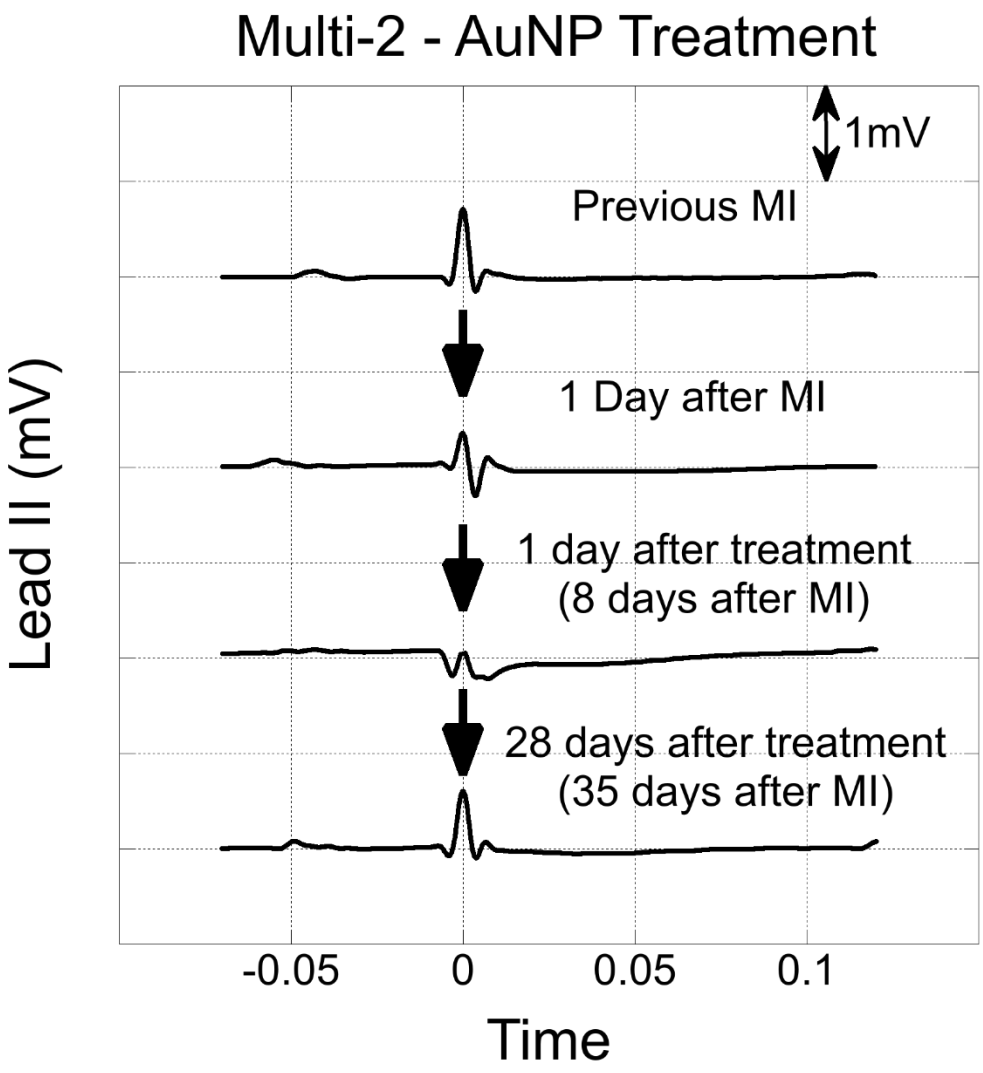

SI Figure S 17 Representative ECG Lead II tracings for animals treated with Multi-2–AuNP from before myocardial infarction (MI), 1 day after MI, 1 day after treatment (8 days after MI), and 28 days after treatment (35 days after MI).

References

(1) Biglu, M.-H.; Ghavami, M.; Biglu, S. Cardiovascular Diseases in the Mirror of Science. *J. Cardiovasc. Thorac. Res.* **2016**, *8* (4), 158–163. https://doi.org/10.15171/jcvtr.2016.32.

(2) Organization, W. H. The Top 10 Causes of Death.

(3) Saleh, M.; Ambrose, J. A. Understanding Myocardial Infarction. *F1000Research* **2018**, *7*. https://doi.org/10.12688/f1000research.15096.1.

(4) Fomovsky, G. M.; Holmes, J. W. Evolution of Scar Structure, Mechanics, and Ventricular Function after Myocardial Infarction in the Rat. *Am. J. Physiol. Heart Circ. Physiol.* **2010**, *298* (1), H221-8. https://doi.org/10.1152/ajpheart.00495.2009.

(5) Kanashiro-Takeuchi, R. M.; Szalontay, L.; Schally, A. V; Takeuchi, L. M.; Popovics, P.; Jaszberenyi, M.; Vidaurre, I.; Zarandi, M.; Cai, R.-Z.; Block, N. L.; Hare, J. M.; Rick, F. G. New Therapeutic Approach to Heart Failure Due to Myocardial Infarction Based on Targeting Growth Hormone-Releasing Hormone Receptor. *Oncotarget* **2015**, *6* (12), 9728–9739. https://doi.org/10.18632/oncotarget.3303.

(6) Fisher, S. A.; Brunskill, S. J.; Doree, C.; Mathur, A.; Taggart, D. P.; Martin-Rendon, E. Stem Cell Therapy for Chronic Ischaemic Heart Disease and Congestive Heart Failure. *Cochrane database Syst. Rev.* **2014**, No. 4, CD007888. https://doi.org/10.1002/14651858.CD007888.pub2.

(7) St. John Sutton, M. G.; Sharpe, N. Left Ventricular Remodeling After Myocardial Infarction. *Circulation* **2000**, *101* (25), 2981–2988. https://doi.org/10.1161/01.CIR.101.25.2981.

(8) Nabel, E. G.; Braunwald, E. A Tale of Coronary Artery Disease and Myocardial Infarction. *N. Engl. J. Med.* **2012**, *366* (1), 54–63. https://doi.org/10.1056/NEJMra1112570.

(9) Mozaffarian, D.; Benjamin, E. J.; Go, A. S.; Arnett, D. K.; Blaha, M. J.; Cushman, M.; de Ferranti, S.; Despres, J. P.; Fullerton, H. J.; Howard, V. J.; Huffman, M. D.; Judd, S. E.; Kissela, B. M.; Lackland, D. T.; Lichtman, J. H.; Lisabeth, L. D.; Liu, S.; Mackey, R. H.; Matchar, D. B.; McGuire, D. K.; Mohler E. R., 3rd; Moy, C. S.; Muntner, P.; Mussolino, M. E.; Nasir, K.; Neumar, R. W.; Nichol, G.; Palaniappan, L.; Pandey, D. K.; Reeves, M. J.; Rodriguez, C. J.; Sorlie, P. D.; Stein, J.; Towfighi, A.; Turan, T. N.; Virani, S. S.; Willey, J. Z.; Woo, D.; Yeh, R. W.; Turner, M. B.; American Heart Association Statistics, C.; Stroke Statistics, S. Heart Disease and Stroke Statistics--2015 Update: A Report from the American Heart Association. *Circulation* **2015**, *131* (4), e29-322. https://doi.org/10.1161/CIR.0000000000000152.

(10) Pryds, K.; Bøttcher, M.; Sloth, A. D.; Munk, K.; Rahbek Schmidt, M.; Bøtker, H. E. Influence of Preinfarction Angina and Coronary Collateral Blood Flow on the Efficacy of Remote Ischaemic Conditioning in Patients with ST Segment Elevation Myocardial Infarction: Post Hoc Subgroup Analysis of a Randomised Controlled Trial. *BMJ Open* **2016**, *6* (11), e013314. https://doi.org/10.1136/bmjopen-2016-013314.

(11) Wickline, S. A.; Verdonk, E. D.; Wong, A. K.; Shepard, R. K.; Miller, J. G. Structural Remodeling of Human Myocardial Tissue after Infarction. Quantification with Ultrasonic Backscatter. *Circulation* **1992**, *85* (1), 259–268. https://doi.org/10.1161/01.CIR.85.1.259.

(12) Frangogiannis, N. G. The Mechanistic Basis of Infarct Healing. *Antioxid. Redox Signal.* **2006**, *8* (11–12), 1907–1939. https://doi.org/10.1089/ars.2006.8.1907.

(13) Nathan, C. Points of Control in Inflammation. *Nature* **2002**, *420* (6917), 846–852. https://doi.org/10.1038/nature01320.

(14) Prabhu, S. D.; Frangogiannis, N. G. The Biological Basis for Cardiac Repair After Myocardial Infarction: From Inflammation to Fibrosis. *Circ. Res.* **2016**, *119* (1), 91–112. https://doi.org/10.1161/CIRCRESAHA.116.303577.

(15) Sommese, L.; Zullo, A.; Schiano, C.; Mancini, F. P.; Napoli, C. Possible Muscle Repair in the Human Cardiovascular System. *Stem cell Rev. reports* **2017**, *13* (2), 170–191. https://doi.org/10.1007/s12015-016-9711-3.

(16) Ingason, A. B.; Goldstone, A. B.; Paulsen, M. J.; Thakore, A. D.; Truong, V. N.; Edwards, B. B.; Eskandari, A.; Bollig, T.; Steele, A. N.; Woo, Y. J. Angiogenesis Precedes Cardiomyocyte Migration in Regenerating Mammalian Hearts. *J. Thorac. Cardiovasc. Surg.* **2018**, *155* (3), 1118-1127.e1. https://doi.org/10.1016/j.jtcvs.2017.08.127.

(17) Virag, J. I.; Murry, C. E. Myofibroblast and Endothelial Cell Proliferation during Murine Myocardial Infarct Repair. *Am. J. Pathol.* **2003**, *163* (6), 2433–2440. https://doi.org/10.1016/S0002-9440(10)63598-5.

(18) Sarig, U.; Sarig, H.; de-Berardinis, E.; Chaw, S.-Y.; Nguyen, E. B. V; Ramanujam, V. S.; Thang, V. D.; Al-Haddawi, M.; Liao, S.; Seliktar, D.; Kofidis, T.; Boey, F. Y. C.; Venkatraman, S. S.; Machluf, M. Natural Myocardial ECM Patch Drives Cardiac Progenitor Based Restoration Even after Scarring. *Acta Biomater.* **2016**, *44*, 209–220. https://doi.org/10.1016/j.actbio.2016.08.031.

(19) Pfeffer, M. A.; Braunwald, E. Ventricular Remodeling after Myocardial Infarction. Experimental Observations and Clinical Implications. *Circulation* **1990**, *81* (4), 1161–1172. https://doi.org/10.1161/01.cir.81.4.1161.

(20) Daley, W. P.; Yamada, K. M. ECM-Modulated Cellular Dynamics as a Driving Force for Tissue Morphogenesis. *Curr. Opin. Genet. Dev.* **2013**, *23* (4), 408–414. https://doi.org/10.1016/j.gde.2013.05.005.

(21) Kai, D.; Prabhakaran, M. P.; Jin, G.; Ramakrishna, S. Guided Orientation of Cardiomyocytes on Electrospun Aligned Nanofibers for Cardiac Tissue Engineering. *J. Biomed. Mater. Res. B. Appl. Biomater.* **2011**, *98* (2), 379–386. https://doi.org/10.1002/jbm.b.31862.

(22) Janson, I. A.; Putnam, A. J. Extracellular Matrix Elasticity and Topography: Material-Based Cues That Affect Cell Function via Conserved Mechanisms. *J. Biomed. Mater. Res. A* **2015**, *103* (3), 1246–1258. https://doi.org/10.1002/jbm.a.35254.

(23) Banerjee, I.; Fuseler, J. W.; Price, R. L.; Borg, T. K.; Baudino, T. A. Determination of Cell Types and Numbers during Cardiac Development in the Neonatal and Adult Rat and

Mouse. *Am. J. Physiol. Heart Circ. Physiol.* **2007**, *293* (3), H1883-91. https://doi.org/10.1152/ajpheart.00514.2007.

(24) Wang, L.; Yu, P.; Zhou, B.; Song, J.; Li, Z.; Zhang, M.; Guo, G.; Wang, Y.; Chen, X.; Han, L.; Hu, S. Single-Cell Reconstruction of the Adult Human Heart during Heart Failure and Recovery Reveals the Cellular Landscape Underlying Cardiac Function. *Nat. Cell Biol.* **2020**, *22* (1), 108–119. https://doi.org/10.1038/s41556-019-0446-7.

(25) Chen, W.; Frangogiannis, N. G. Fibroblasts in Post-Infarction Inflammation and Cardiac Repair. *Biochim. Biophys. Acta* **2013**, *1833* (4), 945–953. https://doi.org/10.1016/j.bbamcr.2012.08.023.

(26) Hassanabad, Z. F.; Furman, B. L.; Parratt, J. R.; Aughey, E. Coronary Endothelial Dysfunction Increases the Severity of Ischaemia-Induced Ventricular Arrhythmias in Rat Isolated Perfused Hearts. *Basic Res. Cardiol.* **1998**, *93* (4), 241–249. https://doi.org/10.1007/s003950050091.

(27) Parratt, J. R.; Vegh, A. Delayed Protection against Ventricular Arrhythmias by Cardiac Pacing. *Heart (British Cardiac Society)*. November 1997, pp 423–425. https://doi.org/10.1136/hrt.78.5.423.

(28) Miyagawa, S.; Sawa, Y.; Taketani, S.; Kawaguchi, N.; Nakamura, T.; Matsuura, N.; Matsuda, H. Myocardial Regeneration Therapy for Heart Failure: Hepatocyte Growth Factor Enhances the Effect of Cellular Cardiomyoplasty. *Circulation* **2002**, *105* (21), 2556–2561. https://doi.org/10.1161/01.cir.0000016722.37138.f2.

(29) Gordon, M. K.; Hahn, R. A. Collagens. *Cell Tissue Res.* **2010**, *339* (1), 247–257. https://doi.org/10.1007/s00441-009-0844-4.

(30) Weber, K. T. Cardiac Interstitium in Health and Disease: The Fibrillar Collagen Network. *J. Am. Coll. Cardiol.* **1989**, *13* (7), 1637–1652. https://doi.org/10.1016/0735-1097(89)90360-4.

(31) Graham, H. K.; Horn, M.; Trafford, A. W. Extracellular Matrix Profiles in the Progression to Heart Failure. European Young Physiologists Symposium Keynote Lecture-Bratislava 2007. *Acta Physiol. (Oxf).* **2008**, *194* (1), 3–21. https://doi.org/10.1111/j.1748-1716.2008.01881.x.

(32) Liu, X.; Wu, H.; Byrne, M.; Krane, S.; Jaenisch, R. Type III Collagen Is Crucial for Collagen I Fibrillogenesis and for Normal Cardiovascular Development. *Proc. Natl. Acad. Sci.* **1997**, *94* (5), 1852 LP – 1856. https://doi.org/10.1073/pnas.94.5.1852.

(33) Bayomy, A. F.; Bauer, M.; Qiu, Y.; Liao, R. Regeneration in Heart Disease-Is ECM the Key? *Life Sci.* **2012**, *91* (17–18), 823–827. https://doi.org/10.1016/j.lfs.2012.08.034.

(34) Marijianowski, M. M.; Teeling, P.; Mann, J.; Becker, A. E. Dilated Cardiomyopathy Is Associated with an Increase in the Type I/Type III Collagen Ratio: A Quantitative Assessment. *J. Am. Coll. Cardiol.* **1995**, *25* (6), 1263–1272. https://doi.org/10.1016/0735-1097(94)00557-7.

(35) Dobaczewski, M.; Gonzalez-Quesada, C.; Frangogiannis, N. G. The Extracellular Matrix as a Modulator of the Inflammatory and Reparative Response Following Myocardial

Infarction. *J. Mol. Cell. Cardiol.* **2010**, *48* (3), 504–511. https://doi.org/10.1016/j.yjmcc.2009.07.015.

(36) Mewhort, H. E. M.; Turnbull, J. D.; Meijndert, H. C.; Ngu, J. M. C.; Fedak, P. W. M. Epicardial Infarct Repair with Basic Fibroblast Growth Factor-Enhanced CorMatrix-ECM Biomaterial Attenuates Postischemic Cardiac Remodeling. *J. Thorac. Cardiovasc. Surg.* **2014**, *147* (5), 1650–1659. https://doi.org/10.1016/j.jtcvs.2013.08.005.

(37) Bernhard, D.; Laufer, G. The Aging Cardiomyocyte: A Mini-Review. *Gerontology* **2008**, *54* (1), 24–31. https://doi.org/10.1159/000113503.

(38) Meschiari, C. A.; Ero, O. K.; Pan, H.; Finkel, T.; Lindsey, M. L. The Impact of Aging on Cardiac Extracellular Matrix. *GeroScience* **2017**, *39* (1), 7–18. https://doi.org/10.1007/s11357-017-9959-9.

(39) Nguyen, T. P.; Qu, Z.; Weiss, J. N. Cardiac Fibrosis and Arrhythmogenesis: The Road to Repair Is Paved with Perils. *J. Mol. Cell. Cardiol.* **2014**, *70*, 83–91. https://doi.org/10.1016/j.yjmcc.2013.10.018.

(40) Kocabey, S.; Ceylan, H.; Tekinay, A. B.; Guler, M. O. Glycosaminoglycan Mimetic Peptide Nanofibers Promote Mineralization by Osteogenic Cells. *Acta Biomater.* **2013**, *9* (11), 9075–9085. https://doi.org/10.1016/j.actbio.2013.07.007.

(41) Eren Cimenci, C.; Uzunalli, G.; Uysal, O.; Yergoz, F.; Karaca Umay, E.; Guler, M. O.; Tekinay, A. B. Laminin Mimetic Peptide Nanofibers Regenerate Acute Muscle Defect. *Acta Biomater.* **2017**, *60*, 190–200. https://doi.org/10.1016/j.actbio.2017.07.010.

(42) Patel, Z. S.; Mikos, A. G. Angiogenesis with Biomaterial-Based Drug- and Cell-Delivery Systems. *J. Biomater. Sci. Polym. Ed.* **2004**, *15* (6), 701–726. https://doi.org/10.1163/156856204774196117.

(43) Allaman, I.; Bélanger, M.; Magistretti, P. J. Methylglyoxal, the Dark Side of Glycolysis. *Front. Neurosci.* **2015**, *9*, 23. https://doi.org/10.3389/fnins.2015.00023.

(44) Papagrigoraki, A.; Del Giglio, M.; Cosma, C.; Maurelli, M.; Girolomoni, G.; Lapolla, A. Advanced Glycation End Products Are Increased in the Skin and Blood of Patients with Severe Psoriasis. *Acta Derm. Venereol.* **2017**, *97* (7), 782–787. https://doi.org/10.2340/00015555-2661.

(45) Han, Y.; Sun, T.; Tao, R.; Han, Y.; Liu, J. Clinical Application Prospect of Umbilical Cord-Derived Mesenchymal Stem Cells on Clearance of Advanced Glycation End Products through Autophagy on Diabetic Wound. *Eur. J. Med. Res.* **2017**, *22* (1), 11. https://doi.org/10.1186/s40001-017-0253-1.

(46) Wells-Knecht, K. J.; Zyzak, D. V; Litchfield, J. E.; Thorpe, S. R.; Baynes, J. W. Mechanism of Autoxidative Glycosylation: Identification of Glyoxal and Arabinose as Intermediates in the Autoxidative Modification of Proteins by Glucose. *Biochemistry* **1995**, *34* (11), 3702–3709. https://doi.org/10.1021/bi00011a027.

(47) Hartog, J. W. L.; Voors, A. A.; Schalkwijk, C. G.; Scheijen, J.; Smilde, T. D. J.; Damman, K.; Bakker, S. J. L.; Smit, A. J.; van Veldhuisen, D. J. Clinical and Prognostic Value of Advanced Glycation End-Products in Chronic Heart Failure. *Eur. Heart J.* **2007**, *28* (23),

2879–2885. https://doi.org/10.1093/eurheartj/ehm486.

(48) Mulder, D. J.; van Haelst, P. L.; Graaff, R.; Gans, R. O.; Zijlstra, F.; Smit, A. J. Skin Autofluorescence Is Elevated in Acute Myocardial Infarction and Is Associated with the One-Year Incidence of Major Adverse Cardiac Events. *Netherlands Hear. J. Mon. J. Netherlands Soc. Cardiol. Netherlands Hear. Found.* **2009**, *17* (4), 162–168. https://doi.org/10.1007/BF03086239.

(49) Distler, M. G.; Palmer, A. A. Role of Glyoxalase 1 (Glo1) and Methylglyoxal (MG) in Behavior: Recent Advances and Mechanistic Insights. *Front. Genet.* **2012**, *3*, 250. https://doi.org/10.3389/fgene.2012.00250.

(50) Rabbani, N.; Thornalley, P. J. Methylglyoxal, Glyoxalase 1 and the Dicarbonyl Proteome. *Amino Acids* **2012**, *42* (4), 1133–1142. https://doi.org/10.1007/s00726-010-0783-0.

(51) Rabbani, N.; Xue, M.; Thornalley, P. J. Methylglyoxal-Induced Dicarbonyl Stress in Aging and Disease: First Steps towards Glyoxalase 1-Based Treatments. *Clin. Sci. (Lond).* **2016**, *130* (19), 1677–1696. https://doi.org/10.1042/CS20160025.

(52) Yao, D.; Brownlee, M. Hyperglycemia-Induced Reactive Oxygen Species Increase Expression of the Receptor for Advanced Glycation End Products (RAGE) and RAGE Ligands. *Diabetes* **2010**, *59* (1), 249–255. https://doi.org/10.2337/db09-0801.

(53) Thornalley, P. J. Glyoxalase I--Structure, Function and a Critical Role in the Enzymatic Defence against Glycation. *Biochem. Soc. Trans.* **2003**, *31* (Pt 6), 1343–1348. https://doi.org/10.1042/bst0311343.

(54) Sena, C. M.; Matafome, P.; Crisóstomo, J.; Rodrigues, L.; Fernandes, R.; Pereira, P.; Seiça, R. M. Methylglyoxal Promotes Oxidative Stress and Endothelial Dysfunction. *Pharmacol. Res.* **2012**, *65* (5), 497–506. https://doi.org/10.1016/j.phrs.2012.03.004.

(55) Abordo, E. A.; Minhas, H. S.; Thornalley, P. J. Accumulation of Alpha-Oxoaldehydes during Oxidative Stress: A Role in Cytotoxicity. *Biochem. Pharmacol.* **1999**, *58* (4), 641–648. https://doi.org/10.1016/s0006-2952(99)00132-x.

(56) Giacco, F.; Brownlee, M. Oxidative Stress and Diabetic Complications. *Circ. Res.* **2010**, *107* (9), 1058–1070. https://doi.org/10.1161/CIRCRESAHA.110.223545.

(57) Yim, H. S.; Kang, S. O.; Hah, Y. C.; Chock, P. B.; Yim, M. B. Free Radicals Generated during the Glycation Reaction of Amino Acids by Methylglyoxal. A Model Study of Protein-Cross-Linked Free Radicals. *J. Biol. Chem.* **1995**, *270* (47), 28228–28233. https://doi.org/10.1074/jbc.270.47.28228.

(58) Brownlee, M. Biochemistry and Molecular Cell Biology of Diabetic Complications. *Nature* **2001**, *414* (6865), 813–820. https://doi.org/10.1038/414813a.

(59) Kumagai, T.; Nangaku, M.; Kojima, I.; Nagai, R.; Ingelfinger, J. R.; Miyata, T.; Fujita, T.; Inagi, R. Glyoxalase I Overexpression Ameliorates Renal Ischemia-Reperfusion Injury in Rats. *Am. J. Physiol. Renal Physiol.* **2009**, *296* (4), F912-21. https://doi.org/10.1152/ajprenal.90575.2008.

(60) Masoud, W. G. T.; Ussher, J. R.; Wang, W.; Jaswal, J. S.; Wagg, C. S.; Dyck, J. R.;

Lygate, C. A.; Neubauer, S.; Clanachan, A. S.; Lopaschuk, G. D. Failing Mouse Hearts Utilize Energy Inefficiently and Benefit from Improved Coupling of Glycolysis and Glucose Oxidation. *Cardiovasc. Res.* **2014**, *101* (1), 30–38. https://doi.org/10.1093/cvr/cvt216.

(61) Kalra, B. S.; Roy, V. Efficacy of Metabolic Modulators in Ischemic Heart Disease: An Overview. *J. Clin. Pharmacol.* **2012**, *52* (3), 292–305. https://doi.org/10.1177/0091270010396042.

(62) Blackburn, N. J. R.; Vulesevic, B.; McNeill, B.; Cimenci, C. E.; Ahmadi, A.; Gonzalez-Gomez, M.; Ostojic, A.; Zhong, Z.; Brownlee, M.; Beisswenger, P. J.; Milne, R. W.; Suuronen, E. J. Methylglyoxal-Derived Advanced Glycation End Products Contribute to Negative Cardiac Remodeling and Dysfunction Post-Myocardial Infarction. *Basic Res. Cardiol.* **2017**, *112* (5), 57. https://doi.org/10.1007/s00395-017-0646-x.

(63) Aruoma, O. I. Free Radicals, Oxidative Stress, and Antioxidants in Human Health and Disease. *J. Am. Oil Chem. Soc.* **1998**, *75* (2), 199–212. https://doi.org/10.1007/s11746-998-0032-9.

(64) Singh, R. B.; Niaz, M. A.; Rastogi, S. S.; Rastogi, S. Usefulness of Antioxidant Vitamins in Suspected Acute Myocardial Infarction (the Indian Experiment of Infarct Survival-3). *Am. J. Cardiol.* **1996**, *77* (4), 232–236. https://doi.org/10.1016/s0002-9149(97)89384-8.

(65) Bernier, M.; Hearse, D. J.; Manning, A. S. Reperfusion-Induced Arrhythmias and Oxygen-Derived Free Radicals. Studies with "Anti-Free Radical" Interventions and a Free Radical-Generating System in the Isolated Perfused Rat Heart. *Circ. Res.* **1986**, *58* (3), 331–340. https://doi.org/10.1161/01.res.58.3.331.

(66) Gelderblom, M.; Leypoldt, F.; Lewerenz, J.; Birkenmayer, G.; Orozco, D.; Ludewig, P.; Thundyil, J.; Arumugam, T. V; Gerloff, C.; Tolosa, E.; Maher, P.; Magnus, T. The Flavonoid Fisetin Attenuates Postischemic Immune Cell Infiltration, Activation and Infarct Size after Transient Cerebral Middle Artery Occlusion in Mice. *J. Cereb. Blood Flow Metab.* **2012**, *32* (5), 835–843. https://doi.org/10.1038/jcbfm.2011.189.

(67) Zheng, L. T.; Ock, J.; Kwon, B.-M.; Suk, K. Suppressive Effects of Flavonoid Fisetin on Lipopolysaccharide-Induced Microglial Activation and Neurotoxicity. *Int. Immunopharmacol.* **2008**, *8* (3), 484–494. https://doi.org/10.1016/j.intimp.2007.12.012.

(68) Maher, P.; Dargusch, R.; Ehren, J. L.; Okada, S.; Sharma, K.; Schubert, D. Fisetin Lowers Methylglyoxal Dependent Protein Glycation and Limits the Complications of Diabetes. *PLoS One* **2011**, *6* (6), e21226. https://doi.org/10.1371/journal.pone.0021226.

(69) Khan, N.; Syed, D. N.; Ahmad, N.; Mukhtar, H. Fisetin: A Dietary Antioxidant for Health Promotion. *Antioxid. Redox Signal.* **2013**, *19* (2), 151–162. https://doi.org/10.1089/ars.2012.4901.

(70) Ehren, J. L.; Maher, P. Concurrent Regulation of the Transcription Factors Nrf2 and ATF4 Mediates the Enhancement of Glutathione Levels by the Flavonoid Fisetin. *Biochem. Pharmacol.* **2013**, *85* (12), 1816–1826. https://doi.org/10.1016/j.bcp.2013.04.010.

(71) Raghavendra, G. M.; Varaprasad, K.; Jayaramudu, T. Biomaterials: Design, Development

and Biomedical Applications. *Nanotechnol. Appl. Tissue Eng.* **2015**, 21–44. https://doi.org/10.1016/B978-0-323-32889-0.00002-9.

(72) Ruvinov, E.; Cohen, S. Alginate Biomaterial for the Treatment of Myocardial Infarction: Progress, Translational Strategies, and Clinical Outlook: From Ocean Algae to Patient Bedside. *Adv. Drug Deliv. Rev.* **2016**, *96*, 54–76. https://doi.org/10.1016/j.addr.2015.04.021.

(73) Shachar, M.; Cohen, S. Cardiac Tissue Engineering, Ex-Vivo: Design Principles in Biomaterials and Bioreactors. *Heart Fail. Rev.* **2003**, *8* (3), 271–276. https://doi.org/10.1023/a:1024729919743.

(74) Leor, J.; Aboulafia-Etzion, S.; Dar, A.; Shapiro, L.; Barbash, I. M.; Battler, A.; Granot, Y.; Cohen, S. Bioengineered Cardiac Grafts: A New Approach to Repair the Infarcted Myocardium? *Circulation* **2000**, *102* (19 Suppl 3), III56-61. https://doi.org/10.1161/01.cir.102.suppl_3.iii-56.

(75) Chen, Q.-Z.; Harding, S. E.; Ali, N. N.; Lyon, A. R.; Boccaccini, A. R. Biomaterials in Cardiac Tissue Engineering: Ten Years of Research Survey. *Mater. Sci. Eng. R Reports* **2008**, *59* (1), 1–37. https://doi.org/https://doi.org/10.1016/j.mser.2007.08.001.

(76) Dar, A.; Shachar, M.; Leor, J.; Cohen, S. Optimization of Cardiac Cell Seeding and Distribution in 3D Porous Alginate Scaffolds. *Biotechnol. Bioeng.* **2002**, *80* (3), 305–312. https://doi.org/10.1002/bit.10372.

(77) Leor, J.; Tuvia, S.; Guetta, V.; Manczur, F.; Castel, D.; Willenz, U.; Petnehazy, O.; Landa, N.; Feinberg, M. S.; Konen, E.; Goitein, O.; Tsur-Gang, O.; Shaul, M.; Klapper, L.; Cohen, S. Intracoronary Injection of in Situ Forming Alginate Hydrogel Reverses Left Ventricular Remodeling after Myocardial Infarction in Swine. *J Am Coll Cardiol* **2009**, *54* (11), 1014–1023. https://doi.org/10.1016/j.jacc.2009.06.010.

(78) Huyer, L. D.; Montgomery, M.; Zhao, Y.; Xiao, Y.; Conant, G.; Korolj, A.; Radisic, M. Biomaterial Based Cardiac Tissue Engineering and Its Applications. *Biomed. Mater.* **2015**, *10* (3), 34004. https://doi.org/10.1088/1748-6041/10/3/034004.

(79) Seif-Naraghi, S. B.; Singelyn, J. M.; Salvatore, M. A.; Osborn, K. G.; Wang, J. J.; Sampat, U.; Kwan, O. L.; Strachan, G. M.; Wong, J.; Schup-Magoffin, P. J.; Braden, R. L.; Bartels, K.; DeQuach, J. A.; Preul, M.; Kinsey, A. M.; DeMaria, A. N.; Dib, N.; Christman, K. L. Safety and Efficacy of an Injectable Extracellular Matrix Hydrogel for Treating Myocardial Infarction. *Sci. Transl. Med.* **2013**, *5* (173), 173ra25. https://doi.org/10.1126/scitranslmed.3005503.

(80) Dvir, T.; Timko, B. P.; Brigham, M. D.; Naik, S. R.; Karajanagi, S. S.; Levy, O.; Jin, H.; Parker, K. K.; Langer, R.; Kohane, D. S. Nanowired Three-Dimensional Cardiac Patches. *Nat Nanotechnol* **2011**, *6* (11), 720–725. https://doi.org/10.1038/nnano.2011.160.

(81) Navaei, A.; Saini, H.; Christenson, W.; Sullivan, R. T.; Ros, R.; Nikkhah, M. Gold Nanorod-Incorporated Gelatin-Based Conductive Hydrogels for Engineering Cardiac Tissue Constructs. *Acta Biomater.* **2016**, *41*, 133–146. https://doi.org/10.1016/j.actbio.2016.05.027.

(82) Hosoyama, K.; Ahumada, M.; Goel, K.; Ruel, M.; Suuronen, E. J.; Alarcon, E. I. Electroconductive Materials as Biomimetic Platforms for Tissue Regeneration. *Biotechnol Adv* **2019**, *37* (3), 444–458. https://doi.org/10.1016/j.biotechadv.2019.02.011.

(83) Solazzo, M.; O'Brien, F. J.; Nicolosi, V.; Monaghan, M. G. The Rationale and Emergence of Electroconductive Biomaterial Scaffolds in Cardiac Tissue Engineering. *APL Bioeng.* **2019**, *3* (4), 41501. https://doi.org/10.1063/1.5116579.

(84) Esmaeili, H.; Patino-Guerrero, A.; Hasany, M.; Ansari, M. O.; Memic, A.; Dolatshahi-Pirouz, A.; Nikkhah, M. Electroconductive Biomaterials for Cardiac Tissue Engineering. *Acta Biomater.* **2021**. https://doi.org/10.1016/j.actbio.2021.08.031.

(85) Cristallini, C.; Vitale, E.; Giachino, C.; Rastaldo, R. Nanoengineering in Cardiac Regeneration: Looking Back and Going Forward. *Nanomater. (Basel, Switzerland)* **2020**, *10* (8), 1587. https://doi.org/10.3390/nano10081587.

(86) Suarez, S.; Almutairi, A.; Christman, K. L. Micro- and Nanoparticles for Treating Cardiovascular Disease. *Biomater. Sci.* **2015**, *3* (4), 564–580. https://doi.org/10.1039/C4BM00441H.

(87) Vaishya, R. D.; Mandal, A.; Gokulgandhi, M.; Patel, S.; Mitra, A. K. Reversible Hydrophobic Ion-Paring Complex Strategy to Minimize Acylation of Octreotide during Long-Term Delivery from PLGA Microparticles. *Int. J. Pharm.* **2015**, *489* (1–2), 237–245. https://doi.org/10.1016/j.ijpharm.2015.04.075.

(88) Kitsara, M.; Kontziampasis, D.; Agbulut, O.; Chen, Y. Heart on a Chip: Micro-Nanofabrication and Microfluidics Steering the Future of Cardiac Tissue Engineering. *Microelectron. Eng.* **2019**, *203–204*, 44–62. https://doi.org/https://doi.org/10.1016/j.mee.2018.11.001.

(89) Benjamin, E. J.; Blaha, M. J.; Chiuve, S. E.; Cushman, M.; Das, S. R.; Deo, R.; de Ferranti, S. D.; Floyd, J.; Fornage, M.; Gillespie, C.; Isasi, C. R.; Jiménez, M. C.; Jordan, L. C.; Judd, S. E.; Lackland, D.; Lichtman, J. H.; Lisabeth, L.; Liu, S.; Longenecker, C. T.; Mackey, R. H.; Matsushita, K.; Mozaffarian, D.; Mussolino, M. E.; Nasir, K.; Neumar, R. W.; Palaniappan, L.; Pandey, D. K.; Thiagarajan, R. R.; Reeves, M. J.; Ritchey, M.; Rodriguez, C. J.; Roth, G. A.; Rosamond, W. D.; Sasson, C.; Towfighi, A.; Tsao, C. W.; Turner, M. B.; Virani, S. S.; Voeks, J. H.; Willey, J. Z.; Wilkins, J. T.; Wu, J. H.; Alger, H. M.; Wong, S. S.; Muntner, P. Heart Disease and Stroke Statistics-2017 Update: A Report From the American Heart Association. *Circulation* **2017**, *135* (10), e146–e603. https://doi.org/10.1161/CIR.0000000000000485.

(90) Morrow, D. A. The Fourth Universal Definition of Myocardial Infarction and the Emerging Importance of Myocardial Injury. *Circulation*. United States January 2020, pp 172–175. https://doi.org/10.1161/CIRCULATIONAHA.119.044125.

(91) Menasché, P. Cardiac Cell Therapy: Current Status, Challenges and Perspectives. *Arch. Cardiovasc. Dis.* **2020**, *113* (4), 285–292. https://doi.org/10.1016/j.acvd.2020.01.002.

(92) Lo, T. W.; Westwood, M. E.; McLellan, A. C.; Selwood, T.; Thornalley, P. J. Binding and Modification of Proteins by Methylglyoxal under Physiological Conditions. A Kinetic and Mechanistic Study with N Alpha-Acetylarginine, N Alpha-Acetylcysteine, and N

Alpha-Acetyllysine, and Bovine Serum Albumin. *J. Biol. Chem.* **1994**, *269* (51), 32299–32305.

(93) Ahmed, N.; Thornalley, P. J.; Dawczynski, J.; Franke, S.; Strobel, J.; Stein, G.; Haik, G. M. Methylglyoxal-Derived Hydroimidazolone Advanced Glycation End-Products of Human Lens Proteins. *Invest. Ophthalmol. Vis. Sci.* **2003**, *44* (12), 5287–5292. https://doi.org/10.1167/iovs.03-0573.

(94) Nabavi, S. F.; Braidy, N.; Habtemariam, S.; Sureda, A.; Manayi, A.; Nabavi, S. M. Neuroprotective Effects of Fisetin in Alzheimer's and Parkinson's Diseases: From Chemistry to Medicine. *Curr. Top. Med. Chem.* **2016**, *16* (17), 1910–1915. https://doi.org/10.2174/1568026616666160204121725.

(95) Maslov, M.; Foianini, S.; Lovich, M. Delivery of Drugs, Growth Factors, Genes and Stem Cells via Intrapericardial, Epicardial and Intramyocardial Routes for Sustained Local Targeted Therapy of Myocardial Disease. *Expert Opin. Drug Deliv.* **2017**, *14* (10), 1227–1239. https://doi.org/10.1080/17425247.2017.1292249.

(96) Pala, R.; Anju, V. T.; Dyavaiah, M.; Busi, S.; Nauli, S. M. Nanoparticle-Mediated Drug Delivery for the Treatment of Cardiovascular Diseases. *Int. J. Nanomedicine* **2020**, *15*, 3741–3769. https://doi.org/10.2147/IJN.S250872.

(97) Zhang, R.; Xing, R.; Jiao, T.; Ma, K.; Chen, C.; Ma, G.; Yan, X. Carrier-Free, Chemophotodynamic Dual Nanodrugs via Self-Assembly for Synergistic Antitumor Therapy. *ACS Appl. Mater. Interfaces* **2016**, *8* (21), 13262–13269. https://doi.org/10.1021/acsami.6b02416.

(98) Sedlakova, V.; Ruel, M.; Suuronen, E. J. Therapeutic Use of Bioengineered Materials for Myocardial Infarction. *Nanoeng. Mater. Biomed. Uses* **2019**, 161–193. https://doi.org/10.1007/978-3-030-31261-9_9.

(99) Xing, R.; Liu, K.; Jiao, T.; Zhang, N.; Ma, K.; Zhang, R.; Zou, Q.; Ma, G.; Yan, X. An Injectable Self-Assembling Collagen-Gold Hybrid Hydrogel for Combinatorial Antitumor Photothermal/Photodynamic Therapy. *Adv. Mater.* **2016**, *28* (19), 3669–3676. https://doi.org/10.1002/adma.201600284.

(100) Song, J.; Yuan, C.; Jiao, T.; Xing, R.; Yang, M.; Adams, D. J.; Yan, X. Multifunctional Antimicrobial Biometallohydrogels Based on Amino Acid Coordinated Self-Assembly. *Small* **2020**, *16* (8), 1907309. https://doi.org/10.1002/SMLL.201907309.

(101) Ahmadi, A.; McNeill, B.; Vulesevic, B.; Kordos, M.; Mesana, L.; Thorn, S.; Renaud, J. M.; Manthorp, E.; Kuraitis, D.; Toeg, H.; Mesana, T. G.; Davis, D. R.; Beanlands, R. S.; DaSilva, J. N.; deKemp, R. A.; Ruel, M.; Suuronen, E. J. The Role of Integrin A2 in Cell and Matrix Therapy That Improves Perfusion, Viability and Function of Infarcted Myocardium. *Biomaterials* **2014**, *35* (17), 4749–4758. https://doi.org/10.1016/j.biomaterials.2014.02.028.

(102) Blackburn, N. J. R.; Sofrenovic, T.; Kuraitis, D.; Ahmadi, A.; McNeill, B.; Deng, C.; Rayner, K. J.; Zhong, Z.; Ruel, M.; Suuronen, E. J. Timing Underpins the Benefits Associated with Injectable Collagen Biomaterial Therapy for the Treatment of Myocardial Infarction. *Biomaterials* **2015**, *39*, 182–192.

https://doi.org/10.1016/j.biomaterials.2014.11.004.

(103) McLaughlin, S.; McNeill, B.; Podrebarac, J.; Hosoyama, K.; Sedlakova, V.; Cron, G.; Smyth, D.; Seymour, R.; Goel, K.; Liang, W.; Rayner, K. J.; Ruel, M.; Suuronen, E. J.; Alarcon, E. I. Injectable Human Recombinant Collagen Matrices Limit Adverse Remodeling and Improve Cardiac Function after Myocardial Infarction. *Nat. Commun.* **2019**, *10* (1), 4866. https://doi.org/10.1038/s41467-019-12748-8.

(104) Wang, T.; Douglass, E. F.; Fitzgerald, K. J.; Spiegel, D. A. A "Turn-On" Fluorescent Sensor for Methylglyoxal. *J. Am. Chem. Soc.* **2013**, *135* (33), 12429–12433. https://doi.org/10.1021/ja406077j.

(105) Ong, S.-B.; Hernández-Reséndiz, S.; Crespo-Avilan, G. E.; Mukhametshina, R. T.; Kwek, X.-Y.; Cabrera-Fuentes, H. A.; Hausenloy, D. J. Inflammation Following Acute Myocardial Infarction: Multiple Players, Dynamic Roles, and Novel Therapeutic Opportunities. *Pharmacol. Ther.* **2018**, *186*, 73–87. https://doi.org/10.1016/j.pharmthera.2018.01.001.

(106) Han, J.; Kim, Y. S.; Lim, M.-Y.; Kim, H. Y.; Kong, S.; Kang, M.; Choo, Y. W.; Jun, J. H.; Ryu, S.; Jeong, H.-Y.; Park, J.; Jeong, G.-J.; Lee, J.-C.; Eom, G. H.; Ahn, Y.; Kim, B.-S. Dual Roles of Graphene Oxide To Attenuate Inflammation and Elicit Timely Polarization of Macrophage Phenotypes for Cardiac Repair. *ACS Nano* **2018**, *12* (2), 1959–1977. https://doi.org/10.1021/acsnano.7b09107.

(107) Mastrocola, R. AGEs and Neurodegeneration: The Nrf2/Glyoxalase-1 Interaction. *Oncotarget* **2017**, *8* (4), 5645–5646. https://doi.org/10.18632/oncotarget.14232.

(108) Cheng, S.-B.; Liu, H.-T.; Chen, S.-Y.; Lin, P.-T.; Lai, C.-Y.; Huang, Y.-C. Changes of Oxidative Stress, Glutathione, and Its Dependent Antioxidant Enzyme Activities in Patients with Hepatocellular Carcinoma before and after Tumor Resection. *PLoS One* **2017**, *12* (1), e0170016–e0170016. https://doi.org/10.1371/journal.pone.0170016.

(109) Chakraborty, S.; Karmakar, K.; Chakravortty, D. Cells Producing Their Own Nemesis: Understanding Methylglyoxal Metabolism. *IUBMB Life* **2014**, *66* (10), 667–678. https://doi.org/10.1002/iub.1324.

(110) Aleshin, A.; Ananthakrishnan, R.; Li, Q.; Rosario, R.; Lu, Y.; Qu, W.; Song, F.; Bakr, S.; Szabolcs, M.; D'Agati, V.; Liu, R.; Homma, S.; Schmidt, A. M.; Yan, S. F.; Ramasamy, R. RAGE Modulates Myocardial Injury Consequent to LAD Infarction via Impact on JNK and STAT Signaling in a Murine Model. *Am. J. Physiol. Heart Circ. Physiol.* **2008**, *294* (4), H1823-32. https://doi.org/10.1152/ajpheart.01210.2007.

(111) Garg, S.; Khan, S. I.; Malhotra, R. K.; Sharma, M. K.; Kumar, M.; Kaur, P.; Nag, T. C.; RumaRay; Bhatia, J.; Arya, D. S. The Molecular Mechanism Involved in Cardioprotection by the Dietary Flavonoid Fisetin as an Agonist of PPAR-γ in a Murine Model of Myocardial Infarction. *Arch. Biochem. Biophys.* **2020**, *694*, 108572. https://doi.org/10.1016/j.abb.2020.108572.

(112) Shanmugam, K.; Ravindran, S.; Kurian, G. A.; Rajesh, M. Fisetin Confers Cardioprotection against Myocardial Ischemia Reperfusion Injury by Suppressing Mitochondrial Oxidative Stress and Mitochondrial Dysfunction and Inhibiting Glycogen

Synthase Kinase 3β Activity. *Oxid. Med. Cell. Longev.* **2018**, *2018*, 9173436. https://doi.org/10.1155/2018/9173436.

(113) Ma, T.; Kandhare, A. D.; Mukherjee-Kandhare, A. A.; Bodhankar, S. L. Fisetin, a Plant Flavonoid Ameliorates Doxorubicin-Induced Cardiotoxicity in Experimental Rats: The Decisive Role of Caspase-3, COX-II, CTn-I, INOs and TNF-α. *Mol. Biol. Rep.* **2019**, *46* (1), 105–118. https://doi.org/10.1007/s11033-018-4450-y.

(114) Garg, S.; Malhotra, R. K.; Khan, S. I.; Sarkar, S.; Susrutha, P. N.; Singh, V.; Goyal, S.; Nag, T. C.; Ray, R.; Bhatia, J.; Arya, D. S. Fisetin Attenuates Isoproterenol-Induced Cardiac Ischemic Injury in Vivo by Suppressing RAGE/NF-KB Mediated Oxidative Stress, Apoptosis and Inflammation. *Phytomedicine* **2019**, *56*, 147–155. https://doi.org/10.1016/j.phymed.2018.09.187.

(115) Dong, B.; Liu, C.; Xue, R.; Wang, Y.; Sun, Y.; Liang, Z.; Fan, W.; Jiang, J.; Zhao, J.; Su, Q.; Dai, G.; Dong, Y.; Huang, H. Fisetin Inhibits Cardiac Hypertrophy by Suppressing Oxidative Stress. *J. Nutr. Biochem.* **2018**, *62*, 221–229. https://doi.org/10.1016/j.jnutbio.2018.08.010.

(116) Rodius, S.; de Klein, N.; Jeanty, C.; Sánchez-Iranzo, H.; Crespo, I.; Ibberson, M.; Xenarios, I.; Dittmar, G.; Mercader, N.; Niclou, S. P.; Azuaje, F. Fisetin Protects against Cardiac Cell Death through Reduction of ROS Production and Caspases Activity. *Sci. Rep.* **2020**, *10* (1), 2896. https://doi.org/10.1038/s41598-020-59894-4.

(117) Bothiraja, C.; Yojana, B. D.; Pawar, A. P.; Shaikh, K. S.; Thorat, U. H. Fisetin-Loaded Nanocochleates: Formulation, Characterisation, in Vitro Anticancer Testing, Bioavailability and Biodistribution Study. *Expert Opin. Drug Deliv.* **2014**, *11* (1), 17–29. https://doi.org/10.1517/17425247.2013.860131.

(118) Currais, A.; Prior, M.; Dargusch, R.; Armando, A.; Ehren, J.; Schubert, D.; Quehenberger, O.; Maher, P. Modulation of P25 and Inflammatory Pathways by Fisetin Maintains Cognitive Function in Alzheimer's Disease Transgenic Mice. *Aging Cell* **2014**, *13* (2), 379–390. https://doi.org/10.1111/acel.12185.

(119) Vulesevic, B.; McNeill, B.; Giacco, F.; Maeda, K.; Blackburn, N. J. R.; Brownlee, M.; Milne, R. W.; Suuronen, E. J. Methylglyoxal-Induced Endothelial Cell Loss and Inflammation Contribute to the Development of Diabetic Cardiomyopathy. *Diabetes* **2016**, *65* (6), 1699–1713. https://doi.org/10.2337/db15-0568.

(120) Bhan, A.; Sirker, A.; Zhang, J.; Protti, A.; Catibog, N.; Driver, W.; Botnar, R.; Monaghan, M. J.; Shah, A. M. High-Frequency Speckle Tracking Echocardiography in the Assessment of Left Ventricular Function and Remodeling after Murine Myocardial Infarction. *Am. J. Physiol. Heart Circ. Physiol.* **2014**, *306* (9), H1371-83. https://doi.org/10.1152/ajpheart.00553.2013.

(121) Li, S.-Y.; Sigmon, V. K.; Babcock, S. A.; Ren, J. Advanced Glycation Endproduct Induces ROS Accumulation, Apoptosis, MAP Kinase Activation and Nuclear O-GlcNAcylation in Human Cardiac Myocytes. *Life Sci.* **2007**, *80* (11), 1051–1056. https://doi.org/10.1016/j.lfs.2006.11.035.

(122) Paramita, D.; Wisnubroto, J. D. P. Effect of Methylglyoxal on Reactive Oxygen Species,

KI-67, and Caspase-3 Expression in MCF-7 Cells. *Exp. Mol. Pathol.* **2018**, *105* (1), 76–80. https://doi.org/10.1016/j.yexmp.2018.05.005.

(123) Hsieh, P. C. H.; Davis, M. E.; Lisowski, L. K.; Lee, R. T. Endothelial-Cardiomyocyte Interactions in Cardiac Development and Repair. *Annu. Rev. Physiol.* **2006**, *68*, 51–66. https://doi.org/10.1146/annurev.physiol.68.040104.124629.

(124) Li, B.; Xiao, J.; Li, Y.; Zhang, J.; Zeng, M. Gene Transfer of Human Neuregulin-1 Attenuates Ventricular Remodeling in Diabetic Cardiomyopathy Rats. *Exp Ther Med* **2013**, *6* (5), 1105–1112. https://doi.org/10.3892/etm.2013.1273.

(125) FR, F.; B, P.; E, G.; I, I.; P, D.-H.; G, A.; JJ, G.; T, S.-Y.; E, A.; E, T.; F, P.; MJ, B.-P. Controlled Delivery of Fibroblast Growth Factor-1 and Neuregulin-1 from Biodegradable Microparticles Promotes Cardiac Repair in a Rat Myocardial Infarction Model through Activation of Endogenous Regeneration. *J. Control. Release* **2014**, *173* (1), 132–139. https://doi.org/10.1016/J.JCONREL.2013.10.034.

(126) K, B.; S, A.; B, H.; B, K. Neuregulin1/ErbB4 Signaling Induces Cardiomyocyte Proliferation and Repair of Heart Injury. *Cell* **2009**, *138* (2), 257–270. https://doi.org/10.1016/J.CELL.2009.04.060.

(127) Lee, J. H.; Parveen, A.; Do, M. H.; Kang, M. C.; Yumnam, S.; Kim, S. Y. Molecular Mechanisms of Methylglyoxal-Induced Aortic Endothelial Dysfunction in Human Vascular Endothelial Cells. *Cell Death Dis. 2020 115* **2020**, *11* (5), 1–15. https://doi.org/10.1038/s41419-020-2602-1.

(128) Herrera-Zelada, N.; Zuñiga-Cuevas, U.; Ramirez-Reyes, A.; Lavandero, S.; Riquelme, J. A. Targeting the Endothelium to Achieve Cardioprotection. *Front. Pharmacol.* **2021**, *12*, 636134. https://doi.org/10.3389/fphar.2021.636134.

(129) Luxán, G.; Dimmeler, S. The Vasculature: A Therapeutic Target in Heart Failure? *Cardiovasc. Res.* **2021**. https://doi.org/10.1093/cvr/cvab047.

(130) Nigro, C.; Leone, A.; Longo, M.; Prevenzano, I.; Fleming, T. H.; Nicolò, A.; Parrillo, L.; Spinelli, R.; Formisano, P.; Nawroth, P. P.; Beguinot, F.; Miele, C. Methylglyoxal Accumulation De-Regulates HoxA5 Expression, Thereby Impairing Angiogenesis in Glyoxalase 1 Knock-down Mouse Aortic Endothelial Cells. *Biochim. Biophys. acta. Mol. basis Dis.* **2019**, *1865* (1), 73–85. https://doi.org/10.1016/j.bbadis.2018.10.014.

(131) Chen, T.; Dong, J.; Zhou, H.; Deng, X.; Li, R.; Chen, N.; Luo, M.; Li, Y.; Wu, J.; Wang, L. Glycation of Fibronectin Inhibits VEGF-Induced Angiogenesis by Uncoupling VEGF Receptor-2-c-Src Crosstalk. *J. Cell. Mol. Med.* **2020**, *24* (16), 9154–9164. https://doi.org/10.1111/JCMM.15552.

(132) Shirazi, L. F.; Bissett, J.; Romeo, F.; Mehta, J. L. Role of Inflammation in Heart Failure. *Curr. Atheroscler. Rep.* **2017**, *19* (6), 27. https://doi.org/10.1007/s11883-017-0660-3.

(133) Bezold, V.; Rosenstock, P.; Scheffler, J.; Geyer, H.; Horstkorte, R.; Bork, K. Glycation of Macrophages Induces Expression of Pro-Inflammatory Cytokines and Reduces Phagocytic Efficiency. *Aging (Albany. NY).* **2019**, *11* (14), 5258–5275. https://doi.org/10.18632/aging.102123.

(134) Kim, J. H.; Kim, M.-Y.; Kim, J.-H.; Cho, J. Y. Fisetin Suppresses Macrophage-Mediated Inflammatory Responses by Blockade of Src and Syk. *Biomol. Ther. (Seoul).* **2015**, *23* (5), 414–420. https://doi.org/10.4062/biomolther.2015.036.

(135) Liu, S.-H.; Lin, C.-H.; Hung, S.-K.; Chou, J.-H.; Chi, C.-W.; Fu, S.-L. Fisetin Inhibits Lipopolysaccharide-Induced Macrophage Activation and Dendritic Cell Maturation. *J. Agric. Food Chem.* **2010**, *58* (20), 10831–10839. https://doi.org/10.1021/jf1017093.

(136) Kim, S.-C.; Kang, S.-H.; Jeong, S.-J.; Kim, S.-H.; Ko, H. S.; Kim, S.-H. Inhibition of C-Jun N-Terminal Kinase and Nuclear Factor κ B Pathways Mediates Fisetin-Exerted Anti-Inflammatory Activity in Lipopolysccharide-Treated RAW264.7 Cells. *Immunopharmacol. Immunotoxicol.* **2012**, *34* (4), 645–650. https://doi.org/10.3109/08923973.2011.648270.

(137) Agarwal, G.; Kumar, N.; Srivastava, A. Highly Elastic, Electroconductive, Immunomodulatory Graphene Crosslinked Collagen Cryogel for Spinal Cord Regeneration. *Mater. Sci. Eng. C* **2021**, *118*, 111518. https://doi.org/https://doi.org/10.1016/j.msec.2020.111518.

(138) Das, A.; Abas, M.; Biswas, N.; Banerjee, P.; Ghosh, N.; Rawat, A.; Khanna, S.; Roy, S.; Sen, C. K. A Modified Collagen Dressing Induces Transition of Inflammatory to Reparative Phenotype of Wound Macrophages. *Sci. Rep.* **2019**, *9* (1), 14293. https://doi.org/10.1038/s41598-019-49435-z.

(139) Chen, P.; Cescon, M.; Zuccolotto, G.; Nobbio, L.; Colombelli, C.; Filaferro, M.; Vitale, G.; Feltri, M. L.; Bonaldo, P. Collagen VI Regulates Peripheral Nerve Regeneration by Modulating Macrophage Recruitment and Polarization. *Acta Neuropathol.* **2015**, *129* (1), 97–113. https://doi.org/10.1007/s00401-014-1369-9.

(140) de Couto, G. Macrophages in Cardiac Repair: Environmental Cues and Therapeutic Strategies. *Exp. Mol. Med.* **2019**, *51* (12), 1–10. https://doi.org/10.1038/s12276-019-0269-4.

(141) Vichova, T.; Motovska, Z. Oxidative Stress: Predictive Marker for Coronary Artery Disease. *Exp. Clin. Cardiol.* **2013**, *18* (2), e88–e91.

(142) Desai, K. M.; Chang, T.; Wang, H.; Banigesh, A.; Dhar, A.; Liu, J.; Untereiner, A.; Wu, L. Oxidative Stress and Aging: Is Methylglyoxal the Hidden Enemy? *Can. J. Physiol. Pharmacol.* **2010**, *88* (3), 273–284. https://doi.org/10.1139/Y10-001.

(143) PHILLIPS, S. A.; THORNALLEY, P. J. Formation of Methylglyoxal and D-Lactate in Human Red Blood Cells in Vitro. *Biochem. Soc. Trans.* **1993**, *21* (2), 163S-163S. https://doi.org/10.1042/bst021163s.

(144) Xue, J.; Ray, R.; Singer, D.; Böhme, D.; Burz, D. S.; Rai, V.; Hoffmann, R.; Shekhtman, A. The Receptor for Advanced Glycation End Products (RAGE) Specifically Recognizes Methylglyoxal-Derived AGEs. *Biochemistry* **2014**, *53* (20), 3327–3335. https://doi.org/10.1021/bi500046t.

(145) Cheng, A.-S.; Cheng, Y.-H.; Chiou, C.-H.; Chang, T.-L. Resveratrol Upregulates Nrf2 Expression to Attenuate Methylglyoxal-Induced Insulin Resistance in Hep G2 Cells. *J.*

Agric. Food Chem. **2012**, *60* (36), 9180–9187. https://doi.org/10.1021/jf302831d.

(146) Kim, S.; Choi, K. J.; Cho, S.-J.; Yun, S.-M.; Jeon, J.-P.; Koh, Y. H.; Song, J.; Johnson, G. V. W.; Jo, C. Fisetin Stimulates Autophagic Degradation of Phosphorylated Tau via the Activation of TFEB and Nrf2 Transcription Factors. *Sci. Rep.* **2016**, *6*, 24933. https://doi.org/10.1038/srep24933.

(147) Venkatraman, J.; Aggarwal, K.; Balaram, P. Helical Peptide Models for Protein Glycation: Proximity Effects in Catalysis of the Amadori Rearrangement. *Chem. Biol.* **2001**, *8* (7), 611–625. https://doi.org/10.1016/s1074-5521(01)00036-9.

(148) Verzijl, N.; DeGroot, J.; Thorpe, S. R.; Bank, R. A.; Shaw, J. N.; Lyons, T. J.; Bijlsma, J. W.; Lafeber, F. P.; Baynes, J. W.; TeKoppele, J. M. Effect of Collagen Turnover on the Accumulation of Advanced Glycation End Products. *J. Biol. Chem.* **2000**, *275* (50), 39027–39031. https://doi.org/10.1074/jbc.M006700200.

(149) Maeda, K.; Seymour, R.; Ruel, M.; Suuronen, E. J. Echocardiography-Guided Intramyocardial Injection Method in a Murine Model. *Methods Mol. Biol.* **2017**, *1553*, 217–225. https://doi.org/10.1007/978-1-4939-6756-8_17.

(150) Bauer, M.; Cheng, S.; Jain, M.; Ngoy, S.; Theodoropoulos, C.; Trujillo, A.; Lin, F.-C.; Liao, R. Echocardiographic Speckle-Tracking Based Strain Imaging for Rapid Cardiovascular Phenotyping in Mice. *Circ. Res.* **2011**, *108* (8), 908–916. https://doi.org/10.1161/CIRCRESAHA.110.239574.

(151) de Lucia, C.; Wallner, M.; Eaton, D. M.; Zhao, H.; Houser, S. R.; Koch, W. J. Echocardiographic Strain Analysis for the Early Detection of Left Ventricular Systolic/Diastolic Dysfunction and Dyssynchrony in a Mouse Model of Physiological Aging. *J. Gerontol. A. Biol. Sci. Med. Sci.* **2019**, *74* (4), 455–461. https://doi.org/10.1093/gerona/gly139.

(152) Want, E. J.; Masson, P.; Michopoulos, F.; Wilson, I. D.; Theodoridis, G.; Plumb, R. S.; Shockcor, J.; Loftus, N.; Holmes, E.; Nicholson, J. K. Global Metabolic Profiling of Animal and Human Tissues via UPLC-MS. *Nat. Protoc.* **2013**, *8* (1), 17–32. https://doi.org/10.1038/nprot.2012.135.

(153) Jin, M. J.; Kim, I. S.; Rehman, S. U.; Dong, M.-S.; Na, C.-S.; Yoo, H. H. A Liquid Chromatography-Tandem Mass Spectrometry Method for Simultaneous Quantitation of 10 Bioactive Components in Rhus Verniciflua Extracts. *J. Chromatogr. Sci.* **2016**, *54* (3), 390–396. https://doi.org/10.1093/chromsci/bmv152.

(154) Takagawa, J.; Zhang, Y.; Wong, M. L.; Sievers, R. E.; Kapasi, N. K.; Wang, Y.; Yeghiazarians, Y.; Lee, R. J.; Grossman, W.; Springer, M. L. Myocardial Infarct Size Measurement in the Mouse Chronic Infarction Model: Comparison of Area- and Length-Based Approaches. *J. Appl. Physiol.* **2007**, *102* (6), 2104–2111. https://doi.org/10.1152/japplphysiol.00033.2007.

(155) Savarese, G.; Lund, L. H. Global Public Health Burden of Heart Failure. *Card. Fail. Rev.* **2017**, *3* (1), 7–11. https://doi.org/10.15420/cfr.2016:25:2.

(156) Webster, K. A.; Discher, D. J.; Kaiser, S.; Hernandez, O.; Sato, B.; Bishopric, N. H.

Hypoxia-Activated Apoptosis of Cardiac Myocytes Requires Reoxygenation or a PH Shift and Is Independent of P53. *J. Clin. Invest.* **1999**, *104* (3), 239–252. https://doi.org/10.1172/JCI5871.

(157) Ramachandra, C. J. A.; Hernandez-Resendiz, S.; Crespo-Avilan, G. E.; Lin, Y.-H.; Hausenloy, D. J. Mitochondria in Acute Myocardial Infarction and Cardioprotection. *EBioMedicine* **2020**, *57*, 102884. https://doi.org/10.1016/j.ebiom.2020.102884.

(158) Tsutsui, H.; Kinugawa, S.; Matsushima, S. Oxidative Stress and Heart Failure. *Am. J. Physiol. Heart Circ. Physiol.* **2011**, *301* (6), H2181-90. https://doi.org/10.1152/ajpheart.00554.2011.

(159) Ceradini, D. J.; Yao, D.; Grogan, R. H.; Callaghan, M. J.; Edelstein, D.; Brownlee, M.; Gurtner, G. C. Decreasing Intracellular Superoxide Corrects Defective Ischemia-Induced New Vessel Formation in Diabetic Mice. *J. Biol. Chem.* **2008**, *283* (16), 10930–10938. https://doi.org/10.1074/jbc.M707451200.

(160) Akhand, A. A.; Hossain, K.; Mitsui, H.; Kato, M.; Miyata, T.; Inagi, R.; Du, J.; Takeda, K.; Kawamoto, Y.; Suzuki, H.; Kurokawa, K.; Nakashima, I. Glyoxal and Methylglyoxal Trigger Distinct Signals for Map Family Kinases and Caspase Activation in Human Endothelial Cells. *Free Radic. Biol. Med.* **2001**, *31* (1), 20–30. https://doi.org/10.1016/s0891-5849(01)00550-0.

(161) Lee, J. H.; Parveen, A.; Do, M. H.; Kang, M. C.; Yumnam, S.; Kim, S. Y. Molecular Mechanisms of Methylglyoxal-Induced Aortic Endothelial Dysfunction in Human Vascular Endothelial Cells. *Cell Death Dis.* **2020**, *11* (5), 403. https://doi.org/10.1038/s41419-020-2602-1.

(162) Cimenci, C. E.; Blackburn, N. J. R.; Sedlakova, V.; Pupkaite, J.; Munoz, M.; Rotstein, B. H.; Spiegel, D. A.; Alarcon, E. I.; Suuronen, E. J. Combined Methylglyoxal Scavenger and Collagen Hydrogel Therapy Prevents Adverse Remodeling and Improves Cardiac Function Post-Myocardial Infarction. *Adv. Funct. Mater.* **2022**, *32* (1), 2108630. https://doi.org/https://doi.org/10.1002/adfm.202108630.

(163) Zhong, Y.; Zhang, J.; Cheng, R.; Deng, C.; Meng, F.; Xie, F.; Zhong, Z. Reversibly Crosslinked Hyaluronic Acid Nanoparticles for Active Targeting and Intelligent Delivery of Doxorubicin to Drug Resistant CD44+ Human Breast Tumor Xenografts. *J. Control. Release* **2015**, *205*, 144–154. https://doi.org/10.1016/j.jconrel.2015.01.012.

(164) Fang, H.; Zhao, X.; Gu, X.; Sun, H.; Cheng, R.; Zhong, Z.; Deng, C. CD44-Targeted Multifunctional Nanomedicines Based on a Single-Component Hyaluronic Acid Conjugate with All-Natural Precursors: Construction and Treatment of Metastatic Breast Tumors in Vivo. *Biomacromolecules* **2020**, *21* (1), 104–113. https://doi.org/10.1021/acs.biomac.9b01012.

(165) Chen, J.; He, H.; Deng, C.; Yin, L.; Zhong, Z. Saporin-Loaded CD44 and EGFR Dual-Targeted Nanogels for Potent Inhibition of Metastatic Breast Cancer in Vivo. *Int. J. Pharm.* **2019**, *560*, 57–64. https://doi.org/10.1016/j.ijpharm.2019.01.040.

(166) Chen, J.; Ouyang, J.; Chen, Q.; Deng, C.; Meng, F.; Zhang, J.; Cheng, R.; Lan, Q.; Zhong, Z. EGFR and CD44 Dual-Targeted Multifunctional Hyaluronic Acid Nanogels Boost

Protein Delivery to Ovarian and Breast Cancers In Vitro and In Vivo. *ACS Appl. Mater. Interfaces* **2017**, *9* (28), 24140–24147. https://doi.org/10.1021/acsami.7b06879.

(167) Chen, J.; Zou, Y.; Deng, C.; Meng, F.; Zhang, J.; Zhong, Z. Multifunctional Click Hyaluronic Acid Nanogels for Targeted Protein Delivery and Effective Cancer Treatment in Vivo. *Chem. Mater.* **2016**, *28* (23), 8792–8799. https://doi.org/10.1021/acs.chemmater.6b04404.

(168) Mushtaq, G.; A. Khan, J.; Joseph, E.; A. Kamal, M. Nanoparticles, Neurotoxicity and Neurodegenerative Diseases.

(169) Spuch, C.; Saida, O.; Navarro, C. Advances in the Treatment of Neurodegenerative Disorders Employing Nanoparticles. *Recent Pat. Drug Deliv. Formul.* **2012**, *6* (1), 2–18. https://doi.org/10.2174/187221112799219125.

(170) Saraiva, C.; Praça, C.; Ferreira, R.; Santos, T.; Ferreira, L.; Bernardino, L. Nanoparticle-Mediated Brain Drug Delivery: Overcoming Blood–Brain Barrier to Treat Neurodegenerative Diseases. *J. Control. Release* **2016**, *235*, 34–47. https://doi.org/https://doi.org/10.1016/j.jconrel.2016.05.044.

(171) Lin, Y. D.; Yeh, M. L.; Yang, Y. J.; Tsai, D. C.; Chu, T. Y.; Shih, Y. Y.; Chang, M. Y.; Liu, Y. W.; Tang, A. C.; Chen, T. Y.; Luo, C. Y.; Chang, K. C.; Chen, J. H.; Wu, H. L.; Hung, T. K.; Hsieh, P. C. Intramyocardial Peptide Nanofiber Injection Improves Postinfarction Ventricular Remodeling and Efficacy of Bone Marrow Cell Therapy in Pigs. *Circulation* **2010**, *122* (11 Suppl), S132-41. https://doi.org/10.1161/CIRCULATIONAHA.110.939512.

(172) Patel, D. N.; Bailey, S. R. Nanotechnology in Cardiovascular Medicine. *Catheter. Cardiovasc. Interv. Off. J. Soc. Card. Angiogr. Interv.* **2007**, *69* (5), 643–654. https://doi.org/10.1002/ccd.21060.

(173) Khan, S.; Hasan, A.; Attar, F.; Sharifi, M.; Siddique, R.; Mraiche, F.; Falahati, M. Gold Nanoparticle-Based Platforms for Diagnosis and Treatment of Myocardial Infarction. *ACS Biomater. Sci. Eng.* **2020**, *6* (12), 6460–6477. https://doi.org/10.1021/acsbiomaterials.0c00955.

(174) Chacko, R. T.; Ventura, J.; Zhuang, J.; Thayumanavan, S. Polymer Nanogels: A Versatile Nanoscopic Drug Delivery Platform. *Adv. Drug Deliv. Rev.* **2012**, *64* (9), 836–851. https://doi.org/10.1016/j.addr.2012.02.002.

(175) Zhang, X.; Malhotra, S.; Molina, M.; Haag, R. Micro- and Nanogels with Labile Crosslinks – from Synthesis to Biomedical Applications. *Chem. Soc. Rev.* **2015**, *44* (7), 1948–1973. https://doi.org/10.1039/C4CS00341A.

(176) Lim, R. K. V; Lin, Q. Photoinducible Bioorthogonal Chemistry: A Spatiotemporally Controllable Tool to Visualize and Perturb Proteins in Live Cells. *Acc. Chem. Res.* **2011**, *44* (9), 828–839. https://doi.org/10.1021/ar200021p.

(177) Li, S.; Zhang, J.; Deng, C.; Meng, F.; Yu, L.; Zhong, Z. Redox-Sensitive and Intrinsically Fluorescent Photoclick Hyaluronic Acid Nanogels for Traceable and Targeted Delivery of Cytochrome c to Breast Tumor in Mice. *ACS Appl. Mater. Interfaces* **2016**, *8* (33), 21155–

21162. https://doi.org/10.1021/acsami.6b05775.

(178) Rao, N. V.; Yoon, H. Y.; Han, H. S.; Ko, H.; Son, S.; Lee, M.; Lee, H.; Jo, D.-G.; Kang, Y. M.; Park, J. H. Recent Developments in Hyaluronic Acid-Based Nanomedicine for Targeted Cancer Treatment. *Expert Opin. Drug Deliv.* **2016**, *13* (2), 239–252. https://doi.org/10.1517/17425247.2016.1112374.

(179) Mattheolabakis, G.; Milane, L.; Singh, A.; Amiji, M. M. Hyaluronic Acid Targeting of CD44 for Cancer Therapy: From Receptor Biology to Nanomedicine. *J. Drug Target.* **2015**, *23* (7–8), 605–618. https://doi.org/10.3109/1061186X.2015.1052072.

(180) Garcia, L. F.; Mataveli, F. D.; Mader, A. M. A. A.; Theodoro, T. R.; Justo, G. Z.; Pinhal, M. A. da S. Cells Involved in Extracellular Matrix Remodeling after Acute Myocardial Infarction. *Einstein (Sao Paulo).* **2015**, *13* (1), 89–95. https://doi.org/10.1590/S1679-45082015AO2970.

(181) Huebener, P.; Abou-Khamis, T.; Zymek, P.; Bujak, M.; Ying, X.; Chatila, K.; Haudek, S.; Thakker, G.; Frangogiannis, N. G. CD44 Is Critically Involved in Infarct Healing by Regulating the Inflammatory and Fibrotic Response. *J. Immunol.* **2008**, *180* (4), 2625–2633. https://doi.org/10.4049/jimmunol.180.4.2625.

(182) Chen, L.; Fu, C.; Zhang, Q.; He, C.; Zhang, F.; Wei, Q. The Role of CD44 in Pathological Angiogenesis. *FASEB J. Off. Publ. Fed. Am. Soc. Exp. Biol.* **2020**, *34* (10), 13125–13139. https://doi.org/10.1096/fj.202000380RR.

(183) Iyer, R. P.; Patterson, N. L.; Zouein, F. A.; Ma, Y.; Dive, V.; de Castro Brás, L. E.; Lindsey, M. L. Early Matrix Metalloproteinase-12 Inhibition Worsens Post-Myocardial Infarction Cardiac Dysfunction by Delaying Inflammation Resolution. *Int. J. Cardiol.* **2015**, *185*, 198–208. https://doi.org/10.1016/j.ijcard.2015.03.054.

(184) Rouschop, K. M. A.; Roelofs, J. J. T. H.; Claessen, N.; da Costa Martins, P.; Zwaginga, J.-J.; Pals, S. T.; Weening, J. J.; Florquin, S. Protection against Renal Ischemia Reperfusion Injury by CD44 Disruption. *J. Am. Soc. Nephrol.* **2005**, *16* (7), 2034–2043. https://doi.org/10.1681/ASN.2005010054.

(185) Lam, P.-L.; Wong, W.-Y.; Bian, Z.; Chui, C.-H.; Gambari, R. Recent Advances in Green Nanoparticulate Systems for Drug Delivery: Efficient Delivery and Safety Concern. *Nanomedicine (Lond).* **2017**, *12* (4), 357–385. https://doi.org/10.2217/nnm-2016-0305.

(186) Obeid, M. A.; Al Qaraghuli, M. M.; Alsaadi, M.; Alzahrani, A. R.; Niwasabutra, K.; Ferro, V. A. Delivering Natural Products and Biotherapeutics to Improve Drug Efficacy. *Ther. Deliv.* **2017**, *8* (11), 947–956. https://doi.org/10.4155/tde-2017-0060.

(187) Chen, F.; Ehlerding, E. B.; Cai, W. Theranostic Nanoparticles. *J. Nucl. Med.* **2014**, *55* (12), 1919–1922. https://doi.org/10.2967/jnumed.114.146019.

(188) Anani, T.; Rahmati, S.; Sultana, N.; David, A. E. MRI-Traceable Theranostic Nanoparticles for Targeted Cancer Treatment. *Theranostics* **2021**, *11* (2), 579–601. https://doi.org/10.7150/thno.48811.

(189) Zhong, Y.; Goltsche, K.; Cheng, L.; Xie, F.; Meng, F.; Deng, C.; Zhong, Z.; Haag, R. Hyaluronic Acid-Shelled Acid-Activatable Paclitaxel Prodrug Micelles Effectively Target

and Treat CD44-Overexpressing Human Breast Tumor Xenografts in Vivo. *Biomaterials* **2016**, *84*, 250–261. https://doi.org/10.1016/j.biomaterials.2016.01.049.

(190) Zhao, Q.; Geng, H.; Wang, Y.; Gao, Y.; Huang, J.; Wang, Y.; Zhang, J.; Wang, S. Hyaluronic Acid Oligosaccharide Modified Redox-Responsive Mesoporous Silica Nanoparticles for Targeted Drug Delivery. *ACS Appl. Mater. Interfaces* **2014**, *6* (22), 20290–20299. https://doi.org/10.1021/am505824d.

(191) GLO1 protein expression summary - The Human Protein Atlas https://www.proteinatlas.org/ENSG00000124767-GLO1 (accessed Jan 13, 2022).

(192) Hirsch, V.; Kinnear, C.; Moniatte, M.; Rothen-Rutishauser, B.; Clift, M. J. D.; Fink, A. Surface Charge of Polymer Coated SPIONs Influences the Serum Protein Adsorption, Colloidal Stability and Subsequent Cell Interaction in Vitro. *Nanoscale* **2013**, *5* (9), 3723–3732. https://doi.org/10.1039/C2NR33134A.

(193) NJR, B.; B, V.; B, M.; CE, C.; A, A.; M, G.-G.; A, O.; Z, Z.; M, B.; PJ, B.; RW, M.; EJ, S. Methylglyoxal-Derived Advanced Glycation End Products Contribute to Negative Cardiac Remodeling and Dysfunction Post-Myocardial Infarction. *Basic Res. Cardiol.* **2017**, *112* (5). https://doi.org/10.1007/S00395-017-0646-X.

(194) Li, F.; Wang, Z.; Hu, F.; Su, L. Cell Culture Models and Animal Models for HBV Study. *Adv. Exp. Med. Biol.* **2020**, *1179*, 109–135. https://doi.org/10.1007/978-981-13-9151-4_5.

(195) Herweijer, H.; Wolff, J. A. Gene Therapy Progress and Prospects: Hydrodynamic Gene Delivery. *Gene Ther.* **2007**, *14* (2), 99–107. https://doi.org/10.1038/sj.gt.3302891.

(196) Dalsgaard, T.; Cecchi, C. R.; Askou, A. L.; Bak, R. O.; Andersen, P. O.; Hougaard, D.; Jensen, T. G.; Dagnæs-Hansen, F.; Mikkelsen, J. G.; Corydon, T. J.; Aagaard, L. Improved Lentiviral Gene Delivery to Mouse Liver by Hydrodynamic Vector Injection through Tail Vein. *Mol. Ther. - Nucleic Acids* **2018**, *12*, 672–683. https://doi.org/https://doi.org/10.1016/j.omtn.2018.07.005.

(197) Cieslewicz, M.; Tang, J.; Yu, J. L.; Cao, H.; Zavaljevski, M.; Motoyama, K.; Lieber, A.; Raines, E. W.; Pun, S. H. Targeted Delivery of Proapoptotic Peptides to Tumor-Associated Macrophages Improves Survival. *Proc. Natl. Acad. Sci.* **2013**, *110* (40), 15919–15924. https://doi.org/10.1073/PNAS.1312197110.

(198) Callmann, C. E.; Barback, C. V; Thompson, M. P.; Hall, D. J.; Mattrey, R. F.; Gianneschi, N. C. Therapeutic Enzyme-Responsive Nanoparticles for Targeted Delivery and Accumulation in Tumors. *Adv. Mater.* **2015**, *27* (31), 4611–4615. https://doi.org/10.1002/adma.201501803.

(199) He, S.; Hu, Q.; Xu, X.; Niu, Y.; Chen, Y.; Lu, Y.; Su, Q.; Qin, L. Advanced Glycation End Products Enhance M1 Macrophage Polarization by Activating the MAPK Pathway. *Biochem. Biophys. Res. Commun.* **2020**, *525* (2), 334–340. https://doi.org/https://doi.org/10.1016/j.bbrc.2020.02.053.

(200) Masterjohn, C.; Mah, E.; Park, Y.; Pei, R.; Lee, J.; Manautou, J. E.; Bruno, R. S. Acute Glutathione Depletion Induces Hepatic Methylglyoxal Accumulation by Impairing Its Detoxification to D-Lactate. *Exp. Biol. Med. (Maywood).* **2013**, *238* (4), 360–369.

https://doi.org/10.1177/1535370213477987.

(201) Kammerscheit, X.; Hecker, A.; Rouhier, N.; Chauvat, F.; Cassier-Chauvat, C. Methylglyoxal Detoxification Revisited: Role of Glutathione Transferase in Model Cyanobacterium Synechocystis Sp. Strain PCC 6803 . *MBio* **2020**, *11* (4). https://doi.org/10.1128/MBIO.00882-20/ASSET/2C70EF35-7BCD-4F5C-9614-FCDE28CC6EFA/ASSETS/GRAPHIC/MBIO.00882-20-F0007.JPEG.

(202) Delle Monache, S.; Pulcini, F.; Frosini, R.; Mattei, V.; Talesa, V. N.; Antognelli, C. Methylglyoxal-Dependent Glycative Stress Is Prevented by the Natural Antioxidant Oleuropein in Human Dental Pulp Stem Cells through Nrf2/Glo1 Pathway. *Antioxidants (Basel, Switzerland)* **2021**, *10* (5), 716. https://doi.org/10.3390/antiox10050716.

(203) Turner, P. V; Brabb, T.; Pekow, C.; Vasbinder, M. A. Administration of Substances to Laboratory Animals: Routes of Administration and Factors to Consider. *J. Am. Assoc. Lab. Anim. Sci.* **2011**, *50* (5), 600–613.

(204) Human Glyoxalase I (GLO1) ELISA Kit | Abbexa Ltd https://www.abbexa.com/glo1-elisa-kit-1 (accessed Jan 6, 2022).

(205) Organization, W. H. Noncommunicable Diseases.

(206) of Canada, P. H. A. No Title. 2017.

(207) Vujic, A.; Natarajan, N.; Lee, R. T. Molecular Mechanisms of Heart Regeneration. *Semin Cell Dev Biol* **2020**, *100*, 20–28. https://doi.org/10.1016/j.semcdb.2019.09.003.

(208) Stroke, H. The Burden of Heart Failure. 2016.

(209) Puntmann, V. O.; Carerj, M. L.; Wieters, I.; Fahim, M.; Arendt, C.; Hoffmann, J.; Shchendrygina, A.; Escher, F.; Vasa-Nicotera, M.; Zeiher, A. M.; Vehreschild, M.; Nagel, E. Outcomes of Cardiovascular Magnetic Resonance Imaging in Patients Recently Recovered From Coronavirus Disease 2019 (COVID-19). *JAMA Cardiol* **2020**, *5* (11), 1265–1273. https://doi.org/10.1001/jamacardio.2020.3557.

(210) Buono, A.; Ammirati, E. ST-Elevation Acute Myocardial Infarction during COVID-19 Pandemic: Are We Missing the Boat? *Int J Cardiol Hear. Vasc* **2020**, *29*, 100578. https://doi.org/10.1016/j.ijcha.2020.100578.

(211) Gluckman, T. J.; Wilson, M. A.; Chiu, S. T.; Penny, B. W.; Chepuri, V. B.; Waggoner, J. W.; Spinelli, K. J. Case Rates, Treatment Approaches, and Outcomes in Acute Myocardial Infarction During the Coronavirus Disease 2019 Pandemic. *JAMA Cardiol* **2020**, *5* (12), 1419–1424. https://doi.org/10.1001/jamacardio.2020.3629.

(212) Hosoyama, K.; Ahumada, M.; McTiernan, C. D.; Davis, D. R.; Variola, F.; Ruel, M.; Liang, W.; Suuronen, E. J.; Alarcon, E. I. Nanoengineered Electroconductive Collagen-Based Cardiac Patch for Infarcted Myocardium Repair. *ACS Appl Mater Interfaces* **2018**, *10* (51), 44668–44677. https://doi.org/10.1021/acsami.8b18844.

(213) Shevach, M.; Fleischer, S.; Shapira, A.; Dvir, T. Gold Nanoparticle-Decellularized Matrix Hybrids for Cardiac Tissue Engineering. *Nano Lett* **2014**, *14* (10), 5792–5796. https://doi.org/10.1021/nl502673m.

(214) Orza, A.; Soritau, O.; Olenic, L.; Diudea, M.; Florea, A.; Rus Ciuca, D.; Mihu, C.; Casciano, D.; Biris, A. S. Electrically Conductive Gold-Coated Collagen Nanofibers for Placental-Derived Mesenchymal Stem Cells Enhanced Differentiation and Proliferation. *ACS Nano* **2011**, *5* (6), 4490–4503. https://doi.org/10.1021/nn1035312.

(215) Yang, F.; Liu, Y. H.; Yang, X. P.; Xu, J.; Kapke, A.; Carretero, O. A. Myocardial Infarction and Cardiac Remodelling in Mice. *Exp Physiol* **2002**, *87* (5), 547–555. https://doi.org/10.1113/eph8702385.

(216) Christia, P.; Bujak, M.; Gonzalez-Quesada, C.; Chen, W.; Dobaczewski, M.; Reddy, A.; Frangogiannis, N. G. Systematic Characterization of Myocardial Inflammation, Repair, and Remodeling in a Mouse Model of Reperfused Myocardial Infarction. *J Histochem Cytochem* **2013**, *61* (8), 555–570. https://doi.org/10.1369/0022155413493912.

(217) Lazurko, C.; Khatoon, Z.; Goel, K.; Sedlakova, V.; Eren Cimenci, C.; Ahumada, M.; Zhang, L.; Mah, T. F.; Franco, W.; Suuronen, E. J.; Alarcon, E. I. Multifunctional Nano and Collagen-Based Therapeutic Materials for Skin Repair. *ACS Biomater Sci Eng* **2020**, *6* (2), 1124–1134. https://doi.org/10.1021/acsbiomaterials.9b01281.

(218) Khatoon, Z.; Guzmán-Soto, I.; McTiernan, C. D.; Lazurko, C.; Simpson, F.; Zhang, L.; Cortes, D.; Mah, T.-F.; Griffith, M.; Alarcon, E. I. Nanoengineering the Surface of Corneal Implants: Towards Functional Anti-Microbial and Biofilm Materials. *RSC Adv.* **2020**, *10* (40), 23675–23681. https://doi.org/10.1039/d0ra03659e.

(219) Goel, K.; Zuniga-Bustos, M.; Lazurko, C.; Jacques, E.; Galaz-Araya, C.; Valenzuela-Henriquez, F.; Pacioni, N. L.; Couture, J. F.; Poblete, H.; Alarcon, E. I. Nanoparticle Concentration vs Surface Area in the Interaction of Thiol-Containing Molecules: Toward a Rational Nanoarchitectural Design of Hybrid Materials. *ACS Appl Mater Interfaces* **2019**, *11* (19), 17697–17705. https://doi.org/10.1021/acsami.9b03942.

(220) Hosoyama, K.; Ahumada, M.; McTiernan, C. D.; Bejjani, J.; Variola, F.; Ruel, M.; Xu, B.; Liang, W.; Suuronen, E. J.; Alarcon, E. I. Multi-Functional Thermo-Crosslinkable Collagen-Metal Nanoparticle Composites for Tissue Regeneration: Nanosilver vs. Nanogold. *RSC Adv.* **2017**, *7* (75), 47704–47708. https://doi.org/10.1039/c7ra08960k.

(221) Allison, S.; Ahumada, M.; Andronic, C.; McNeill, B.; Variola, F.; Griffith, M.; Ruel, M.; Hamel, V.; Liang, W.; Suuronen, E. J.; Alarcon, E. I. Electroconductive Nanoengineered Biomimetic Hybrid Fibers for Cardiac Tissue Engineering. *J Mater Chem B* **2017**, *5* (13), 2402–2406. https://doi.org/10.1039/c7tb00405b.

(222) Ahumada, M.; Jacques, E.; Andronic, C.; Comer, J.; Poblete, H.; Alarcon, E. I. Novel Specific Peptides as Superior Surface Stabilizers for Silver Nano Structures: Role of Peptide Chain Length. *J Mater Chem B* **2017**, *5* (45), 8925–8928. https://doi.org/10.1039/c7tb02349a.

(223) Poblete, H.; Agarwal, A.; Thomas, S. S.; Bohne, C.; Ravichandran, R.; Phopase, J.; Comer, J.; Alarcon, E. I. New Insights into Peptide-Silver Nanoparticle Interaction: Deciphering the Role of Cysteine and Lysine in the Peptide Sequence. *Langmuir* **2016**, *32* (1), 265–273. https://doi.org/10.1021/acs.langmuir.5b03601.

(224) Alarcon, E. I.; Vulesevic, B.; Argawal, A.; Ross, A.; Bejjani, P.; Podrebarac, J.;

Ravichandran, R.; Phopase, J.; Suuronen, E. J.; Griffith, M. Coloured Cornea Replacements with Anti-Infective Properties: Expanding the Safe Use of Silver Nanoparticles in Regenerative Medicine. *Nanoscale* **2016**, *8* (12), 6484–6489. https://doi.org/10.1039/c6nr01339b.

(225) Gao, W.; Zhang, Y.; Zhang, Q.; Zhang, L. Nanoparticle-Hydrogel: A Hybrid Biomaterial System for Localized Drug Delivery. *Ann Biomed Eng* **2016**, *44* (6), 2049–2061. https://doi.org/10.1007/s10439-016-1583-9.

(226) Mitsudome, T.; Kaneda, K. Gold Nanoparticle Catalysts for Selective Hydrogenations. *Green Chem.* **2013**, *15* (10), 2636–2654. https://doi.org/10.1039/c3gc41360h.

(227) Kyriazi, M. E.; Giust, D.; El-Sagheer, A. H.; Lackie, P. M.; Muskens, O. L.; Brown, T.; Kanaras, A. G. Multiplexed MRNA Sensing and Combinatorial-Targeted Drug Delivery Using DNA-Gold Nanoparticle Dimers. *ACS Nano* **2018**, *12* (4), 3333–3340. https://doi.org/10.1021/acsnano.7b08620.

(228) Zeng, Y.; Shinada, K.; Hano, K.; Sui, L.; Yang, T.; Li, X.; Himaki, T. Effects of Tris (2-Carboxyethyl) Phosphine Hydrochloride Treatment on Porcine Oocyte in Vitro Maturation and Subsequent in Vitro Fertilized Embryo Developmental Capacity. *Theriogenology* **2021**, *162*, 32–41. https://doi.org/10.1016/j.theriogenology.2020.12.027.

(229) Menchise, V.; Digilio, G.; Gianolio, E.; Cittadino, E.; Catanzaro, V.; Carrera, C.; Aime, S. In Vivo Labeling of B16 Melanoma Tumor Xenograft with a Thiol-Reactive Gadolinium Based MRI Contrast Agent. *Mol Pharm* **2011**, *8* (5), 1750–1756. https://doi.org/10.1021/mp2001044.

(230) Swanson, K. I.; Schlieve, C. R.; Lieven, C. J.; Levin, L. A. Neuroprotective Effect of Sulfhydryl Reduction in a Rat Optic Nerve Crush Model. *Invest Ophthalmol Vis Sci* **2005**, *46* (10), 3737–3741. https://doi.org/10.1167/iovs.05-0155.

(231) Federal Register / Vol. 77 No. 58 / Monday, M. 26 2012 / R.; Regulations. Safety Data Sheet Tris (2-Carboxyethyl) Phosphine-HCl. 2017.

(232) Marini, J. L.; Saxena, S. J. Luminate Eye Gel. 2015.

(233) Surh, I.; Behl, M.; Elmore, S. A.; Chhabra, R. S. Comparative Dermal Toxicity of Dicyclohexylcarbodiimide and Diisopropylcarbodiimide in Rodents. *Cutan Ocul Toxicol* **2012**, *31* (3), 177–187. https://doi.org/10.3109/15569527.2011.629384.

(234) Ahn, J. I.; Kuffova, L.; Merrett, K.; Mitra, D.; Forrester, J. V; Li, F.; Griffith, M. Crosslinked Collagen Hydrogels as Corneal Implants: Effects of Sterically Bulky vs. Non-Bulky Carbodiimides as Crosslinkers. *Acta Biomater* **2013**, *9* (8), 7796–7805. https://doi.org/10.1016/j.actbio.2013.04.014.

(235) Vyborny, K.; Vallova, J.; Koci, Z.; Kekulova, K.; Jirakova, K.; Jendelova, P.; Hodan, J.; Kubinova, S. Genipin and EDC Crosslinking of Extracellular Matrix Hydrogel Derived from Human Umbilical Cord for Neural Tissue Repair. *Sci Rep* **2019**, *9* (1), 10674. https://doi.org/10.1038/s41598-019-47059-x.

(236) Thoreson, A. R.; Hiwatari, R.; An, K. N.; Amadio, P. C.; Zhao, C. The Effect of 1-Ethyl-3-(3-Dimethylaminopropyl) Carbodiimide Suture Coating on Tendon Repair Strength and

Cell Viability in a Canine Model. *J Hand Surg Am* **2015**, *40* (10), 1986–1991. https://doi.org/10.1016/j.jhsa.2015.06.117.

(237) Nagai, N.; Saijo, S.; Song, Y.; Kaji, H.; Abe, T. A Drug Refillable Device for Transscleral Sustained Drug Delivery to the Retina. *Eur J Pharm Biopharm* **2019**, *136*, 184–191. https://doi.org/10.1016/j.ejpb.2019.01.024.

(238) Fischer, M. J. E. Amine Coupling Through EDC/NHS: A Practical Approach. In *Surface Plasmon Resonance: Methods and Protocols*; Mol, N. J., Fischer, M. J. E., Eds.; Humana Press: Totowa, NJ, 2010; pp 55–73. https://doi.org/10.1007/978-1-60761-670-2_3.

(239) Bailly, A. L.; Correard, F.; Popov, A.; Tselikov, G.; Chaspoul, F.; Appay, R.; Al-Kattan, A.; Kabashin, A. V; Braguer, D.; Esteve, M. A. In Vivo Evaluation of Safety, Biodistribution and Pharmacokinetics of Laser-Synthesized Gold Nanoparticles. *Sci Rep* **2019**, *9* (1), 12890. https://doi.org/10.1038/s41598-019-48748-3.

(240) Yang, L.; Kuang, H.; Zhang, W.; Aguilar, Z. P.; Wei, H.; Xu, H. Comparisons of the Biodistribution and Toxicological Examinations after Repeated Intravenous Administration of Silver and Gold Nanoparticles in Mice. *Sci Rep* **2017**, *7* (1), 3303. https://doi.org/10.1038/s41598-017-03015-1.

(241) Sani, A.; Cao, C.; Cui, D. Toxicity of Gold Nanoparticles (AuNPs): A Review. *Biochem Biophys Rep* **2021**, *26*, 100991. https://doi.org/10.1016/j.bbrep.2021.100991.

(242) Fratoddi, I.; Venditti, I.; Cametti, C.; Russo, M. V. How Toxic Are Gold Nanoparticles? The State-of-the-Art. *Nano Res.* **2015**, *8* (6), 1771–1799. https://doi.org/10.1007/s12274-014-0697-3.

(243) Lin, J.; Alexander-Katz, A. Cell Membranes Open "Doors" for Cationic Nanoparticles/Biomolecules: Insights into Uptake Kinetics. *ACS Nano* **2013**, *7* (12), 10799–10808. https://doi.org/10.1021/nn4040553.

(244) Bei, Y.; Pan, L. L.; Zhou, Q.; Zhao, C.; Xie, Y.; Wu, C.; Meng, X.; Gu, H.; Xu, J.; Zhou, L.; Sluijter, J. P. G.; Das, S.; Agerberth, B.; Sun, J.; Xiao, J. Cathelicidin-Related Antimicrobial Peptide Protects against Myocardial Ischemia/Reperfusion Injury. *BMC Med* **2019**, *17* (1), 42. https://doi.org/10.1186/s12916-019-1268-y.

(245) Edfeldt, K.; Agerberth, B.; Rottenberg, M. E.; Gudmundsson, G. H.; Wang, X. B.; Mandal, K.; Xu, Q.; Yan, Z. Q. Involvement of the Antimicrobial Peptide LL-37 in Human Atherosclerosis. *Arter. Thromb Vasc Biol* **2006**, *26* (7), 1551–1557. https://doi.org/10.1161/01.ATV.0000223901.08459.57.

(246) Mooney, E.; Mackle, J. N.; Blond, D. J.; O'Cearbhaill, E.; Shaw, G.; Blau, W. J.; Barry, F. P.; Barron, V.; Murphy, J. M. The Electrical Stimulation of Carbon Nanotubes to Provide a Cardiomimetic Cue to MSCs. *Biomaterials* **2012**, *33* (26), 6132–6139. https://doi.org/10.1016/j.biomaterials.2012.05.032.

(247) Hardy, J. G.; Lee, J. Y.; Schmidt, C. E. Biomimetic Conducting Polymer-Based Tissue Scaffolds. *Curr Opin Biotechnol* **2013**, *24* (5), 847–854. https://doi.org/10.1016/j.copbio.2013.03.011.

(248) Wang, J. J.; Christman, K. L. Hydrogels for Cardiac Repair. In *Cardiac Regeneration and*

Repair; Li, R.-K., Weisel, R. D., Eds.; Woodhead Publishing, 2014; pp 17–48. https://doi.org/10.1533/9780857096715.1.17.

(249) Dorsey, S. M.; McGarvey, J. R.; Wang, H.; Nikou, A.; Arama, L.; Koomalsingh, K. J.; Kondo, N.; Gorman J. H., 3rd; Pilla, J. J.; Gorman, R. C.; Wenk, J. F.; Burdick, J. A. MRI Evaluation of Injectable Hyaluronic Acid-Based Hydrogel Therapy to Limit Ventricular Remodeling after Myocardial Infarction. *Biomaterials* **2015**, *69* (1878-5905 (Electronic)), 65–75. https://doi.org/10.1016/j.biomaterials.2015.08.011.

(250) Lakshmanan, R.; Krishnan, U. M.; Sethuraman, S. Polymeric Scaffold Aided Stem Cell Therapeutics for Cardiac Muscle Repair and Regeneration. *Macromol Biosci* **2013**, *13* (9), 1119–1134. https://doi.org/10.1002/mabi.201300223.

(251) Rao, S. V; Zeymer, U.; Douglas, P. S.; Al-Khalidi, H.; Liu, J.; Gibson, C. M.; Harrison, R. W.; Joseph, D. S.; Heyrman, R.; Krucoff, M. W. A Randomized, Double-Blind, Placebo-Controlled Trial to Evaluate the Safety and Effectiveness of Intracoronary Application of a Novel Bioabsorbable Cardiac Matrix for the Prevention of Ventricular Remodeling after Large ST-Segment Elevation Myocardial Inf. *Am Hear. J* **2015**, *170* (5), 929–937. https://doi.org/10.1016/j.ahj.2015.08.017.

(252) Anker, S. D.; Coats, A. J.; Cristian, G.; Dragomir, D.; Pusineri, E.; Piredda, M.; Bettari, L.; Dowling, R.; Volterrani, M.; Kirwan, B. A.; Filippatos, G.; Mas, J. L.; Danchin, N.; Solomon, S. D.; Lee, R. J.; Ahmann, F.; Hinson, A.; Sabbah, H. N.; Mann, D. L. A Prospective Comparison of Alginate-Hydrogel with Standard Medical Therapy to Determine Impact on Functional Capacity and Clinical Outcomes in Patients with Advanced Heart Failure (AUGMENT-HF Trial). *Eur Hear. J* **2015**, *36* (34), 2297–2309. https://doi.org/10.1093/eurheartj/ehv259.

(253) Rane, A. A.; Chuang, J. S.; Shah, A.; Hu, D. P.; Dalton, N. D.; Gu, Y.; Peterson, K. L.; Omens, J. H.; Christman, K. L. Increased Infarct Wall Thickness by a Bio-Inert Material Is Insufficient to Prevent Negative Left Ventricular Remodeling after Myocardial Infarction. *PLoS One* **2011**, *6* (6), e21571. https://doi.org/10.1371/journal.pone.0021571.

(254) Ghasemi-Mobarakeh, L.; Prabhakaran, M. P.; Morshed, M.; Nasr-Esfahani, M. H.; Baharvand, H.; Kiani, S.; Al-Deyab, S. S.; Ramakrishna, S. Application of Conductive Polymers, Scaffolds and Electrical Stimulation for Nerve Tissue Engineering. *J Tissue Eng Regen Med* **2011**, *5* (4), e17-35. https://doi.org/10.1002/term.383.

(255) Jin, G.; Li, K. The Electrically Conductive Scaffold as the Skeleton of Stem Cell Niche in Regenerative Medicine. *Mater Sci Eng C Mater Biol Appl* **2014**, *45*, 671–681. https://doi.org/10.1016/j.msec.2014.06.004.

(256) Baheiraei, N.; Yeganeh, H.; Ai, J.; Gharibi, R.; Azami, M.; Faghihi, F. Synthesis, Characterization and Antioxidant Activity of a Novel Electroactive and Biodegradable Polyurethane for Cardiac Tissue Engineering Application. *Mater Sci Eng C Mater Biol Appl* **2014**, *44*, 24–37. https://doi.org/10.1016/j.msec.2014.07.061.

(257) Bidez P. R., 3rd; Li, S.; Macdiarmid, A. G.; Venancio, E. C.; Wei, Y.; Lelkes, P. I. Polyaniline, an Electroactive Polymer, Supports Adhesion and Proliferation of Cardiac Myoblasts. *J Biomater Sci Polym Ed* **2006**, *17* (1–2), 199–212.

https://doi.org/10.1163/156856206774879180.

(258) Shin, S. R.; Jung, S. M.; Zalabany, M.; Kim, K.; Zorlutuna, P.; Kim, S. B.; Nikkhah, M.; Khabiry, M.; Azize, M.; Kong, J.; Wan, K. T.; Palacios, T.; Dokmeci, M. R.; Bae, H.; Tang, X. S.; Khademhosseini, A. Carbon-Nanotube-Embedded Hydrogel Sheets for Engineering Cardiac Constructs and Bioactuators. *ACS Nano* **2013**, *7* (3), 2369–2380. https://doi.org/10.1021/nn305559j.

(259) Wang, L.; Wu, Y.; Hu, T.; Guo, B.; Ma, P. X. Electrospun Conductive Nanofibrous Scaffolds for Engineering Cardiac Tissue and 3D Bioactuators. *Acta Biomater* **2017**, *59*, 68–81. https://doi.org/10.1016/j.actbio.2017.06.036.

(260) Mihic, A.; Cui, Z.; Wu, J.; Vlacic, G.; Miyagi, Y.; Li, S. H.; Lu, S.; Sung, H. W.; Weisel, R. D.; Li, R. K. A Conductive Polymer Hydrogel Supports Cell Electrical Signaling and Improves Cardiac Function After Implantation into Myocardial Infarct. *Circulation* **2015**, *132* (8), 772–784. https://doi.org/10.1161/CIRCULATIONAHA.114.014937.

(261) Martinelli, V.; Cellot, G.; Toma, F. M.; Long, C. S.; Caldwell, J. H.; Zentilin, L.; Giacca, M.; Turco, A.; Prato, M.; Ballerini, L.; Mestroni, L. Carbon Nanotubes Promote Growth and Spontaneous Electrical Activity in Cultured Cardiac Myocytes. *Nano Lett* **2012**, *12* (4), 1831–1838. https://doi.org/10.1021/nl204064s.

(262) Stout, D. A.; Basu, B.; Webster, T. J. Poly(Lactic-Co-Glycolic Acid): Carbon Nanofiber Composites for Myocardial Tissue Engineering Applications. *Acta Biomater* **2011**, *7* (8), 3101–3112. https://doi.org/10.1016/j.actbio.2011.04.028.

(263) You, J. O.; Rafat, M.; Ye, G. J.; Auguste, D. T. Nanoengineering the Heart: Conductive Scaffolds Enhance Connexin 43 Expression. *Nano Lett* **2011**, *11* (9), 3643–3648. https://doi.org/10.1021/nl201514a.

(264) Stout, D. A.; Yoo, J.; Santiago-Miranda, A. N.; Webster, T. J. Mechanisms of Greater Cardiomyocyte Functions on Conductive Nanoengineered Composites for Cardiovascular Application. *Int J Nanomedicine* **2012**, *7*, 5653–5669. https://doi.org/10.2147/IJN.S34574.

(265) Annabi, N.; Shin, S. R.; Tamayol, A.; Miscuglio, M.; Bakooshli, M. A.; Assmann, A.; Mostafalu, P.; Sun, J. Y.; Mithieux, S.; Cheung, L.; Tang, X. S.; Weiss, A. S.; Khademhosseini, A. Highly Elastic and Conductive Human-Based Protein Hybrid Hydrogels. *Adv Mater* **2016**, *28* (1), 40–49. https://doi.org/10.1002/adma.201503255.

(266) Park, J.; Kim, Y. S.; Ryu, S.; Kang, W. S.; Park, S.; Han, J.; Jeong, H. C.; Hong, B. H.; Ahn, Y.; Kim, B.-S. Graphene Potentiates the Myocardial Repair Efficacy of Mesenchymal Stem Cells by Stimulating the Expression of Angiogenic Growth Factors and Gap Junction Protein. *Adv. Funct. Mater.* **2015**, *25* (17), 2590–2600. https://doi.org/10.1002/adfm.201500365.

(267) Ahadian, S.; Zhou, Y.; Yamada, S.; Estili, M.; Liang, X.; Nakajima, K.; Shiku, H.; Matsue, T. Graphene Induces Spontaneous Cardiac Differentiation in Embryoid Bodies. *Nanoscale* **2016**, *8* (13), 7075–7084. https://doi.org/10.1039/c5nr07059g.

(268) Baei, P.; Jalili-Firoozinezhad, S.; Rajabi-Zeleti, S.; Tafazzoli-Shadpour, M.; Baharvand, H.; Aghdami, N. Electrically Conductive Gold Nanoparticle-Chitosan Thermosensitive

Hydrogels for Cardiac Tissue Engineering. *Mater Sci Eng C Mater Biol Appl* **2016**, *63*, 131–141. https://doi.org/10.1016/j.msec.2016.02.056.

(269) Gosens, I.; Cassee, F. R.; Zanella, M.; Manodori, L.; Brunelli, A.; Costa, A. L.; Bokkers, B. G.; de Jong, W. H.; Brown, D.; Hristozov, D.; Stone, V. Organ Burden and Pulmonary Toxicity of Nano-Sized Copper (II) Oxide Particles after Short-Term Inhalation Exposure. *Nanotoxicology* **2016**, *10* (8), 1084–1095. https://doi.org/10.3109/17435390.2016.1172678.

(270) Falagan-Lotsch, P.; Grzincic, E. M.; Murphy, C. J. One Low-Dose Exposure of Gold Nanoparticles Induces Long-Term Changes in Human Cells. *Proc Natl Acad Sci U S A* **2016**, *113* (47), 13318–13323. https://doi.org/10.1073/pnas.1616400113.

(271) Adewale, O. B.; Davids, H.; Cairncross, L.; Roux, S. Toxicological Behavior of Gold Nanoparticles on Various Models: Influence of Physicochemical Properties and Other Factors. *Int J Toxicol* **2019**, *38* (5), 357–384. https://doi.org/10.1177/1091581819863130.

(272) Alarcon, E. I.; Udekwu, K.; Skog, M.; Pacioni, N. L.; Stamplecoskie, K. G.; Gonzalez-Bejar, M.; Polisetti, N.; Wickham, A.; Richter-Dahlfors, A.; Griffith, M.; Scaiano, J. C. The Biocompatibility and Antibacterial Properties of Collagen-Stabilized, Photochemically Prepared Silver Nanoparticles. *Biomaterials* **2012**, *33* (19), 4947–4956. https://doi.org/10.1016/j.biomaterials.2012.03.033.

(273) Vignoni, M.; de Alwis Weerasekera, H.; Simpson, M. J.; Phopase, J.; Mah, T.-F.; Griffith, M.; Alarcon, E. I.; Scaiano, J. C. LL37 Peptide@silver Nanoparticles: Combining the Best of the Two Worlds for Skin Infection Control. *Nanoscale* **2014**, *6* (11), 5725–5728. https://doi.org/10.1039/c4nr01284d.

(274) Ahumada, M.; Bohne, C.; Oake, J.; Alarcon, E. I. Protein Capped Nanosilver Free Radical Oxidation: Role of Biomolecule Capping on Nanoparticle Colloidal Stability and Protein Oxidation. *Chem Commun* **2018**, *54* (37), 4724–4727. https://doi.org/10.1039/c7cc08629f.

(275) Bromma, K.; Chithrani, D. B. Advances in Gold Nanoparticle-Based Combined Cancer Therapy. *Nanomater.* **2020**, *10* (9). https://doi.org/10.3390/nano10091671.

(276) Singh, P.; Pandit, S.; Mokkapati, V.; Garg, A.; Ravikumar, V.; Mijakovic, I. Gold Nanoparticles in Diagnostics and Therapeutics for Human Cancer. *Int J Mol Sci* **2018**, *19* (7). https://doi.org/10.3390/ijms19071979.

(277) Yang, C.; Tian, A.; Li, Z. Reversible Cardiac Hypertrophy Induced by PEG-Coated Gold Nanoparticles in Mice. *Sci Rep* **2016**, *6*, 20203. https://doi.org/10.1038/srep20203.

(278) Hirota, J.; Shimizu, S. Routes of Administration. In *The Laboratory Mouse*; 2012; pp 709–725. https://doi.org/10.1016/b978-0-12-382008-2.00030-1.

(279) Machholz, E.; Mulder, G.; Ruiz, C.; Corning, B. F.; Pritchett-Corning, K. R. Manual Restraint and Common Compound Administration Routes in Mice and Rats. *J Vis Exp* **2012**, No. 67. https://doi.org/10.3791/2771.

(280) Tang, J.; Vandergriff, A.; Wang, Z.; Hensley, M. T.; Cores, J.; Allen, T. A.; Dinh, P. U.; Zhang, J.; Caranasos, T. G.; Cheng, K. A Regenerative Cardiac Patch Formed by Spray Painting of Biomaterials onto the Heart. *Tissue Eng Part C Methods* **2017**, *23* (3), 146–

155. https://doi.org/10.1089/ten.TEC.2016.0492.

(281) Amoros-Figueras, G.; Jorge, E.; Alonso-Martin, C.; Traver, D.; Ballesta, M.; Bragos, R.; Rosell-Ferrer, J.; Cinca, J. Endocardial Infarct Scar Recognition by Myocardial Electrical Impedance Is Not Influenced by Changes in Cardiac Activation Sequence. *Hear. Rhythm* **2018**, *15* (4), 589–596. https://doi.org/10.1016/j.hrthm.2017.11.031.

(282) Amoros-Figueras, G.; Jorge, E.; Garcia-Sanchez, T.; Bragos, R.; Rosell-Ferrer, J.; Cinca, J. Recognition of Fibrotic Infarct Density by the Pattern of Local Systolic-Diastolic Myocardial Electrical Impedance. *Front Physiol* **2016**, *7*, 389. https://doi.org/10.3389/fphys.2016.00389.

(283) Salazar, Y.; Bragos, R.; Casas, O.; Cinca, J.; Rosell, J. Transmural versus Nontransmural in Situ Electrical Impedance Spectrum for Healthy, Ischemic, and Healed Myocardium. *IEEE Trans Biomed Eng* **2004**, *51* (8), 1421–1427. https://doi.org/10.1109/TBME.2004.828030.

(284) Wolf, T.; Gepstein, L.; Hayam, G.; Zaretzky, A.; Shofty, R.; Kirshenbaum, D.; Uretzky, G.; Oron, U.; Ben-Haim, S. A. Three-Dimensional Endocardial Impedance Mapping: A New Approach for Myocardial Infarction Assessment. *Am J Physiol Hear. Circ Physiol* **2001**, *280* (1), H179-88. https://doi.org/10.1152/ajpheart.2001.280.1.H179.

(285) Cinca, J.; Warren, M.; Carreno, A.; Tresanchez, M.; Armadans, L.; Gomez, P.; Soler-Soler, J. Changes in Myocardial Electrical Impedance Induced by Coronary Artery Occlusion in Pigs with and without Preconditioning: Correlation with Local ST-Segment Potential and Ventricular Arrhythmias. *Circulation* **1997**, *96* (9), 3079–3086. https://doi.org/10.1161/01.cir.96.9.3079.

(286) Jorge, E.; Amoros-Figueras, G.; Garcia-Sanchez, T.; Bragos, R.; Rosell-Ferrer, J.; Cinca, J. Early Detection of Acute Transmural Myocardial Ischemia by the Phasic Systolic-Diastolic Changes of Local Tissue Electrical Impedance. *Am J Physiol Hear. Circ Physiol* **2016**, *310* (3), H436-43. https://doi.org/10.1152/ajpheart.00754.2015.

(287) Kucera, J. P.; Rohr, S.; Kleber, A. G. Microstructure, Cell-to-Cell Coupling, and Ion Currents as Determinants of Electrical Propagation and Arrhythmogenesis. *Circ Arrhythm Electrophysiol* **2017**, *10* (9). https://doi.org/10.1161/CIRCEP.117.004665.

(288) Carmeliet, E. Conduction in Cardiac Tissue. Historical Reflections. *Physiol Rep* **2019**, *7* (1), e13860. https://doi.org/10.14814/phy2.13860.

(289) Rohr, S. Role of Gap Junctions in the Propagation of the Cardiac Action Potential. *Cardiovasc Res* **2004**, *62* (2), 309–322. https://doi.org/10.1016/j.cardiores.2003.11.035.

(290) Schaefer, M.; Gross, W.; Ackemann, J.; Gebhard, M. M. The Complex Dielectric Spectrum of Heart Tissue during Ischemia. *Bioelectrochemistry* **2002**, *58* (2), 171–180. https://doi.org/10.1016/s1567-5394(02)00152-4.

(291) Garcia, S.; Albaghdadi, M. S.; Meraj, P. M.; Schmidt, C.; Garberich, R.; Jaffer, F. A.; Dixon, S.; Rade, J. J.; Tannenbaum, M.; Chambers, J.; Huang, P. P.; Henry, T. D. Reduction in ST-Segment Elevation Cardiac Catheterization Laboratory Activations in the United States During COVID-19 Pandemic. *J Am Coll Cardiol* **2020**, *75* (22), 2871–2872.

https://doi.org/10.1016/j.jacc.2020.04.011.

(292) Huet, F.; Prieur, C.; Schurtz, G.; Gerbaud, E.; Manzo-Silberman, S.; Vanzetto, G.; Elbaz, M.; Tea, V.; Mercier, G.; Lattuca, B.; Duflos, C.; Roubille, F. One Train May Hide Another: Acute Cardiovascular Diseases Could Be Neglected Because of the COVID-19 Pandemic. *Arch. Cardiovasc. Dis.* **2020**, *113* (5), 303–307. https://doi.org/10.1016/j.acvd.2020.04.002.

(293) Dandel, M.; Lehmkuhl, H.; Knosalla, C.; Suramelashvili, N.; Hetzer, R. Strain and Strain Rate Imaging by Echocardiography - Basic Concepts and Clinical Applicability. *Curr Cardiol Rev* **2009**, *5* (2), 133–148. https://doi.org/10.2174/157340309788166642.

(294) Korte, T.; Fuchs, M.; Guener, Z.; v Bonin, J.; de Sousa, M.; Niehaus, M.; Tebbenjohanns, J.; Drexler, H. In-Vivo Electrophysiological Study in Mice with Chronic Anterior Myocardial Infarction. *J Interv Card Electrophysiol* **2002**, *6* (2), 121–132. https://doi.org/10.1023/a:1015359332161.

(295) Boukens, B. J.; Rivaud, M. R.; Rentschler, S.; Coronel, R. Misinterpretation of the Mouse ECG: "Musing the Waves of Mus Musculus." *J Physiol* **2014**, *592* (21), 4613–4626. https://doi.org/10.1113/jphysiol.2014.279380.

(296) Gehrmann, J.; Frantz, S.; Maguire, C. T.; Vargas, M.; Ducharme, A.; Wakimoto, H.; Lee, R. T.; Berul, C. I. Electrophysiological Characterization of Murine Myocardial Ischemia and Infarction. *Basic Res Cardiol* **2001**, *96* (3), 237–250. https://doi.org/10.1007/s003950170054.

(297) Zhang, S. S.; Shaw, R. M. Multilayered Regulation of Cardiac Ion Channels. *Biochim Biophys Acta* **2013**, *1833* (4), 876–885. https://doi.org/10.1016/j.bbamcr.2012.10.020.

(298) Cutler, M. J.; Jeyaraj, D.; Rosenbaum, D. S. Cardiac Electrical Remodeling in Health and Disease. *Trends Pharmacol Sci* **2011**, *32* (3), 174–180. https://doi.org/10.1016/j.tips.2010.12.001.

(299) Ashtari, K.; Nazari, H.; Ko, H.; Tebon, P.; Akhshik, M.; Akbari, M.; Alhosseini, S. N.; Mozafari, M.; Mehravi, B.; Soleimani, M.; Ardehali, R.; Ebrahimi Warkiani, M.; Ahadian, S.; Khademhosseini, A. Electrically Conductive Nanomaterials for Cardiac Tissue Engineering. *Adv Drug Deliv Rev* **2019**, *144*, 162–179. https://doi.org/10.1016/j.addr.2019.06.001.

(300) Qiao, Y.; Zhu, B.; Tian, A.; Li, Z. PEG-Coated Gold Nanoparticles Attenuate Beta-Adrenergic Receptor-Mediated Cardiac Hypertrophy. *Int J Nanomedicine* **2017**, *12*, 4709–4719. https://doi.org/10.2147/IJN.S130951.

(301) O'Rourke, S. A.; Dunne, A.; Monaghan, M. G. The Role of Macrophages in the Infarcted Myocardium: Orchestrators of ECM Remodeling. *Front Cardiovasc Med* **2019**, *6*, 101. https://doi.org/10.3389/fcvm.2019.00101.

(302) Kim, Y.; Nurakhayev, S.; Nurkesh, A.; Zharkinbekov, Z.; Saparov, A. Macrophage Polarization in Cardiac Tissue Repair Following Myocardial Infarction. *Int J Mol Sci* **2021**, *22* (5). https://doi.org/10.3390/ijms22052715.

(303) Spiller, K. L.; Nassiri, S.; Witherel, C. E.; Anfang, R. R.; Ng, J.; Nakazawa, K. R.; Yu, T.;

Vunjak-Novakovic, G. Sequential Delivery of Immunomodulatory Cytokines to Facilitate the M1-to-M2 Transition of Macrophages and Enhance Vascularization of Bone Scaffolds. *Biomaterials* **2015**, *37*, 194–207. https://doi.org/10.1016/j.biomaterials.2014.10.017.

(304) Badylak, S. F.; Valentin, J. E.; Ravindra, A. K.; McCabe, G. P.; Stewart-Akers, A. M. Macrophage Phenotype as a Determinant of Biologic Scaffold Remodeling. *Tissue Eng Part A* **2008**, *14* (11), 1835–1842. https://doi.org/10.1089/ten.tea.2007.0264.

(305) Spiller, K. L.; Anfang, R. R.; Spiller, K. J.; Ng, J.; Nakazawa, K. R.; Daulton, J. W.; Vunjak-Novakovic, G. The Role of Macrophage Phenotype in Vascularization of Tissue Engineering Scaffolds. *Biomaterials* **2014**, *35* (15), 4477–4488. https://doi.org/10.1016/j.biomaterials.2014.02.012.

(306) Hibino, N.; Yi, T.; Duncan, D. R.; Rathore, A.; Dean, E.; Naito, Y.; Dardik, A.; Kyriakides, T.; Madri, J.; Pober, J. S.; Shinoka, T.; Breuer, C. K. A Critical Role for Macrophages in Neovessel Formation and the Development of Stenosis in Tissue-Engineered Vascular Grafts. *FASEB J* **2011**, *25* (12), 4253–4263. https://doi.org/10.1096/fj.11-186585.

(307) Groenewegen, A.; Rutten, F. H.; Mosterd, A.; Hoes, A. W. Epidemiology of Heart Failure. *Eur J Hear. Fail* **2020**, *22* (8), 1342–1356. https://doi.org/10.1002/ejhf.1858.

(308) Roger, V. L. Epidemiology of Heart Failure: A Contemporary Perspective. *Circ Res* **2021**, *128* (10), 1421–1434. https://doi.org/10.1161/CIRCRESAHA.121.318172.

(309) Henkel, D. M.; Redfield, M. M.; Weston, S. A.; Gerber, Y.; Roger, V. L. Death in Heart Failure: A Community Perspective. *Circ Hear. Fail* **2008**, *1* (2), 91–97. https://doi.org/10.1161/CIRCHEARTFAILURE.107.743146.

(310) Phillips, J. C.; Hardy, D. J.; Maia, J. D. C.; Stone, J. E.; Ribeiro, J. V; Bernardi, R. C.; Buch, R.; Fiorin, G.; Henin, J.; Jiang, W.; McGreevy, R.; Melo, M. C. R.; Radak, B. K.; Skeel, R. D.; Singharoy, A.; Wang, Y.; Roux, B.; Aksimentiev, A.; Luthey-Schulten, Z.; Kale, L. V; Schulten, K.; Chipot, C.; Tajkhorshid, E. Scalable Molecular Dynamics on CPU and GPU Architectures with NAMD. *J Chem Phys* **2020**, *153* (4), 44130. https://doi.org/10.1063/5.0014475.

(311) Vanommeslaeghe, K.; Hatcher, E.; Acharya, C.; Kundu, S.; Zhong, S.; Shim, J.; Darian, E.; Guvench, O.; Lopes, P.; Vorobyov, I.; Mackerell A. D., J. CHARMM General Force Field: A Force Field for Drug-like Molecules Compatible with the CHARMM All-Atom Additive Biological Force Fields. *J Comput Chem* **2010**, *31* (4), 671–690. https://doi.org/10.1002/jcc.21367.

(312) Darden, T.; York, D.; Pedersen, L. Particle Mesh Ewald: AnN·log(N) Method for Ewald Sums in Large Systems. *J. Chem. Phys.* **1993**, *98* (12), 10089–10092. https://doi.org/10.1063/1.464397.

(313) Feller, S. E.; Zhang, Y.; Pastor, R. W.; Brooks, B. R. Constant Pressure Molecular Dynamics Simulation: The Langevin Piston Method. *J. Chem. Phys.* **1995**, *103* (11), 4613–4621. https://doi.org/10.1063/1.470648.

(314) Hopkins, C. W.; Le Grand, S.; Walker, R. C.; Roitberg, A. E. Long-Time-Step Molecular Dynamics through Hydrogen Mass Repartitioning. *J Chem Theory Comput* **2015**, *11* (4), 1864–1874. https://doi.org/10.1021/ct5010406.

(315) Wright, L. B.; Rodger, P. M.; Corni, S.; Walsh, T. R. GolP-CHARMM: First-Principles Based Force Fields for the Interaction of Proteins with Au(111) and Au(100). *J Chem Theory Comput* **2013**, *9* (3), 1616–1630. https://doi.org/10.1021/ct301018m.

(316) Humphrey, W.; Dalke, A.; Schulten, K. VMD: Visual Molecular Dynamics. *J Mol Graph* **1996**, *14* (1), 27-28,33-38. https://doi.org/10.1016/0263-7855(96)00018-5.

(317) Blackburn, N. J. R.; Sofrenovic, T.; Kuraitis, D.; Ahmadi, A.; McNeill, B.; Deng, C.; Rayner, K. J.; Zhong, Z.; Ruel, M.; Suuronen, E. J. Timing Underpins the Benefits Associated with Injectable Collagen Biomaterial Therapy for the Treatment of Myocardial Infarction. *Biomaterials* **2015**, *39*, 182–192. https://doi.org/10.1016/j.biomaterials.2014.11.004.

(318) Patten, R. D.; Hall-Porter, M. R. Small Animal Models of Heart Failure: Development of Novel Therapies, Past and Present. *Circ Hear. Fail* **2009**, *2* (2), 138–144. https://doi.org/10.1161/CIRCHEARTFAILURE.108.839761.

(319) Ahmadi, A.; Thorn, S. L.; Alarcon, E. I.; Kordos, M.; Padavan, D. T.; Hadizad, T.; Cron, G. O.; Beanlands, R. S.; DaSilva, J. N.; Ruel, M.; deKemp, R. A.; Suuronen, E. J. PET Imaging of a Collagen Matrix Reveals Its Effective Injection and Targeted Retention in a Mouse Model of Myocardial Infarction. *Biomaterials* **2015**, *49*, 18–26. https://doi.org/10.1016/j.biomaterials.2015.01.016.

(320) Camci-Unal, G.; Aubin, H.; Ahari, A. F.; Bae, H.; Nichol, J. W.; Khademhosseini, A. Surface-Modified Hyaluronic Acid Hydrogels to Capture Endothelial Progenitor Cells. *Soft Matter* **2010**, *6* (20), 5120–5126. https://doi.org/10.1039/c0sm00508h.

(321) Hanssen, N. M. J.; Scheijen, J. L. J. M.; Jorsal, A.; Parving, H.-H.; Tarnow, L.; Rossing, P.; Stehouwer, C. D. A.; Schalkwijk, C. G. Higher Plasma Methylglyoxal Levels Are Associated With Incident Cardiovascular Disease in Individuals With Type 1 Diabetes: A 12-Year Follow-up Study. *Diabetes* **2017**, *66* (8), 2278–2283. https://doi.org/10.2337/db16-1578.

(322) Villanueva, M.; Michie, C.; Parent, S.; Kanaan, G. N.; Rafatian, G.; Kanda, P.; Ye, B.; Liang, W.; Harper, M.-E.; Davis, D. R. Glyoxalase 1 Prevents Chronic Hyperglycemia Induced Heart-Explant Derived Cell Dysfunction. *Theranostics* **2019**, *9* (19), 5720–5730. https://doi.org/10.7150/thno.36639.

(323) Chiong, M.; Wang, Z. V; Pedrozo, Z.; Cao, D. J.; Troncoso, R.; Ibacache, M.; Criollo, A.; Nemchenko, A.; Hill, J. A.; Lavandero, S. Cardiomyocyte Death: Mechanisms and Translational Implications. *Cell Death Dis.* **2011**, *2* (12), e244. https://doi.org/10.1038/cddis.2011.130.

(324) Cascio, W. E.; Johnson, T. A.; Gettes, L. S. Electrophysiologic Changes in Ischemic Ventricular Myocardium: I. Influence of Ionic, Metabolic, and Energetic Changes. *J. Cardiovasc. Electrophysiol.* **1995**, *6* (11), 1039–1062. https://doi.org/10.1111/j.1540-8167.1995.tb00381.x.

(325) Williamson, C. M.; Lee, W.; DeCasien, A. R.; Lanham, A.; Romeo, R. D.; Curley, J. P. Social Hierarchy Position in Female Mice Is Associated with Plasma Corticosterone Levels and Hypothalamic Gene Expression. *Sci. Reports 2019 91* **2019**, *9* (1), 1–14. https://doi.org/10.1038/s41598-019-43747-w.

(326) Pullen, A. B.; Kain, V.; Serhan, C. N.; Halade, G. V. Molecular and Cellular Differences in Cardiac Repair of Male and Female Mice. *J. Am. Heart Assoc.* **2020**, *9* (8). https://doi.org/10.1161/JAHA.119.015672.

(327) Morsink, M.; Severino, P.; Luna-Ceron, E.; Hussain, M. A.; Sobahi, N.; Shin, S. R. Effects of Electrically Conductive Nano-Biomaterials on Regulating Cardiomyocyte Behavior for Cardiac Repair and Regeneration. *Acta Biomater.* **2021**. https://doi.org/10.1016/j.actbio.2021.11.022.

(328) Lin, X.; Liu, Y.; Bai, A.; Cai, H.; Bai, Y.; Jiang, W.; Yang, H.; Wang, X.; Yang, L.; Sun, N.; Gao, H. A Viscoelastic Adhesive Epicardial Patch for Treating Myocardial Infarction. *Nat. Biomed. Eng.* **2019**, *3* (8), 632–643. https://doi.org/10.1038/s41551-019-0380-9.